Unassisted Photocatalytic Overall Pure Water Splitting Using III-Nitride Nanostructures

Mohammad Faqrul Alam Chowdhury

Department of Electrical and Computer Engineering
Faculty of Engineering, McGill University, Montréal
August 2018

A thesis submitted to McGill University in partial fulfillment of the requirements of the degree of Doctor of Philosophy

Dedication

To people who breathed their last during my PhD pursuit, however, had noteworthy influence on myself and my affairs during their lifetime, in numerous aspects:

- *Prof. Mohammad Ali Chowdhury* (EEE, BUET), who had amply motivated me, like he did to countless of his students, both as an exemplary teacher and as a better human being,
- *Muhammad Ali*, the great boxer, humanitarian, and the activist, who had shown extraordinary strength and courage in the face of adversity to overcome insurmountable odds,
- *Dr. Mahabubul Alam*, my eldest brother and the fatherly figure who closely supervised me throughout my academic career, and
- *Mst. Meherunnesa Begum*, my sister, the most loving and caring member of my family.

Significantly, to my mother *Khaleda Begum*, who has shown noticeable endurance while confronting all the challenges, and to all my family members, for their patience and support in every endeavor.

And in general, to all those who find themselves facing a situation in life when the question of why seems to be unanswerable, yet who seek for and side with the truth which may not necessarily be in their favor.

Table of Contents

Chapter-1

Introduction

Chapter-2

Status, Challenges and Scopes for Efficient and Stable Artificial Photosynthesis

Chapter-3

Synthesis, Characterization and Performance Evaluation of Group III-Nitride Nanostructures

Chapter-4

Group III-Nitride Nanowire Heterostructures for Efficient Photocatalytic Hydrogen Production

Chapter-5

A Photochemical Diode Artificial Photosynthesis System for Unassisted High Efficiency Overall Pure Water Splitting

Chapter-6

An Industry-ready Artificial Photosynthesis Device?

Chapter-7

Optically Active Dilute-Antimonide III-Nitride Nanostructures for Solar Energy Harvesting

Chapter-8

Synergetic Effect of In and Sb Incorporation into GaN Nanostructures in Dilute-Sb Regime

Chapter-9

Conclusion and Proposals for Future Direction

Acknowledgement

All praise be to the Almighty God, the Most Gracious, the Most Merciful, for the blessings of the sound health and sanity, the knowledge, enthusiasm and the tenacity He has bestowed upon me during my PhD pursuit. In addition, this thesis would not have been possible without the help and support of many; and I would like to take this as a golden opportunity for me to acknowledge their valuable contributions and convey my heartfelt thanks and gratitude towards them.

I am heartily thankful to my supervisor, Prof. Zetian Mi, for both inspiring and guiding me. Sometimes, it's all his selfless time and care that kept me going without much to complain about the seemingly unsurmountable challenges. He has provided consistent encouragement, guidance and support throughout my thesis works. Significantly, he has introduced me to the arena of competitive as well as state-of-the-art innovative scientific research, the subtlety of clear and accessible scientific writing, the rigors of analytical ability and adherence, the spirit of intellectual integrity and most importantly, the joy of inquisitive exploration. Not to mention, he has always set higher standards and goals to be achieved while pushing me harder towards the apparent limit. And as tiresome as it is, one cannot but appreciate the worth of it once he or she approaches the finishing line after all the arduous efforts. Furthermore, I would like to express my sincere gratitude to Prof. Mi for giving me the free access to the resources in such a well-equipped research facility at McGill University, trusting and relying on me with the usage of the state-of-the-art sophisticated equipment, allowing me to explore challenging ideas without much restrictions, and needless to mention, being available literally 24/7 to provide feedback.

Throughout my journey in this research lab, I am indebted to all my colleagues for their time, suggestions and discussion, support and contribution in my work, their passion for excellence and compassion towards fellow co-workers that prevented the workplace from being dull and gloomy. It is entirely possible that I would have become a monotonous workaholic without really enjoying the work, had it not been my colleagues, with their smiley faces, patiently tolerating hours of my discussions on diverse topics. I acknowledge

the contribution from Srinivas Vanka, Dr. Yichen Wang and Renjie Wang for their assistance with the day to day maintenance of the giant MBE machine to keep it healthy. Special thanks to my other colleagues - Dr. S. Zhao and Dr. Yong-Ho Ra for their support during the MBE maintenances, and Dr. M. G. Kibria for all his discussions, comments and cooperation during the early investigations on efficient photocatalytic water splitting.

I would like to convey my heartfelt gratitude to Dr. Michel L. Trudeau at Science des Matériaux, IREQ, Hydro-Québec and Dr. David Liu at FEMR, McGill University for carrying out number of TEM studies on my samples. Special thanks to Dr. Michel L. Trudeau, for being there for me whenever I needed the feedback. I am grateful to the staff members of McGill Nanotools Microfab (MNM) including Dr. Matthieu Manini, Donald Berry, Jun Lee, Dr. Lino Eugene, Sasa Ristic and Zhao Lu for their technical support, training and discussions on my research.

I am cordially grateful to Prof. Thomas Szkopek and Prof. K. H. Bevan for serving in my PhD evaluation committee by providing with their invaluable suggestions, comments and guidance on my thesis work. I gladly appreciate my PhD defense committee members Prof. Sangyong Jeon, Prof. Geza Joos, Prof. Pouya Valizadeh, Prof. Marta Cerruti, Prof. Xiaozhe Wang and Prof. Patanjali Kambhampati for their consents and time with constructive comments and suggestions on my thesis.

My sincere thanks to Omer Nguena-Timo and Mohammed Senoussaoui for helping me with the draft of the abstract in French, Tiffany Wang for editing it and Nick Pant for cross-checking the relevance and accuracy of scientific terminologies in French.

On a broader perspective, I would like to acknowledge the contribution of some people that I used to interact with on a daily basis, yet who may never come across in touch with this dissertation – the ocean of people in the Metro that never let me go lonely with their lively activities, be it in the freezing cold of the snowy winter or in the gentle breeze of the colorful summer, the staffs at the coffee-shop and at the restaurant, who remembered the combination of my favorite coffee and the ingredients of my sandwich for all these days, specially the one who consistently insisted me to smile whenever I looked tensed reminding me that – It does not cost much to smile, rather smiling is a charity to your fellow beings.

And on this occasion, I also thankfully remember some people, without whom being in my life and affairs, this entire work would have been finished two years earlier, yet they taught me patience and how not to lose sight of the goal! Connecting the dots back, it became evident that their very existence was significantly important for my transformation into who I am today. Additionally, there are those who did not pay back when it was due, be it with their time, assistance, support or service – knowingly or unknowingly, you only made me self-dependent and hard-working, and I sincerely thank all of you for that. In this context, I gratefully thank Prof. Mi again for being patient during my tough times, for being considerate and supportive throughout all my personal problems during the PhD pursuit, providing me with great care, courage and motivation to face and overcome those.

Most of all, I appreciate the continuous support and love from my mother and all my family members, who among all that walk on earth are dearer to me, for being patient on me even though I failed to be there many times when they needed me, and mostly for not giving up on me. My heartfelt thanks to my sister Shamima Begum for providing with her never-ending support and encouragement, to my brothers Sydul Alam, Fasiul Alam and Shamsul Alam for taking diligent care of the family back in home during my absence, thereby allowing me to focus on the work herein. I acknowledge the uninterrupted support from my brother Dr. Jahangir Alam and his wife Dr. Syeda Fatema Zohra throughout my stay in Montreal. I also thank all my nephews and nieces for their innocent and playful interactions, which often made me forget about the stress of workload, and occasionally gave me the realization that – answering to their unlimited, creative, sometimes complex questions is much harder than addressing an experiment-related scientific problem in lab.

I sincerely acknowledge the Vanier Canada Graduate Scholarships (VCGS) for their financial support during my PhD pursuit, which not only gave me financial freedom but also provided the motivation to push towards the apparent limit. The work herein is supported by the Natural Sciences and Engineering Research Council of Canada (NSERC), the Climate Change and Emissions Management Corporation (CCEMC) and the Emission Reduction Alberta (ERA).

Contribution of Authors

The candidate and his supervisor Prof. Zetian Mi primarily conceived the ideas, designed the studies included in this dissertation, and wrote the associated manuscripts in close correlation with each other. All the samples used in this work were prepared and grown by the candidate himself using plasma-assisted MBE. The XPS analyses were performed by the candidate at McGill Institute for Advanced Materials (MIAM). The SEM imaging and analyses were conducted by the candidate both at the Facility for Electron Microscopy Research (FEMR), McGill University and in Université de Montréal. The XRD measurements were performed by the candidate with assistance from Mr. Christophe Chabanier at Institut national de la recherche scientifique (INRS), Varennes (Quebec), Canada. The candidate performed all the Photoluminescence measurements included in this dissertation. The micro-Raman measurements and some of the Photoluminescence experiment were performed by the candidate at Laboratoire de caractérisation des matériaux (LCM) in Université de Montréal. The TEM imaging and analyses were mostly carried out by M. L. Trudeau at Science des Matériaux, IREQ, Hydro-Québec, Canada. Some of the TEM analyses were performed by Dr. David Liu at Facility for Electron Microscopy Research (FEMR), McGill University. The candidate actively participated in the discussion and analyses of the microscopic data, contributed in planning and designing the characterization experiments and organizing the results. The photocatalytic water splitting experiments were performed primarily by the candidate, with some specific exceptions. Dr. M. G. Kibria contributed partly with water splitting experiments in Chapter 4, and Xiangjiu Guan performed the photocatalytic experiments and stability test in Chapter 6 under close supervision of the candidate and Prof. Zetian Mi. Qing Shi and Prof. Hong Guo at the Department of Physics, McGill University actively collaborated on the first-principle analysis of dilute-antimonide GaSbN and contributed to the result analyses and discussions with the candidate and Prof. Mi to investigate the correlations between theoretical estimations and experimental findings. The candidate and Prof. Mi frequently participated in the discussion on the results to decide and design future course of actions.

However, this dissertation work would not have been possible without the support and assistance of many other individuals. Dr. H. P. T. Nguyen and Dr. S. Zhao contributed by training the candidate for the operation and maintenance of the MBE system at the initial stage of PhD study before any experiment was conducted for this dissertation. The candidate worked closely with Dr. M. G. Kibria to familiarize himself with the photocatalytic experiments at the early stage of his PhD study. Subsequently, the candidate contributed to optimize the experimental conditions and prepare the procedures for efficiency calculations. Srinivas Vanka helped the candidate with some wafer cleaning for dilute-Sb GaSbN growths, and with the preliminary photoelectrochemical investigations of GaSbN on Si solar cells. Xianhe Liu, Dr. Yong-Ho Ra, Dr. Binh Huy Le and Yuanpeng Yu occasionally helped the candidate with the optical alignments for Photoluminescence measurements.

This thesis work is the compilation of the major outcomes from multiple selected scientific projects in which the candidate has been directly involved with significant contribution. However, some individuals have contributed specifically in parts of the manuscripts associated with different chapters, as given below:

Chapter 4

Manuscript 1: **Faqrul A. Chowdhury**, Z. Mi, M. G. Kibria, and M. L. Trudeau, "Group III-nitride Nanowire Structures for Photocatalytic Hydrogen Evolution under Visible Light Irradiation", ***APL Materials***, 3, 104408 (2015). **(Editors' Pick, 2015)**

Author contributions: Z.M. and F.A.C. designed the study. F.A.C. conducted MBE growths and the photocatalytic experiments. M.G.K contributed partly in the sample testing. F.A.C performed the characterization measurements and theoretical estimations. M.L.T. and F.A.C. contributed to the TEM analysis. F.A.C., M.G.K. and Z. M. contributed to the result analysis and discussions.

Manuscript 2: M. G. Kibria, **F. A. Chowdhury**, S. Zhao, B. AlOtaibi, M. L. Trudeau, H. Guo, and Z. Mi, "Visible Light Driven Efficient Overall Water Splitting Using p-type Group III-Nitride Nanowire Arrays", ***Nature Communications***, 6, 6797 (2015).

Author contributions: Z.M. and M.G.K. designed the study. F.A.C., S.Z. and Z.M. conducted the MBE growth. M.G.K. and F.A.C. conducted the photocatalytic experiments. M.G.K. and F.A.C. performed the SEM and XPS measurements. M.L.T. and M.G.K. contributed to the TEM analysis. F.A.C. and M.G.K. contributed to efficiency calculation. B.A. and M.G.K. performed the OCP analysis. M.G.K., F.A.C., H.G. and Z.M. contributed to result analysis and discussions. [Chapter 4 is mostly based on Manuscript 1, Only a small discussion from Manuscript 2 is included in the chapter to ensure the continuity.]

Chapter 5

Manuscript: **Faqrul A. Chowdhury**, M. L. Trudeau, H. Guo, and Z. Mi, "A Photochemical Diode Artificial Photosynthesis System for Unassisted High Efficiency Overall Pure Water Splitting", ***Nature Communications***, 9:1707 (2018). **(Featured, Editors' Highlight,** *Nature Communications*; **Collection: Green Chemistry/**Water Splitting, *Nature***)**

Author contributions: F.A.C. and Z.M. designed the study, conducted the MBE growths and wrote the manuscript. F.A.C. performed the photocatalytic water splitting experiments, characterization measurements and theoretical estimations. M.L.T. and F.A.C. contributed to the TEM imaging and analysis. F.A.C., Z.M. and H.G. analyzed and discussed the results. F.A.C. prepared the illustrations.

Chapter 6

Manuscript: **Faqrul A. Chowdhury***, Xiangjiu Guan*, Yongjie Wang, Nick Pant, Srinivas Vanka, Michel L. Trudeau, Liejin Guo, Lionel Vayssieres, and Zetian Mi, "Stable, Efficient and Industry-friendly nanowire device for sustainable solar hydrogen generation", under review, (August 2018). **['*'** ***co-first authors***]

Author contributions: Z.M., L.V. and L.G. proposed the project. The experiments were conducted at McGill University under the direct supervision of Z.M. F.A.C conducted the MBE growths. X.G. conducted the photocatalytic experiments. X.G. and F.A.C. performed SEM measurements. N.P. contributed to part of the stability test. F.A.C., Y.W. and X.G. performed the XPS measurements. M.L.T., X.G. and F.A.C. contributed to the TEM analysis. F.A.C. contributed to the PL measurement and efficiency calculation. X.G. and Y.W. conducted the electro-catalytic test. F.A.C. prepared the illustrations. F.A.C., X.G. and Z.M. analyzed the results and wrote the manuscript.

Chapter 7

Manuscript: **F. A. Chowdhury**, S. M. Sadaf, Q. Shi, Y.-C. Chen, H. Guo, and Z. Mi, "Optically Active Dilute-Antimonide III-Nitride Nanostructures for Optoelectronic Devices", ***Applied Physics Letters***, 111, 061101 (2017). **(Featured, Cover Article)**

Author contributions: Z.M. and F.A.C. designed the study. F.A.C. conducted the MBE growth and developed the material. Q.S., Y.-C.C. and H.G. performed the first principle calculations. F.A.C. conducted the experiments and measurements to characterize the material. S.M.S. fabricated the LED devices. S.M.S and F.A.C. measured the performance of the devices. F.A.C., Z.M., Q.S. and H.G. discussed the results and analyzed the correlation between theoretical calculations and experimental results. F.A.C. and Z.M. wrote the manuscript with contribution from other co-authors.

[N.B.: The characterization and performance analysis of GaSbN LEDs are not included in this chapter. Srinivas Vanka and Dr. Yichen Wang helped the candidate in conducting the preliminary investigations on GaSbN performance for PEC water splitting and CO_2 reduction, respectively.]

Chapter 8

Author contributions: F.A.C. conducted the MBE growths and developed the material, performed the experiments and measurements to characterize the material. M.L.T. and F.A.C. contributed to the TEM analysis.

List of Tables

List of Figures

List of Acronyms

APCE	Absorbed Photon Conversion Efficiency
AQE	Apparent Quantum Efficiency
ARXPS	Angle Resolved X-ray Photoelectron Spectroscopy
BEP	Beam Equivalent Pressure
BF	Bright Field
CB	Conduction Band
CBM	Conduction Band Minimum
DFT	Density Function Theory
DOS	Density of States
ECE	Energy Conversion Efficiency
EDS	Energy Dispersive Spectrum
EDXS	Energy Dispersive X-Ray Spectroscopy
EELS	Electron Energy Loss Spectroscopy
FWHM	Full Width at Half Maximum
HAADF	High Angle Annular Dark Field
HF	Hydrofluoric Acid
HRTEM	High Resolution Transmission Electron Microscopy
IQE	Internal Quantum Efficiency
IR	Infrared
LED	Light Emitting Diode
LO	Longitudinal Optical
LVM	Local Vibrational Modes
MBE	Molecular Beam Epitaxy
MQW	Multi Quantum Well
NHE	Normal Hydrogen Electrode
OCP	Open Circuit Potential
OWS	Overall Water Splitting
PEC	Photoelectrochemical

PL	Photoluminescence
RF	Radio Frequency
RIE	Reactive-Ion Etching
RTA	Rapid Thermal Annealing
SAG	Selective Area Growth
SEM	Scanning Electron Microscopy
SIMS	Secondary Ion Mass Spectroscopy
STH	Solar-to-hydrogen
STEM	Scanning Transmission Electron Microscopy
STEM-SE	Scanning Transmission Electron Microscopy-Secondary Electron
TCD	Thermal Conductivity Detector
TEM	Transmission Electron Microscopy
UV	Ultra-violet
VB	Valence Band
VBM	Valence Band Maximum

Abstract

Direct solar water splitting is considered one of the most promising approaches for an environmental-friendly renewable and sustainable energy resource. Significantly, the capacity to directly split water is ideally suited for large-scale hydrogen fuel production. While tremendous progress has been made in photoelectrochemical (PEC) water splitting in the past decades, it is still not suitable to split pure pH neutral water efficiently without bias or sacrificial agent. On the other hand, direct photocatalytic overall water splitting still suffers from critical issues including low efficiency and poor long-term stability. In this study, we demonstrate that, through controllable dopant incorporation in Ga(In)N nanowire heterostructure, the surface charge properties can be tuned to provide the appropriate Fermi level and/or band bending. This allows the photochemical water splitting to proceed at high rate with an apparent quantum efficiency (AQE) ~20%. Furthermore, the AQE can be boosted up to ~45% in a Ga(In)N photochemical diode nanostructure by creating a p-p^+ lateral junction at nanoscale, to induce unidirectional flow of photogenerated charge carriers. Consequently, a solar-to-hydrogen (STH) efficiency of ~3.3% is achieved, which is significantly higher than many of the state-of-the-art efficiencies in direct water splitting. We have further shown that, by combining the synergistic effect of water oxidation and proton reduction co-catalysts (Co_3O_4 and Rh/Cr_2O_3, respectively) and by optimizing the surface electronic properties, *p*-GaN/InGaN nanowires can exhibit substantially extended long-term performance-stability for >580 hrs in more realistic photocatalytic conditions, that is pure water and concentrated sunlight. Such remarkable long-term stability is the longest ever measured for any semiconductor photocatalysts/photoelectrodes without protection/passivation layers in unassisted solar water splitting with STH >1%. This study further explores the effect of Sb-incorporation in Ga(In)N to selectively tune the band-edges for enhanced absorption. The Ga(In)N nanowire photocatalytic system in this study not only outperforms most of the typical photocatalysts reported so far, in the aspects of both STH efficiency and stability for unassisted overall photocatalytic or photochemical water splitting, but also provides critical insight in achieving high efficiency artificial photosynthesis, including the efficient and selective reduction of CO_2 to hydrocarbon fuels.

Abrégé

L’utilisation de la lumière solaire pour décomposer l’eau en atomes d’oxygène et d’hydrogène (photolyse de l’eau) est considéré comme l'une des approches les plus prometteuses et respectueuses de l'environnement pour produire des ressources énergétiques renouvelables et durables. Notamment, cette approche permet la production d'hydrogène à grande échelle. Dans ces dernières décennies, d'énormes efforts ont été effectués afin d’améliorer les cellules photoélectriques utilisées dans la photolyse de l’eau. Cependant, ces cellules ne permettent toujours pas de décomposer l'eau pure au pH neutre efficacement sans biais ou agent sacrificiel. La décomposition globale de l'eau par photocatalytique direct est toujours aussi peu efficace et peu fiable à long terme. Dans cette étude, nous démontrons que grâce à l'incorporation de dopant contrôlable dans les hétéro-structures Ga(In)N de nanofils, les propriétés de charges de surface peuvent être ajustées pour fournir un niveau adéquat de Fermi et/ou une bande de flexion adéquate. Ceci permet à la décomposition photochimique de l'eau à un taux élevé avec une efficacité quantique apparente (EQA) d'environ 20%. En outre, l'EQA peut être augmenté jusqu'à environ 45% dans une nanostructure de diode Ga(In)N photochimique en créant une jonction latérale p-p^+ à l'échelle nanométrique, afin d’induire un flux unidirectionnel de porteurs de charge photo-générés. Par conséquent, on atteint un rendement lumière-hydrogène (STH) d’environ 3,3%, ce qui est nettement plus élevé que la plupart des rendements par le dernier cri de la technologie utilisée pour la photolyse directe de l’eau. Nous avons également montré qu'en combinant l'effet synergique des co-catalyseurs d'oxydation de l'eau et celui de réduction des protons (Co_3O_4 et Rh/Cr_2O_3, respectivement) et en optimisant les propriétés électroniques de surface, les nanofils p-GaN/InGaN peuvent démontrer des performances avec une durée de plus de 580 heures dans de conditions photocatalytiques plus réalistes, spécifiquement, dans des conditions d’eau pure et de lumière solaire concentrée. Cette durée remarquable est la plus longue qui n’a jamais été mesurée pour la décomposition solaire artificielle non-assisté d’eau, dont le STH est supérieure à 1%, par des photoélectrodes/photocatalyseurs semi-conducteurs sans couches de protection/passivation. Cette étude explore en outre l'effet de l'incorporation de Sb dans

Ga(In)N pour ajuster les bords de bande sélectivement pour une meilleure absorption. Le système photocatalytique Ga(In)N de nanofils de cette étude surpasse la majorité des photocatalyseurs connus en fonction de l’efficacité STH et de la stabilité pour la décomposition d’eau, qui est non-assisté et photocatalytique ou photochimique globale. Également, il fournit des idées subtiles pour la réalisation de la photosynthèse artificielle à haute performance qui comprend la réduction efficace et sélective du CO_2 en hydrocarbures.

Chapter-1

Introduction

1.1 Overview

Exploration of alternative, renewable energy source is one of the most burning topics in scientific researches. Fossil fuels, having the ability to satiate the global energy crisis to some extent, lack significantly in environment-friendliness due to their emission of greenhouse gases; expensive nuclear plant is difficult to be built fast enough to cope up with the energy demand; wind energy, on the other hand, is limited by its low energy density and intermittency [1-4]. Accordingly, a future energy infrastructure based on hydrogen, having high energy-yield compared to other fuels [5], has been perceived as an ideal long-term solution to energy and environment related problems we face today [6-9]. Critical to this development, however, is the realization of a low-cost and scalable solar hydrogen generation process with a balance between minimized system complexity and maximized energy conversion efficiency and device longevity. In this context, photocatalytic and/or photoelectrochemical solar water splitting has emerged as one of the most promising approaches of hydrogen generation using a renewable energy source [6, 10-19]. Considerable efforts have been made in quest for a stable and efficient photocatalyst/photoelectrode since the first demonstration of photoelectrochemical water splitting on n-TiO_2 electrode in 1972 [20].

For the single absorber, the two-photon approach of photocatalytic water splitting (well known as S2 approach), is limited by an ideal (Shockley-Queisser) solar energy conversion efficiency (~34%). In practice, it possesses the potential for maximum feasible efficiency of ~10% considering the reasonable losses [21]. However, the realization of such high efficiency devices has remained extremely difficult due to the lack of suitable photocatalytic materials that possess optimum band-gap, desired conduction and valence band levels, and stability in harsh photocatalytic conditions. In this chapter, we discuss some of the fundamental concepts related to the design and choice of the photocatalyst.

1.2 Fundamentals of Photocatalytic Solar Water Splitting

Photoelectrochemical (PEC) and photochemical (or photocatalytic) water splitting are the two approaches ideally adopted in research community for utilizing photon-energy from the solar spectrum to generate hydrogen as a clean fuel by splitting water into its constituting components, i.e., H_2 and O_2 [4, 22-26]. Therefore, both photoelectrochemical (PEC) and photocatalytic water splitting systems have been intensively studied worldwide [27-41]. In PEC water splitting either, one or both electrodes can be semiconductor photocatalyst to capture solar energy, and a metallic conductor is commonly used to channel through the photogenerated carriers between the electrodes. Effective carrier separation and conduction in this system demands the application of external bias, highly conductive electrolyte and substrate, and requires current matching between the electrodes, and engineering band-edge alignment along the direction of carrier extraction in the tandem/multilayered photocatalysts. Photochemical dissociation of water, on the contrary, is a spontaneous and wireless approach of harnessing solar energy in which either both H_2 and O_2 are generated on the same catalyst surface, or on the electrodes which are mounted on the photocatalyst surface in the form of micro/nano-electrode, commonly defined as co-catalysts. This method, as simple and potentially efficient as it can be, suffers from the limitation of simultaneous production of H_2 and O_2 mixture that needs to be separated from the chamber for practical usage.

1.2.1 Overall Water Splitting (OWS)

Overall water splitting, commonly referred to as the balanced and stoichiometric dissociation of pure water into its constituents ($H_2:O_2 = 2:1$), is an uphill reaction where the solar energy is converted into chemical energy (in the form of hydrogen), resulting in a positive change of Gibbs free energy. As such, water splitting reaction has the capability to store ~237 kJ/mol of energy at 25 °C and 1 bar. However, the actual energy storage capacity and efficiency will greatly depend on the experimental condition.

$$H_2O \rightarrow 1/2O_2 + H_2, \quad \Delta G = +\,237.178 \text{ kJ mol}^{-1} \qquad \text{.....…….. (1)}$$

Figure 1-1 schematically illustrates the fundamental processes associated with the photocatalytic water splitting reaction on a photocatalyst in the simplest manner. Under the above-bandgap excitation ($h\nu > E_g$) of the photocatalyst (M), electron–hole pairs (e^-/h^+) can be generated within the photocatalyst (Fig. 1-1a), and the charge carriers (electrons and holes) can be energetically separated in conduction band (CB) and valence band (VB) respectively (Fig. 1-1b), assuming no defect level or impurity band inside the bandgap.

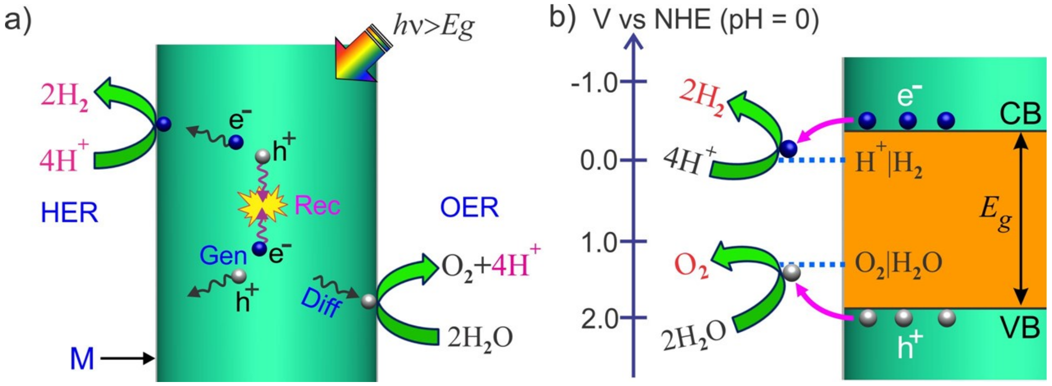

Figure 1-1: a) Simplified schematic illustration of the processes involved in photocatalytic water splitting on a photocatalyst (M). With the above-bandgap excitation, electron-hole pairs will be generated (Gen); followed by bulk recombination (Rec) the holes and electrons will diffuse (Diff) towards surface to participate in water oxidation and proton reduction reaction, respectively. b) Energy band representation of the water splitting process (under flat-band condition).

Photocatalytic efficiency of a catalyst is highly dependant on the efficient spatial separation and migration of the photogenerated carriers towards the reactive sites on the catalyst surface, where carrier transfers occur through the catalyst/electrolyte interface. In a non-ideal condition, charge carrier extraction efficiency is limited by the enhanced recombination probability in the bulk due to the larger size of the photocatalyst and increased defects that act as trapping and recombination centers. Therefore, the development of highly crystalline nanostructured photocatalyst, through precise engineering of the morphology and bandgap is of great interest. In a nanowire photocatalyst, where the carrier transport is no longer diffusion limited, the photogenerated holes and electrons can successfully migrate towards the nanowire/electrolyte interface and take part in water splitting reactions under flat-band condition. Neutral pH overall solar water splitting is a two-step process, where water (H_2O) molecules get oxidized first by the photogenerated holes from the valence band (oxygen evolution reaction, OER), as shown in equation 2, followed by the proton reduction (hydrogen evolution reaction, HER) by the photogenerated electrons from the conduction band (equation 3).

$$2H_2O \leftrightarrow O_2 + 4e^- + 4H^+; \quad E_{anodic} = 1.23 \text{ V} - 0.059 \text{ (pH), vs NHE} \qquad \text{.......... (2)}$$

$$4H^+ + 4e^- \leftrightarrow 2H_2; \quad E_{cathodic} = 0 \text{ V} - 0.059 \text{ (pH), vs NHE} \qquad \text{.......... (3)}$$

Assuming pH = 0, a high anodic potential of ~ 1.23 V (vs. NHE) is required ideally for water oxidation, which suggests that the photogenerated holes in the valence band maxima must have enough energy to drive the reaction forward. In other words, the potential associated with valence band maxima must be more positive than the anodic potential, as shown in Fig. 1-1b. Similarly, for the proton to be reduced on the photocatalyst surface by the extracted electrons, the conduction band minima of the photocatalyst needs to be more negative than the cathodic potential (0 V vs. NHE at pH = 0). The standard potentials required for various chemical reactions to proceed forward (oxidation and reduction by holes and electrons, respectively) are presented in Fig. 1-2 with respect to the conduction and valence band edges of GaN.

1.2.2 Half-Reactions (Test Reactions)

Photocatalytic overall water splitting has stringent requirement on a single-bandgap photocatalyst, as such the band-edges must straddle the water redox potentials to drive both the water oxidation and the proton reduction reaction forward using the photogenerated holes and electrons, respectively, for simultaneous production of O_2 and H_2. However, sacrificial reagents can be used in photochemical reactions to evaluate if a certain photocatalyst satisfies the thermodynamic and kinetic potentials for standalone water oxidation or proton reduction. The reactions are commonly known as half-reactions of water splitting and can be employed as test reactions for photocatalytic H_2 or O_2 evolution. The sacrificial reagents eventually contribute to the second half of the redox reaction, which must be more favourable compared to the second half of the overall water splitting reaction from thermodynamics and kinetics point of view.

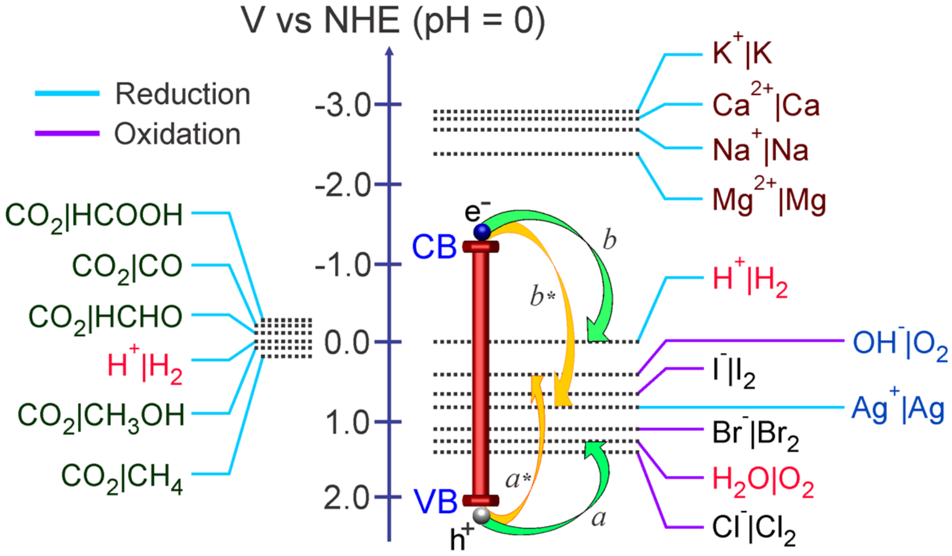

Figure 1-2: Band-edge positions of GaN (bandgap ~3.4 eV) are illustrated along with redox potentials of numerous aqueous electrolyte solution (right). For example, in overall pure water splitting, photogenerated hole (h^+) in valence band (VB) possesses enough over-potential and oxidizes water to produce O_2, whereas photogenerated electron (e^-) in conduction band (CB) reduces proton to produce H_2. The reduction potentials of CO_2 into various value-added products are also shown (left) along with proton reduction potential.

To explain further, for the photocatalytic reaction in an aqueous solution containing a reducing reagent (electron donors or hole scavengers) such as alcohol, sulfide or sulfite ion, the oxidation of a reducing reagent is more favorable than that of water. As shown in Fig. 1-2, the valence band of the photocatalyst needs to be more positive than +0.4 V to oxidize OH^- (*a**) compared to +1.23 V for H_2O oxidation (*a*). Therefore, in the presence of a reducing reagent, *e.g.* CH_3OH, hydrogen evolution will be accelerated in HER half-reaction, as depicted in Fig. 1-3a, provided that the photocatalyst meets the thermodynamic requirement for proton reduction reaction as stated above. Similarly, compared to the proton reduction (*b*) from water using the photogenerated electron, the oxygen evolution in OER half-reaction (as shown in Fig. 1-3b) will be facilitated by reducing Ag^+ (*b**) from the oxidizing reagent $AgNO_3$ (electron scavenger). It is important to mention that, a photocatalyst being active in these half reactions does not necessarily guarantee for it to be active in overall water splitting (OWS) without any sacrificial reagents to produce H_2 and O_2. Therefore, the term *overall water splitting* or *OWS* will be distinguishably used throughout the dissertation to define the dissociation of pure water into its constituent parts, H_2 and O_2 with a stoichiometric ratio of 2:1, in the absence of sacrificial reagents.

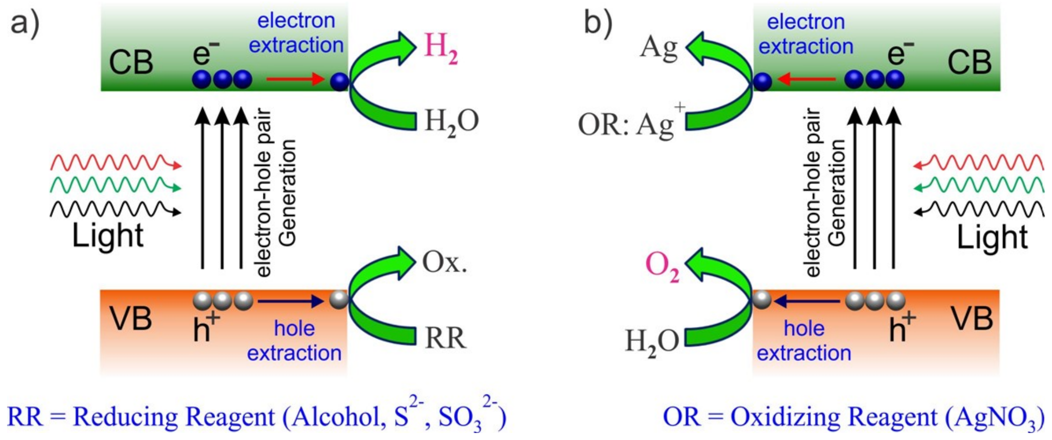

Figure 1-3: a) Hydrogen evolution half-reaction and b) oxygen evolution half-reaction in the presence of sacrificial reducing reagents (RR) and oxidizing reagents (OR), respectively.

1.3 Reaction Mechanism and Kinetics for OWS

Photochemical water splitting does not involve any current conduction through external circuitry, rather it can be considered as an integrated device at the nanoscale. However, like any other electro-chemical system, the phenomena involved at the interface of an electronic conductor (electrode or catalyst) and an ionic conductor (electrolyte or aqueous solution) can be exceedingly complex. Moreover, it is conceptually difficult to link between the mechanisms in the solid and the liquid phase to describe the interfacial reactions. This is because, in literature, there exists very little overlapping in language and terminology while describing the phenomena in an electrode and in an electrolyte (including at their interfaces) from the perspective of condensed-matter physics and chemistry, respectively. Numerous efforts have been made to build the bridge, however, with considerable limitations [42, 43]. This work mostly focuses on the design of nanoscale semiconductor electrode or photocatalyst (solid-state physics) to enhance the efficiency (and stability) in overall pure water splitting reaction (chemistry), without going into details regarding the complex theoretical analysis/estimation for interfacial charge transfer, thermodynamics and kinetics of chemical reactions. However, certain fundamental aspects regarding the reaction mechanism and kinetics are necessary to gain insights for facilitating the design-engineering of photocatalyst, and is therefore, discussed in the following section.

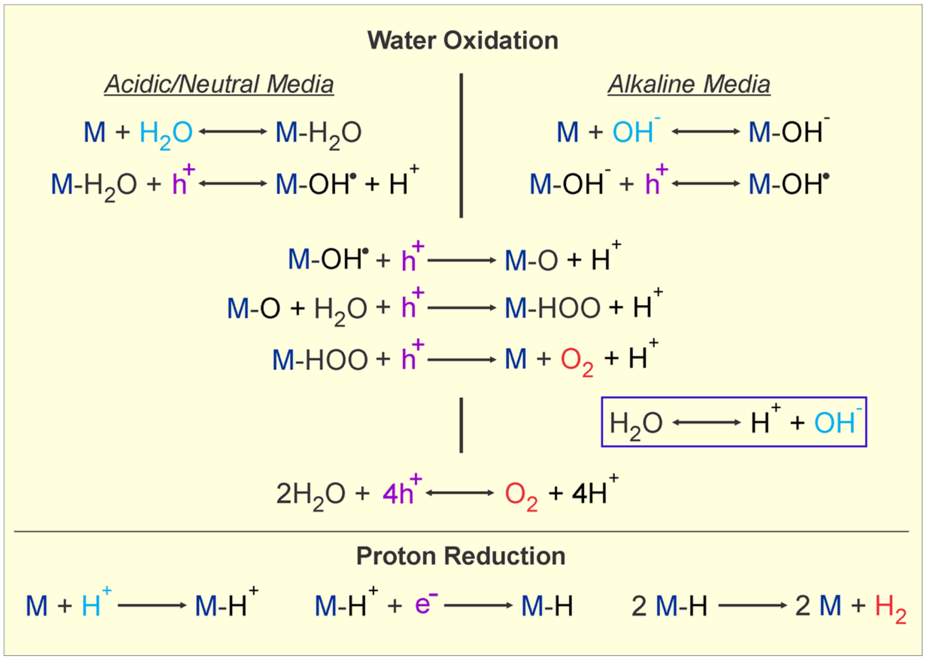

Figure 1-4: Simplified mechanisms for water oxidation and proton reduction, showing the intermediate steps for oxygen and hydrogen evolution in pure overall water splitting reaction. Here, M denotes the active sites (either on the photocatalyst or on the co-catalyst surface).

Electrochemical reactions are classified into two types, namely the inner-sphere and the outer-sphere reactions [44, 45]. So far, the understanding of electrochemical reactions is limited to the simplest possible *outer-sphere electron transfer reaction*, where the electron exchange takes place with the catalyst playing no role, and no specific adsorption of the reactant is required (rather, can be surrounded by inert-ligands), and bond-formation or -breaking is not considered. At the semiconductor-electrolyte interface, the charge transfer is accompanied only by a tunneling event in an outer-sphere reaction, where the tunneling region (10 Å or more) is usually composed of a few monolayers of solvent molecules (typically H_2O). While the reactants need not be in contact with the semiconductor electrode in an outer-sphere reaction, the inner-sphere reactions are invariably accompanied by the transfer of reactant ion from the solvent, followed by its subsequent adsorption and discharging on the electrode surface. Overall water splitting is, therefore, fundamentally an inner sphere reaction, where specific adsorption (chemisorption) and ion transfer is involved in both water oxidation (OER) and proton reduction (HER) reaction. Being an exceedingly complex inner-sphere reaction, there exist very few or no references in the literature which addresses the theoretical aspects of the carrier dynamics and interfacial charge transfer for photocatalytic overall water splitting reactions. Ab-initio molecular dynamic simulations show that the photogenerated holes in III-nitrides (GaN) can energetically drive the water oxidation reaction on their surfaces [17, 46-48]. Similarly, water oxidation mechanism on TiO_2 surface has also been derived in numerous studies for oxygen evolution via water splitting reaction [49-51]. In light of the proposed schemes [52, 53], a simplistic view of the OER and HER reactions for overall photocatalytic water splitting is provided in Fig. 1-4, briefly showing the intermediate steps, while assuming that the reaction site M can energetically drive both the water oxidation and the proton reduction reaction forward simultaneously.

1.3.1 Oxygen Evolution Reaction (OER)

Water oxidation to produce oxygen is a four-electron sluggish process (which requires accumulation and transfer of four charge-carriers to the adsorbed species on a reaction site) and is commonly known as the rate-limiting first-step for overall water splitting. Therefore, it is necessary to understand the dynamics of water oxidation on a reaction site M, for efficient design of overall photocatalytic water splitting device. The reaction scheme differs in its initial step (adsorption) depending on the pH of the aqueous solution. For example, in acidic or nearly pH neutral media, water oxidation is commenced by the adsorption of a H_2O molecule at the cation site (*e.g.* Ga or Ti). Subsequently a hydroxyl radical (adsorbed) is formed through the trapping of a photogenerated hole and a proton is released in the solution. The radical then reacts in three irreversible steps to produce O_2 while consuming a photogenerated hole and releasing a proton in each step, as shown in Fig. 1-4. On the other hand, in an alkaline media, oxygen evolution process is initiated by the adsorption of a hydroxide ion (OH^-) which is more thermodynamically favorable than the oxidation of H_2O (Fig. 1-2). However, no proton is released in the subsequent formation of hydroxyl radical using a photogenerated hole. The irreversible steps for O_2 evolution are similar irrespective of the pH of reactant media. Despite the favorable oxidation of OH^- in alkaline media, consumption of water occurs through an extra step – the dissociation of H_2O into H^+ and OH^- to maintain the equilibrium. Therefore, the net reaction remains same, namely, the evolution of O_2 through splitting of H_2O, where OH^- acts as a catalyst.

1.3.2 Hydrogen Evolution Reaction (HER)

Hydrogen evolution reaction involves both proton and charge transfer, and therefore, the steps are typically classified as the decoupled proton/electron transfer (PT/ET) reaction. The proton released in the solution during the OER physically migrates (PT) towards the catalytic site M, where it gets adsorbed. Subsequently, a photogenerated electron is consumed to produce a hydrogen atom (adsorbed). Two neighboring adsorbed hydrogen atoms can then recombine to form a H_2 molecule (Tafel step). Hydrogen atoms can also be formed in a concerted pathway, namely proton-coupled electron transfer (PCET) where both proton transfer and electron transfer can occur simultaneously [53]. And the H_2 molecule can be formed by protonation of the adsorbed-H coupled to a single electron transfer (Heyrovsky step).

1.3.3 Role of Dissolved Species: Seawater Splitting

For the efficient hydrogen evolution by splitting complex electrolyte, such as sea water, it is very important to consider the role of the dissolved species on water splitting mechanism. Sea water contains various ions such as Na^+, K^+, Mg^{2+}, Ca^{2+}, Cl^-, Br^-, SO_4^{2-}, and CO_3^{2-}, with NaCl being the predominant component [54]. The reduction potential of some common metal cations and the oxidation potential of halide ions are presented in Fig. 1-2. It is evident that, the oxidation of I^- and Br^- ions are thermodynamically more favorable than that of H_2O. Although the oxidation potential of Cl^- (1.33 V) is more positive than that of H_2O (1.23 V), the photo-oxidation of Cl^- to Cl_2 (by Volmer-Tafel or Volmer-Heyrovsky mechanism) can become more effective due to its efficient adsorption (small anion) and relatively simple 2-electron redox process compared to a more complex 4-electron redox process for the photo-oxidation of H_2O [55].

Therefore, depending on the concentration, both Cl^- and H_2O will be simultaneously oxidized in aqueous NaCl solution to produce O_2. The dissolved Cl_2 can react with water and produce HClO ($Cl_2 + H_2O \rightarrow H^+ + Cl^- + HClO$), which can easily be dissociated under irradiation to produce O_2 and release proton into the solution ($2HClO \rightarrow 2H^+ + 2Cl^- + O_2$). For the cathodic reaction, proton will be favorably reduced to H_2 compared to the metal ions. This is because, the standard reduction potential for metal ions are substantially more negative (*e.g.* -2.71 V for Na) than that for proton reduction (0.0 V) to produce hydrogen.

1.4 Contemporary Photocatalysts for OWS: Strengths and Limitations

Typically, photocatalysts are semiconductor materials in powder or colloidal forms, made up of different elements which can integrate with dopants and/or co-catalysts to pursue the goal for improving water splitting performance of the system. However, in some cases, the powders, colloids, nanoparticles, nanowires or nanotubes can be integrated with a planar substrate or photovoltaic devices, which can further serve as a light absorber to contribute photogenerated carriers and separate them for participating in the redox reaction. Conventionally explored photocatalysts for water splitting includes metal oxides, sulfides and (oxy)nitrides, which contain metal cations with d^0 and d^{10} configurations in general. To explain further, the conduction band (CB) of the transition metal oxides with d^0 configuration consists of empty d orbitals of metal cations. On the other hand, the CB of metal oxides with d^{10} configuration consists of hybridized orbitals of empty s and p orbitals of metal cations. The principal contribution to the valence band of metal oxides comes from O 2p orbital, whereas for the metal sulfides and nitrides the dominant contribution is from S 3p and N 2p orbitals. Many of the large-bandgap photocatalysts are frequently doped with several transition metal cations having partially filled d orbitals such as Cr^{3+}, Ni^{2+} and Rh^{3+}, to form some impurity levels within the bandgaps for realizing narrow-bandgap light absorbers.

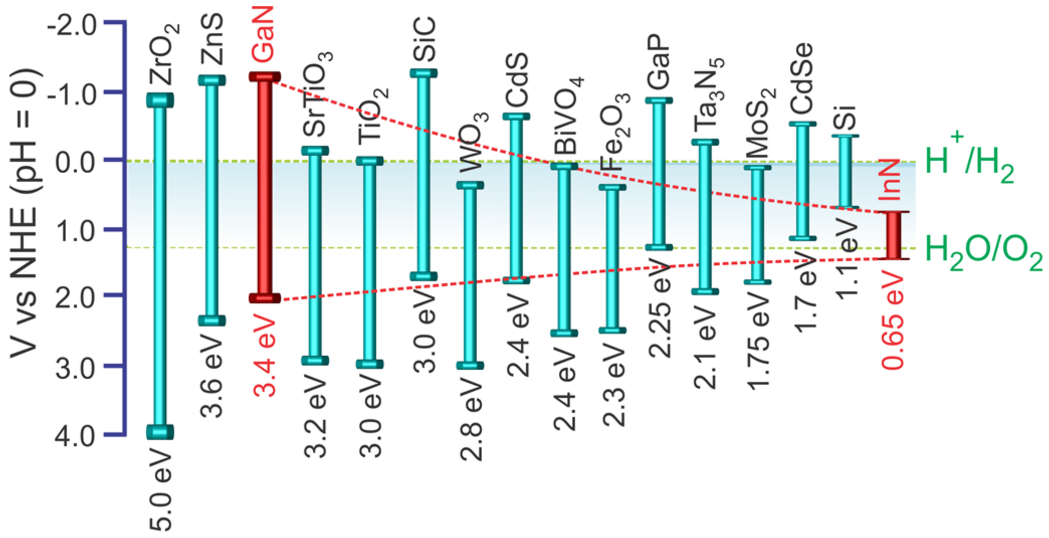

Figure 1-5: Band-gaps (eV) and band edge positions of commonly used photocatalysts with respect to oxidation and reduction potential of water (green dotted line). The red dotted line represents the band edge position of $In_xGa_{1-x}N$ as a function of indium incorporation (0-1 from left to right).

Figure 1-5 shows the band alignments of some photocatalyst materials which are commonly used for water splitting. It can be clearly seen that, the materials which qualify and are active for overall water splitting such as ZrO_2, ZnS, GaN, $SrTiO_3$, TiO_2, SiC etc. have bandgap energy that are too large to absorb visible light. WO_3, $BiVO_4$, and Fe_2O_3, MoS_2 and InN etc. cannot produce hydrogen on the surface even after absorbing visible light. On the other hand, some materials, such as $BaTaO_2N$, CdSe, GaP, and Si, etc. can be employed as a hydrogen evolution photocatalyst. Although these materials are widely explored for the realization of photoanodes or photocathodes in PEC system, to accomplish overall photocatalytic water splitting using such photocatalysts require additional semiconducting materials in Z-scheme photocatalysis. As such, there exists only a handful of single-bandgap semiconductor catalysts, e.g. Ni-doped $InTaO_4$ [41], CDots-C_3N_4

composite [56], and GaN:ZnO solid solution [57] that can drive unassisted photocatalytic overall water splitting under visible-light irradiation [56, 58-61].

1.4.1 Single-bandgap Absorbers for One-step Photocatalytic OWS

Ni-doped $InTaO_4$, La-doped $NaTaO_3$ and Zn-doped Ga_2O_3 can exhibit overall water splitting when modified with NiO and $Rh_{2-y}Cr_yO_3$ co-catalysts, respectively [41, 62]. Rh and Sb-doped $SrTiO_3$ can split water under visible light irradiation with an apparent quantum yield (AQY) of ~0.1% at 420 nm, when loaded with IrO_2. Liao *et al.* have demonstrated overall water splitting capability of CoO NPs prepared by femtosecond laser ablation or mechanical ball milling from CoO micropowders. The system exhibits a solar to hydrogen conversion efficiency (STH) of around ~5% for 30 mins only [61]. Domen's group have sequentially reported numerous examples of visible-light induced overall water splitting on single (oxy)nitride photocatalyst systems. For example, GaN:ZnO solid solutions [57], $(Ga_{1-x}Zn_x)(N_{1-x}O_x)$ loaded with RuO_2 (QY ~0.23% at 410 nm, with $x = 0.12$), Rh_2O_3-Cr_2O_3 loaded $(Ga_{1-x}Zn_x)(N_{1-x}O_x)$ [63], $Rh_{2-y}Cr_yO_3$ loaded $(Ga_{1-x}Zn_x)(N_{1-x}O_x)$ [64] (AQY ~5.1% at 410 nm) and $Rh_{2-y}Cr_yO_3$ loaded $SrTiO_3$ [65] can drive the standalone unassisted photocatalytic overall water splitting. The band-structures of ultra-violet (UV) active Ta_2O_5 can be tuned for visible light absorption through nitridation. Consequently, the absorption spectra of TaON and Ta_3N_5 can be extended up to ~500 and 600 nm, respectively, while the band-edges straddling the redox potentials of water. ZrO_2/TaON heterostructure, when loaded with IrO_2 and RuO_x/Cr_2O_3 co-catalysts can also perform steady overall water splitting. However, despite their extended visible-light absorptions, most of the photocatalysts exhibit significantly poor STH efficiency and longevity in OWS.

1.4.2 Dual-bandgap/Tandem Absorbers for Z-scheme OWS

A wider range of visible-light active semiconductor materials that qualify for either standalone water oxidation or proton reduction had been employed in Z-scheme water splitting, where the requirement for straddling the redox potentials (by band-edges) are relaxed, thereby making it advantageous over one-step water splitting. In the Z-scheme of water splitting, water oxidation and proton reduction occur on two separate materials (layers) by their photogenerated holes and electrons, respectively. The complementary carriers in those layers either recombine through an ohmic contact (Fig. 5.1b) or get recycled via a redox couple.. For example, an enhanced AQE of 6.3% at 420 nm had been achieved with a Z-scheme system based on Pt-loaded ZrO_2/TaON (hydrogen evolution photocatalyst) and Pt-loaded WO_3 (oxygen evolution photocatalyst) using IO_3^-(donor)/I^- (acceptor) as a redox couple. The mixture of Ru-loaded $SrTiO_3$:Rh and $BiVO_4$ can generate hydrogen and oxygen stoichiometrically in the absence of redox mediators (at pH 2-4), and demonstrate an AQE of ~2.1% at 420 nm when $[Co(bpy)_3]^{3+/2}$ is used as a redox couple. A suspension of Ru-loaded $SrTiO_3$:Rh and Ir/CoO_x-coloaded Ta_3N_5 can potentially utilize photons up to 600 nm for oxygen evolution on Ta_3N_5 in Z-scheme water splitting system. Physical contact (direct or through metals) between the two half-redox system can enhance the efficiency further compared to their Z-scheme configurations via mediators. For example, the Ru-loaded $SrTiO_3$:La,Rh and $BiVO_4$:Mo can demonstrate an STH >1% when connected via Au or C (*contact*) [58] compared to that of ~0.1% using with $Fe^{3+/2+}$ redox couples in Z-scheme [66].

Cost-effective metal-free photocatalysts, such as graphitic carbon nitride (g-C_3N_4) and graphene oxide (GO) had also drawn significant attentions lately. As such, the visible-light (>420 nm) illumination on nitrogen-doped GO (NGO-QDs) suspended in pure water can result in stoichiometric H_2 and O_2 evolution (2:1) when configured to form *p-n* junction. The water-splitting activity of the NGO-QDs is about half compared to that of the $Rh_{2-y}Cr_yO_3$ loaded GaN:ZnO (QY = 5.2% at 410 nm), with relatively high stability for 80 hours. The g-C_3N_4, (bandgap ~2.7 eV) can function as a visible-light-active photocatalyst for overall water splitting; and Pt, PtO_x, and CoO_x loaded g-C_3N_4 can demonstrate long-term stability for 510 h [67]. However, the efficiency of water splitting with C_3N_4 is very low and often suffers from poisoning by the H_2O_2 formation. Consequently, Liu *et al.* demonstrated the synthesis of metal-free carbon nanodots-carbon nitride (CDots–C_3N_4) nanocomposites, and by adopting a two-step approach for water splitting (two-electron process for H_2O_2 formation and subsequent decomposition to generate H_2), a quantum yield of 16% for wavelength $\lambda = 420 \pm 20$ nm had been derived with an STH of ~2.0% [56].

It is worthwhile mentioning that, despite the enhanced quantum efficiencies under visible light excitation, the STH efficiency derived from many of these photocatalytic systems are significantly low (<1%). On the other hand, the photocatalysts that demonstrate reasonable STH (>1%), such as CoO nanoparticles [61] and $SrTiO_3$:La,Rh/Au/$BiVO_4$:Mo Z-scheme system [58] exhibit stability of only a few hours, or less, thus keeping the floor open for further exploration of an efficient and stable photocatalyst. A comprehensive summary of the state-of-the-art efficiencies and stabilities is provided in Section 2.2 for photocatalytic and photoelectrochemical water splitting using many of the contemporary photocatalysts.

1.4.3 On the Stability: The Qualifier for an Efficient Photocatalysts

A photocatalyst must meet certain requirements from both the thermodynamic and kinetic point of view to qualify for overall water splitting. For reasonable solar efficiencies, the bandgap should be narrow enough (~2.2 eV) to absorb sufficient visible solar spectrum, whereas for spontaneous overall water splitting, the potentials for oxygen and hydrogen evolution (denoted as $E(O_2|H_2O)$ and $E(H^+|H_2)$, respectively) must lie between the valence and conduction band edges. The stability of any such photocatalyst in overall water splitting additionally depends on the anodic or cathodic decomposition potential (thermodynamic self-reduction or self-oxidation potential) of the semiconductor material, denoted as E^{red} or E^{ox}, respectively [68]. Therefore, careful measures should be taken in identifying the suitable photocatalyst for stable and efficient water splitting. For example, the metal oxides typically have E^{ox} lower than $E(O_2|H_2O)$ at pH = 0, indicating the water oxidation at the interface is more favorable than the self-oxidation of the catalyst by photogenerated holes, thus making them most photochemically stable semiconductors in aqueous solutions. However, in exception, Cu_2O, ZnO, PbO, and $FeTiO_3$, having the lower valences of the cations can be further oxidized to higher valences (Cu^+ to Cu^{2+}, Pb^{2+} to Pb^{4+}, and Fe^{2+} to Fe^{3+} etc.). The non-oxide semiconductors, therefore, are thermodynamically unstable in aqueous solution which can get oxidized by the holes under illumination. This is because the anions such as N^{3-}, P^{3-}, As^{3-}, S^{2-}, Se^{2-}, and Te^{2-} can eventually get oxidized to neutral or positive valence states, e.g. N^{3-} to N_2 or NO_3^- and

S^{2-} to S or SO_4^{2-} etc. However, the non-oxide semiconductors are resistant to the electron reduction under illumination, as their E^{red} is higher than $E(H^+|H_2)$ irrespective of the pH values. In contrast, a few metal oxides with lower E^{red} than $E(H^+|H_2)$ at pH = 0, such as Cu_2O, PbO, $CuWO_4$, $BiFeO_3$, $BiVO_4$, WO_3, and Co_3O_4 are prone to self-reduction by photogenerated electrons [69].

The time-scale of the dynamic processes, schematically illustrated in Fig. 1-1, differ significantly among the steps for overall water splitting. Kinetically, the water oxidation, as discussed in section 1.3, is a sluggish four-electron process and is well-known as the rate-limiting process of overall water splitting. The complex mechanism appears to be a bottleneck which puts forth significant difficulties in the way of developing efficient and stable catalysts for water splitting. For example, using transient absorption spectroscopy**,** the dynamics of photoexcited carriers have been studied in detail for many semiconductors [70]. Sequentially, the dynamic processes that are involved in water splitting are – the generation of electrons and holes (within 200 fs after photoexcitation), relaxation of the surface-trapped and bulk electrons (a few hundred picoseconds), reaction of surface-trapped holes with methanol, ethanol, and 2-propanol (within 300, 1000, and 3000 ps, respectively) etc. if present in the solution, reaction of the photoexcited electrons with dissolved O_2 (10–100 μs), reduction of water by photogenerated electrons (*e.g.* in 10–900 μs on platinized TiO_2), and proton reduction to H_2 which occurs on the hundreds of microseconds time scale, and most importantly, water oxidation for O_2 evolution on the timescale of microseconds to seconds [70]. Further details on the redox time-scale and the limiting factors of overall water splitting are provided in section 2.4.

Certain approaches for tuning the kinetics, such as charge carrier separation, surface modification and co-catalyst loading can improve both the efficiency and the stability of the photocatalyst. It is evident from the discussion so far that the water oxidation for O_2 evolution goes through many more complicated intermediate steps, compared that of proton reduction for H_2 evolution. There remains an additional challenge in water oxidation other than the longer time-scale and complex intermediate steps, and that is - the effective accumulation of four-holes to simultaneously oxidize two water molecules. This can make the water oxidation more sluggish and endanger the photochemical stability of the semiconductor material, despite meeting the thermodynamic requirements. In other words, the inefficient accumulation of holes and the long-awaiting time for water oxidation can accelerate the decomposition of the material (via self-oxidation by photogenerated holes), even for the case where water oxidation is the favorable pathway, *i.e.* E^{ox} lower than $E(O_2|H_2O)$. Proton reduction, being a faster process can surpass the self-reduction process, if it is the favorable process from thermodynamic point of view.

Kinetically, the carrier accumulation and the storage capacity can be engineered by adopting numerous approaches. In natural photosynthesis, the process is ensured by the changes of catalyst charge-state (S_1 to S_4) with increasingly oxidizing capacities, *e.g.* the charge-state of the redox-active metal Mn in the $CaMn_4$ complex varies in each S-state. In artificial photosynthetic devices, band-structure engineering and suitable co-catalyst loading on the semiconductor (meeting the energetic requirements of the band-edges) are applied to ensure charge-carrier separation and trapping in distinct redox sites. For example, in case of failure to provide favourable reaction site for the O_2 formation, O_2 adsorption can surpass H_2 adsorption on the sites of surface oxygen vacancies, subsequently forming O_2^- or other undesired species, which can further inhibit O_2 evolution. To summarize, efficient charge carrier separation in the bulk and near the surface, migration of photogenerated active carriers towards the distinct catalytic sites (reactive surfaces), faster carrier transport and their effective trapping into the co-catalysts can have enormous impact on the efficiency and the stability of the photocatalysts in OWS. More details about these factors and their impacts will be discussed in section 2.4.

1.5 III-Nitride Semiconductor Nanowires as Photocatalyst for OWS

To date, metal oxides have been widely explored as a photocatalyst for water-splitting [27, 29, 71], which, however, offer the limiting efficiency of ~2.3% due to their large band-gaps and lack of significant activities under visible light irradiation (~ 46% of energy in solar spectrum) [29, 72, 73]. Previously reported visible light responsive photocatalysts often suffer from the propensity for oxidation (known as photo-corrosion) and lack in stability while providing with very limited efficiency in the visible spectrum [74, 75]. Moreover, the photocatalytic activity of conventionally used powder samples is low due to their inefficient light absorption and carrier separation, low crystalline quality and small surface-to-volume ratio [76-78]. Therefore, it is imperative to explore new, visible light driven, stable and efficient photocatalytic system for practical usage and large-scale hydrogen production.

Group III-nitride compound semiconductors exhibit direct energy bandgap encompassing nearly the entire solar spectrum. Apart from being reasonably stable in photocatalytic environment, InGaN possesses an additional advantage over other known photocatalysts in that its bandgap can be tuned to straddle water redox potential over a substantial portion of solar spectrum, namely, ultraviolet, visible and near-infrared [79-86]. Figure 1-5 shows the band alignments of InGaN alongside with other commonly used photocatalyst materials, depicting optimum band edge potential for water splitting up to ~ 50% of indium incorporation [82]. On the other hand, one dimensional nanowire structures are expected to have significantly improved photocatalytic activity due to their high surface-to-volume ratio to provide more catalytic sites for efficient adsorption of cations and anions, and substantially efficient charge carrier separation, transport and reduced bulk recombination [87-92]. Significantly, 1D nanowires can be grown/synthesized on virtually any substrate, providing a distinct opportunity to integrate with low cost Si based solar cells. Moreover, one dimensional nanowires allow control over the photocatalyst crystal plane to tune it for promoting either H_2 or O_2 evolution. Most importantly, the non-polar surfaces of III-nitride nanowire heterostructures are highly reactive for spontaneous dissociation of water molecules while possessing low energy barrier for proton diffusion. These attributes, therefore, make III-nitride nanowire structures a very promising, yet less explored candidate as a photocatalyst.

1.6 Defining Efficiencies for Photocatalytic Solar Water Splitting

There exists substantial confusion in the research community about the methods to calculate and to compare the efficiency of different devices that are used to harness solar energy. Efficiency is a deceptively simple concept but can be quite elusive in terms of performance comparison because of the variations in defining the efficiency terms, associated with the underlying assumptions and conditions. Some of the most common efficiency terms that are thoroughly used for the evaluation of device performance in photocatalytic water splitting are defined here. The apparent quantum efficiency (AQE) for the photocatalytic overall water splitting is derived by calculating the number of high energy above-bandgap photons corresponding to the incident power. The incident power on the nanostructured photocatalyst can be expressed as:

$$P_{\text{incident}}(\lambda) = \rho_{\text{incident}}(\lambda) \times A_{\text{substrate}} \times \beta_{\text{ff}} \tag{4}$$

where $A_{\text{substrate}}$ is the area of the substrate on which the nanostructured photocatalysts are standing, β_{ff} is the aerial fill factor for the nanostructures, $\rho_{\text{incident}}(\lambda)$ is the incident power intensity on the substrate, which can be derived by measurements using a broadband detector. The β_{ff} is considered unity (assuming all the incident photons are absorbed) for the calculation of AQE. The number of incident photons per second, as a function of wavelength is calculated from,

$$N_{\text{ph}}(\lambda) = \frac{P_{\text{incident}}(\lambda)}{E_{\text{ph}}(\lambda)} \tag{5}$$

where $E_{\text{ph}}(\lambda) = \frac{hc}{\lambda}$ is the photon energy for the corresponding wavelength. The total number of incident photons per second within $(\lambda_1 - \lambda_2)$ wavelength range can be calculated as follows:

$$N_{\text{ph,inc}}(\lambda_1 - \lambda_2) = \int_{\lambda_1}^{\lambda_2} \frac{P_{\text{incident}}(\lambda) \times \lambda}{hc} d\lambda \tag{6}$$

The AQE for the S2 approach is then derived from the following equation:

$$\text{AQE} = 2 \times \frac{\text{Number of evolved H}_2 \text{ molecules per hour}}{\text{Number of incident photons per hour}} \times 100\ \% \tag{7}$$

If we neglect the light trapping and scattering effect in the photocatalyst nanostructure, the APCE can be estimated from equation (7) by replacing the number of incident photons with that of the absorbed photons, derived as:

$$N_{\text{ph,abs}}(\lambda_1 - \lambda_2) = \int_{\lambda_1}^{\lambda_2} \frac{P_{\text{absorbed}}(\lambda) \times \lambda}{hc} d\lambda \tag{8}$$

Here, $P_{\text{absorbed}}(\lambda)$ can be calculated from the power incident on the sample and depends on the absorption co-efficient and threshold wavelength associated with the bandgap of the material, and on the morphology ($\beta_{\text{ff}} \leq 1$) and dimension of the nanostructured photocatalyst. Clearly, this APCE of the nanowire structure is only limited by the charge transport efficiency to the solid-liquid interface ($\eta_{\text{transport}}$) and the efficiency of interfacial charge transfer ($\eta_{\text{interface}}$). Energy conversion efficiency (ECE) is defined as the ratio of the storable chemical energy (from photocatalysis) to the absorbable photonic energy that is available to the photocatalyst on the substrate (limited by the absorption threshold), and is calculated as

$$\text{ECE} = \frac{H_2 \left(\frac{\text{mmol}}{\text{s}}\right) \times 237\ (\text{kJ}) \times 1000}{\rho_{\text{incident\_total}}\ (\lambda_1 - \lambda_2) \left(\frac{\text{mW}}{\text{sq.cm}}\right) \times A_{\text{substrate}}(\text{sq.cm})} \times 100\ \% \tag{9}$$

Solar-to-hydrogen conversion efficiency (STH) is the most common platform for comparing how efficiently a photocatalyst material can utilize the energy available from the entire solar spectrum. For one-sun (non-concentrated) irradiation (100 mW cm^{-2}), STH can be calculated as

$$\text{STH} = \frac{H_2 \left(\frac{\text{mmol}}{\text{s}}\right) \times 237\ (\text{kJ}) \times 1000}{100 \left(\frac{\text{mW}}{\text{sq.cm}}\right) \times A_{substrate}(\text{sq.cm})} \times 100\ \% \tag{10}$$

1.7 Optical Limits for the Efficiency of Solar Water Splitting

To estimate the efficiency that can possibly be achieved based on realistic assumptions, it is very important to analyze the limits on the efficiency of the photocatalyst. Here we examine the theoretical limits on the amount of hydrogen evolution, ECE and STH efficiency of a photocatalyst (Figs. 1-6b, c and d) in a one-step photocatalysis, assuming 100% quantum yield and using AM1.5 Global-tilt solar spectrum (Fig. 1-6a). The inherent assumption here is that the energy from the photons with wavelength shorter than the threshold can be converted to hydrogen. From the analysis, it can be derived that for a photocatalyst with a threshold absorption wavelength of ~485 nm (Eg ~2.56 eV), maximum of ~103.4 µmol $h^{-1}cm^{-2}$ H_2 can be produced with a limit on STH of ~6.81% and on ECE of ~41.84% under intensity of one sun irradiation. On the other hand, to achieve the solar-to-hydrogen conversion efficiency of ~10% under similar excitation condition by using a photocatalyst with narrower bandgap of ~1.9 eV (extended absorption threshold wavelength ~650 nm), the minimum quantum yield (AQE) required is ~49% while producing ~153.4 µmol of hydrogen per unit area (cm^2) per hour.

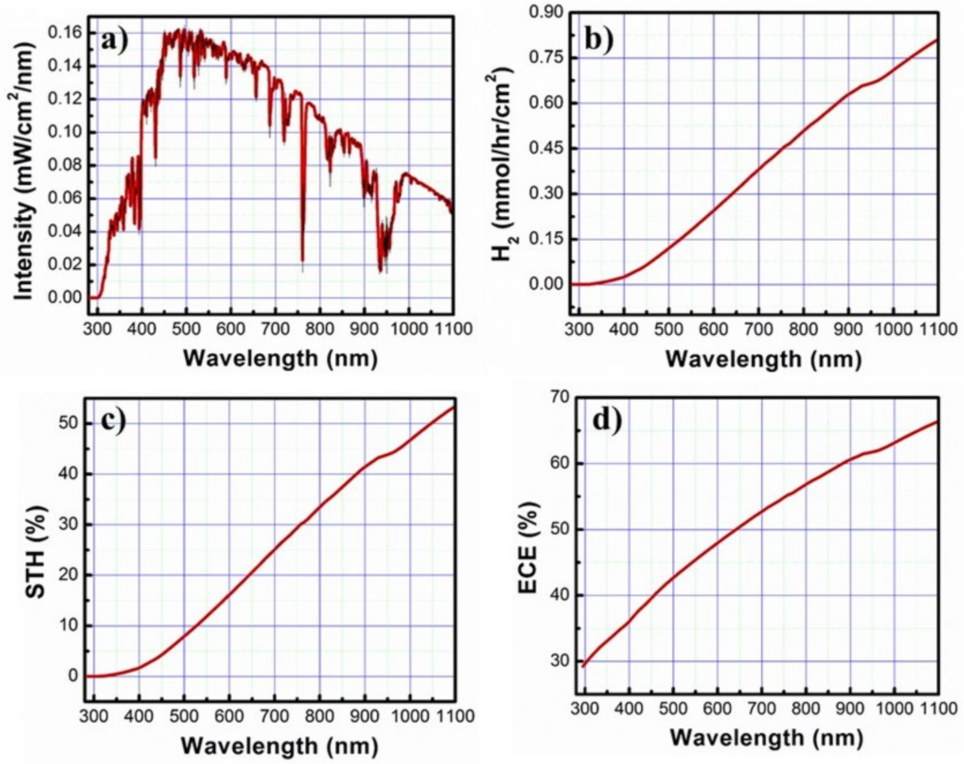

Figure 1-6: a) Solar intensity spectrum for AM1.5 Global-tilt from 290-1100 nm. Ideal theoretical limit of b) hydrogen evolution, c) solar to hydrogen conversion efficiency (STH), and d) the energy conversion efficiency (ECE), for different absorption threshold wavelength (corresponding to bandgap) of the photocatalyst, while assuming ideal apparent quantum efficiency (AQE) of 100%.

However, apart from the band-edge potential requirements, sufficient overpotential is also necessary for spontaneously driving the water oxidation and proton reduction reaction in photocatalytic solar water splitting, while overcoming various inherent losses. Given that the redox potential of water is 1.23 eV, considering an overpotential of ~0.4 eV for each of the half reactions, minimum excitation energy required for overall water splitting becomes ~2.03 eV (<610 nm). Hence, for a given reaction with associated losses, there will be a threshold wavelength (λ_t) limited by the chemical conversion efficiency, which is just capable of driving the reaction forward. Figure 1-7 illustrates the efficiencies for conversion of solar radiation to stored Gibbs energy for single-bandgap (Fig. 1-7a) and for dual-bandgap devices with equal photon flux absorption within each band (Fig. 1-7b). It is predicted that a reasonably operating system in practice would introduce U_{loss} of ~0.8 eV, thus limiting the efficiency to a maximum of ~17% for S_2 approach, which would require a photocatalyst with threshold wavelength (λ_g) < 610 nm (E_g ~2.03 eV).

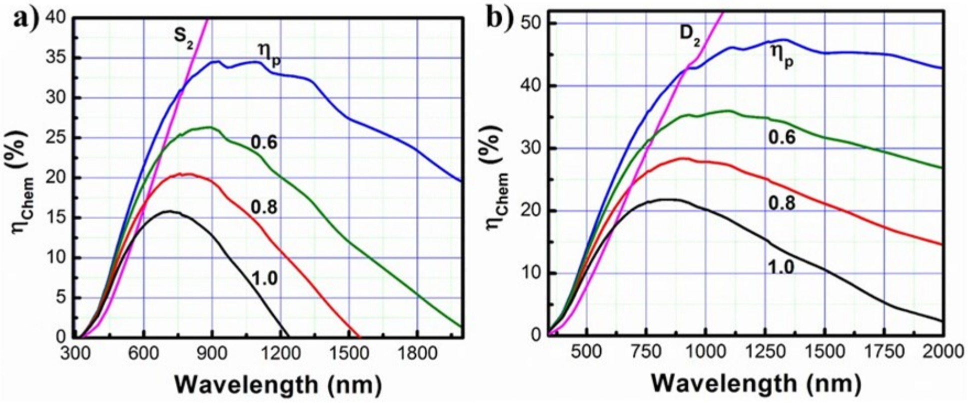

Figure 1-7: Efficiencies of solar to stored Gibbs energy conversion for a) Single-bandgap devices and b) Dual-bandgap devices as a function of narrow bandgap wavelength, assuming equal photon flux absorption. The top curve (blue) shows the ideal limiting efficiencies (η_p), and the lower curves represent chemical conversion efficiencies for U_{loss} = 0.6 (green), 0.8 (red), and 1.0 (black) eV per photon, respectively, assuming ideal apparent quantum efficiency (AQE) of 100%. Intersection with the S2 or D2 (magenta) curve shows the threshold wavelength and efficiencies for the corresponding system.

In a single band-gap system, the photogenerated high energy electrons (hot carriers being an exception) will rapidly (<10 ps) relax to an energy close to the bandgap and dissipate the extra energy into heat. Therefore, to minimize the energy loss due to thermal relaxation, dual-bandgap system can be considered a better approach. In a dual-bandgap system, two or more absorbing materials with complementary bandgaps are stacked, where the large bandgap material is directly exposed to the irradiation and can absorb photons with $\lambda \le \lambda_1$. The lower bandgap material is placed underneath the larger-bandgap material to absorb the rest of the photons with $\lambda_1 < \lambda \le \lambda_2$, including the high energy photons not absorbed by the top large-bandgap layer. If we assume that equal number of photons are absorbed in each layer (to make the presentation simpler), it can be seen from Fig. 1-7b that for a system with ~0.8 eV loss per photon, the realizable limiting efficiency increases up to ~24% allowing longer threshold wavelength of ~690 nm for the bottom absorber (λ_2) with corresponding threshold wavelength of ~550 nm for the top layer (λ_1). Considering the increased interest in dual-bandgap (tandem) photosystem, ideal limiting efficiencies and those with ~0.8 eV loss per photon are presented in Figs. 1-8a and b, respectively.

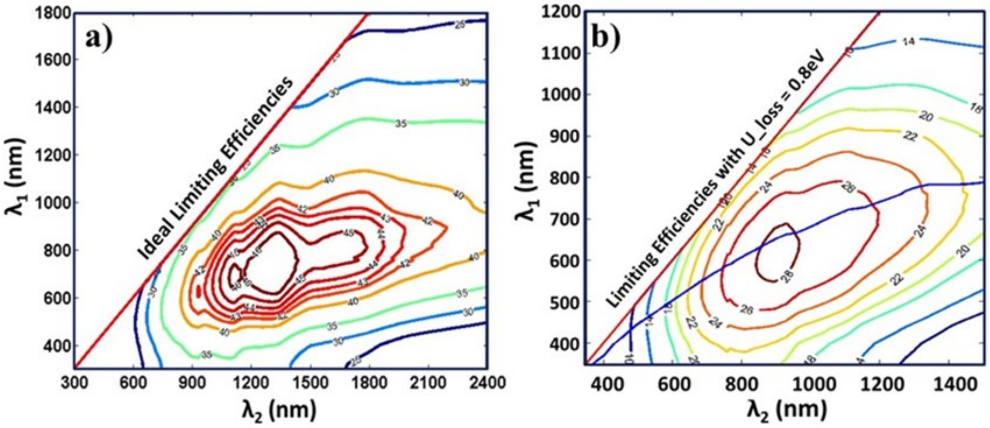

Figure 1-8: Contour diagram, representing a) Ideal limiting efficiencies (η_p), and b) efficiencies with U_{loss} = 0.8 eV per photon for dual-bandgap devices with wavelengths λ_1 and λ_2. Path of equal photon absorbed are shown by the blue line crossing through the contours in b).

1.8 Conclusion

The chemical transformation of sunlight, water and carbon dioxide into high-energy-rich fuels, commonly known as artificial photosynthesis, is perceived to be one of the key sustainable energy technologies in the future energy arena. Although considerable progress has been made over the last four decades, the development of efficient, long-term stable, scalable, and cost-competitive photocatalysts still remains considerably challenging. Group-III nitride nanostructures possess immense potential for efficiently harnessing clean energy just from sunlight and water. Proficient design of the photocatalyst nanostructures, optimization of the surface charge properties and charge-carrier dynamics to tune the reaction kinetics can lead the community towards the goal of developing a highly efficient artificial photosynthetic system. The goal of the thesis is, therefore, to explore technology options for providing sustainable photocatalytic water splitting system which can generate hydrogen efficiently from the renewable energy sources. The brief outline of the thesis is as follows:

We briefly elucidate the status of the photocatalytic and photoelectrochemical water splitting in Chapter 2, in terms of efficiency and stability of the photocatalyst. In Chapter 3, we have discussed the methodologies for the growth/synthesis and characterization of nanostructured III-nitride photocatalyst. In Chapter 4, we have investigated the impact of surface charge properties on the photocatalytic activity of Ga(In)N nanowires. Consequently, Chapter 5 addresses the issue of carrier trapping and recombination, and their detrimental effects on significantly limiting the efficiency. Chapter 6 carefully highlights on the burning issue of suppressed interfacial charge transfer and limited photochemical stability of semiconductor catalysts, especially under concentrated irradiation. An artificial photosynthetic system, with enhance solar-to-hydrogen conversion efficiency and long-term stability is demonstrated therein. Subsequently, a new generation of semiconductor, namely dilute-antimonide (Sb) III-nitride is explored in Chapter 7, both theoretically and experimentally, for extended visible light absorption. Synergistic incorporation of In and Sb into GaN is briefly discussed in Chapter 8 within the dilute-Sb limit (<1%), demonstrating the controllable tuning of conduction- and valence-band edges. Finally, the major findings of the thesis are summarized in Chapter 9, followed by the discussion on some of the very promising preliminary investigations and detailed proposals for future direction.

Chapter-2

Status, Challenges and Scopes for Efficient and Stable Artificial Photosynthesis

2.1 Introduction

Hydrogen production nowadays is mostly dependent either on the high-temperature steam reforming via reaction with fossil fuels (e.g. $CH_4 + H_2O \rightarrow CO + 3H_2$) or coal gasification in the presence of oxygen (e.g. $3C + O_2 + H_2O \rightarrow H_2 + 3CO$). Both the processes produce CO, which contributes indirectly to global warming – by reducing OH radicals that help decreasing the lifetimes of strong greenhouse gases (like methane). As such, only 4% of the world's hydrogen is produced from the electrical energy by promisingly electrolyzing water, compared to more than 90% driven by thermal energy. However, in the pursuit of carbon-free clean energy, there had been a significantly increased interest in hydrogen generation from renewable energy sources, namely, the most abundant solar and water resources on Earth, via artificial photosynthesis.

Numerous approaches have been pursued so far to construct an artificial photosynthetic system, and many photocatalysts (comprised of organic or inorganic semiconductors) with adsorbed co-catalysts have been vigorously developed. Metal oxides including the pioneer TiO_2 and others such as iron oxide, zinc oxide, copper oxide have also been widely explored. Besides, metal sulfides including cadmium sulfides, and zinc sulfides, in addition to nitrides and nanocomposite materials have been intensively studied as light-absorbing photocatalysts for water splitting. Photocatalytic/photochemical and photoelectrochemical (PEC) water splitting are two of the most widely used approaches for producing hydrogen as a green fuel. The electrolysis of water, which accounts for ~4% of today's hydrogen production, has been used commercially since early 1900s. Electrolysis in conjunction with renewable energy sources also drew significant attention lately, where the solar radiation is converted into electrical energy through a photovoltaic (PV) system for driving an external electrolyser to produce hydrogen. This approach is highly durable, as the photovoltaic system (solar cells) does not need to be immersed into the electrolyte, and therefore, is not susceptible to corrosion.

However, the implementation of such system involves high production and installation cost of photovoltaic devices. To alleviate the limitations, electrolysers integrated with photovoltaics are also investigated (PV-electrolysers), in which the light absorbers consist of single or multiple junctions of a material (p/n or p-i-n), or materials with complementary bandgaps (tandem configurations) stacked on top of each other, thereby increasing the photo-potential and utilizing a larger part of the solar spectrum. PV integration approach has also been frequently applied to realize both the photocatalytic and the photoelectrochemical (PV-PEC) water splitting for hydrogen generation (using wireless and wired configuration). This chapter elucidates some of the key issues and challenges associated with the realization of highly efficient and stable state-of-the-art water splitting systems, namely the photochemical, PEC, PV-PEC water splitting and PV-electrolyser approaches. Subsequently, the opportunities and strategies to address some of the problems while making progress towards efficient and stable hydrogen generation from overall pure water splitting are also discussed.

2.2 State-of-the-art Efficiencies and Stabilities in Water Splitting

The discussion in the following sections will exclude the efficiency values and duration of long-term stability achieved and reported in this dissertation. As per the discussion so far, there are various forms of water splitting, each approach having certain benefits and limitations associated with it. Therefore, the efficiency values differ significantly depending on the approach, both theoretically and experimentally.

2.2.1 Photochemical or Photocatalytic Water Splitting

Due to the much simpler configuration, photocatalytic water splitting is amenable to cheap and large-scale hydrogen generation, and therefore, is largely explored for decades.

Some of the best efficiencies and stabilities reported for photocatalytic water splitting systems are listed in Table 2-1.

Table 2-1: State-of-the-art photocatalytic systems for overall water splitting.

Photocatalyst material	STH	Stability	Reference
CoO nanoparticles	5%	1 h	[61]
Co-Ci/ Mo:$BiVO_4$-$CH_3NH_3PbI_3$/TiO_2/Pt	3%	12 h	[93]
Co-OEC/3-jn Si SC/Ni/NiMoZn	2.5%	10 - 24 h	[94]
CDots-C_3N_4	2%	200 days	[56]
Rh/Cr_2O_3 load InGaN/GaN nanowire	1.8%	10 h	[95]
Ru-loaded $SrTiO_3$:La,Rh/C/$BiVO_4$:Mo sheet	1.2%	6 h	[96]
Ru-loaded $SrTiO_3$:La,Rh/Au/$BiVO_4$:Mo sheet	1.1%	10 h	[58]
Si/TiO_2 nano-tree array	0.12%	4.5 h	[97]
Pt, PtO_x, and CoO_x loaded g-C_3N_4	N/A	510 h	[67]
NiO_y loaded $In_{0.90}Ni_{0.10}TaO_4$	N/A	120 h	[98]
Rh/Cr_2O_3 loaded GaN nanowire	N/A	21 h	[99]
Rh-Cr_2O_3 loaded $Bi_{0.375}Y_{0.625}VO_4$	N/A	18 h	[100]
Rh_2O_3-Cr_2O_3 loaded $(Ga_{1-x}Zn_x)(N_{1-x}O_x)$	N/A	15 h	[63]
RuO_2 loaded $(Zn_{1.44}Ge)(N_{2.08}O_{0.38})$	N/A	8 h	[101]
NiO loaded $NaTaO_3$:La	N/A	6 h	[62]
$Rh_{2-y}Cr_yO_3$ loaded $(Ga_{1-x}Zn_x)(N_{1-x}O_x)$	N/A	5 h	[64]
$Rh_{2-y}Cr_yO_3$ loaded $SrTiO_3$	N/A	5 h	[65]

To achieve unassisted overall water splitting using the two-photon photocatalytic process, the conduction and valence band edges of the photocatalyst must straddle the redox potentials, while possessing a sufficiently narrow bandgap to absorb a large part of the solar spectrum. Due to such stringent requirements, there are very few photocatalysts e.g. Ni-doped $InTaO_4$, CDots-C_3N_4 composite, and GaN:ZnO solid solution, that can perform standalone unassisted, overall water splitting reaction under visible light irradiation [5, 41, 56-60]. On the other hand, tandem heterostructures using narrow bandgap semiconductor materials suffer from low carrier extraction efficiency in overall pH neutral water splitting under no-applied bias. Therefore, the best reported solar-to-hydrogen (STH) conversion efficiency for pH neutral photocatalytic water splitting is limited to ~1%, or less, compared to the 10-16% reported for PEC devices.

For example, as reported by Liu *et al.*, the integrated TiO_2|(contact)|Si structure with complementary bandgaps in nanowire form exhibits STH efficiency of only ~0.12% in direct overall water splitting, which is significantly low compared to the complexity associated with the device fabrication [97]. Wang *et al.* reported an STH efficiency of ~1.1% for 10 hours in 2016 [58] and ~1.2% for 6 hours in 2017 [96] for one-step neutral pH overall water splitting on Ru-catalyst loaded $SrTiO_3$:La,Rh|(contact)|$BiVO_4$:Mo device, with Au and C as sandwiched contact, respectively. Reece *et al.* reported a wireless water splitting device comprised of triple-junction Si solar cell to perform as a narrow bandgap absorber and to provide intrinsic (spontaneous) performance in the absence of an external bias [94]. When immersed in conductive electrolyte of 0.5 M KBi/1.5 M KNO_3 at pH ~9.2, the device provides an STH of ~2.5% which is stable for less than 24 hours, despite the higher photon conversion efficiency of the Si solar cell (6.2%). A similar approach is reported by Kim *et al.* at near-neutral pH (~7.0) condition in 0.1 M K_2HCO_3, which consist of extrinsic/intrinsic dual(Mo)-doped $BiVO_4$ on Perovskite solar cell, and when loaded with cobalt carbonate (Co-Ci) the device provides an STH efficiency ~3.0% for 12 hours [93].

On the other hand, the highly stable photocatalysts reported so far, either provides with extremely low efficiency or limited absorption threshold. For example, 21 hours of photocatalytic stability for Rh/Cr_2O_3 loaded GaN nanowire is reported by Kibria *et al.* under UV excitation showing ~51% internal quantum efficiency [99]. In contrast, Zou *et al.* demonstrated the stability of NiO_y loaded $In_{0.90}Ni_{0.10}TaO_4$ for 400 hours under >420nm excitation [98], with only 0.66% quantum yield for NiO_y loaded $In_{0.80}Ni_{0.20}TaO_4$. Similarly, the study conducted by Zhang *et al.* on Pt, PtO_x, and CoO_x loaded g-C_3N_4 exhibits excellent long-term stability for 510 hours, however, with limited apparent quantum yield (AQY) of

~0.3% at 405 nm in overall water splitting reaction [67]. Other best reported stabilities are limited to less than 20 hours with very low efficiencies [62-65, 100, 101].

It is worth mentioning that an STH of ~5% had been reported on CoO nanocrystals by Liao *et al.* [61], which are barely stable (<1 hour) in harsh photocatalytic environment. The nanocrystal surfaces become corroded due to difficulties in co-catalyst loading, and further studies seem to be necessary to understand the mechanism and to confirm the reproducibility [58]. On the other hand, a different 2-step approach of water splitting by Liu *et al.* using CDots-C_3N_4 showed ~2% of STH for 200 days [56], which requires efficient generation as well as subsequent decomposition of H_2O_2, putting further constraints on the bandgap of suitable photocatalyst (>1.78 eV, compared to ~1.23 eV for neutral pH overall water splitting, excluding necessary over-potentials).

Table 2-2: State-of-the-art paired-electrode PEC systems without photovoltaics.

Anode	OER cocat.	Cathode	HER cocat.	Electrolyte	Surface protection	STH	Stability	Ref.
Re-grown haematite	$NiFeO_x$	TiO_2/ a-Si	Pt	0.5M phosphate (pH~11.8)	TiO_2 layer	0.91%	10 h	[102]
Bi-$BiVO_4$	$NiFeO_x$	Mo/Ti/ CdS/ $(ZnSe)_{0.85}$- $(CIGS)_{0.15}$	Pt	0.5 M potassium borate (pH~9.5)	N/A	0.91%	~1.5h	[103]
Mo: $BiVO_4$	NiOOH /FeOOH	CdS /$CuGa_3Se_5$ /(Ag,Cu) $GaSe_2$	Pt	0.1 M KH_2PO_4 (pH~7)	N/A	0.67%	2 h	[104]
TiO_2 /$BiVO_4$	CoO_x	TiO_2/p-Si	NiO_x	0.1M K_2SO_4 (pH~9.2)	TiO_2 layer	0.59%	5 h	[105]
$BiVO_4$	CoPi	p-Si nanoarray	Pt	0.1 M K_3PO_4 (pH~5.5)	N/A	0.57%	3.5 h	[106]
W:$BiVO_4$	CoPi	TiO_2 /Al:ZnO /Cu_2O	RuO_x	1 M NaOH phosphate (pH~6)	TiO_2 layer	0.5%	80% current in 2 min	[107]

2.2.2 PEC Water Splitting without Photovoltaics

In contrast to unassisted photocatalytic overall neutral pH water splitting at zero-bias, photoelectrochemical (PEC) water splitting devices are typically assisted in numerous ways, such as, by imposing –

a. an external bias voltage,
b. an internal bias voltage with different concentration of hydrogen ions,
c. an internal bias voltage with the use of integrated photovoltaics (the PV-layers can also contribute as a low-bandgap absorber and enhance photon conversion efficiency).

Therefore, PV-PEC systems typically demonstrate higher efficiencies in acidic or alkaline condition, and hence, is not likely to compare with the efficiency values achieved using *photocatalytic or photochemical* approach of neutral pH water splitting. It is worthwhile mentioning that, the high STH reported for PEC water splitting are mostly designed for either photocathodic or photoanodic performance of the electrode which requires noble-metal counter electrode to perform one redox half-reaction. Significantly, the STH efficiency is very low till today for paired-electrode PEC system, where both the photocathode and the photoanode are designed using semiconductors (single or tandem/dual-absorber). For example, the performance of conventional 2-photon tandem photoelectrodes are generally very poor, exhibiting efficiency in the range of ~0.5-0.9% or less [104-107] (see Table 2-2), which are significantly less than the best reported single photoelectrode (~1.8%) [108, 109] and PV-PEC devices (16%) [110]. However, slightly higher efficiency values (~0.9%) have been demonstrated in two independent studies, using a hematite (Bi-$BiVO_4$) as photoanode and amorphous Si (solid solution of ZnSe and $Cu(In,Ga)Se_2$) as photocathode with $NiFeO_x$ and TiO_2/Pt (Pt, Mo, Ti, and CdS) overlayers [102, 103]. Attempts have been made to connect two (GaN/InGaN) nanowire photoanode and photocathode, which only leads to a power conversion efficiency of ~2.0% [111]. A recent study further demonstrated that, by mimicking the functions of photosystem II (PSII) with $BiVO_4$ semiconductor (light harvester) protected by a layered double hydroxide (NiFeLDH, hole storage layer), an STH efficiency ~2.0% can be achieved. The system uses a partially oxidized graphene (pGO) as biomimetic tyrosine for charge transfer, and molecular Co-cubane as oxygen evolution complex [112]. The stability of the photoelectrodes are, however, extremely poor, mostly limited to ~10 hours or less.

Table 2-3: State-of-the-art PEC systems/electrolysers with integrated photovoltaics.

Anode	OER cocat.	Cathode	HER cocat.	Electrolyte	Surface protection	STH	Stability	Ref.
PV-PEC Systems								
RuO_x	N/A	$Ga_{0.41}In_{0.59}P$/ $Ga_{0.89}In_{0.11}As$	Rh	1 M $HClO_4$ (pH~0)	AlInP / $AlInPO_x$ / TiO_2	19.3%	33% reduced in 30min	[113]
				0.5 M KH_2PO_4/ K_2HPO_4 (pH~7)		18.5%	17% reduced after 20h	
RuO_x	N/A	GaInP/ GaInAs	PtRu	3M H_2SO_4 1 mM Triton X	n-AlInP passivation	16%	15% reduced over 1h	[110]
RuO_2	N/A	Ge/GaInAs/ GaInP/ $Al_xIn_{1-x}P$/ $AlInPO_x$	Rh	1 M $HClO_4$ (pH~0)	N/A	14%	50% reduced over 35h	[114]
n-p GaAs/ Pt/Ti/Pt/Au	$IrO_x\cdot nH_2O$	p-n GaAs /AuGe/Ni/Au	Pt	0.5 M H_2SO_4 (pH~0.55)	Metal-passivation layer	13.1%	N/A	[115]
Pt counter	N/A	$GaInP_2$/GaAs p/n	N/A	3M H_2SO_4 0.01 M Triton X	N/A	12.4%	~20 min, to 87.5% in 20 h	[116]
IrO_2	N/A	Ge/GaAs/ InGaP/TiO_2	Pt	3.0 M $KHCO_3$	N/A	11.2%	7~9 h	[117]
PV-Electrolysers								
InGaP/GaAs/ GaInNAsSb 3-jn SC	Ir black	InGaP/GaAs/ GaInNAsSb 3-jn SC	Pt black	PEM electrolyser	N/A	30%	48 h	[118]
AlGaAs/Si	RuO_2	AlGaAs/Si	Pt black	1 M $HClO_4$ (pH~0)	N/A	18.3%	14 h	[119]
$Ga_{0.35}In_{0.65}P$/ $Ga_{0.83}In_{0.17}As$ 2-jn SC	Ir	$Ga_{0.35}In_{0.65}P$/ $Ga_{0.83}In_{0.17}As$ 2-jn SC	Pt	PEM electrolyser	N/A	18%	2.3 h outdoor	[120]
n/p-GaInP/ GaAs	Pt	n/p-GaInP/ GaAs	Pt	2M KOH	N/A	16.5%	9 h outdoor	[121]

2.2.3 PEC Water Splitting with Integrated Photovoltaics

Since the demonstration of an STH ~12.4% with limited stability by J. Turner in 1998 [116], PV-PEC devices on Ga(In)As/Ga(In)P platform are consistently being reported till today with an efficiency in the range 10-14% and stability < 80 hours [114, 115, 117, 122]. An enhanced STH efficiency of ~16% is reported by Young *et al.* [110] using GaInP/GaInAs tandem absorber with significantly limited photocurrent stability. Higher stability had been demonstrated on triple-junction Si solar cell for 31 days, however, with reduced efficiency of ~5% [123]. Recently, a stability study through electrolyte engineering has shown that, the use of a vanadium-saturated solution can suppress the photo-corrosion of vanadium-containing catalysts *e.g.* $BiVO_4$, with photocurrent stability up to ~450 hours [124]. The state-of-the-art efficiencies for the PV integrated electrolysers are typically higher than that of PV-PEC systems (in the range of 15-30%).

In summary, as for unassisted PEC water splitting, the state-of-the-art STH efficiency is limited to ~1-2% while being stable for duration as low as 12 hours without the incorporation of any photovoltaic (solar cell). Although the STH efficiency is boosted up to 16% for PEC [110], and to 30% for electro-catalysis [118] when integrated with photovoltaic cells (see Table 2-3), most of the reported unassisted PEC water splitting systems still suffer from the instability (limited to < 100 hrs). Despite comparatively lower STH efficiency than that from PEC water splitting, *photochemical or photocatalytic* dissociation of water has been intensively studied as an alternative, due to its simplistic configuration and the capacity to directly split water, which is ideally suited for large scale solar fuel production. While tremendous progress has been made in photoelectrochemical (PEC) water splitting in the past decades, it is not suited to split nearly pH neutral water such as sea water, due to the need of conductive electrolyte. Although it has often been referred to as a *wireless* version of PEC water splitting, the *photocatalytic or photochemical* approach of water splitting does not require any external bias (zero bias, unassisted) and conductive electrolyte due to the monolithically integrated nature of the micro-/nano-electrode (in the form of co-catalyst), and therefore, is of great interest.

2.3 Challenges in Designing Efficient and Stable Photocatalyst for OWS

Designing an efficient photocatalyst requires simultaneous improvement in all the three key steps in photocatalytic water splitting reactions:

i. maximize the photon-harvesting ability through *bandgap engineering* for promoting the generation of active electron–hole pairs,

ii. minimize detrimental recombination through *interface engineering* for efficient charge carrier separation and migration towards reaction sites, and

iii. enhance the reactivity and stability of the photocatalyst through *surface engineering*.

Progress in this field, however, has been severely limited by the lack of suitable photocatalyst whose energy bands can straddle the water redox potential. In this context, group III-nitride semiconductors, e.g. Ga(In)N, with its extreme chemical stability emerges to be the only material among the currently known photocatalysts, whose energy bandgap can be tuned across nearly the entire solar spectrum and can straddle water redox potentials over a wide absorption range (UV, visible, and near-infrared), thereby holding an enormous promise for high efficiency one-step overall water splitting. To date, however, the efficiency of overall water splitting using Ga(In)N and other visible light responsive photocatalysts has remained extremely low [125-127]. While much of the prior state-of-the-art researches are focused on enhancing the optical absorption through extension of threshold wavelength via bandgap engineering [27, 29, 71, 127], the detrimental effects of unbalanced charge carrier extraction/collection, their recombination and trapping (in the bulk and on the surface), on the efficiency of water splitting reaction and the stability of the photocatalyst has remained largely unaddressed. Accordingly, it would be essential to address the reduced efficiency arising from unbalanced charge carrier extraction/collection and realize an effective and standalone photocatalytic hydrogen generation through solar powered water splitting.

Recently, nanoscale photocatalysts have been intensively studied which can increase light absorption and charge carrier separation, and therefore enhance the quantum efficiency [128]. Fermi-level pinning, however, has been commonly measured on nanowire surfaces such that the resulting surface band bending creates an additional energy barrier for charge carrier transport to the photocatalyst-water interface leading to significantly reduced reaction rate and extremely low efficiency. To date, the rational synthesis of nanostructured photocatalysts with suitable bandgap, and the engineering of carrier transport for reduced recombination at nanoscale, with controlled surface charge properties has remained a near-universal challenge. Such uncontrolled carrier transport and surface charge properties can further contribute to the reduced photocatalytic efficiency of the system, and to the photo-corrosion and instability of various nanostructured photocatalyst under harsh photocatalysis conditions, severely limiting their practical applications.

2.4 Factors Affecting Photocatalytic Performance in OWS

A semiconductor with sufficiently narrow bandgap (or extended absorption threshold) and crystalline quality (no carrier-trapping centers) does not guarantee efficient photocatalytic performance, despite its possessing the necessary over-potentials for water oxidation and proton reduction. As such, there are some internal and external factors that have substantial influence on the performance of the semiconductor catalyst in photochemical reaction, and therefore, can be engineered accordingly. In the following sections, we will focus on the role of some influential factors, while considering photocatalytic water splitting on a semiconductor-based photocatalysts.

2.4.1 Charge Carrier Separation and Enhanced Carrier Lifetime

The underlying reason for the low photo-activity of various catalysts are the inherent mismatch between the bulk charge carrier lifetimes and the rates of charge transfer reactions. Kinetically, one of the key requirement for photocatalytic water splitting is the generation of charge carriers with lifetime in the order of at least milliseconds (ms). The bulk charge carrier lifetimes of metal oxides, such as TiO_2, hematite, $BiVO_4$, or in metal nitrides *e.g.* Ga(In)N range from picoseconds (ps) to nanoseconds (ns). Considering the water oxidation mechanism, interfacial charge transfer occurs on the millisecond to second timescales, as shown in Fig. 2-1. Evidently, a staggering 12 orders of magnitude mismatch in the lifetimes of interfacial charge transfer (i.e. *productive*) and charge recombination (i.e. *energy loss*) steps can cause substantial reduction in the photochemical activity. Therefore, to enhance the charge transfer rate for efficiently competing with the carrier recombination, strategies need to be applied that significantly increase the charge carrier lifetime within the semiconductor catalyst. Various approaches are proved to be promising and are widely implemented in the design of semiconductor photocatalyst, which include - increased width (W) of space charge region (SCR) by applying external bias, using the internal electric field in ferroelectric materials, heterojunction formation with metal oxides or plasmonic metals, donor–acceptor dyads, integration of photovoltaic cells (*p-i-n* heterojunctions) etc.

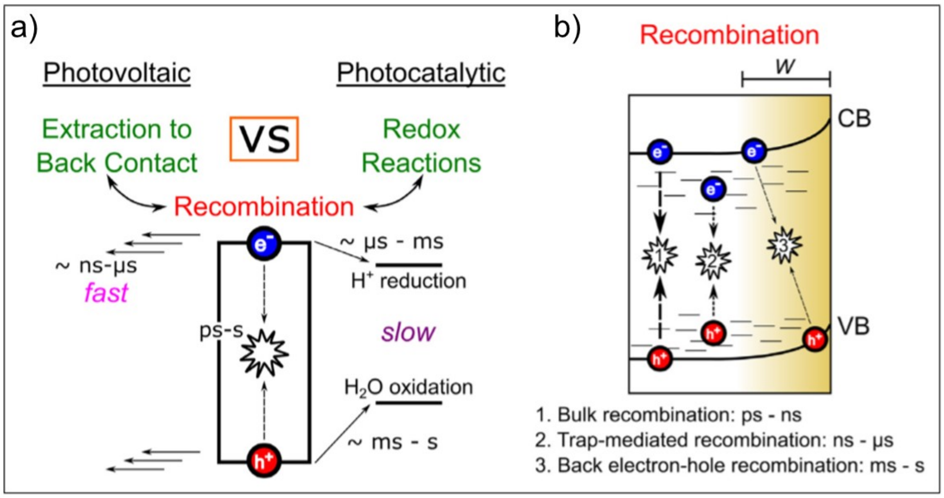

Figure 2-1: a) Schematic illustration of the timescales and competition between the dynamic processes, such as carrier recombination and charge extraction from a semiconductor. b) Typical recombination pathways and timescales. W denotes the width of the depletion layer [129].

The p-n junction is an effective approach for charge carrier separation to individually engineer either oxidation or reduction reaction forward at the nanoscale [130-133], and are widely used for PEC devices. By increasing the width of the depletion layer (W) through applied bias, and by transferring the carriers into SCR where back electron–hole recombination across the SCR (process 3 in Fig. 2-1b) is significantly retarded - the lifetime of the holes can be effectively prolonged from picoseconds to the second timescale.

However, the junction engineering approaches offer internal electric field as a driving force for spontaneous and unidirectional charge transfer only at the *near-surface* region and *near the space-charge* region (SCR) at the interface, which further limits the carrier separation efficiency at zero bias. For overall unassisted photocatalytic water splitting, it offers band-bending at the semiconductor-electrolyte interface that hinders the migration of the appropriate carriers (both electrons and holes) to participate in respective half-reactions, resulting in reduced efficiency. Moreover, interfaces (junctions) need to be carefully optimized in order to improve the photocatalytic performance, by tailoring the interfacial parameters, namely, compositions, interfacial area, defects, electronic coupling between surfaces, and the distance from the interface to the active redox sites [97], thus making the implementation more challenging. If the distance from the interface to the surface is large (thick semiconductor layers), potential difference is required to govern the charge transfer from the semiconductor interface to the bulk or from within the bulk to the reactive surfaces, thus limiting its performance in zero-bias overall water splitting. Some effective approaches of charge carrier separation for enhanced photocatalytic performance in overall neutral pH water splitting will further be discussed in Chapter 5.

2.4.2 Role of Co-catalyst on Photocatalytic Performance

As discussed in section 1.6, for efficient solar fuel production, both $\eta_{\text{transport}}$ to the solid-liquid interface and $\eta_{\text{interface}}$ need to be enhanced, *i.e.*, charges not only need to reach the semiconductor–electrolyte interface, but interfacial charge transfer must also occur to extract the charges. Kinetic competition between surface recombination (including carrier trapping in surface states) and interfacial charge transfer determines the rate of surface reactions. To provide the surface charges with sufficiently longer lifetime so that they can cope up with the slow surface-reaction kinetics, carrier sinks, commonly known as co-catalysts, are employed for individually extracting electrons and holes to facilitate HER and OER, respectively (Fig. 2-2a). Dispersion of co-catalyst (for HER and OER) on the semiconductor surface needs to be engineered such that it leads to the formation of atomically well-defined junctions between them for efficient collection of photoinduced charges (electrons and holes respectively). Although the rate of water splitting is relevant to both oxidation and reduction reactions, the slower one will be the rate determining step for the overall reaction.

However, the co-catalysts perform more than just being a carrier sink to provide longer carrier lifetime. For example, nanoparticulate co-catalysts dispersed on the semiconductor surface provide effective and distinct reaction sites (Fig. 2-2a) and suppresses back reaction. Apart from enhancing the charge carrier separation at the interface, loading of co-catalyst nanoparticles also electro-catalyze the surface redox reactions while decreasing the activation energy (E_a) for water splitting. In this context, Platinum-group metals (Pt, Rh, Pd, etc.) are proved to be excellent HER electrocatalysts, which however, are also active for the OER in most cases. Therefore, it is necessary to make the co-catalyst surfaces insensitive to the back-reaction (*i.e.* the products forming reactants) and make them HER-selective. Metal/metal oxide surfaces with a core-shell structure (Metal/CrOx) had been successfully used, where the shell material functions as selectively permeable membrane for proton and H_2 but not for O_2.

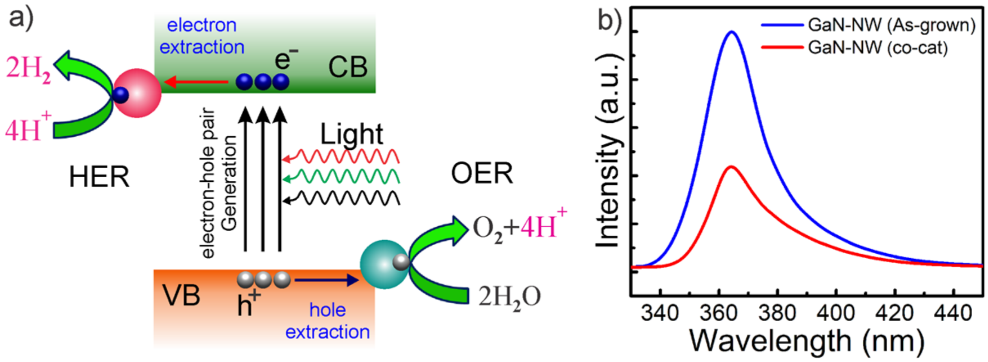

Figure 2-2: a) Carrier dynamics and mechanism for overall water splitting on a semiconductor photocatalyst, loaded with HER and OER co-catalyst simultaneously. b) Reduction of photoluminescence intensity from GaN nanowire due to carrier trapping in the co-catalysts.

The photoluminescence (PL) signal strength has often been directly correlated with the charge carrier trapping, their migration and transfer efficiency, and corresponding photocatalytic activity of the device. In numerous studies, the PL intensity of photocatalytic material was found to decrease as a function of noble metal loading. This has been ascribed to the electron-scavenging effect of metal nanoparticles that act as electron acceptor owing to their larger work function[134-136]. Apart from noble metals, PL intensity also gets reduced in general due to the efficient electron and hole capture by hydrogen evolution reaction (HER) co-catalyst (such as WO_3, WSe_2, SnO_2) and oxygen evolution reaction (OER) co-catalyst (such as PbS, MnO_2, Co_3O_4), respectively [137, 138]. In this dissertation, Rh/Cr_2O_3 core-shell structure had been successfully used as efficient HER co-catalyst on III-nitride nanowires. The PL intensity from co-catalyst nanoparticle decorated GaN nanowires was found to be reduced by 50-60% (Fig. 2-2b) due to electron trapping by Rh/Cr_2O_3, and therefore, reduced recombination. Simultaneous deposition of both HER and OER co-catalysts can also reduce the PL intensity further [138, 139].

It is worthwhile mentioning that, efficient charge separation through controlled exposure of facets that are either highly reactive or anisotropic, or possess different work function had been well-reported on various semiconductors, such as TiO_2, $BiVO_4$, Cu_2WS_4, Cu_2O, BiOCl, $Sr_2Nb_2O_7$, $BaTi_4O_7$, $BaLa_4Ti_4O$, WO_3, $BiVO_4$, $PbTiO_3$, Ag_3PO_4 and $SrTiO_3$ [29, 71, 140]. The enhanced photocatalytic activity derived from these structures though selective distribution of co-catalysts is mostly ascribed to the spatial separation of redox sites and reduced charge carrier recombination. Spatial separation of the co-catalyst nanoparticles further reduce the probability of charge carrier recombination and back reaction [141, 142]. Synergetic effect of the facet-preferential charge separation and subsequent distinction of active redox sites had been analyzed in numerous studies [143-145] through selective deposition of OER (for oxidation) and HER (for reduction) co-catalysts on the hole- and electron-rich facets, respectively. In situ photo-deposition of noble metals and metal-oxides successfully determines the locations of the respective photo-generated carriers corresponding to the deposition mechanism [146-148].

2.4.3 Role of Electrolyte on Photocatalytic Redox Reaction

The electrolyte properties play very crucial role in systems where the electrochemical reactions are involved. And hence, the electrolyte selection varies greatly across different solar fuel production systems, starting from the very acidic to very basic condition. The pH of the electrolyte contributes in multiple ways by – adjusting the band-edge position for sufficient over-potential, controlling the reaction kinetics and intermediate steps in a favorable way, increasing the ionic conductivity to reduce ohmic losses in the electrolyte. As discussed in section 1.3, the reaction mechanism of overall water splitting is significantly influenced by the electrolyte condition. Depending on the medium (acidic, neutral or basic), the reactants of the oxidation reaction, the rate limiting step for overall water splitting differs (hydronium ion, water or hydroxide ions), consequently affecting the efficiency of the photocatalytic reactions. In addition, the local pH near the electrode surfaces can be completely different from each other and from the pH level in the bulk, even at near-neutral pH condition of the electrolyte. For example, in overall water splitting, protons are released at the photoanode (OER) and are consumed at the photocathode (HER). Therefore, it will rapidly develop a significant pH gradient (>6 pH units) in seemingly near-neutral electrolytes. This in turn increases the voltage required to drive the reaction forward even at low operating current densities and limits the system efficiency severely. To minimize the pH gradients, strongly acidic or strongly alkaline electrolytes are frequently used, which also reduces the resistivity for the mass transport in the electrolytes of a system where the two electrodes are distant from each other. However, ionic conductivity can also be increased in near-neutral pH condition by adding a supporting electrolyte or buffer solution. The commonly used buffered species are the phosphate, carbonate and borate anions, which also influence the reaction kinetics.

Therefore, careful attentions are required while designing the integrated solar fuel production systems (photocatalytic and photoelectrochemical water splitting), as the mass transport can become the limiting factor for the overall performance, particularly in buffered condition. Photocatalytic or photochemical water splitting uses an integrated system of photocatalyst where the electrodes are close to each other, as such the problem of the ionic diffusion is largely eliminated, providing an enormous potential for neutral pH pure and sea water splitting. However, this increases the probability of back reaction due to the proximity of HER and OER half-reaction sites, and hence requires measured engineering approach for designing an efficient and stable photosynthesis system, as addressed in Chapter 5 in detail.

2.5 Scope of the Thesis

The goal of the thesis is to explore technology option that would provide sustainable photocatalytic water splitting system - to generate hydrogen as a green fuel from the renewable energy sources, namely, the ubiquitous and abundant water and the sunlight. Therefore, the experimental conditions are designed to imitate a more realistic water splitting device, such that a *concentrated irradiation source* is used to split *neutral pH pure water*. The concentrated illumination is of utmost interest for economically viable industrial production of hydrogen from photolysis [14] within the limited space, while using lesser amount of photocatalyst material. A realistic limit of the concentrated light that can be used for water splitting is estimated in the range of 10-20 suns [13, 14, 16, 149]. Unfortunately, most of the photocatalysts are not stable in water splitting reaction under high-intensity excitation. On the other hand, highly acidic/alkaline electrolytes (with extreme pH) are conventionally explored to ensure maximum efficiency in photo-/electro-chemical reactions. However, when hydrogen production process is considered with respect to the use of renewable energy sources, factors other than the photocatalytic performance must be considered [53]. For example, in the localized system for energy management, safety concerns can be overcome more easily under milder conditions, which can subsequently contribute to the reduction of the capital cost. Therefore, despite the additional challenges, understanding and improving the performance of the photocatalyst in neutral pH pure water and under concentrated excitation is of immense importance in the construction of a future sustainable fuel community, and hence, is the primary objective of this thesis.

Each year, over 10,000 million square inches of Si wafers are produced, which largely drives the nearly US$3 trillion consumer electronics market. Similarly, GaN, which is the second most invested semiconductor material only next to Si, has been widely used industrially in solid-state lighting, blue/green laser diodes, and high-power electronic devices with a combined market value exceeding $100-billion. Therefore, design and synthesis of reproducible GaN-based nanostructures and its alloys, e.g. InGaN on commercial Si wafers, is of great interest for leading towards commercially viable large-scale clean hydrogen generation from unassisted solar-driven pure water splitting. In this context, this dissertation gradually and sequentially addresses some the key challenges associated with the design of a nanostructured Ga(In)N photocatalyst for efficient and stable hydrogen generation, which includes – tuning the bandgap and surface charge properties for enhanced visible light absorption while ensuring sufficient over-potentials for both water oxidation and proton reduction reaction, engineering the structure/interface for efficient charge carrier separation within the nanostructure to suppress back reaction and carrier recombination, and engineering the surface for enhanced stability and efficient interfacial charge transfer between the photocatalyst and the electrolyte. The detailed outline of the thesis is as follows.

In Chapter 1, we have discussed the fundamentals of photocatalytic water splitting, the reaction mechanisms and the prospect of III-nitride as an efficient and stable photocatalyst. Conventional terminologies to evaluate the performance of a photocatalyst and their theoretical limits are also described therein. Chapter 2 briefly elucidates the status of the photocatalytic and photoelectrochemical water splitting in terms of efficiency and stability of the photocatalyst. The challenges that lies in the path of designing efficient and stable photocatalyst, and the scopes and opportunities to address those issues are also highlighted.

In Chapter 3, we have discussed the growth/synthesis of nanostructured III-nitride photocatalyst using Molecular Beam Epitaxy (MBE). The characterization techniques for their structural, optical and surface charge properties, and methods for their performance evaluation are also described therein, along with the influential factors that can potentially contribute to achieving high-efficiency overall neutral pH water splitting.

In Chapter 4, we have investigated the impact of surface charge properties on the photocatalytic activity of Ga(In)N nanowires. In addition to the optimization of energy bandgap and band edge positions, it addresses the issues related to imbalance in redox reactions, reduced efficiency, and poor stability. Subsequently, through controllable dopant incorporation during the growth process, the surface charge properties of the nanoscale photocatalyst were tuned to provide the appropriate Fermi level and/or band bending to allow the balanced extraction of electrons and holes for the photochemical water splitting to proceed at high rate and high efficiency.

Chapter 5 addresses the issue of carrier trapping and recombination in the bulk of the semiconductor and their detrimental effects on significantly limiting the efficiency. For semiconductor-based photocatalysts, efficient separation of photo-generated charge carriers (electrons and holes) towards the appropriate catalytic sites has remained challenging, particularly for photocatalytic water splitting wherein no external bias is applied. Accordingly, we proposed and demonstrated a new class of multi-band InGaN nanosheet photochemical diode structure, which can spontaneously induce charge carrier separation and steer charge carriers toward the distinct redox sites for water oxidation and proton reduction, respectively. During the growth process, p-type dopant (Mg) concentrations were rationally tailored, leading to a large work function difference (up to 300 meV) between the two parallel surfaces and resulting in the formation of p-p^+ nanoscale lateral junction. In addition to the efficient charge carrier separation and extraction, the spatial separation of catalytic sites in such a nanoscale photochemical diode can effectively reduce carrier recombination and back reaction. Consequently, an impressive STH efficiency of ~3.3% had been derived for pH neutral overall water splitting.

Chapter 6 highlights the burning issue of suppressed interfacial charge transfer and limited photochemical stability of semiconductor catalysts, especially under concentrated irradiation. Although the use of wide-bandgap protection/passivation layers such as TiO_2, are largely reported to improve the stability for PEC water splitting, such extra protective layers significantly compromise the charge carrier extraction, with additional level of complexity in the design and synthesis of the photoelectrodes. In this chapter, we have investigated the distinct, as well as the synergistic effect of the water oxidation co-catalyst CoO_x, the proton reduction co-catalyst Rh/Cr_2O_3, and the surface band bending of the nanowires on the performance and long-term stability for photocatalytic overall water splitting reactions. Ga(In)N nanowires, carefully engineered with atomically thin N-rich surfaces, together with the reduced surface band bending through Mg-dopant incorporation and faster water oxidation enabled by Co_3O_4, can overwhelmingly enhance the injection of photogenerated holes into the aqueous solution, and can exhibit long-term stable operation (>580 hours) in unassisted pure water splitting.

Chapter 7 explores, both theoretically and experimentally, a new generation of semiconductor (III-nitride) for extended visible light absorption, namely dilute-antimonide (Sb) III-nitrides. The study demonstrates the first ever realization of optically active dilute-Sb GaSbN nanostructures, which emits (absorbs) visible light due to very small amount of Sb incorporation into GaN in the dilute limit (<1%) and holds enormous promise for visible-light driven water splitting. The synergistic effect of In and Sb incorporation into GaN is briefly discussed in Chapter 8 within the dilute-Sb limit (<1%), demonstrating the controllable tuning of conduction- and valence-band edges to realize narrow-bandgap quaternary Ga(In, Sb)N heterostructures.

In Chapter 9**,** we have summarized the major findings in this thesis and concluded with discussions on some promising investigations and detailed proposals for future direction.

2.6 Conclusion

Herein, we have briefly summarized some of the highly efficient, stable and best performing photocatalyst for hydrogen and oxygen evolution till today; and their design and synthesis technique to ensure high quality material and performance are growing more mature day by day. Subsequently, the unresolved challenges that limit the performance for some of the promising photocatalyst families - such as non-tunable wide band gap, large overpotential for hydrogen evolution, rapid recombination of produced electron-hole pairs and uncontrolled surface charge properties, to name a few, are discussed. Fundamental concepts and useful insights of various approaches to address these shortcomings, such as doping with different elements, forming heterojunction, noble metal deposition, surface modification and electrolyte engineering etc. are also elucidated. With that in mind, the works in this thesis aim to gradually develop photocatalytic corrosion resistant, visible light absorbing, defect-free crystalline photocatalyst using III-nitride nanostructures, for efficient and stable hydrogen generation from overall neutral pH water splitting under concentrated irradiation.

Chapter-3

Synthesis, Characterization and Performance Evaluation of Group III-Nitride Nanostructures

3.1 Introduction

The most commonly used techniques for the growth/synthesis of III-nitride nanostructures include direct reaction between gallium (Ga) or indium (In) metals with NH_3, chemical vapor deposition (CVD), molecular beam epitaxy (MBE), chemical beam epitaxy (CBE), and hydride vapor phase epitaxy (HVPE). Significantly, MBE is being widely used in industry nowadays to produce III-V electronic and photonic devices, as well as the emerging low-dimensional semiconductors such as quantum dots (QDs) and nanowires (NWs). MBE provides with some fundamental advantages in growing high-quality Wurtzite III-nitride nanowire heterostructures which had been thoroughly used in this study. The spontaneous formation of III-nitride nanowires is commonly realized under nitrogen (N_2) rich condition by MBE technique. The underlying reasons are, - the material purity is significantly increased as the growth mechanism requires no foreign metal catalyst, and the growth is performed under ultrahigh vacuum condition. Therefore, the MBE grown materials can possess extremely high quality with drastically improved electrical and optical properties, and atomically thin and abrupt interfaces can be achieved due to the low growth rate.

Experimental characterization of material properties is of critical importance to optimize the growth process and to realize high performance devices. For instance, to evaluate the utility of a new material or a new structure, it is crucial to derive the intrinsic material properties such as the morphology, optical bandgap, material composition, crystalline quality, the free carrier concentration, and the electron drift mobility, etc. Moreover, the material quality might vary from each growth as well as from position to position in the same sample, specially when highly complex and sophisticated systems such as MBE are involved in the process. To provide with vital information about the nanostructures for further optimization, numerous characterization techniques were employed in this study, such as - scanning electron microscopy (SEM), transmission electron microscopy (TEM), X-ray diffraction (XRD) analysis, X-ray photoelectron spectroscopy (XPS), Photoluminescence (PL) and micro-Raman spectroscopy, photocatalytic/photochemical and photoelectrochemical measurements for performance evaluation, to name a few.

3.2 Molecular Beam Epitaxial Growth

Although the commercialized Ga(In)N planar structures are generally grown by metal organic CVD (MOCVD) technique nowadays, it requires the use of large amount of ammonia and high growth temperature. Consequently, it incorporates large dislocation density and poorly controlled hetero-interface due to the thermal mismatch, which severely limits the device performance. Moreover, realization of high-In content material is extremely difficult due to high growth temperature. In contrast, ammonia-free plasma assisted MBE can produce high quality In-rich narrow-bandgap materials due to its low growth temperature. In addition, the MBE grown Mg-doped III-nitrides do not need annealing to activate p-type conductivity, which had been extensively used in this study, due to the much-reduced hydrogen incorporation during growth process. With the rapid development of MBE technology, the growth on large-area wafer (up to 12 inch) has been very mature. Most importantly, the throughput now is comparable to that by metal organic CVD system, providing the distinct opportunity for the realization and large-scale production of efficient and stable III-nitride nanostructured photocatalyst.

In this study, vertically aligned GaN/InGaN nanowire heterostructures were grown on Si (111) substrate (nanowire tilt-angle: 80°-90° w.r.t the substrate) by a Veeco Gen II MBE system equipped with a radio frequency (RF) plasma-assisted nitrogen source. Figure 3-1 shows the simplified schematics of the MBE system which consists of three main vacuum chambers including an intro-chamber, a buffer chamber, and a growth chamber. Thermal effusion cells were used for gallium (Ga), indium (In), aluminium (Al), germanium (Ge), antimony (Sb) and magnesium (Mg). Ge and Mg were used as dopants for *n*-type and *p*-type conductivity, respectively. Nitrogen radicals were supplied from the RF plasma source. Additionally, the MBE system was equipped with a reflection high energy electron diffraction (RHEED) system which facilitates the *in-situ* monitoring of surface properties and the quality of nanostructures.

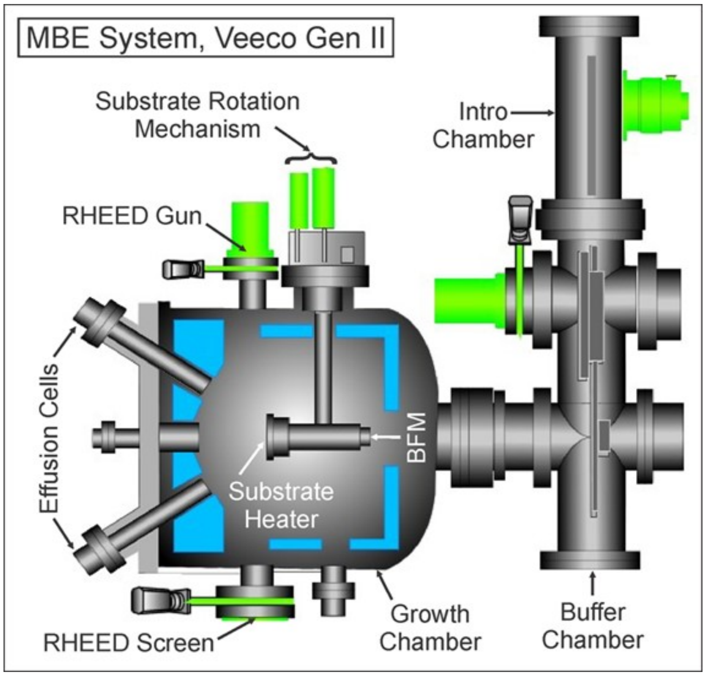

Figure 3-1: Schematic diagram of a molecular beam epitaxy (MBE) system (Courtesy – Veeco, Gen II), depicting the arrangements of the effusion cells and the substrate in the growth chamber. The position of Intro- and Buffer-chamber for substrate preparation, and the filament for beam flux monitoring (BFM) are also shown.

The primary challenges involved in the synthesis of nanowire photocatalysts are the control of the wire uniformity, height, diameter, shape, density, and orientation/alignment, while eliminating the stacking faults and other form of defects. In that regard, optimum growth conditions, including the substrate temperature, III/V fluxes, and growth rate play critical roles. The work in this dissertation focuses on developing efficient III-nitride photocatalyst nanostructures on cheap and recyclable substrate (the surface of which can be re-used for MBE growth), such as silicon. The orientation of the substrate also plays a key role in the nanowire alignment. The <111> growth direction of Si substrate is commonly used in the growth of III-nitride nanowires rather than that the <001> direction, due to the reduced surface energy of the exposed sidewall facet during growth. Conventional mechanism for the growth/synthesis of semiconductor nanowires on amorphous substrate involves the use of foreign metal catalysts. This in turn leads to the incorporation of significant level of impurity, while providing little or no control on their structural, electrical and optical properties. Alternatively, a foreign catalyst-free mechanism for nanowire synthesis can be employed by introducing a thin layer (one monolayer ~ 0.6 nm) of Ga or In, which acts as a seeding layer for the nucleation of nanowires. Consequently, Ga or In droplets are formed at elevated temperature, providing controllable and uniform nuclei size, compared to the random nuclei sizes during the spontaneous formation of nanowires.

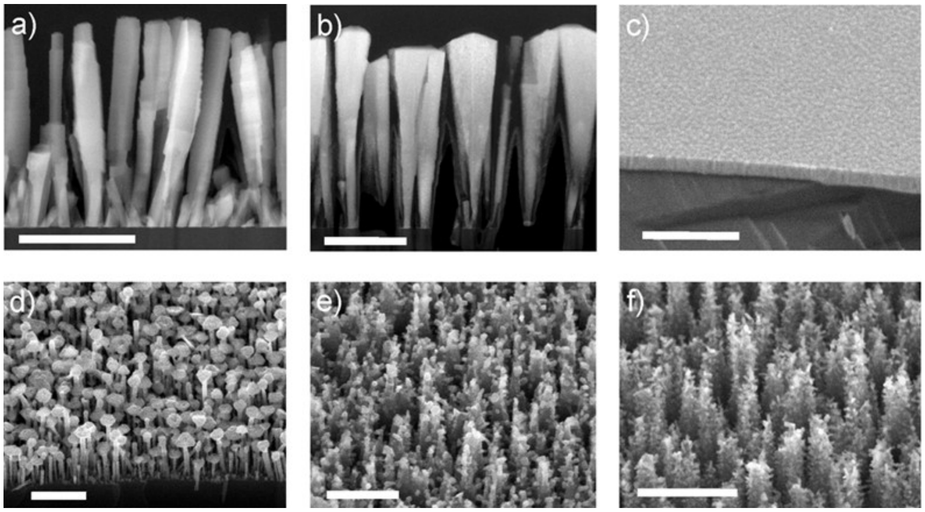

Figure 3-2: Electron energy loss spectroscopy (EELS) image of the cross-section of a) *p*-type and b) *n*-type GaN nanowires, doped with Mg and Ge, respectively. The nanowires are vertically aligned on Si substrate. Scale bar, 300 nm. SEM images of c) GaSbN epilayer d) InGaN disc on GaN nanowire (mushroom-like) structure, grown on Si substrate. Scale bar, 1 µm and 300 nm, respectively. SEM images of e) InGaN nanoparticles and f) GaN branched nanowires, grown on the sidewalls of Si nanopillars. Scale bar, 300 nm.

In this study, the III-nitride nanostructures were grown under nitrogen rich conditions without using any foreign catalyst. Figure 3-2 shows the morphology and typical dimensions of the nanostructures grown either on planar Si substrates or on Si nanopillar templates fabricated by etching planar Si wafer. The Si (111) substrate was thoroughly cleaned with acetone and methanol solvent to remove organic contaminants and subsequently with 10% hydrofluoric acid (HF) to remove native oxide, prior to loading into the MBE chamber. *In situ* oxide desorption was performed at ~780 °C before the growth initiation until the formation of a clean Si (111) 7×7 reconstructed surface was confirmed by reflection high-energy electron diffraction (RHEED). A thin (~ 1ML) Ga seeding layer was *in situ* deposited, which promotes the nucleation of nanowires. The growth parameters were optimized after several iterations for better crystalline quality and photocatalytic performance in overall water splitting reaction. A nitrogen flow rate of 1.0 standard cubic centimeters per minute (sccm), and a forward plasma power of ~350 W were used during the growth in general, unless mentioned otherwise. Other growth parameters include Ga beam equivalent pressure (BEP) of $\sim 6\times10^{-8}$ Torr and In BEP of $\sim 8\times10^{-8}$ Torr. Mg BEP was varied from $\sim 2\times10^{-11}$ Torr corresponding to Mg effusion cell temperature (T_{Mg}) of ~ 200 °C, to Mg BEP of $\sim 5.5\times10^{-9}$ Torr which corresponds to Mg effusion cell temperature (T_{Mg}) of ~ 300 °C. Amount of nitrogen species and metal fluxes in the growth environment were further optimized depending on the desired structure to ensure essential nitrogen vapor pressure in the vicinity of the growth front, and to reduce long-distance diffusion of indium atom along the growth axis. The growth temperature for GaN template was ~ 780 °C, and the growth temperature for InGaN typically varied in the range of 650 to 705 °C.

3.3 Structural Characterization

Structural properties of the III-nitride nanostructures can be analyzed using numerous techniques. For example, the morphology (dimensions, *i.e.* height, thickness, diameter and the areal density) of the MBE-grown nanostructures can be analyzed using field emission scanning electron microscopy (SEM) images, as shown in Fig. 3-2. The as-grown samples are assessed herein by using FEI Inspect F-50 FE-SEM equipment, operated at an accelerating voltage of 5-10 KV and emission current of 5-10 μA. As the nanostructures in this study are grown on Si substrate, the measurement requires no pre-treatment of the sample due to the highly conductive nature of the silicon substrate. Structural properties at the atomic scale are assessed by non-destructive X-ray diffraction (XRD) measurement and destructive transmission electron microscopy (TEM) analysis.

X-ray Diffraction (XRD): The scattering of X-rays from atoms produces a diffraction pattern which contains the signature of material crystalline quality, characterized by the long-range orderly periodic arrangements of atoms. Distance between parallel planes of atoms can be extracted from the position of the diffraction peaks, whereas the intensity of the diffraction peaks reveals the information about the atomic arrangement in the entire crystal. For example, group III nitrides can be of three crystalline structures, such as the wurtzite (Wz), zinc blende (ZB), and rock salt. Under ambient conditions. only the wurtzite structure is thermodynamically stable for bulk III-nitrides.

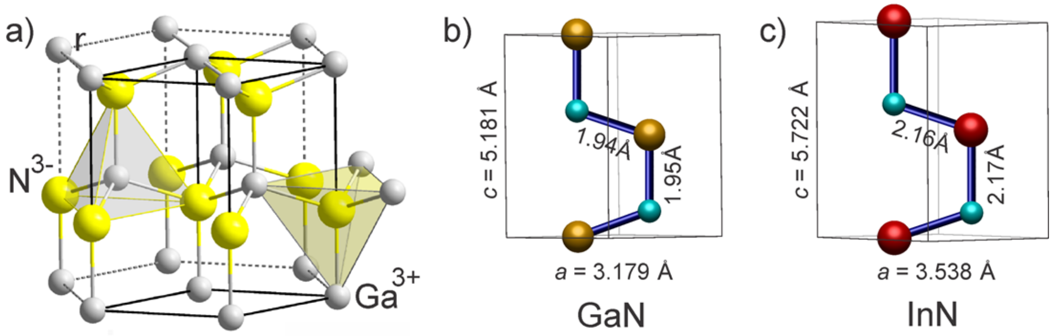

Figure 3-3: a) GaN wurtzite crystal structure [150] showing the arrangement of Ga and N atoms. Unit cell of b) GaN and c) InN wurtzite crystal, showing the dimension along the *c*-axis and non-polar *m*-plane. In is larger cation than Ga, and hence, the incorporation of In into Ga(In)N increases the lattice size.

The wurtzite structure for GaN, as schematically shown in Fig. 3-3a, is composed of two hexagonal close-packed (hcp) sublattices, shifted with respect to each other along the three-fold *c*-axis by the amount of u = 3/8 in fractional coordinates. The ideal hexagonal unit cell has two lattice parameters a and c in ratio $\frac{c}{a} = \sqrt{8/3} = 1.633$. However, the ratios in III-nitrides differ significantly from the ideal condition (1.6010, 1.6259 and 1.6116 for AlN, GaN and InN, respectively), which in turn induces spontaneous polatization in unstrained lattices. The incorporation of a larger indium (In) atom in binary GaN by replacing a smaller gallium (Ga) atom will proportionally increase the size of the unit cell in ternary Ga(In)N alloy. The Ga(In)N nanowires are polar along the *c*-axis and non-polar in the radial *m*-plane, where the parameter c ranges from 5.181 Å to 5.722 Å, and the parameter a varies from 3.179 Å to 3.538 Å (shown in Fig. 3-3b and Fig. 3-3c) for 0% to full compositional range of In (100%). The diffraction peak from GaN nanowires grown on Si substrate reveals the GaN (002) and GaN (004) peaks in the diffraction pattern, as shown in Fig. 3-4a, which correspond to the lattice spacing of c ~0.518 nm, thus confirming the wurtzite structure of the nanowires. The peak position will shift to smaller detector angle (2θ) as the size of the unit cell increases with In incorporation (InGaN), and to larger angle as the size of the unit cell decreases with Al incorporation into GaN (AlGaN). For X-ray diffraction (XRD) measurement in this study, Bruker D8 Advanced Diffractometer with Cu Kα (radiation λ= 1.5418 Å) was used to record the XRD patterns.

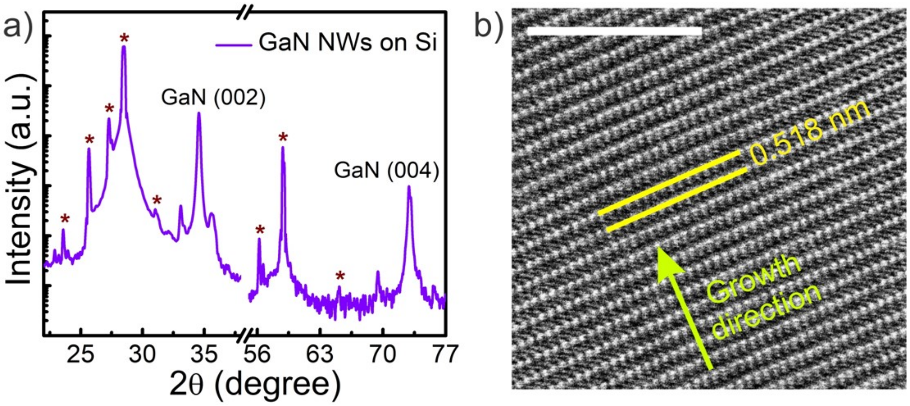

Figure 3-4: a) The prominent reflections of 002 and 004 in the XRD pattern for GaN nanowires on Si substrate. Contributions from Si substrate are marked with '*'. b) HRTEM image of GaN nanowire surface, showing the lattice fringes along the *c*-axis (growth direction).

Transmission Electron Microscopy (TEM): Transmission electron microscopy is based on the electron beam transmission or scattering and transmission, which requires the specimen to be sufficiently thin. The electrons scattered from the specimen is collected on an image plane to form an image of the specimen, whereas the electrons scattered in the same direction is collected on the diffraction plane to generate a diffraction pattern of the specimen. To obtain better understanding of the sample structure, TEM is usually operated in different modes. For example, in bright field (BF) TEM mode, thicker regions or regions with high atomic number, or the parts of the samples that diffract the electron will appear darker and thin areas with small atomic number will appear brighter without diffracting the beam. In high-resolution TEM (HRTEM) imaging, the electron beam can be focused to nanometer size that allows the imaging of the crystallographic structure of a sample at an atomic scale including individual atoms and crystalline defects. On the other hand, in scanning transmission electron microscopy (STEM), the electron beam is focused on the sample with spot size about nanometers while the beam scans the sample with spatial resolution of about atomic distances. A high-resolution STEM-BF image of GaN nanowire surface is shown in Fig. 3-4b, which revealed high crystallinity of the as-grown wurtzite GaN nanowire grown along the c-axis. The distance between the adjacent GaN nanowire lattice fringes is ~0.518 nm, which corresponds to the <0001> direction of GaN, with lateral surface being the nonpolar *m*-plane [151].

The change in lattice fringes of Ga(In)N due to increase in unit cell size can also be precisely measured using this imaging technique. For the layered heterostructures, individual layers can be separately identified with their abrupt interfaces using an imaging technique, called high angle annular dark field (HAADF) imaging, also known as Z-contrast mode. The imaging is based on the scattering of electrons at high angle, which are collected by a ring shaped annular dark-field detector. Therefore, this imaging is highly sensitive to the atomic number (Z) of the elements, as the strength of interaction between the incident electrons and the atoms in the specimen depends on the size and weight of the atom (proportional to Z^2). For example, atomic number (proton numbers) of the elements involved in this study are N (7), Ga (31), In (49). Therefore, in contrast to BF mode, a region with heavier indium atom (InN, InGaN) will appear brighter in HAADF/Z-contrast mode compared to the region with only gallium (GaN). For STEM-SE, -BF and -HAADF imaging, a Hitachi HD2700 Cs-corrected dedicated STEM was used with a cold field emission emitter operated at 200 kV and with an electron beam diameter of ~ 0.1 nm (~0.2 nm in HR mode, and 0.1 nm in UHR mode). STEM energy dispersive X-ray scanning (EDXS) analysis was performed using a 60 mm^2 silicon drift detector (SDD) from Bruker.

3.4 Optical Characterization

Photoluminescence Spectroscopy: Photoluminescence (PL) spectroscopy and Raman spectroscopy are two of the contactless, and non-destructive techniques for optical characterization of the photocatalyst materials (bulk). PL spectroscopy is the analysis of luminescence caused by absorption of photons (light) and then subsequent re-radiation of photons. The spectra can reveal the fundamental electrical and optical properties of materials, namely, the optical band gap, excitonic states, dopant incorporation, impurity states and recombination mechanism etc. When a material is excited with above-bandgap photons, the photogenerated electrons and holes thermally relax to the lowest energy states, *i.e.* conduction band minima (CBM) and valence band maxima (VBM). The thermal relaxation of the charge carriers through the emission of phonons is a faster non-radiative process. Subsequently, the carriers (e^-/h^+) from the band-edges can recombine through the emission of phonons (non-radiative) or photons (radiative) with energy equivalent to the energy difference between the band-edges (*i.e.* bandgap). For example, GaN with bandgap of ~3.4 eV will reveal an emission peak at 365 nm (~3.4 eV) in the photoluminescence spectra (as shown in Fig. 2-2b). Herein, the μ-PL measurement was typically performed with either a 405 nm laser or a 325 nm He-Cd laser (Kimmon Koha) as excitation source (unless mentioned otherwise). The laser beam was focused on the sample through a 60× objective, with a circular beam size of around 5 μm. The emitted light was collected by the same objective, and spectrally resolved by a high-resolution spectrometer (JY HR-550) and detected by a CCD and a photon counting mode photomultiplier tube (PMT).

Micro-Raman Spectroscopy: Raman scattering is a very powerful tool for providing reliable information about the crystalline quality, composition and strain of semiconductors. The technique had been widely used on GaN and related compound heterostructures to investigate their lattice, electronic and magnetic properties [152]. Among eight sets of phonon-normalmodes ($2A_1 + 2E_1 + 2B_1 + 2E_2$) typically predicted in GaN, one set of A_1 and E_1 modes are acoustic, while the remaining six modes ($A_1 + E_1 + 2B_1 + 2E_2$) are optical (see Fig. 3-5a). Here, the A_1 and E_1 modes are both Raman and infrared (IR) active, and the two B_1 modes are known as silent modes as they are neither

Raman nor IR active. On the other hand, the two E_2 modes are only Raman active. Therefore, typically predicted Raman-active optical modes from wurtzite GaN are $A_1+E_1+2E_2$. However, only two E_2 phonon peaks (E_2^H, E_2^L) and one LO phonon peak, A_1(LO), can be well resolved from c-plane using the backscattering geometry with no polarization.

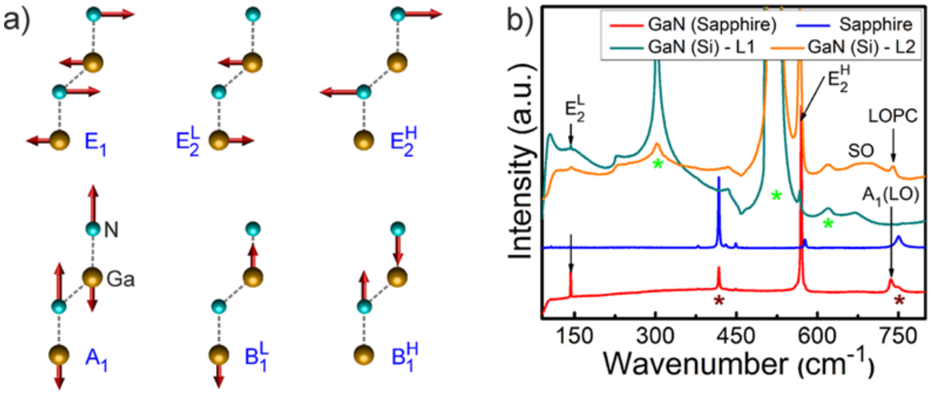

Figure 3-5: a) Atomic arrangement and their displacement (vibration) trajectories for different modes in GaN. (b) Typical micro-Raman spectra of GaN nanowires (films) on Si (Sapphire) substrate, highlighting the prominent modes. Raman modes of Sapphire substrate are also presented as reference. Contributions from the substrates are marked with '*'.

In non-doped GaN nanowires, the presence of a longitudinal optical phonon-plasmon coupled (LOPC) mode at 740 cm^{-1} and a broad surface-optic mode (SO) at 700 cm^{-1} was revealed [153] under 488 nm (and 514 nm) excitation. In GaN epilayer, the LOPC mode intensity and SO mode was suppressed due to reduced surface electrons (reduced surface to volume ratio) which results in the decoupling of A_1(LO) phonon mode at 736 cm^{-1} (Fig. 3-5b). The A_1(LO) mode can also get decoupled from LOPC in p-type GaN due to heavy damping of hole-plasmons. Free standing GaN nanowires, in addition, showed strong and narrow E_2^H peak at ~567 cm^{-1} and typical E_2^L peak at ~142-144 cm^{-1} under 514 nm (L_1) excitation. However, both the E_2 modes of GaN nanowires become weaker (and broader) under low energy excitation (L_2 ~785 nm) with no signature of the A_1(LO) or LOPC modes in the spectrum.

The micro-Raman measurements were carried out at room-temperature using an external 514 nm argon ion laser (unless mentioned otherwise) through a 50× objective with numerical aperture ~0.9. The focused laser spot size was ~1 μm and the estimated power on the sample was ~7 mW. The Raman signal was detected by a CCD detector mounted on the inVia confocal Raman spectrometer from Renishaw. In this dissertation, all Raman spectra were taken in the backscattering geometry with the incident laser parallel to the hexagonal c-axis ([0001] direction) of the nanostructures. The laser light was scattered without polarization analysis (z(..)z direction) and dispersed with an 1800 l mm^{-1} grating. The resolution of a given peak position under these conditions is on the order of 0.2 cm^{-1}.

3.5 Surface Charge Properties

X-ray photoelectron spectroscopy (XPS), also known as ESCA (Electron Spectroscopy for Chemical Analysis), is another non-destructive technique for measuring chemical composition, chemical bonds, as well as electronic states by analyzing the surface/near-surface region of a given material. The XPS spectra typically reveal the kinetic energy (with respect to a reference) and counts of the excited electrons while probing the surface (1-10 nm) by an X-ray beam. In general, the vacuum energy level (E_{vac}) is used as a reference for analyzing the materials in gas-phase, whereas the Fermi energy level (E_F) is the reference for solid-phase materials. Therefore, the surface of the sample and the substrate are universally grounded with the equipment (spectrometer) to set the reference to zero (E_F = 0 eV), as shown in Fig. 3-6a. Highly conductive samples can be calibrated against the standard reference metals (Cu-2$p_{3/2}$, Ag-3$d_{5/2}$, and Au-4$f_{7/2}$ peaks) mounted on the sample holder. However, for the non-conductive or poorly conductive samples, the binding energy needs to be carefully calibrated against carbon C-1s peak (284.8 eV) arising from the adsorption of aliphatic hydrocarbons from the atmosphere.

For the angle-resolved XPS (ARXPS) measurement, Thermo-Fisher Scientific K-Alpha XPS system was used herein. The system was equipped with a monochromatic Al-Kα X-ray source ($h\nu$ = 1486.6 eV) and 180° double focusing hemispherical analyzer. The analysis chamber pressure was as low as 10^{-8} Torr. The non-polar surfaces of the nanostructure arrays were excited with the X-ray source, located at 60° with the surface normal. The E_{FS}-E_{VS} was estimated for each sample by measuring the ARXPS valence band spectrum, and the binding energies were calibrated with both Au *4f* (84.0 eV) and C *1s* (284.8 eV) peaks. XPS analysis is a very useful technique for qualitatively deriving significant information about elemental compositions of nanostructure surfaces and the chemical bonding between semiconductor (photocatalyst) and co-catalyst. Analyzing the photocatalytic devices before and after the experiment can reveal the possible mechanism of activity droop, whereas information about chemical bonding of co-catalysts can promote understanding of the origin of catalytic activity. In addition, the presence of any particular component or the co-catalyst materials on the photocatalyst surface can be confirmed along with their chemical states. Fermi-level position on the surface relative to valence band maximum (VBM) can also be derived by measuring the valence spectra. As shown in Fig. 3-6b, the position of surface valence band (E_{VS}) with respect to the surface Fermi level (E_{FS}, binding energy=0 eV) can be estimated by measuring the intersection point between the linear extrapolation of the valence band leading edge and the baseline.

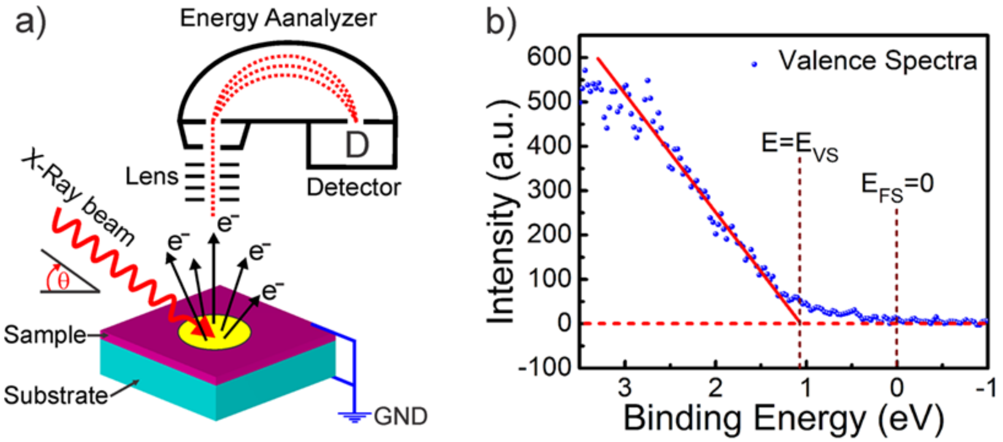

Figure 3-6: a) Schematic illustration of X-ray photoelectron spectroscopy (XPS), briefly showing the operating principal. b) Angle-resolved XPS (ARXPS) valence spectrum measured on GaN nanowires, depicting the position of surface valence band maximum (E_{VS}) relative to surface Fermi-level ($E_{FS} \sim 0$ eV).

3.6 Photoelectrochemical Characterization

Photo-electrochemical cell is a very powerful and efficient tool to characterize certain properties of the photocatalytic material, such as the conductivity behavior, the junction properties of the photocatalysts, and the role of the co-catalysts etc. To analyze the photoelectrochemical properties of the photocatalytic materials used in this thesis, the electrodes were prepared using GaN/InGaN nanowire heterostructures grown on Si substrate. In-Ga eutectic alloy metal was deposited on the backside of the Si substrate to serve as an ohmic contact. The measurements were performed by using a 300 W Xenon lamp as an irradiation source with an intensity ~100-160 mW cm^{-2} on the sample surface. The reactor chamber was made of quartz to ensure ample transmittance for both UV and visible light. An electrochemical potentiostat was used for cyclic voltammetry (CV), chronoamperometry (CA), chronopotentiometry (CP), open circuit potential (OCP), Mott-Schottky measurement (MS) and electrochemical impedance spectroscopy (EIS) etc. The impedance spectroscopy was performed to acquire the Mott-Schottky (M-S) plot in the dark. A dominant photo-cathodic performance of the p-type photoelectrode can be derived by the steep negative slope in the M-S plot, whereas the positive slope reveals the n-type (photoanodic) behavior of the photocatalyst material.

The InGaN nanostructures were further characterized by open circuit potential (OCP) measurement in 1 mol L^{-1} HBr using three-electrode electrochemical cell configuration. The nanostructure arrays (on Si substrate) was used as the photoactive working electrode, whereas a Pt wire, and a double-junction Ag/AgCl were used as counter electrode and reference electrode, respectively. The dominant conductivity type of the material in the electrolyte can be determined by the sign of OCP shift upon illumination. For *p*-type material, the OCP shifts towards more positive potential with respect to Ag/AgCl upon illumination whereas the negative potential difference (with respect to Ag/AgCl) between light and dark under full arc illumination indicates *n*-type behavior of the nanostructures. The typical parameters used for the characterization are as follows. A scan rate of 20 mV/s was used for the linear sweep voltammetry (LSV) with step size ~10 mV and equilibrium time ~5 s within 1 V to -1 V range. The OCP measurements were carried out with sample period of ~1-2 s for 10 minutes, and the MS measurements were conducted using AC voltage of ~10 mV (rms) with stepsize ~0.01 V at a frequency of 1-2 KHz.

3.7 Photocatalytic Water Splitting: Performance Evaluation

The experimental configuration was composed of a reaction system and an evaluation system. The wafer sample, fixed by a homemade PTFE holder was placed in a Pyrex chamber containing appropriate solutions. Distilled water was purged with Ar for 20-30 mins before each experiment. After evacuating the chamber, the system was illuminated using a 300 W Xenon lamp (Cermax, PE300BUV); adequate transmittance for both UV and visible light was secured by placing a quartz lid in between the reaction chamber and the lamp. The evolved gases were then evaluated by a gas chromatograph (GC, Shimadzu GC-8A) equipped with a molecule sieve 5A column and a thermal conducting detector (TCD), and high purity Ar was used as carrier gas. A vacuum tight syringe was used for sampling. Wavelength dependence of the photocatalytic activity and quantum efficiency was systematically analyzed and measured by using appropriate high-pass and band-pass filters. Experimental error in evolution of H_2 and O_2 was estimated to be ~10% due to slight inconsistencies in manual sampling of the evolved gases and/or misalignment between the light source and the sample during water splitting reaction and leakage through the septum. As discussed in section 1.2.2, the half reaction for H_2 evolution was performed on the Rh-nanoparticles decorated Ga(In)N nanostructures in aqueous CH_3OH (20 vol.%) solution, whereas $AgNO_3$ (0.1 M) was used as electron acceptor in the half reaction for O_2 evolution.

Photodeposition of Co-catalyst Nanoparticles

The deposition of noble metals as HER co-catalysts on nanowire surfaces can typically be achieved either through impregnation, adsorption, or photodeposition. Using photodeposition method (reduction of metal cations in aqueous solution into metal nanoparticles by photogenerated electrons), uniform or random distribution of noble-metal nanoparticles can be achieved by readily available electrons (as shown in Fig. 3-7) on axially symmetric nanowire surfaces. Moreover, this method also facilitates the selective deposition of co-catalyst nanoparticles on electron or hole-enriched surfaces of the photocatalysts, which will further be discussed in Chapter 5. In this dissertation, the nanostructure arrays on Si substrate were primarily decorated with Rh/Cr_2O_3 core-shell nanoparticles as HER co-catalyst using a two-step photodeposition process from their respective liquid precursors. In the first step, Rh nanoparticles were photodeposited from 0.5 M sodium hexachlororhodate (III) (Na_3RhCl_6, Sigma-Aldrich) precursor in the presence of 20% methanol in water. The reaction mechanism follows that of the typical photo-reduction processes, as discussed in section 1.3.2 (for proton reduction), which includes the adsorption of Rh^{3+} ion followed by its subsequent reduction to Rh^0 by consuming photoexcited electrons available on the surface. However, in the presence of aqueous CH_3OH as hole scavenger, H_2 will also be generated simultaneously from the available protons (H^+) in the solution due to the oxidation of CH_3OH by the photogenerated holes. And in this process, fraction of the electrons that participate in H^+ and Rh^{3+} reduction can come from the decomposition of the intermediates during the oxidation of CH_3OH, the details of which are described in section 4.2.2.

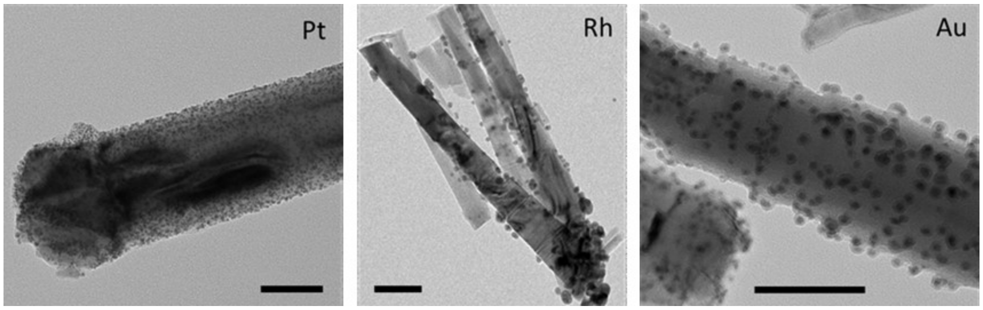

Figure 3-7: Uniform distribution of noble metal nanoparticles (Pt, Rh and Au) on the non-polar surface of axially symmetric GaN nanowires. The nanoparticles were photo-deposited using respective precursors, and the loading was not optimized for enhanced photocatalytic activity. Scale bar, 50 nm.

In the second step, Cr_2O_3 was photodeposited from 0.5 M potassium chromate (K_2CrO_4, Sigma-Aldrich) precursor in the presence of 20% methanol in water, to form the Rh/Cr_2O_3 core-shell structure and to prevent the back reaction. Rh nanoparticles act as proton reduction co-catalysts by scavenging photoexcited electrons and enhanced charge separation on the surface, and they do not take part in water oxidation independently. This is supported by a more negative Fermi level of Rh (-4.9 eV) compared to the electron affinity of InGaN (-3.95 eV) and demonstrated by the reduction in PL intensity on Rh-decorated GaN nanowires. As discussed in section 2.4.2, further deposition of Cr_2O_3 shell on Rh nanoparticles prevents the back reaction on Rh nanoparticles (to form water by combining hydrogen and oxygen) through the formation of a diffusion barrier which is permeable to H^+ and H_2 but not to O_2 [78]. Co_3O_4 nanoparticle, on the other hand, was used as OER co-catalyst which was deposited by a photo-oxidation process under full arc illumination from cobalt nitrate ($Co(NO_3)_2$, Sigma-Aldrich) precursor in 0.01 M potassium iodate (KIO_3, Sigma-Aldrich) aqueous solutions.

3.8 Conclusion

An overview of the growth/synthesis and properties of III-nitride nanostructures is presented in this chapter while considering the building block - GaN and its ternary alloy, Ga(In)N. The MBE growth of high quality, crystalline and non-tapered nanowire heterostructures using an in situ deposited Ga or In seeding layer (prior to growth initiation) are discussed. The realization of catalyst-free InGaN/GaN nanoscale heterostructures on Si (111) substrate, along with their controllable properties, serve as the groundwork of the thesis - towards the goal for an efficient and stable photocatalytic or photochemical water splitting device. Different characterization techniques that have been used thoroughly in the thesis to investigate the structural and optical properties of the as-grown nanostructures are also described. Subsequently, the details of the experimental procedure for post-growth sample preparation and water splitting reaction are discussed along with the performance evaluation techniques.

Chapter-4

Group III-Nitride Nanowire Heterostructures for Efficient Photocatalytic Hydrogen Production

4.1 Introduction

Development of III-nitride photocatalyst in the form of vertically grown nanowires/nanotubes/nanosheets with larger surface area is very critical for achieving high efficiency solar water splitting. But the performance of photochemical water splitting over these emerging nanostructured photocatalysts is often restrained by their surface electronic properties, in addition to the energy bandgap and band-edge positions, which can lead to imbalance in redox reactions, reduced efficiency, and poor stability. Preliminary studies on the successful demonstration of overall water splitting using GaN [126] and InGaN [125] nanowires exhibited substantially low efficiency, both under UV and visible irradiation, respectively. To find out the underlying reasons, we have investigated herein the impact of surface charge properties on the photocatalytic activity of GaN and InGaN nanowires.

Water oxidation, the rate-limiting step of overall neutral pH water splitting, is a four-electron sluggish process and the efficiency of water splitting depends on effective rate of water oxidation. Even though the carrier transport is no longer diffusion limited in the lateral direction of a 1D nanowire heterostructure, the surface charge properties and the built-in electric field (band-bending) plays vary crucial role in determining the redox reaction rate. Therefore, it is significantly important to find out whether the band-bending can be engineered to promote controllable and efficient overall water splitting. From first principles calculation on the nonpolar m-plane of GaN [79], it was revealed that the occupied surface states are positioned at ~ 0.7 eV below the CBM, which leads to Fermi level pinning on *n*-type GaN surfaces. These occupied surface states are derived from the Ga dangling bond. However, the occupied surface states, which are associated with the dangling bond of nitrogen (N), overlap with the valence band without creating any individual levels within the bandgap. Therefore, in *p*-type GaN, Fermi-level pinning is not predicted. This outcome of the study is very exciting, as it leads to the possibility of engineering the surface charge properties through controlled dopant incorporation.

4.2 Photocatalytic Hydrogen Evolution using Visible Light Irradiation

MBE grown non-doped GaN/InGaN nanowires are weakly n-type, which, together with surface depletion effect, creates a high degree of upward band-bending in near-surface region and suppresses electron transfer to the adsorbates. The upward band-bending of the nanostructures becomes more severe with n-type dopant incorporation (Si/Ge), and hence, it provides no control over interfacial charge transfer at the semiconductor-electrolyte interface for overall water splitting. On the contrary, downward band-bending in a weakly p-type GaN/InGaN nanowires can be controllably reduced with additional *p*-type dopant incorporation (Mg). Therefore, p-type doping of GaN/InGaN nanowires can provide controllable tuning of band-bending and surface properties for enhanced photocatalytic efficiency under optimum condition.

In this context, we have investigated the photocatalytic properties of InGaN nanowire arrays under visible light irradiation and demonstrated hydrogen (H_2) evolution both from half reaction with aqueous methanol (CH_3OH) as sacrificial reagent, and from overall neutral-pH water splitting with sunlight as the only energy input. It is observed that the efficiency of H_2 generation, from both half reactions (HER) and overall water splitting (OWS) reactions, depends critically on the p-type dopant (Mg) incorporation in InGaN nanowires. By optimizing the surface charge properties of the nanostructures through controlled p-type dopant (Mg) incorporation, photocatalytic activity of the III-Nitride nanowire photocatalysts can be significantly enhanced by certain orders of magnitude [99, 126]. An apparent quantum efficiency of 17.1% and 12.3% was measured under visible light irradiation (400 - 490 nm) from the HER and OWS reactions for InGaN nanowire photocatalysts with an optimum Mg dopant incorporation, which is explained by the efficient electron and hole migration for balanced surface redox reactions, due to the optimized surface band bending.

4.2.1 Growth and Properties of Multi-stacked GaN/InGaN NWs

In this work, multi-stacked GaN:Mg/InGaN:Mg nanowire photocatalyst were grown on Si substrate without any external catalyst by plasma-assisted molecular beam epitaxy (MBE). Results presented in this work are based on extensive studies on the growth and characterization of Mg doped InGaN nanostructures, which includes careful optimizations of the III/V flux ratio, doping concentration, growth temperature, and growth duration for maintaining higher photocatalytic activity. After *in situ* oxide desorption at ~ 770 °C, a thin (~ 1ML) Ga seeding layer was deposited to promote the nucleation of nanowires. InGaN nanowire arrays were grown on top of a GaN nanowire template for controlled formation of InGaN nanowires to achieve superior structural and optical properties [154].

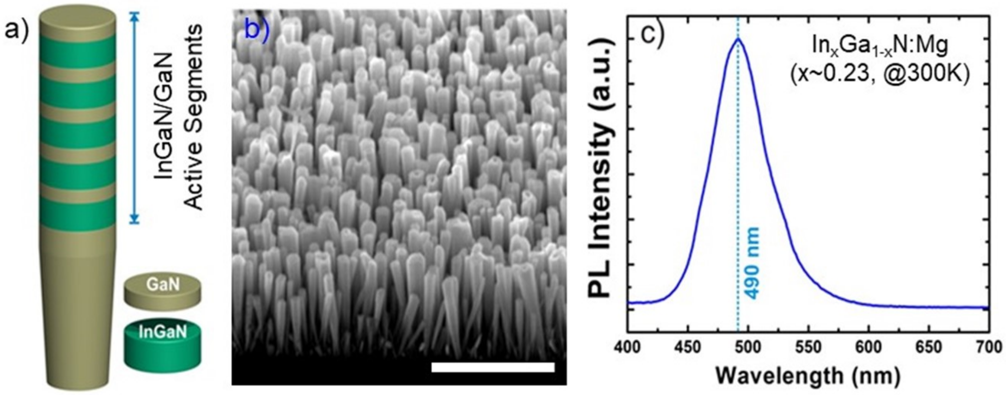

Figure 4-1: a) Schematic of Mg-doped $In_{0.23}Ga_{0.77}N$/GaN (active/capping layer) nanowire structures grown on GaN nanowire template. b) A 45^0 tilted SEM image of $In_{0.23}Ga_{0.77}N$/GaN nanowires grown on Si (111) substrate. Scale bar, 1µm. c) Room temperature micro-photoluminescence spectrum of as grown nanowires, depicting an emission peak at 490nm.

As shown in the schematic of Fig. 4-1a, several segments of InGaN ternary nanowires, capped with a thin GaN layer were incorporated to minimize the formation of misfit dislocations [155]. Other growth parameters include a nitrogen flow rate of 1.0 standard cubic centimeters per minute (sccm), a forward plasma power of ~350 W, Ga beam equivalent pressure (BEP) of ~6×10^{-8} Torr, and In BEP of ~ 8×10^{-8} Torr. The Mg effusion cell temperature (T_{Mg}) was varied and optimized to be ~ 200 °C for InGaN nanowire photocatalyst, which corresponds to a Mg BEP of ~2×10^{-11} Torr. Shown in Fig. 4-1b, the nanowires are vertically aligned along the growth direction (*c*-axis) on the Si substrate, with the areal density in the range of ~1.5×10^{10} cm^{-2}, average height ~ 400–600 nm, and lateral dimensions of ~ 40–80 nm. The photoluminescence (PL) spectrum measured at room-temperature is shown in Fig. 4-1c, with a single band-to-band optical emission peak at ~490 nm, corresponding to a bandgap of 2.53 eV and an average of ~23% indium incorporation. The broad emission peak suggests intra- and inter-nanowire indium fluctuations.

4.2.2 Hydrogen Evolution from Aqueous Methanol Solution

It is important to realize that the conduction band edge of InGaN descends to lower energy faster compared to the valence band edge with increasing In incorporation (bandgap reduction, as shown in Fig. 1-5). Therefore, the photocatalytic performance for H_2 evolution reaction of $In_{0.23}Ga_{0.77}N$/GaN nanowires was first studied to evaluate if they possess sufficient proton reduction over-potential. The experiments were performed using aqueous methanol (CH_3OH) solution. CH_3OH, an organic sacrificial reagent and a frequently used electron (e^-) donor, reacts in an irreversible manner with the photogenerated valence band holes (h^+), enhancing the separation efficiency of photogenerated e^-/h^+ pair and hence reducing the surface recombination. In addition, particulate co-catalysts are often incorporated to promote H_2 evolution, which also function as charge carrier extraction centers to minimize bulk recombination of photogenerated e^-/h^+ pairs [138].

In this study, Rhodium (Rh), a noble metal with a relatively large work function (~ 4.98 eV) were loaded on $In_{0.23}Ga_{0.77}N$/GaN nanowires as co-catalysts (schematically shown in Fig. 4-2a) by photodeposition from the liquid precursor (Na_3RhCl_6) [99, 125, 126]. Subsequently, H_2 evolution reaction using aqueous CH_3OH solution was performed under 300W Xenon lamp irradiation with different long-pass filters. Water (H_2O) to methanol volume ratios of ~ 5:1 was maintained to ensure direct oxidation of methanol rather than the indirect oxidation of interfacially formed *OH radicals [156]. A simplistic illustration of the reaction mechanism is depicted in Fig. 4-2b, showing irreversible oxidation of CH_3OH by photogenerated holes from the valence band of $In_{0.23}Ga_{0.77}N$ segment [157]. In an oxygen (O_2) free environment, the intermediate compound eventually injects e^- into the conduction band of the semiconductor, leading to the formation of formaldehyde (HCHO) as a stable product which could further be oxidized to methanoic acid (HCOOH) and subsequently to CO_2 along with H_2 generation [27, 157, 158]. Rh nanoparticles on the nanowire surfaces, behave as an electron sink and reduce H^+ to H_2.

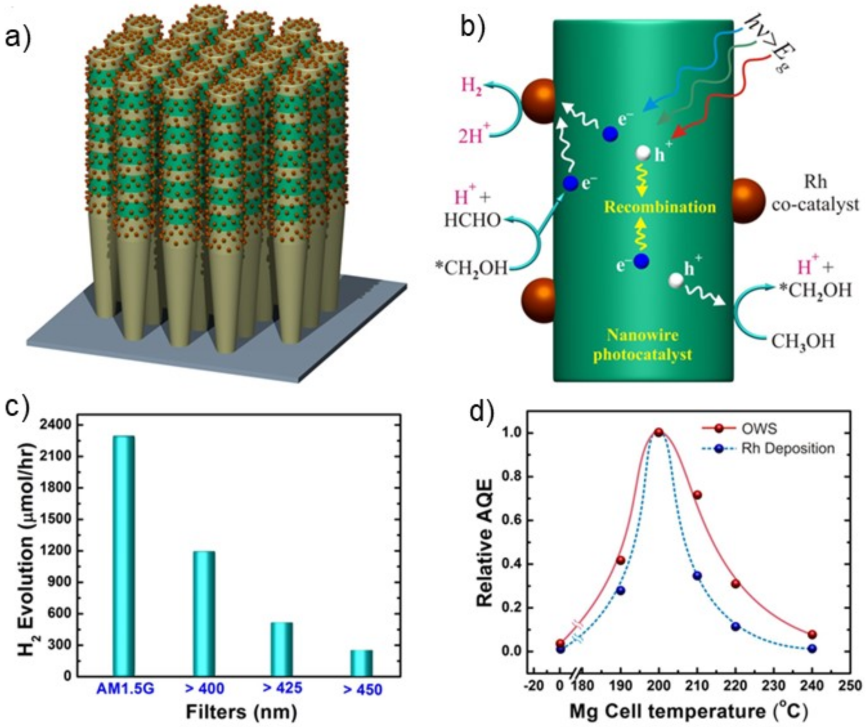

Figure 4-2: a) Schematic of Rh co-catalyst nanoparticles decorated $In_{0.23}Ga_{0.77}N$/GaN nanowires on Si substrate. b) Simplified schematic of photocatalytic H_2 evolution process from methanol solution (aq.) on co-catalyst loaded $In_{0.23}Ga_{0.77}N$ nanowire segment, illustrating the oxidation step of CH_3OH, followed by HCHO formation through electron injection (current doubling) into the conduction band of InGaN, bulk recombination and reduction of H^+ into H_2. c) Photocatalytic H_2 evolution rate measured from wafer level nanowire sample (area ~ 3 cm^2) in the presence of CH_3OH as a sacrificial reagent under with AM1.5G filter and with various long-pass filters, clearly demonstrating activity under visible light (>400nm) irradiation. d) Relative AQE for Rh co-catalyst deposition under full arc and corresponding overall water splitting reaction under visible light (>400 nm) with different Mg-doped $In_{0.26}Ga_{0.74}N$/GaN nanowire arrays with the incorporation of 3-segments of InGaN.

Figure 4-2c depicts the average H_2 evolution rate derived from ~ 6h of photocatalytic reaction for $In_{0.23}Ga_{0.77}N$ nanowires with an optimum Mg doping level (T_{Mg} = 200 ºC), under illumination by a 300W Xenon lamp, with AM1.5G filter and with various long-pass filters. The measurements were performed on samples of areal sizes ~3.0 cm^2. Steady evolution of H_2 was clearly observed using aqueous CH_3OH solution and under different illumination condition. The decreased H_2 evolution rate with increasing wavelength can be correlated to the reduced incident light intensity and reduced photon absorption. The direct measurement of H_2 evolution under visible light illumination provides unambiguous evidence that $In_{0.23}Ga_{0.77}N$ nanowire photocatalysts, with an energy bandgap of ~ 2.53 eV, possess the capacity for proton reduction.

4.2.3 Tuning the Surface Charge Properties of InGaN Nanowires

In this study, it is also observed that the photocatalytic activity for H_2 generation depends critically on the Mg dopant incorporation. We performed extensive studies on the photocatalytic activities of InGaN nanowire photocatalysts with various levels of Mg dopant incorporation by changing the effusion cell temperature of Mg (T_{Mg}) from 190 to 300 °C with corresponding BEP of $\sim 1.0 \times 10^{-11}$ to $\sim 7.3 \times 10^{-9}$ Torr. Shown in Fig. 3d is the relative apparent quantum efficiencies (AQE) measured for (blue dotted line) Rh co-catalyst depositions from its precursor (Na_3RhCl_6:$2H_20$ and aqueous CH_3OH solution). The AQE was estimated as a ratio of the total number of reacted electrons (two electrons per molecule of H_2) to incident photons. It is seen that the maximum photocatalytic activity occurs for Mg effusion cell temperature of 200 °C. The significant variations in photocatalytic performances with Mg dopant incorporation (variations in Mg cell temperatures) are attributed to the tuning of the near surface band-bending by altering the surface Fermi-level (E_{FS}) position, relative to the surface valence band edge (E_{VS}).

At low Mg cell temperature, the nanowire surface is barely doped (almost intrinsic) compared to the bulk (p-type), due to the surface desorption of Mg atoms, which creates a large downward band-bending towards the surface, shown in Figure 4-3a. This band-bending is further subject to change when the nanowires are in equilibrium with solution and under photo-excitation. The downward band bending may accelerate proton reduction at the nanowire surface, but it elevates the barrier for hole-diffusion and impedes the hole transport towards the nanowire-liquid interface (schematically shown in Fig. 4-3a). With increasing Mg incorporation (higher T_{Mg}), the surface of InGaN nanowires can be transformed to be p-type, due to the dopant segregation effect. This leads to a significant reduction of the downward band bending in the near-surface region. Consequently, the transport of both photogenerated electrons and holes to the surfaces can be maximized by optimizing Mg doping level (T_{Mg} ~ 200 °C in this experiment). Water oxidation, the primary and limiting step for overall water splitting, is enhanced due to accelerated hole transport (as shown in Fig. 4-3b). This results in more balanced redox reaction for water splitting, which in turn, enhances the photocatalytic efficiency and stability of the nanowires and enhances the efficiency.

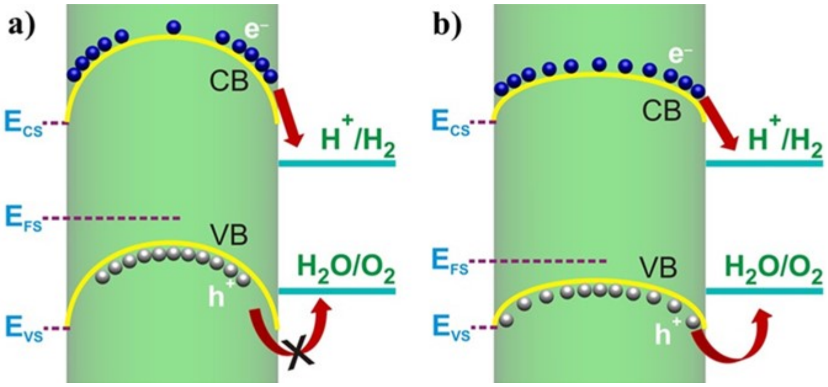

Figure 4-3: a) Severe downward band bending at the surface which hinders hole transport towards the nanowire-electrolyte interface, and b) Reduced downward band bending with optimum Mg dopant incorporation to enhance hole transport for water oxidation.

It is also observed that the photocatalytic performance of the nanowires decreases at high doping level due to the degradation of nanowire crystalline quality and the resulting enhanced nonradiative recombination. Besides, at high Mg concentration, nitrogen vacancy related defects increase. These defects function as n-type dopants and compensate Mg doping (p-type). Detailed studies of the near-surface band structure properties and their correlation with p-type dopant incorporation can be found elsewhere. The relative AQE of overall water splitting from Rh/Cr_2O_3 co-catalyst decorated Mg-doped $In_{0.26}Ga_{0.74}N$ nanowires is also shown in Fig. 4-2d (red solid line) for comparison. Cr_2O_3-shell on Rh co-catalyst was photodeposited to hinder the back reaction that forms water in the presence of O_2. It is seen that variations of the quantum efficiency with respect to the Mg dopant incorporation is in exact agreement with that measured from half reaction, further confirming the significant role of surface band bending on the charge carrier extraction and surface redox reactions.

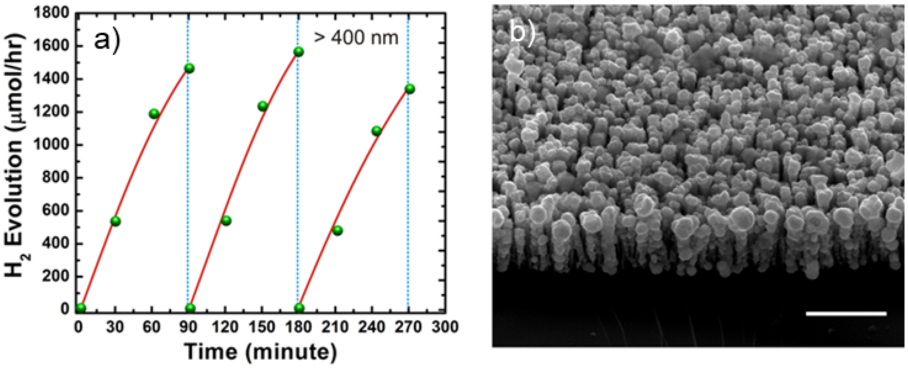

Figure 4-4: Repeated cycles of photocatalytic H_2 evolution from a) aqueous methanol solution using Mg-doped InGaN/GaN nanowire arrays under visible light excitation (>400nm). b) SEM image of the corresponding nanowires after ~6h of photocatalytic reaction shown in a), which clearly demonstrates the stability of nanowire photocatalysts and Rh co-catalysts. Scale bar, 1μm.

4.2.4 Performance Evaluation in Aqueous Methanol Solution

We have further performed repeated experiments on the same sample, in both the half reaction and overall water splitting reaction to study the stability of Mg-doped $In_{0.23}Ga_{0.77}N$/GaN nanowires in photocatalytic reaction. Shown in Fig. 4-4a are the repeated cycles of H_2 evolution measurement in the half reaction under visible excitation (> 400 nm). Under full arc illumination with AM1.5G filter (~26 suns), the photocatalytic activity of Mg-doped InGaN/GaN nanowire catalysts in aqueous CH_3OH solution provided H_2 evolution rate ~ 2292 μmol h^{-1}, and the AQE was estimated to be ~24% for an incident intensity of ~544.5 mW cm^{-2} in the wavelength range of 200-490 nm. The H_2 evolution rate under visible light irradiation (400-490 nm) was measured ~ 1177 μmol h^{-1} with an estimated AQE of ~17.1%. No degradation or obvious etching was observed, further confirming the stability of defect-free III-nitride nanowire photocatalysts in harsh photocatalysis conditions. Compared to other III-V semiconductors, the strong ionic bonding of III-nitrides, due to the significant difference in electro-negativity between group III and N elements [87, 159-162], suppresses the formation of surface states within the fundamental energy gap [163, 164]. Moreover, the balanced surface redox reactions, due to the optimized surface electronic properties with controlled Mg dopant incorporation, also contribute to the enhanced stability [99, 165-167]. The SEM image of the nanowires after ~ 6 hours of photocatalytic reaction is shown in Fig. 4-4b.

4.3 Harnessing UV Photons with GaN Nanowires for Water Splitting

Meanwhile, we have also explored the effect of Mg-doping on the GaN nanowires to enhance the UV photon harnessing for water splitting, and as expected, with optimized doping - significant enhancement in overall water splitting has been realized successfully on the GaN nanowires photodeposited with Rh(core)/Cr_2O_3 (shell) nanostructures. On the co-catalyst decorated GaN nanowires, the H_2 evolution was promoted by the noble metal (Rh) core as shown in Fig. 4-5a, while the backward reaction over the noble metal was prevented by the Cr_2O_3 shell. Without a Cr_2O_3 shell (as in HER reaction described in section 4.2.2) to cover the Rh nanoparticle core, pure water splitting activity was degraded. The reason can be attributed to the fact that noble metals such as Rh and Pt, usually act to promote the back reaction to form water from the oxygen and proton evolved.

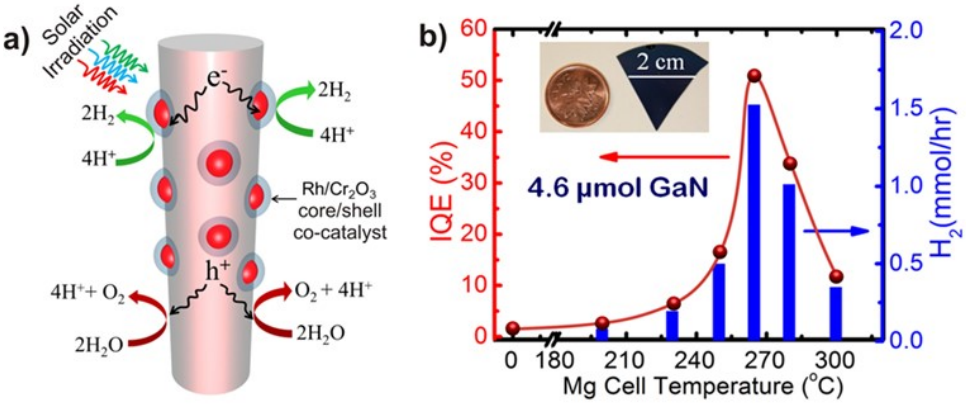

Figure 4-5: a) Schematic of Rh/Cr_2O_3 core-shell co-catalyst nanoparticles decorated single p-type GaN nanowire, illustrating the mechanism of overall pure water splitting. b) Internal quantum efficiency (IQE) and corresponding hydrogen evolution from GaN samples, doped at different Mg effusion cell temperature [99]. The inset shows the relative size of sample substrate. The area exposed to irradiation for redox reaction was ~ 2.8 cm^2.

For subsequent experiments, a wafer sample of ~2.8 cm^2 area, corresponding to ~0.387 mg (~4.62 µmol) GaN materials, was used for overall neutral pH water splitting under concentrated full arc. Figure 4-5b shows the H_2 evolution rates evaluated from 6-hrs of overall water splitting reaction on each sample for different GaN:Mg nanowire photocatalyst. Significantly enhanced hydrogen evolution of nearly 4.0 mol $h^{-1}g^{-1}$, was measured for sample with T_{Mg} = 265 °C, which is more than two orders of magnitude higher, compared to the nominally undoped GaN nanowires. For optimum Mg-doping concentration, the apparent quantum efficiency (AQE) can reach ~18% for the corresponding internal quantum efficiency (IQE) of ~51% under ~200-365 nm wavelength, the highest value reported for spontaneous overall water splitting under any broadband UV light irradiation to our knowledge. The optimum Mg doping for InGaN happens at relatively lower Mg-effusion cell temperature (~200 °C, as shown in Fig. 4-2d), compared to that in GaN nanowire samples. This can be attributed to the lower ionization energy of Mg in InGaN than that in GaN.

4.4 Double-band GaN/InGaN Nanowires for Enhanced Efficiency

Subsequently, we have studied the overall water splitting reaction of Mg-doped InGaN/GaN nanowire photocatalyst. A dual-bandgap p-$In_{0.20}Ga_{0.80}N$/p-GaN nanowire photocatalyst structure was developed, by separately optimizing the doping condition for both InGaN and GaN segments. This approach was adopted to ensure better matching and utilization of the solar spectrum, and to minimize the energy loss due to thermal relaxation of high energy charge carriers. The application of GaN as a photocatalyst is limited due to its low absorption threshold (wavelengths ≤ 365 nm), *i.e.* large bandgap (E_g ~ 3.4 eV). To ensure efficient utilization of visible photons in solar spectrum, low-bandgap InGaN segments (visible-band) were incorporated into GaN nanowire. Indium composition within InGaN segments had been tuned to ensure sufficient overpotentials for both water oxidation and proton reduction reaction, while extending the absorption threshold to harness more visible photons from solar spectrum. In other words, the bandgap of InGaN is tuned to be narrow enough (E_g ~2.61 eV, x~20%) to drive both the redox half-reactions forward. Five $In_{0.20}Ga_{0.80}N$ segments (~45-60 nm each) were incorporated in the visible-band, each capped by a thin (~10 nm) GaN layer (Fig. 4-1a) in order to prevent In desorption along the axial direction and phase separation in the vicinity of growth front [155, 168]. Subsequently, a Mg-doped *p*-GaN layer (UV-band) was incorporated on top of the nanowire. GaN and InGaN bands were individually tuned to have optimum Mg doping [169] and band-bending at the non-polar lateral surfaces.

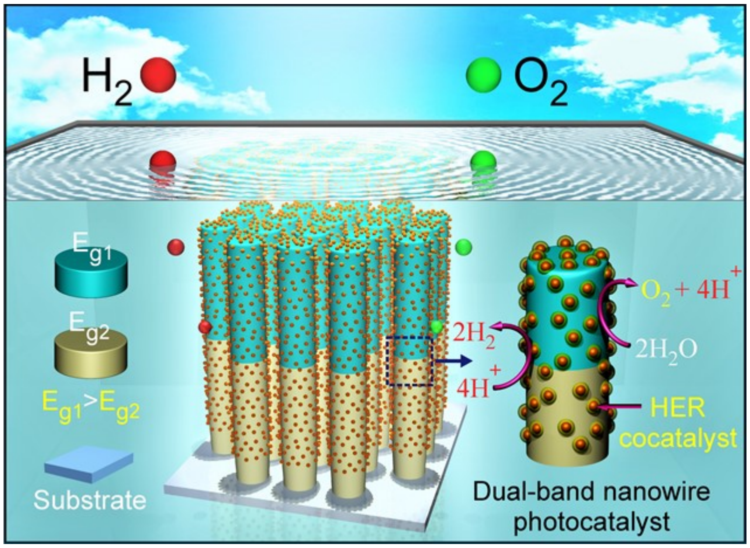

Figure 4-6: Schematic illustration of wafer-level unassisted overall water splitting on double-band nanowire arrays [169], which are vertically aligned on a planar substrate and decorated with co-catalysts for hydrogen evolution reaction (HER). Unlike tandem PEC cells or photovoltaic (PV) devices [170-173] this approach does not require any carrier recombination/transfer or current matching between the layers along *vertical direction*. Both water oxidation and proton reduction reaction occur on the radial non-polar surfaces of each layer.

Theoretically, stacking a higher bandgap material on top should neither increase nor decrease the photon conversion efficiency (calculated using absorption threshold). The bands in the heterostructure are electrochemically connected in parallel, but optically connected in series. For example, a single InGaN layer (E_g ~2.61 eV) will absorb the photons within wavelength 200-475 nm ($E \geq 2.61$ eV) to produce photo-generated carriers; whereas, stacking a GaN layer (reasonably shorter in length) on top will distribute the photon absorption as such – photons with energy, $E \geq 3.4$ eV (200-365 nm) will be absorbed by GaN and photons with energy, $2.61 \text{ eV} \leq E \leq 3.4$ eV (365-475 nm) will be absorbed by bottom InGaN layer, along with transmitted UV photons that were not absorbed by top GaN layer, consequently generating same number of photo-induced carriers. However, from thermodynamics and kinetics point of view, the top GaN layer enhances solar-to-hydrogen (STH) efficiency by accelerating the water splitting (W-S) reaction rate. This is because, a photon with an energy $E \geq 3.4$ eV can produce one electron-hole pair, both in GaN (E_g ~3.4 eV) and $In_{0.20}Ga_{0.80}N$ (E_g ~2.61 eV). Owing to carrier relaxation towards the band-edges, additional photon-energy in InGaN will be lost as thermal energy. By incorporating a large-bandgap layer (GaN) on top, that excess energy can be utilized to contribute as added over-potential for carriers, simultaneously for both water oxidation and proton reduction, without sacrificing the carrier generation efficiency. For a lossy *photocatalytic or photochemical* system, larger over-potential plays crucial role in increasing interfacial charge transfer efficiency for enhanced photochemical activity (under unassisted/zero-bias condition). Therefore, increasing interfacial charge transfer rate will further accelerate redox reaction, eventually enhancing the solar-to-hydrogen conversion efficiency in photocatalytic/photochemical water splitting.

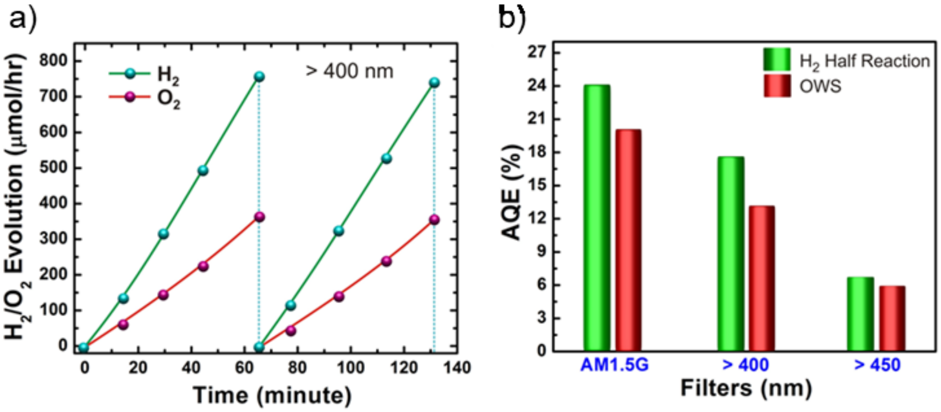

Figure 4-7: a) Repeated cycles of photocatalytic H_2 evolution from overall neutral water splitting reaction, using Mg-doped InGaN/GaN nanowire arrays under visible light excitation (>400nm). b) Estimated apparent quantum efficiency (AQE) of overall water splitting (red bar) and photocatalytic H_2 evolution from aqueous methanol solution (Half-reaction, green bar).

Figure 4-7a depicts the stoichiometric H_2 and O_2 evolution from repeated cycles of overall water splitting under visible light illumination; and the evolution rate was measured as ~ 684 μmol h^{-1} H_2 and ~ 332 μmol h^{-1} O_2, resulting in an AQE ~12.3% for an incident intensity of ~280.9 mW cm^{-2} in the visible wavelength range (400-475 nm). However, the

AQE increases up to ~20% under full arc irradiation using AM1.5G filter with an incident intensity of ~488 mW cm^{-2} in the wavelength range of 200-475 nm. Variations of the AQE for different long-pass filters are also shown in Fig. 4-7b. The decrease of efficiency with increasing wavelength is directly related to the reduced light absorption and carrier trapping effect.

4.5 Conclusions

In summary, we have investigated the photocatalytic performance of InGaN nanowire structures for H_2 evolution from both aqueous methanol solution and overall neutral pH water splitting under visible light excitation. It is observed that the efficiency for H_2 evolution, in both half reaction and overall water splitting reaction, depends critically on Mg-dopant incorporation, which is explained by variations of the surface electronic properties and the resulting impact on the charge carrier (electron/hole) migration to the nanowire surfaces. Under optimum condition, this, therefore, can simultaneously drive the water oxidation and the proton reduction reactions forward while minimizing defects in the nanostructures. By optimizing Mg-doping levels, we have demonstrated an apparent quantum efficiency of 17.1% and 12.3% for the half reaction and overall water splitting in the visible spectral range (> 400 nm), respectively. Further improvement in the energy conversion efficiency can be achieved by extending the absorption spectrum of InGaN nanowire structures with enhanced indium incorporation.

Chapter-5

A Photochemical Diode Artificial Photosynthesis System for Unassisted High Efficiency Overall Pure Water Splitting

5.1 Introduction

To achieve unassisted overall water splitting using the single-absorber photocatalytic process, the conduction and valence band edges of the photocatalyst must straddle the proton reduction and water oxidation (redox) potentials, respectively, while possessing a sufficiently narrow bandgap to absorb a large part of the solar spectrum. Due to such stringent requirements, there are very few photocatalysts that can perform unassisted, overall water splitting reaction under visible light irradiation. Consequently, to date, the search of highly efficient photocatalyst has been focused primarily on energy-band engineering methods. The primary goal of the approach is to achieve photocatalyst materials which posses sufficiently narrow bandgap with suitable band-edge potentials for overall water splitting and are capable of harnessing as much of the longer-wavelength visible photons as possible. However, in addition to that, there are certain aspects that often play very crucial roles in determining the photophysical and photocatalytic properties of the materials, namely the morphology, the surface and crystal structures, and carrier dynamics etc. One-dimensional (1D) nanostructures, due to their extremely large surface-to-volume ratio lead to significantly enhanced light absorption and photochemical reactions. Although most of the conventional photocatalysts are in the powder form, 1D structures such as nanowires, nanobelts and nanotubes are highly preferable as described in Chapter 1 and Chapter 2.

In Chapter 4, we have demonstrated the wafer-level approach of water splitting using GaN and InGaN nanowire structures grown by Plasma Assisted Molecular Beam Epitaxy

(PA-MBE). Dual-band GaN/InGaN nanowire photocatalyst, with significantly enhanced efficiency has also been developed by minimizing the potential barrier at the nanowire surface through precise tuning of the surface Fermi-level via Mg dopant incorporation. The dual-band InGaN/GaN nanowire structure shows energy conversion efficiency (ECE) of ~7.5% and apparent quantum efficiency (AQE) of ~20% with AM1.5 filter (in the wavelength range of 200-475 nm) under concentrated illumination intensity equivalent to ~26 Suns, which results in solar to hydrogen (STH) conversion efficiency of ~1.5%. This efficiency is, although higher compared to that of other recently reported values for one-step overall water splitting and comparable to that of the wireless water splitting cell comprised of integrated photovoltaic cells, not however, up to the fullest potential yet. This is because, for such semiconductor-based photocatalysts, efficient separation of photo-generated charge carriers (electrons and holes) towards the appropriate catalytic sites has remained challenging, particularly for photocatalytic water splitting wherein no external bias is applied. While numerous efforts have been undertaken to address the critical issue of efficient charge separation through surface and interface engineering and the selective loading of co-catalysts to create spatially separated redox reaction sites [29, 71, 140, 174-177], it has remained elusive to achieve a precise control of charge carrier flow within the bulk and to steer photo-excited electrons and holes to their reduction and oxidation sites, respectively. To date, the best reported solar-to-hydrogen (STH) conversion efficiency for pH neutral photocatalytic water splitting is limited to ~1-1.5%, or less, compared to the 10-16% reported for PEC devices [58, 97, 113, 116, 178-182] in conductive electrolytes.

In this context, we propose and demonstrate multi-band InGaN nanosheet photochemical diode (PCD) structures, which can spontaneously induce charge carrier separation and steer charge carriers toward the distinct redox sites for water oxidation and proton reduction. During the synthesis of InGaN photochemical diode nanosheet structure, *p*-type dopant (Mg) concentrations are rationally tailored, which induces a large built-in electric field between the two parallel surfaces. Consequently, the two surfaces are enriched with photo-generated holes and electrons to perform water oxidation and proton reduction reactions, respectively. In addition to the efficient charge carrier separation and extraction, the spatial separation of catalytic sites in such a nanoscale photochemical diode effectively reduces carrier recombination and back reaction. Subsequently, we demonstrate herein a double-band InGaN nanosheet device, which exhibits a solar-to-hydrogen conversion efficiency of ~3.3% for pH neutral overall water splitting. The capacity to achieve controllable charge carrier separation at the nanoscale will also be instrumental to break the efficiency bottleneck for artificial photosynthesis, including reduction of CO_2 to hydrocarbon fuels.

5.2 Charge-carrier Separation: Conventions and Challenges

The photochemical diode offers the advantages of enhanced charge carrier separation within the photon absorber(s) due to built-in electric field and can efficiently steer them towards distinct catalytic surfaces for redox-half reactions [183]. Schematic depiction of a conventional Schottky-type photochemical diode in Fig. 5-1a shows that the n-type semiconductor performs as a single bandgap absorber, and the photo-generated carriers (holes and electrons) are separated due to built-in electric field, migrates towards semiconductor-electrolyte interface and metal-electrolyte interface for water oxidation and proton reduction reaction, respectively. Schematic of a conventional *p-n* photochemical diode energy levels for overall water splitting are presented in Fig. 5-1b. The *p-n* photochemical diode is a minority carrier device, i.e. the minority holes in *n*-type (photo-anode) and electrons in *p*-type (photo-cathode) migrates towards semiconductor/electrolyte interface and participates in water oxidation and proton reduction reaction, respectively. Majority carriers, on the other hand, recombine in the ohmic contact. With appropriate band-bending at the semiconductor-electrolyte interfaces, conventional *p-n* photochemical diode offers the advantage of efficient charge carrier separation and the use of single semiconductor with narrow-bandgap or with complementary bandgaps for simultaneous extended absorption of UV and visible light. However, it requires eight photons to produce four active electron-hole pairs due to majority carrier recombination, and hence, for a particular threshold absorption wavelength the maximum efficiency for solar energy conversion gets reduced to half compared to that for a single-absorber approach of overall water splitting [21, 58, 184]. Besides, for semiconductors with complementary bandgaps, matching in threshold and equal photon absorption wavelength is required for balanced redox reaction in order to prevent back reaction and corrosion [15, 21, 185]. Realization of nanoscale ohmic contact at the lateral (*p*/*n*) interfaces of vertically aligned photochemical diode is critically difficult, therefore making it suitable only for planar devices.

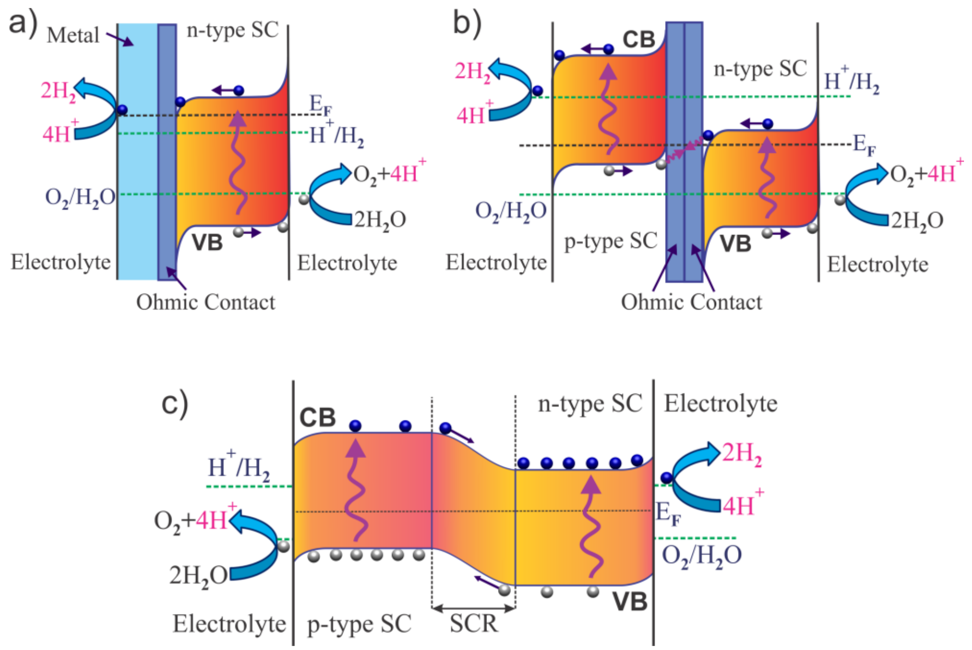

Figure 5-1: a) Schematic illustration of a Schottky-type) photochemical diode for overall water splitting, where a single-bandgap *n*-type semiconductor absorber forms a metal-semiconductor junction via an ohmic contact. Water oxidation occurs on the semiconductor surface and proton reduction occurs on the surface of metal electrode. b) Energy-level representation of *p-n* photochemical diode and redox potentials for overall water splitting, where two semiconductor absorber layers (*p*-/*n*-type, assuming identical bandgap) are connected via an ohmic contact as a recombination layer for majority carriers. c) Schematic of a *p-n* junction for overall water splitting. In this majority carrier-device, electrons and holes in the space charge region (SCR) are drifted in opposite direction by the built-in electric field.

On the other hand, through junction engineering, it is typically hard to ensure enough over-potentials and appropriate band-bending for both oxidation and reduction reactions in overall photocatalytic water splitting (Fig. 5-1c). The p-n junction is an effective approach to individually engineer either oxidation or reduction reaction forward at the nanoscale [130-133]. However, for overall unassisted photocatalytic water splitting, it offers band-bending at the semiconductor-electrolyte interface that hinders the migration of the appropriate carriers (both electrons and holes) to participate in respective redox half-reactions, resulting in reduced efficiency. To a great extent, both approaches offer internal electric field as a driving force for unidirectional electron and hole transfer only at the *near-surface* region and *near the space-charge* region (SCR) at the interface. Moreover, interfaces (junctions) need to be carefully optimized in order to improve the photocatalytic performance, by tailoring the interfacial parameters, namely, compositions, interfacial area, defects, electronic coupling between surfaces, and the distance from the interface to the active redox sites [97], thus making the implementation more challenging. If the distance from the interface to the surface is large (thick semiconductor layers), potential difference is required to govern the charge transfer from the semiconductor interface to the bulk or from within the bulk to the reactive surfaces, thus limiting its performance in zero-bias overall water splitting.

5.3 A One-photon InGaN Photochemical Diode Nanostructure

As schematically shown in Fig. 4-6 (section 4.4), for the typical overall neutral pH water splitting on multi-band (GaN/InGaN) nanowire photocatalysts, the redox sites (and co-catalysts) are randomly distributed on the surfaces. In contrast, during the synthesis of InGaN photochemical diode nanosheet structure, *p*-type dopant (Mg) concentrations are rationally tailored, which leads to a large work function difference (up to 300 meV) between the two parallel surfaces. The resulting p-p^+ nanoscale lateral junction, schematically illustrated in Fig. 5-2a, induces unidirectional flow of photo-generated charge carriers, *i.e.* electrons and holes migrate toward the surfaces with a relatively small and large work function (Φ_{red} and Φ_{ox}), respectively. As shown in Fig. 4-6, the energy bandgap of the nanosheet structures can be further varied along the vertical direction, *i.e.* the photon absorption path. The resulting multi-band photocatalysts promise photocatalytic solar water splitting with the highest efficiency possible [15, 21].

5.3.1 Synthesis and Properties of InGaN Photochemical Diode

Figure 5-2a schematically illustrates the energy bands of the proposed InGaN nanosheet structures, which are grown directly on Si substrate using plasma-assisted molecular beam epitaxy. During the epitaxy process, p-type dopants (Mg) are impingent primarily on one side of the nanosheet structure. The resulting Mg-doping gradient along the lateral dimension of the nanosheet establishes a strong built-in electric field, schematically shown in Fig. 5-2a, which separates the photo-generated electrons and holes, and drives them towards opposite surfaces, thus reducing the probability of recombination. Figure 5-2b shows the typical bird's-eye-view SEM images of InGaN nanostructures, which are comprised of axially asymmetric nanosheets with parallel non-polar surfaces.

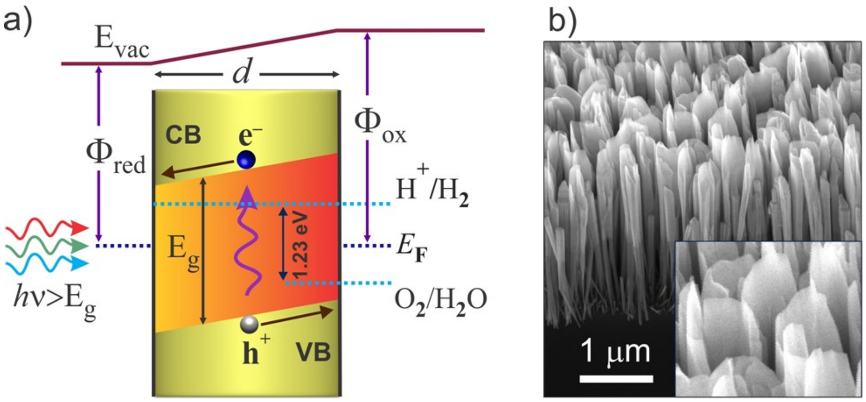

Figure 5-2: a) Energy-band representation of the proposed photochemical diode (PCD) with radial thickness *'d'*, showing built-in electric field (band-bending) that separates the charge carriers (electron and hole) and drives towards opposite cathode and anode surfaces. In contrast to conventional *p-n* PCD, only single photon absorption is required to generate one active electron-hole pair to participate in redox reaction (like Schottky-type photochemical diode). b) A 45° tilted SEM image of InGaN:Mg PCD nanostructures, vertically aligned on Si substrate. The magnified image of the nanosheets is also presented in the inset for clarity.

To facilitate the formation of Mg-doping gradient in the lateral direction and to counteract the spinodal decomposition of In-N in the surface, the substrate was kept steady during the growth of the photochemical diode. Amount of nitrogen species and metal fluxes in the growth environment were further optimized to ensure essential nitrogen vapor pressure in the vicinity of the growth front, and to reduce long-distance diffusion of indium atom along the growth axis. Mg-doping gradient (due to the surface dependent incorporation) can also be influenced by the super-saturation for Ga- or N-rich condition at the localized level. Instead of multi-stack InGaN:Mg/GaN:Mg layers (as discussed in Chapter 4), a continuous InGaN:Mg layer was grown spontaneously on top of GaN:Ge nanowire. A nitrogen flow rate of 1.0 standard cubic centimeters per minute (sccm), and a forward plasma power of ~350 W were used during the growth. Other growth parameters include Ga beam equivalent pressure (BEP) of ~6×10^{-8} Torr, In BEP of ~ 7.8×10^{-8} Torr, Mg BEP of ~2×10^{-11} Torr corresponding to Mg effusion cell temperature (T_{Mg}) of ~ 200 °C, and Mg BEP of ~1.5×10^{-9} Torr which corresponds to Mg effusion cell temperature (T_{Mg}) of ~ 270 °C. The GaN template was grown at ~ 780 °C, and the growth temperatures for InGaN were varied from 650 to 705 °C.

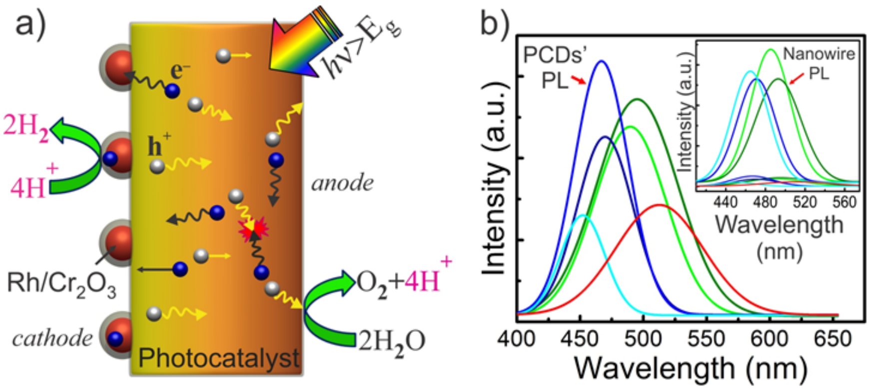

Figure 5-3: a) Schematic (real space) depiction of the dynamic behaviors of charge carriers in a single-photon PCD upon photoexcitation. Electron enriched surface (cathode) of the PCD is largely decorated with photo-deposited HER co-catalysts (Rh/Cr_2O_3 core/shell nanoparticles). b) Room temperature photoluminescence (PL) spectrum from as-grown *p*-InGaN PCDs for different indium incorporations (correspond to different bandgaps, depicted using distinct colors). The inset shows ~20-fold reduction in PL intensity for the photochemical diodes compared to that of nanowires.

A simplistic view of the dynamic behaviors of charge carriers are depicted in Fig. 5-3a, which includes electron-hole pair generation upon photo-excitation, bulk recombination, carrier separation and migration towards laterally opposite direction. Consequently, the two catalytic surfaces are enriched with electrons and holes, respectively. The electron enriched surface (cathode) of the photochemical diode largely facilitates photo-deposition of proton reduction co-catalysts (Rh/Cr_2O_3 core/shell nanoparticles), which in turn enhances the hydrogen evolution reaction (HER) significantly. Water oxidation reaction, on the other hand, takes place on the hole-enriched surface (anode). One direct evidence for the efficient charge carrier separation and extraction of the presented InGaN nanosheet structures, compared to the conventional nanowires, is the significantly reduced photoluminescence intensity. Illustrated in the inset of Fig. 5-3b, the photoluminescence emission intensity of InGaN nanosheets is nearly 20 times smaller, compared to that of InGaN nanowires grown under similar conditions. Therefore, with significantly reduced charge carrier recombination, InGaN nanosheets are expected to exhibit noticeably higher photocatalytic activity than corresponding nanowire structures [134]. By varying the epitaxy conditions, the energy bandgap of InGaN nanosheets, evident by the photoluminescence emission spectra, can be tuned over a large part of the visible spectral range, shown in Fig. 5-3b. More details about the properties and behavior of a photochemical diode can be found in APPENDIX-B.

5.3.2 Surface Selectivity for Oxidation and Reduction

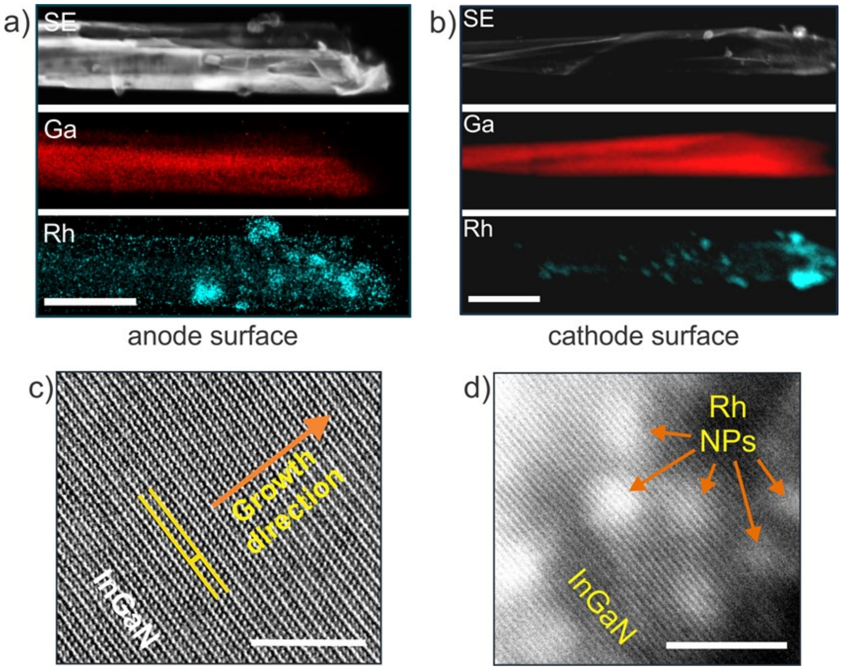

Figure 5-4: Comparison of STEM-SE and EDXS elemental mapping on two different surfaces of InGaN nanosheet (decorated with Rh-nanoparticles) shows that a) very few Rh nanoparticles were deposited on the anode (outer) surface, whereas b) significantly large number of Rh-nanoparticles get deposited on the cathode (inner) surface. Scale bars, 400 nm. HRSTEM-BF lattice fringe image from InGaN photochemical diode nanosheet, illustrating c) defect-free single crystalline $In_{0.22}Ga_{0.78}N$ anode surface, and d) Rh nanoparticles on the crystalline cathode surface of photochemical diode. Scale bars, 5 nm. A radial density filter was used for Fig. 5-4c.

Scanning transmission electron microscopy (STEM) and energy dispersive X-ray scanning (EDXS) analysis on *p*-type InGaN nanosheet photochemical diodes, decorated with Rh-nanoparticles, shows a significant difference in the number of nanoparticles loading between the two parallel surfaces. Shown in Fig. 5-4b, preferential photo-reduction of Rh-metal precursors to Rh-nanoparticles is facilitated on the reduction surface (cathode) due to its electron enrichment compared to that on the oxidation surface (anode) in Fig. 5-4a. Scanning transmission electron microscopy (STEM)-ZC/BF images further confirm Rh-nanoparticles' deposition on the reduction sites of InGaN photochemical diode nanostructure (Fig. AP-A1). High-resolution STEM bright-field lattice image also depicts high crystalline quality of the defect-free $In_{0.22}Ga_{0.78}N$ nanostructure surfaces, shown in Figs. 5-4c and d. For comparison, the distribution of noble metal nanoparticles on the non-polar surfaces of conventional nanowires are non-selective, rather random, as shown in Fig. 3-7.

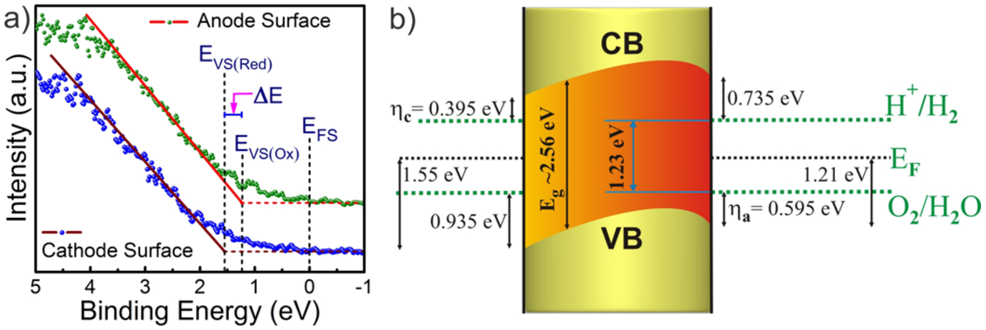

Figure 5-5: a) ARXPS valence spectrum for cathode and anode surface of *p*-InGaN photochemical diode nanosheets, depicting the offset in surface valence band maximum (E_{VS}) relative to surface Fermi-level (E_{FS}). b) A quantitative estimation of the band-diagram of InGaN nanosheet photochemical diode, supported by the TEM and XPS analysis for optimum bandgap, as shown in Fig. 5-4 and Fig. 5-5a. Under concentrated sunlight, the band-bending in the bulk can be reduced due to the band-flattening effect. The effect can lower the recombination probability (for both bulk and surface recombination) further by leading to linear built-in electric field and hence making the flow/separation of the charge carriers unidirectional (opposite), as shown in Fig. 5-2a.

To further gain a deep insight regarding the deviation in photo-deposition behavior, near-surface band-structure of as-grown *p*-InGaN nanowires and *p*-InGaN nanosheets were characterized using angle resolved X-ray photoelectron spectroscopy (ARXPS). Illustrated in Fig. 5-5a, the measured surface valence band maximum (E_{VS}) values between the two non-polar surfaces (relative to surface Fermi-level, E_{FS}) are significantly different, with E_{VS} for the cathode surface being ~300 meV larger than that for the anode surface. This suggests the presence of a built-in potential ~300 meV (ΔE) along the lateral dimension of the nanosheet structure, as shown schematically in Fig. 5-2a. A quantitative estimation for the band-diagram of InGaN nanosheet structures is shown in Fig. 5-5b, which is derived from the XPS and TEM analysis performed on InGaN nanosheets with optimum bandgap for enhanced photocatalytic activity.

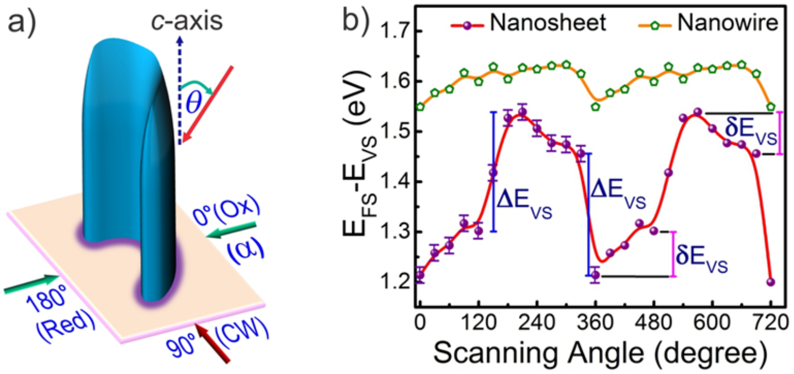

Figure 5-6: a) Schematic illustration of probing photochemical diode surfaces for valence spectra using ARXPS. Angles on the imaginary plane normal to *c*-axis (parallel to the substrate) are the radial scanning angles (α, clockwise), and *'θ'* denotes the angle of X-ray excitation relative to *c*-axis (section 3.5 and Fig. 3-6a). b) E_{FS}-E_{VS} for Mg-doped $\mathrm{In_{0.22}Ga_{0.78}N}$ nanosheets and nanowire arrays, derived from ARXPS valence spectrum as a function of scanning angle. Periodic fluctuation is clearly observed for E_{FS} position on the photochemical diode nanosheets relative to E_{VS}. An error bar of ~ ±0.03 eV corresponds to uncertainties involved in measuring E_{VS} and C 1s peak.

Subsequently, surface dependence of E_{VS} was analyzed by measuring the valence spectra *vs* radial scanning angle, α (Fig. 5-6a). Variations of E_{FS}-E_{VS} as a functional of scanning angle is illustrated in Fig. 5-6b for the entire range of α, further confirming the strong dependence of E_{VS} on different surfaces. The sharp change in E_{FS}-E_{VS} (ΔE_{VS}) vs. scanning angle can be ascribed to the transition from one parallel surface to another, *e.g.* from anode to cathode surface, whereas the slow and gradual change (δE_{VS}) is attributed to the curvature and orientation of nanosheet arrays. In contrast, conventional InGaN nanowires exhibit nearly constant E_{VS} at different scanning angles, also shown in Fig. 5-6b for comparison. It is evident that the large built-in potential leads to the spontaneous accumulation of electrons and holes on the cathode and anode surfaces, respectively [169]. This implies that the origin of preferential photo-deposition of noble metal nanoparticles on cathode surface of *p*-InGaN photochemical diode, as shown in Fig. 5-4, is due to the reduction of noble metal precursors by photo-excited electrons enriched on that surface.

It is worthwhile mentioning that anisotropic facet-dependent co-catalyst deposition had been reported previously to ensure spatial separation of oxygen evolution reaction (OER) and HER co-catalysts [143-148, 186], and thus to provide enhanced carrier separation in the *near-surface region*. However, bulk recombination remains a limiting factor for their low apparent quantum efficiency in water splitting. Unique to the presented photochemical diode nanostructure is the net lateral band-bending between two spatially separated redox surfaces. Water oxidation and proton reduction reactions occur at the two distinct reaction sites on photochemical diode nanosheets, and are coupled between the parallel anode and cathode surfaces [187, 188]. Under concentrated sunlight, the band-bending in Fig. 5-5b can be reduced in the bulk, which can further lower the recombination probability by making the built-in electric field linear and hence the flow/separation of charge carriers unidirectional (Fig. 5-2a).

5.3.3 Photoelectrochemical Characterization of the Nanostructure

Photo-electrochemical cell is a very powerful and efficient tool to characterize certain properties of the photocatalytic material. To analyze the conductivity behavior and the junction properties, a single band p-InGaN layer was grown on top of n-GaN nanowire templates on Si n (111) substrate. In-Ga eutectic alloy metal was deposited on the backside of the Si substrate to serve as an Ohmic contact. The measurements were performed by using a 300 W Xenon lamp as an irradiation source with an intensity ~160 mW cm^{-2} on the sample surface. The reactor chamber was made of quartz to ensure ample transmittance for both UV and visible light. Impedance spectroscopy was performed to acquire the Mott-Schottky (M-S) plot in the dark. As shown in Fig. 5-7a, a p-n junction characteristic was observed in the M-S plot where a 'V-shape' was present. However, the dominant photocathodic performance of the photoelectrode can clearly be observed by the steep negative slope in the M-S plot, which is well supported by the onset potential and negative current in the dark. The shift in the onset potential for photocurrent generation, as depicted in Fig. 5-7a, reflects the catalytic activity of the photoelectrode.

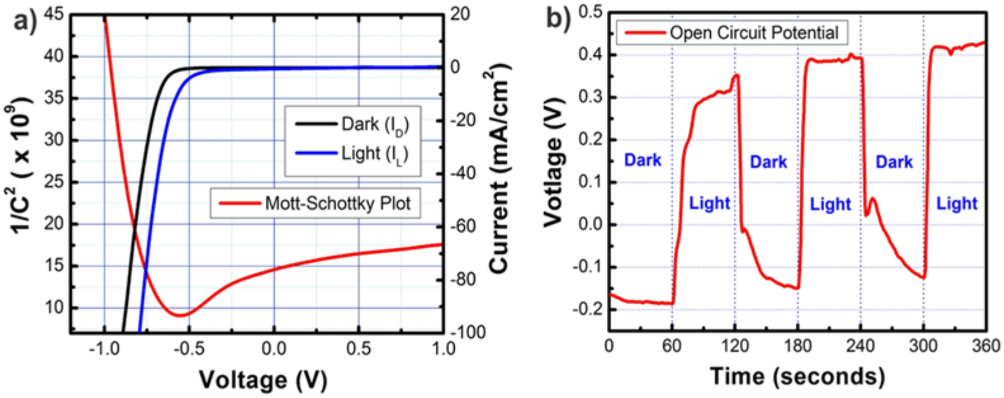

Figure 5-7: a) Mott-Schottky plot of the *p*-InGaN photochemical diode nanostructure arrays in the dark, and I-V curve of the same under light illumination (full arc) and in dark. b) Open circuit potential (OCP) measurement on *p*-InGaN photochemical diode nanostructure arrays under dark and full arc illumination. The potential difference between light and dark is positive, indicating *p*-type behavior of the photochemical diodes.

The Mg-doped InGaN nanostructures were further characterized by open circuit potential (OCP) measurement in 1 mol L^{-1} HBr using three-electrode electrochemical cell configuration. The nanostructure arrays (on Si substrate) was used as the photoactive working electrode, whereas a Pt wire, and a double-junction Ag/AgCl were used as counter electrode and reference electrode, respectively. While the nanostructure shows p-n junction characteristics, dominant conductivity type of the material in the electrolyte can be determined by the sign of OCP shift upon illumination. For *p*-type material, the OCP shifts towards more positive potential with respect to Ag/AgCl upon illumination. As shown in Fig. 5-7b, the positive potential difference (with respect to Ag/AgCl) between light and dark under full arc illumination indicates the *p*-type behavior of the nanostructures. The weakly *n*-type behavior in the M-S plot and OCP measurement can be ascribed to the contribution from GaN:Ge template on the Si substrate.

5.4 Characterization and Performance Analysis of Double-band PCD

Double-band GaN:Mg/InGaN:Mg nanostructures were grown on Si substrate by plasma-assisted molecular beam epitaxy (MBE) [99, 168, 169]. The nanosheet structures are vertically aligned along the growth direction (*c*-axis) on the Si substrate, with an areal density in the range of ~1.5×10^{10} cm^{-2} (Fig. 5-2b). The photochemical diodes have an average height ~1.5-2 µm, and the thickness varies from ~50-120 nm. A single band-to-band optical emission peak at ~485 nm is shown in Fig. 5-8a, which corresponds to a bandgap of 2.56 eV. The average indium incorporation is estimated to be ~22% for the grown nanostructures. Detailed STEM and EDXS analysis confirms the existence of a continuous long InGaN segment, simultaneously showing the distribution of Rh/Cr_2O_3 nanoparticles on the surface [99, 169]. The *p*-type behaviour of Mg-doped crystalline $In_{0.22}Ga_{0.78}N$ photochemical diodes is confirmed by photo-electrochemical characterization that includes open-circuit potential (OCP), Mott-Schottky (M-S) and photocurrent measurements, as discussed in the previous section.

The nanosheet arrays were tested for both hydrogen evolution reaction (HER) in aqueous methanol (CH_3OH) solution, and neutral pH overall water splitting (OWS) reaction (Fig. AP-A2). A 300W Xenon lamp was used as a concentrated irradiation source for photo-excitation, which has an intensity equivalent to ~32 suns when measured on the nanostructure substrate. Rh nanoparticles and Rh/Cr_2O_3 core-shell nanostructures were photo-deposited as the co-catalysts for HER and OWS reactions, respectively. For an incident intensity of ~610.8 mW cm^{-2} in the wavelength range of 200-485 nm, stoichiometric gas evolution rate in neutral pH water splitting was measured as ~1.62 mmol $h^{-1}cm^{-2}$ of H_2 and ~0.784 mmol $h^{-1}cm^{-2}$ of O_2 gases, resulting in an AQE ~45.85%, which is more than twofold higher than previously reported AQE of ~20% for double-band nanowire heterostructures [169]. Under visible light irradiation (> 400 nm), the evolution rate was measured as ~0.5 mmol $h^{-1}cm^{-2}$ for H_2, and the AQE from the photochemical diode nanosheets (nanowires) was estimated to be ~19.93% (12.3%). Further details about the photocatalytic efficiency of the PCDs can be found in APPENDIX-C.

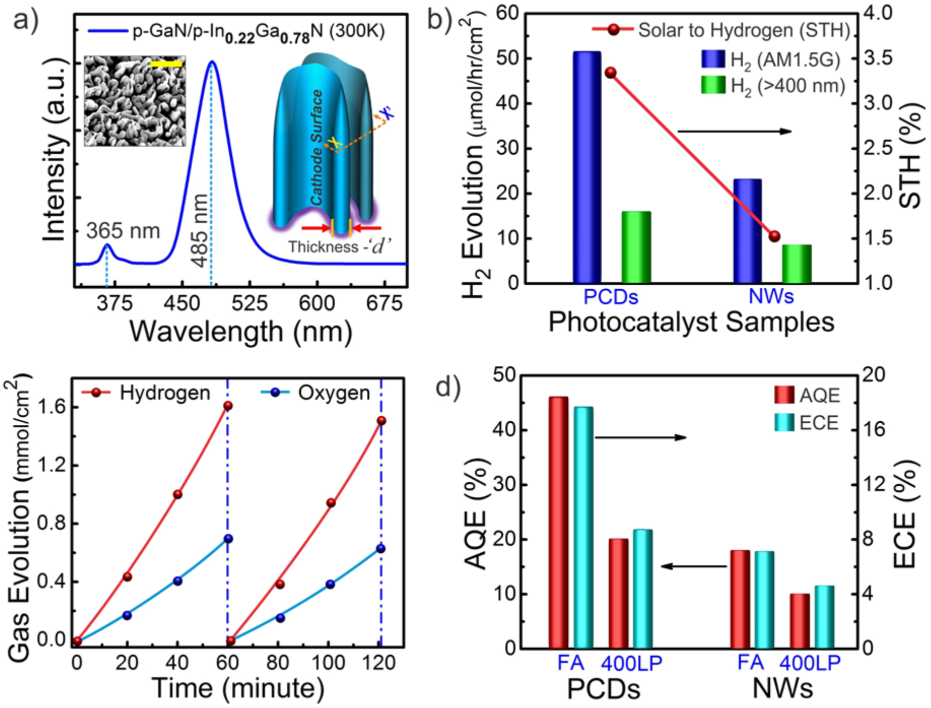

Figure 5-8: a) Room temperature photoluminescence (PL) spectrum depicting single band-to-band optical emission peak at ~365 nm (GaN) and at ~485 nm (InGaN). 3D depiction of photochemical diode nanosheets with an arbitrary radial thickness *'d'* is shown in inset (left). Inner surface of the curved nanosheet is denoted as the *cathode surface* as per Fig. 5-4. The inset (right) shows 15° tilted SEM image of the photochemical diodes. Scale bar, 1 μm. b) H_2 evolution rate in overall neutral (pH~7.0) water splitting for various photocatalyst samples under different excitation conditions. All the photocatalysts contain Rh/Cr_2O_3 as HER co-catalyst, photo-deposited on the surface. Photochemical diodes provided two-fold enhancement in solar to hydrogen (STH) conversion efficiency compared to their nanowire counterparts. c) Stoichiometric H_2 and O_2 evolution rate and the repeated cycles from overall water splitting, demonstrating balanced redox reaction and stability of nanowire photochemical diodes. d) Comparative illustration of apparent quantum efficiency (AQE) and energy conversion efficiency (ECE) for different photocatalyst samples, derived under full arc using AM1.5G filter (FA) and 400 nm long-pass filter (400LP).

Evidently, significant enhancement in overall photocatalytic water splitting activity had been derived from photochemical diode nanosheets compared to that from nanowire heterostructures. For comparison, the amount of hydrogen evolution from the photochemical diodes is increased by more than a factor of two (50.6 μmol $h^{-1}cm^{-2}$ compared to 21.3 μmol $h^{-1}cm^{-2}$ from nanowires, under normalized intensity, per 100 mW cm^{-2}) using full arc illumination with AM1.5G filter. This, in turn, enhanced the energy conversion efficiency (ECE) from ~7.5% to ~17.5%. Moreover, an impressive ~3.3% of solar-to-hydrogen conversion efficiency has been measured in this study, which is significantly higher than that estimated from dual-band nanowire structures, as depicted in Fig. 5-8b. Repeated cycles for the stoichiometric hydrogen and oxygen evolution in neutral pH water splitting using AM1.5G filter are demonstrated in Fig. 5-8c. Illustrated in Fig. 5-8b and d are the comparative study of intensity-normalized hydrogen evolution and corresponding AQE and ECE from neutral pH overall water splitting under full arc illumination using AM1.5G filter and under visible light irradiation using a 400 nm long-pass filter. The photochemical diode nanostructures remain stable after the photocatalytic reactions, and negligible signs of degradation was observed after ~4 hrs of overall neutral pH water splitting and hydrogen evolution reaction from aqueous methanol solution (Fig. AP-A3). The stability of the co-catalyst nanoparticles on photocatalyst surface was further confirmed from TEM analysis.

5.5 Discussion on Photocatalytic Efficiency and Material Stability

In nanostructured photocatalysts, charge carrier transport is no longer diffusion limited; the effective extraction of photo-generated charge carrier is often restricted by surface and interface electronic properties, e.g., the presence of surface band bending [99, 169, 189-191]. To date, it has remained a grand challenge to precisely steer charge carrier flow in nanostructured photocatalysts, due to the lack of control over their surface band bending. In our previous studies, we have demonstrated that by minimizing the surface potential for hole transport, the STH efficiency for photocatalytic overall water splitting on InGaN nanowires was significantly enhanced from <0.1% to over 1% [99, 168, 169]. Further improvement of the STH efficiency, however, has been fundamentally limited by charge carrier trapping and recombination, including both surface and bulk recombination. In this work, we have shown that such a critical challenge can be effectively addressed in nanosheet photochemical diodes. The asymmetric dopant incorporation in InGaN nanosheets and the resulting built-in electric field, schematically shown in Fig. 5-2a, offers several essential benefits for photocatalytic overall water splitting. It leads to the unidirectional charge carrier flow, *i.e.* the accumulation of photo-generated electrons and holes on the anode and cathode surfaces of the same nanosheet structure, respectively. The efficient separation of photo-generated charge carriers is unambiguously supported by the preferential deposition of HER co-catalysts only on the cathode surfaces of InGaN nanosheets (Fig. 5-4b), the significant reduction of photoluminescence emission compared to conventional nanowires (inset of Fig. 5-3b), and the large difference in surface potential (~300 meV) between the anode and cathode surfaces (Fig. 5-5a).

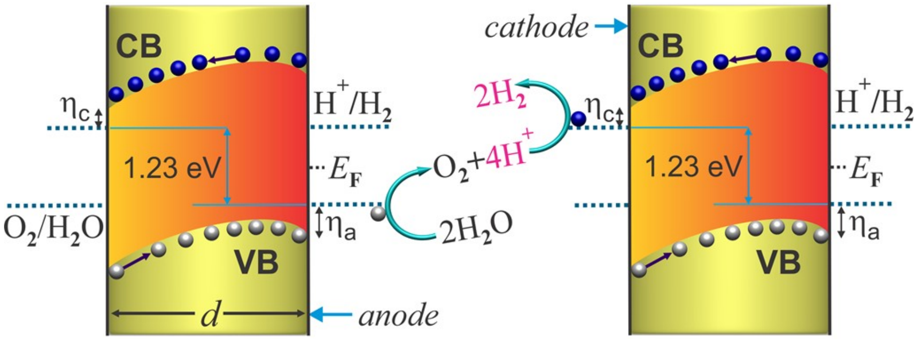

Figure 5-9: Neutral pH overall water splitting on the surfaces of photochemical diode nanostructures, presented schematically as a top view at the plane (*X-X'*) of cross-section in the inset of Fig. 5-8a. η_a and η_c represents the anodic and cathodic over-potentials for water oxidation and proton reduction reaction, respectively. With the directional (opposite) migration of electrons and holes, redox reactions can be coupled between parallel (cathode and anode) surfaces of vertically aligned adjacent photochemical diode nanosheets.

Over 90% of the photo-generated electrons and holes are spatially separated on the cathode and anode surfaces [169], thereby minimizing both surface and bulk recombination [192]. Moreover, reverse diffusion currents due to the concentration gradient is minimized by the energy barriers and surface trapping of carriers in co-catalyst nanoparticles [71, 140, 175-177]. Significantly, the rational design and synthesis of anode and cathode surfaces in nanostructured photocatalysts can effectively increase the surface area for water oxidation reaction, which is often the rate-limiting step for overall water splitting [129, 193-196]. Water oxidation and proton reduction reactions can be coupled between spatially separated reaction sites (parallel electrodes), *i.e.* the cathode and anode surfaces [187, 188] of two adjacent photochemical diodes (Fig. 5-9), thereby drastically suppressing back reaction. In addition, the effective surface relaxation of nanosheet structures allows for the optimization of the bandgap and band-bending of InGaN photochemical diodes through variations in indium incorporation and Mg-doping concentration, to ensure sufficient cathodic and anodic over-potentials, and to minimize the surface potential barrier for achieving high photocatalytic efficiency.

The demonstrated STH ~3.3% is significantly higher than previously reported efficiency values for neutral pH one-step overall water splitting [58, 178, 197], which generally range from 0.1% to 1.1%, or 1.5% achieved herein using double-band GaN/InGaN nanowires. It is worth mentioning that an STH of ~5% had been reported on CoO nanocrystals [198], which are barely stable in harsh photocatalytic environment. The nanocrystal surfaces become corroded due to difficulties in co-catalyst loading, and further studies seem to be necessary to understand the mechanism and to confirm the reproducibility [58]. Recent studies on a different 2-step approach of water splitting [56] showed ~2% of STH using CDots-C_3N_4. This approach requires efficient generation as well as subsequent decomposition of H_2O_2, putting further constraints on the bandgap of suitable photocatalyst (>1.78 eV, compared to ~1.23 eV for neutral pH overall water splitting, excluding necessary over-potentials). A device comprised of catalysts loaded on triple-junction photovoltaic cell demonstrated STH of ~2.5% in an earlier study [94], which, however, utilizes conductive 1M potassium borate electrolyte (pH ~9.2). Noticeably, many of these relatively high efficiency devices [58, 94] were designed based on conventional photochemical diode [90] which requires the use of ohmic-contact for efficient charge carrier transport. For example, the co-catalyst loaded $SrTiO_3$:La,Rh|Au(*contact*)|$BiVO_4$:Mo device [58] increases the STH up to ~1.1% compared to that of ~0.1% using their powder suspensions in Z-scheme with $Fe^{3+/2+}$ redox couples [66]. The use of planar ohmic-contact reduces active surface area for redox reaction and often requires conductive electrolyte to compensate for the distance between cathode and anode surfaces (by selectively adjusting the pH or adding supporting electrolyte in near-neutral pH condition). Moreover, it has been extremely difficult to realize such ohmic-contact in nanostructured photocatalysts. In this context, our nanosheet photochemical diodes do not require ohmic-contact or majority carrier recombination. They offer larger (and hole-enriched) anode surface for water oxidation, while enabling selective deposition of HER co-catalysts (Rh/Cr_2O_3) on electron-enriched cathode surface, with the least probability of carrier interference, crowding, and recombination. Moreover, solar energy, being a planar resource, can be more effectively harvested (per unit area) in such vertically aligned wafer-level nanosheet structures.

5.6 Carrier Transport in PCDs: Impact on Efficiency Transformation

It is important to realize that, the photocatalytic activity of a semiconductor is greatly affected by the dynamic behaviors of photo-generated charge carriers. The separation/migration and the recombination process of the photo-generated electron-hole pairs are two competitive pathways. The overall water splitting becomes most efficient when the bulk-separation and surface-trapping of the charge carriers surpasses their recombination while retarding the latter one. As discussed in section 4.2, MBE grown non-doped GaN/InGaN nanowires are weakly n-type, which creates a high degree of upward band-bending in near-surface region. The band-bending increased further due to surface depletion effect when the nanowire surface is in contact with the water/electrolyte, which suppresses electron transfer to the adsorbates. With n-type dopant incorporation (Si/Ge), the upward band-bending of the nanostructures becomes more severe, providing little or no control. On the contrary, band-bending and surface properties can be optimized in Mg-doped p-type GaN/InGaN nanowires to provide significantly enhanced photocatalytic efficiency, while simultaneously driving the water oxidation and the proton reduction reactions forward and minimizing defects in the nanostructures [99, 168, 169]. The decoration of nanowire surface with reduction co-catalysts (HER), in addition, accelerates carrier separation from *near-surface* region.

Bulk recombination, however, persists due to its flat-band nature, which results in trapping of photo-generated holes in the bulk of nanowires. Owing to the barrier for directional (radial) migration towards the non-polar surface, these trapped holes cannot participate in the surface reaction and hence diffuse randomly [168] with higher probability of recombination (Fig. 5-10a). Under concentrated excitation, the band bending is reduced which lowers the barrier for hole diffusion with enhanced water oxidation reaction, however, not to its full potential. One of the reasons is that, the random distribution of HER-cocatalyst on nanowire surface greatly limits available surface area for water oxidation, which is a four-electron sluggish process, and the efficiency of overall water splitting depends on effective rate of water oxidation. Even though the transport is no longer diffusion limited, under flat-band condition the concentration-gradient for holes in valence band is reduced. This leads to overlapping of electron and hole distribution with enhanced probability of recombination (Fig. 5-10b).

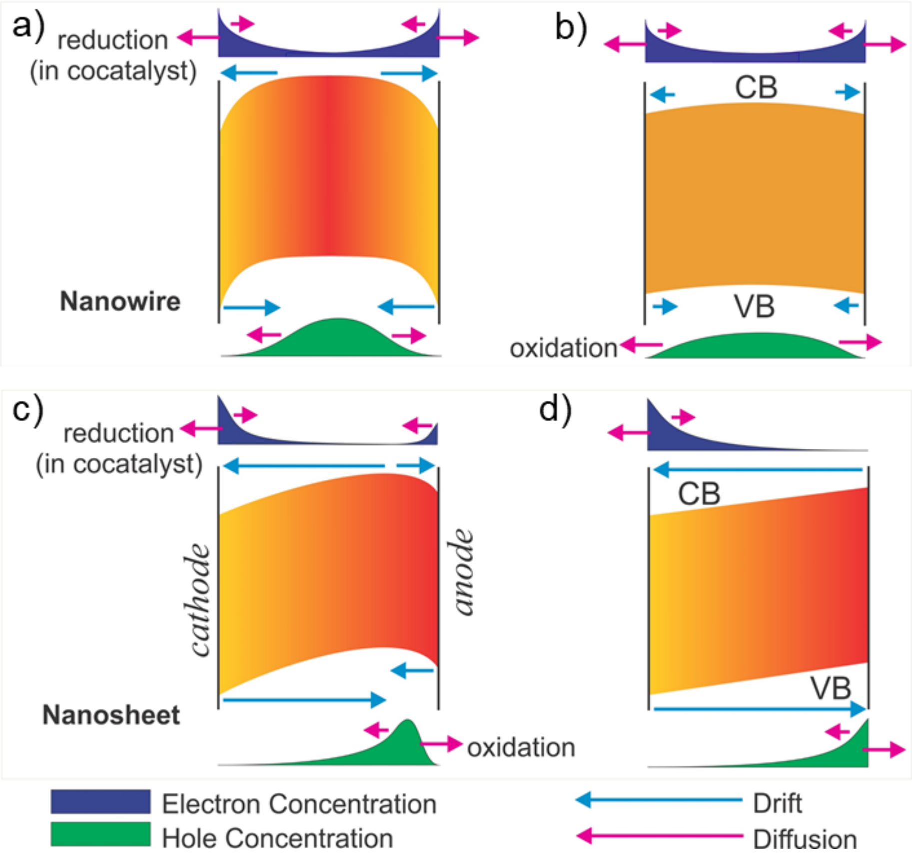

Figure 5-10: a) Optimally doped nanowire provides carrier separation in *near-surface* region under low excitation, however, with low photocatalytic activity due to trapping of photo-generated holes in the bulk. b) Under concentrated irradiation, reduced band-bending in nanowire lowers the hole-diffusion barrier for water oxidation, the rate-limiting step for overall water splitting. Carrier transport mechanism in a photochemical diode nanosheet under c) low excitation and d) concentrated high excitation. Built-in potential and associated band bending due to Mg-doping gradient plays critical role in carrier separation, thereby suppressing charge carrier recombination in both the bulk and surface region.

The photochemical diode nanosheet breaks the bottleneck of charge carrier separation by electric-field driven drift-dominated carrier transport. While the band bending in a photochemical diode is favorable for carrier separation towards catalytic surfaces (cathode and anode), it also largely prevents reverse diffusion current (Fig. 5-10c and d) against electric-filed induced barrier, thereby making the carrier-flow unidirectional. HER co-catalysts on the cathode surface further eliminate the gradient in electron concentration (conduction band) and associated reverse diffusion current, by trapping the accumulated electrons from near-surface region to accelerate proton reduction. Critically important is that, electrons and holes in photochemical diode can freely diffuse along the non-polar surfaces (parallel cathode and anode) towards cocatalyst-enriched or reaction-prone regions, respectively, with the least probability of interference, crowding, and recombination. This leads to further enhancement in charge transport efficiency to the solid-liquid interface ($\eta_{\text{transport}}$) and the efficiency of interfacial charge transfer ($\eta_{\text{interface}}$). Consequently, an impressive solar-to-hydrogen conversion efficiency can be derived from the photochemical diode nanosheet.

5.7 Conclusion

In summary, we have demonstrated photochemical diode artificial photosynthesis system that can enable relatively efficient overall pure water splitting (STH ~3.3%). The wafer level photochemical diodes consist of vertically aligned InGaN nanosheets, with well-defined anode and cathode surfaces for water oxidation and proton reduction, respectively. Unique to such nanosheet photochemical diodes is that charge carrier flow can be precisely controlled at the nanoscale without any external bias: photo-generated electrons and holes are instantaneously separated due to the built-in electric field along the lateral dimension of nanosheets, leading to the spontaneous population of anode and cathode surfaces by holes and electrons, respectively. The spatially separated electron and hole gas significantly minimizes surface and bulk recombination and suppresses back reaction, which have been some of the major challenges in achieving efficient photocatalytic water splitting to date. The effective manipulation and control of charge carrier flow in nanostructured photocatalysts not only significantly enhances the efficiency of photocatalytic water splitting, but also provides critical insight in achieving high efficiency artificial photosynthesis, including the efficient and selective reduction of CO_2 to hydrocarbon fuels. Future work also includes the development of an axial photochemical diode by connecting the two semiconductor segments of the nanowire/nanosheet with a transparent tunnel junction or transparent ohmic contact, which can significantly enhance the STH efficiency [199, 200].

Chapter-6

An Industry-ready Artificial Photosynthesis Device?

6.1 Introduction

Challenge towards realizing a practical artificial photosynthesis system goes beyond achieving higher efficiency in photocatalytic water splitting, although that is one of the most important driving factors. Alongside, it is also important to make sure that the efficient photosynthetic device can be synthesized by large scale mature techniques, and the system is robust and stable in the harsh photocatalytic environment. As we have discussed on numerous occasions so far, the stringent requirements on the energy band structure of the semiconductor catalyst have left us with noticeably fewer options to explore for photocatalytic overall water splitting. For example, only a handful of semiconductor catalysts, e.g. Ni-doped $InTaO_4$ [41], CDots-C_3N_4 composite [56], and GaN:ZnO solid solution [57] can drive photocatalytic overall water splitting under visible-light irradiation [56, 58-61]. Moreover, many of these photocatalysts, such as CoO nanoparticles [61] and $SrTiO_3$:La,Rh/Au/$BiVO_4$:Mo Z-scheme system [58] exhibit stability of only a few hours, or less.

Recent studies have shown that, with the use of wide-bandgap protection/passivation layers such as TiO_2 for instance, the stability can be significantly improved for PEC water splitting [10, 36, 68, 201, 202]. Such extra protective layers, however, do compromise the charge carrier extraction and add an additional level of complexity in the design and synthesis of the photoelectrodes. In an effort to achieve highly efficient photocatalytic water splitting systems, extensive studies have also been carried out to incorporate suitable co-catalysts, including Rh, Pt, RuO_2 [203] and IrO_x [204], as well as earth abundant ones such as NiO_x [205-207], MnO_x [207], CoO_x [207-209], which provide distinct reactive sites for H_2 and O_2 evolution [210-212] and further enhancing the charge carrier separation and extraction processes [29, 138]. To date, however, the solar-to-hydrogen (STH) efficiency of photocatalytic overall water splitting on these materials has been generally limited to ~1%, or less, and the realization of long-term stable operation has remained somehow elusive.

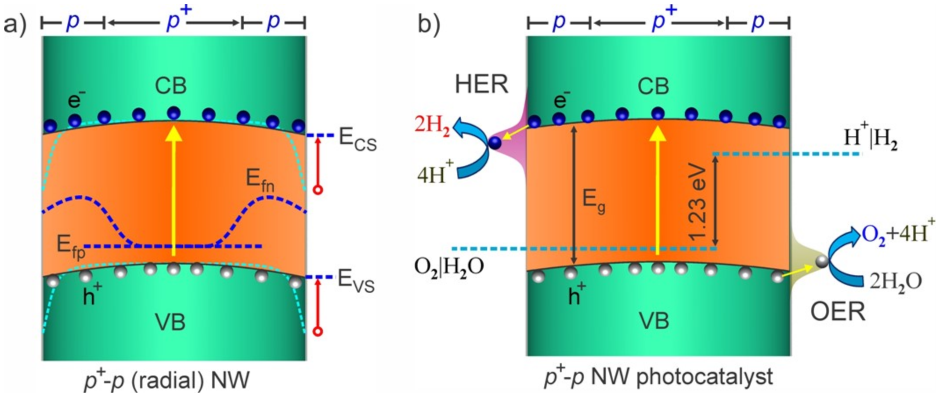

Figure 6-1: a) Schematic depiction of a nanowire p^+-p junction in the radial direction. By varying the p-type dopant incorporation in the near-surface region of the nanowire, the band bending can be experimentally tuned (from dashed-line to solid-line CB and VB edges) and the hole diffusion barrier on p-doped nanowire can be reduced. This allows for the simultaneous extraction of both photogenerated electrons and holes. E_{fn} and E_{fp} denotes their quassi Fermi levels. b) The simultaneous incorporation of water oxidation and proton reduction co-catalysts, which, together with the optimized surface band-bending on p^+-p nanowire, enables the efficient extraction of photogenerated holes and electrons in the radial direction and promotes water oxidation reaction and hydrogen evolution reaction, respectively, for overall photocatalytic water splitting.

Here, we report on an artificial photosynthetic device using standard materials widely used in the industry, i.e. gallium nitride (GaN) and its alloys (InGaN) on silicon wafers, which produces hydrogen efficiently by directly splitting pure water with long-term stable operation without applied bias or sacrificial agents. Due to the complex four-electron process involved in the reaction [51], water oxidation has always been regarded as the major limiting factor for overall water splitting and is the direct reason for the observed poor stability. Moreover, as discussed in Chapter 4, the presence of a hole depletion layer in a p-type nanowire catalyst, strongly limits the efficiency and compromises the functionality of the water oxidation co-catalyst. To date, there have been only few studies on the interplay between co-catalysts and surface electronic properties of the semiconductor. Such a critical issue in photocatalytic water splitting can be partly addressed by exploiting a p^+-p nanowire junction, as schematically shown in Fig. 6-1a, which can reduce the hole depletion layer. Moreover, the surface band bending can be tuned experimentally by varying the Mg-dopant incorporation in the p^+ bulk and the p-type near-surface region to optimize the extraction of the photogenerated electrons and holes.

In this study, we have investigated the distinct, as well as the synergistic effect of the water oxidation co-catalyst CoO_x, the proton reduction co-catalyst Rh/Cr_2O_3, and the surface band bending of the nanowires on the performance and long-term stability for photocatalytic overall water splitting reactions, as shown schematically in Fig. 6-1b. It is observed that, when these techniques are optimally combined, GaN nanowire photocatalysts can exhibit an unprecedented, near 100% absorbed-photon-conversion efficiency (APCE) for unassisted overall pure water splitting. We have further demonstrated that the dual-cocatalyst decorated double-band GaN/InGaN nanowire-arrays can exhibit an STH efficiency of ~2.7% for overall pure water splitting without bias, nor sacrificial reagent. More importantly, no performance degradation was observed in over 580 hrs of water splitting reaction under concentrated sunlight (27 Suns), which is the longest stability ever reported for any inorganic semiconductor photocatalysts or photoelectrodes without any protection layer for unbiased overall photocatalytic pure water splitting with STH >1%.

6.2 Signature of OER and HER Co-catalysts on GaN Nanowires

We have first studied the synergistic effect of water oxidation co-catalyst, *i.e.* CoO_x for oxygen evolution reaction (OER), and surface electronic properties of GaN nanowire photocatalyst in overall water splitting reaction. Cobalt oxide was deposited on GaN nanowires by a photo-oxidation process using the cobalt nitrate $Co(NO_3)_2$ precursor; and from the STEM and XPS analyses, the deposited oxide was characterized to be Co_3O_4. A high-resolution scanning transmission electron microscopy bright-field (STEM-BF) image of CoO_x-decorated GaN nanowire is shown in Fig. 6-2a, which revealed high crystallinity from both the GaN nanowire and the CoO_x nanoparticles. The distance between the adjacent GaN nanowire lattice fringes is ∼0.518 nm, which corresponds to the <0001>

direction of GaN, with lateral surface being the nonpolar *m*-plane [151]. The (222) facet of Co_3O_4 reveals lattice fringe distance of ~0.233 nm [213]. The crystalline quality and the core-shell structure of proton reduction co-catalyst, i.e. Rh/Cr_2O_3 for hydrogen evolution reaction (HER) were also revealed from the STEM-BF and STEM-HAADF images, as shown in Fig. 6-2b.

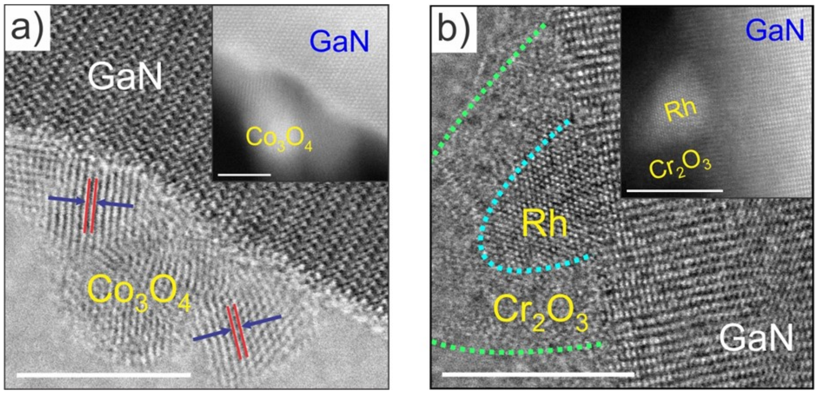

Figure 6-2: a) Scanning transmission electron microscopy STEM-BF (bright field) image of Co_3O_4 nanoparticles on GaN nanowire surface. Scale bar, 5 nm. STEM-HAADF (high angle annular dark field) image of the same region is shown in the inset. Scale bar, 2 nm. b) STEM-BF image and STEM- HAADF image (inset) of Rh/Cr_2O_3 (core-shell) nanostructure on GaN nanowire surface. Scale bar, 5nm.

The signature of Co_3O_4, as an oxygen evolution reaction (OER) co-catalyst was revealed from water oxidation half-reaction which was carried out in the presence of $AgNO_3$ as a sacrificial reagent. The amount of O_2 evolution is significantly higher from Co_3O_4-decorated GaN nanowires, compared to that from bare GaN nanowire photocatalyst, clearly indicating the role of Co_3O_4 as an OER co-catalyst (Fig. AP-A4a). To further gain a deep insight, electro-catalytic water oxidation was carried out on electrodes composed of bare GaN nanowires and Co_3O_4 decorated GaN nanowires, by recording linear sweep voltammetry (LSV) curve in potassium phosphate buffer solution (pH~7) in the dark. Silver chloride electrode (Ag/AgCl) and Pt was used as the reference and the counter electrode, respectively. The negative shift of applied (onset) potential on GaN/Co_3O_4 electrode compared to that on GaN electrode (as shown in Fig. AP-A4b) further reveals that Co_3O_4 functioned as an OER co-catalyst by lowering the overpotential and facilitating the surface water oxidation process [214, 215].

Therefore, water oxidation is facilitated on Co_3O_4 surfaces, which can be attributed to the trapping of photo-generated holes into Co_3O_4 nanoparticles [67] from the *near-surface region* of GaN nanowires. One direct evidence for the efficient charge carrier separation and extraction of holes into OER co-catalyst nanoparticles is - the significantly reduced photoluminescence intensity. the photoluminescence emission intensity from the Co_3O_4 loaded GaN nanowires is nearly half, compared to that from the bare GaN nanowires (Fig. AP-A4c). Hence, with efficient charge carrier extraction and significantly reduced recombination, the co-catalyst loaded GaN nanowires is expected to exhibit noticeably higher photocatalytic activity than the bare GaN nanowire structures. It is worthwhile mentioning that the enhanced H_2 production with Rh/Cr_2O_3 as a co-catalyst for hydrogen evolution reaction (HER), and subsequent reduction of PL intensity due to electron trapping in HER-cocatalyst nanoparticles had been demonstrated in our previous studies [126, 216] (Chapter 4 and 5, Fig. AP-B1a).

6.3 Simultaneous Loading of HER and OER Co-catalyst on Nanowires

To promote overall water splitting reaction, both Rh/Cr_2O_3 and Co_3O_4 co-catalysts were simultaneously loaded on the nanowire surfaces using step by step photodeposition method [217]. The high-resolution transmission electron microscopy (HRTEM) image is shown in Fig. 6-3a, which demonstrates simultaneous deposition of both Rh/Cr_2O_3 and Co_3O_4 co-catalysts on GaN nanowire surfaces. HRTEM images (Fig. 6-3b) taken from region A and B of Fig. 6-3a revealed the formation of a Rh/Cr_2O_3 core/shell nanostructure, and the presence of Co_3O_4 nanoparticles. The oxidation states of Rh, Cr, and Co on the dual-cocatalyst decorated GaN nanowires were also confirmed from the XPS analysis. XPS spectrum of the Rh 3d, Cr 2p, and Co 2p obtained from the dual-cocatalyst decorated GaN nanowires are shown in Fig. AP-A5. The Rh $3d_{5/2}$ peaks observed at 307.5 eV and 309.5 eV are attributed to metallic Rh^0 and native Rh oxide [218], respectively. The Cr $2p_{3/2}$ peak appeared at 576.9 eV is ascribed to the presence of Cr_2O_3 [218], indicating that the valence state of Cr is trivalent. Co $2p_{3/2}$, Co $2p_{1/2}$, and the satellite peaks of Co were resolved for Co 2p peaks. Figure 6-3c shows the x-ray photoelectron spectroscopy (XPS) spectra of the Co *2p* orbital, which further confirm the chemical form of Co and the presence of Co_3O_4.

Co $2p_{3/2}$ and $2p_{1/2}$ peaks located at 780.5 and 795.5 eV from CoO_x-modified GaN nanowires match well with the spin-orbit splitting value of commercial Co_3O_4 [219]. These analyses conclusively support that Co_3O_4 nanoparticles were successfully loaded onto the nonpolar surfaces of GaN by photodeposition. In addition, EDX spectrum (Fig. 6-3d) obtained from region A and B of Fig. 6-3a further confirms the simultaneous loading of HER and OER co-catalysts on GaN nanowire surfaces.

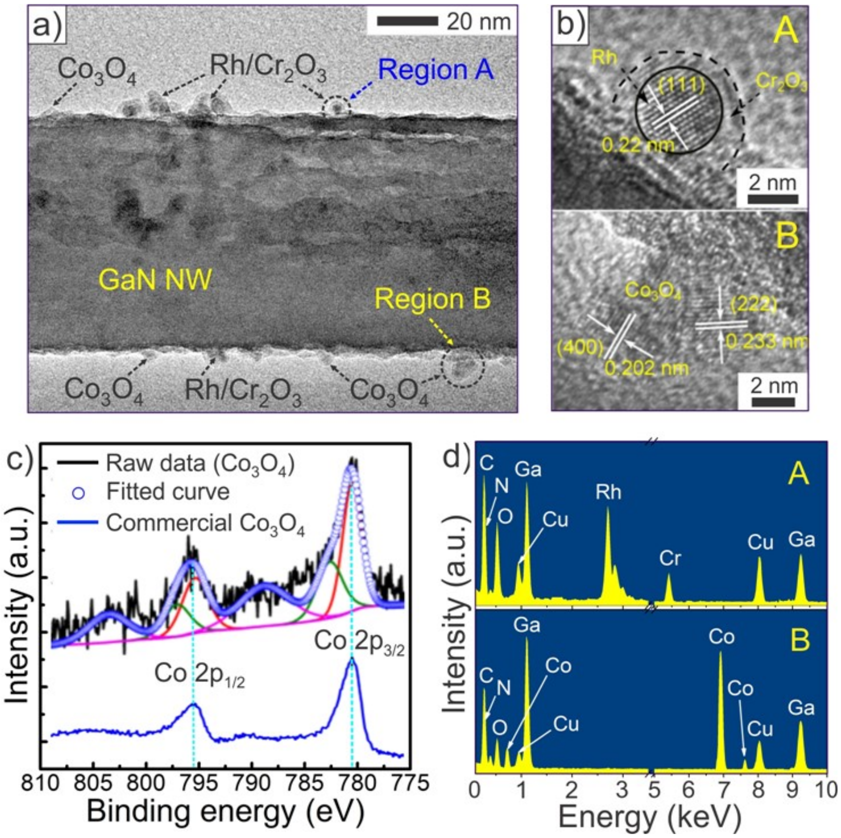

Figure 6-3: a) TEM image of a cocatalyst-decorated GaN nanowire, which depicts simultaneous loading (not optimized) of HER and OER co-catalysts (Rh/Cr_2O_3 and Co_3O_4, respectively) for overall pure water splitting. b) HRTEM images of region A (top) and B (bottom), as highlighted in a). c) ARXPS spectra of the Co 2p orbitals on bare GaN and Co_3O_4-decorated GaN nanowires, revealing the presence of Co_3O_4 nanoparticle deposition. Spectra measured on the commercial Co_3O_4 reveals very close correlation with that of the GaN/CoO_x system. Two typical peaks were observed from both the CoO_x modified GaN nanowires and the commercial Co_3O_4, locating at 780.5 and 795.5 eV, which were ascribed to Co $2p_{3/2}$ and Co $2p_{1/2}$ orbitals, respectively. d) EDX spectrum of region A (top) and B (bottom) as shown in a) and b). Both HRTEM and EDX measurements confirm the formation of Rh/Cr_2O_3 core-shell nanostructures and the deposition of Co_3O_4 nanoparticles on the non-polar surfaces of GaN nanowires.

6.3.1 Nanowire Surface Charge Properties: Impact of Co_3O_4 Loading

In this study, GaN nanowires were grown onto commercial Si wafer substrates by radio frequency plasma-assisted molecular beam epitaxy (MBE) under nitrogen-rich conditions, which promotes the formation of the crucial N-terminated surfaces, not only for the top (polar) facet but also for the lateral (non-polar) surfaces [99, 220]. Mg was used as *p*-type dopant, and the concentration of Mg-dopant was tuned by controlling the effusion cell temperature of Mg (T_{Mg}) from 220 to 290 °C, which correspond to average Mg concentrations in the range of 5×10^{17} to $\sim1\times10^{20}$ cm^{-3} within the nanowires. The nanowires are vertically aligned on the substrate, with lengths of ~600 nm and lateral dimensions of ~40-70 nm. As briefly discussed in section 4.3, experimentally the photocatalytic performance of GaN nanowires in water splitting is very poor under relatively low Mg-doping levels (due to large downward band bending at the *near-surface region*); and significantly enhanced activity can be obtained at $T_{Mg} = 260$ °C, which is ascribed to a more balanced and efficient redox reaction due to reduced downward band bending. Decreased activity at very high Mg-cell temperature is observed due to the degradation of nanowire crystalline quality [221]. However, optimum Mg-cell temperature for *p*-InGaN is was found to be $T_{Mg} = 200$ °C which can be ascribed to the lower activation energy of Mg-dopant in InGaN. With optimum surface charge properties, the decoration of nanowire surfaces with Rh/Cr_2O_3 reduction co-catalysts (HER) accelerates carrier separation from *near-surface* region by trapping electrons for proton reduction reaction. Under concentrated excitation, the band bending is reduced, further lowering the barrier for hole diffusion towards the semiconductor-electrolyte interface, and in addition, the deposition of OER-cocatalyst (CoOx) facilitates the collection/trapping of photo-generated holes with enhanced water oxidation reaction.

E_F-E_V was estimated from ARXPS valence band spectrum, measured on the non-polar (lateral) surfaces of GaN nanowires. The position of surface valence band maximum (E_V), with respect to the surface Fermi level (E_F, binding energy = 0 eV) [221] is measured from the intersection between the linear extrapolation of valence band leading edge and the extended baseline (Fig. AP-A6a). The E_F-E_V in the near-surface region of Mg-doped GaN nanowires (which quantitatively represents the downward band bending) decreases with the increment of Mg cell temperature [221]. The reduction of E_F-E_V values, measured on the Co_3O_4-nanoparticle decorated GaN nanowires compared to that measured on the bare GaN nanowires, reveals that the downward band bending on the near-surface region of *p*-GaN nanowire is further reduced due to the incorporation of Co_3O_4 (Fig. AP-A6b).

6.3.2 Photocatalytic Performance of Dual-cocatalyst Decorated GaN

A schematic representation of the dual-cocatalyst decorated *p*-GaN nanowire is shown in Fig. 6-4a, illustrating the mechanisms of overall water splitting on the lateral surface of the GaN nanowires. The standalone effect of Co_3O_4 and Rh/Cr_2O_3 co-catalysts in enhancing the efficiency of water oxidation and proton reduction reactions respectively, are discussed in previous section. The non-polar surfaces of GaN are well-known to be highly reactive to water oxidation. Therefore, overall water splitting on *p*-GaN nanowires was first investigated in the presence of only reductive co-catalyst Rh/Cr_2O_3 for hydrogen evolution reaction (HER). Shown in Fig. 6-4b (green bars), it is observed that the evolved H_2 rate exhibits a critical dependence on the Mg-dopant incorporation, which was also revealed in previous studies and attributed to variations of the surface band bending as a function of Mg-dopant incorporation [222]. The H_2 evolution rate first increased with the increment of Mg doping temperature due to the reduced downward bending in more heavily Mg-doped GaN nanowires and reached an optimum value at T_{Mg} = 260 °C (Mg concentration $\sim 1\times10^{20}$ cm^{-3}). Further increment of Mg doping resulted in decreased activity, due to the formation of defects and resulting poor material quality [222].

By additionally incorporating Co_3O_4 co-catalyst on GaN:Mg nanowires, it is observed that the H_2 generation rate is substantially enhanced for the overall water splitting reaction (red bars in Fig. 6-4b), which had been consistently measured for GaN:Mg nanowire photocatalysts with various Mg doping concentration. The underlying mechanisms can be explained by the significantly accelerated water oxidation process, facilitated by the co-catalytic effect of Co_3O_4. The role of the co-catalysts on the enhancement of the solar H_2

generation rate is further illustrated in Fig. 6-4c for GaN nanowire photocatalyst with an optimum Mg doping level (T_{Mg} = 260 °C).

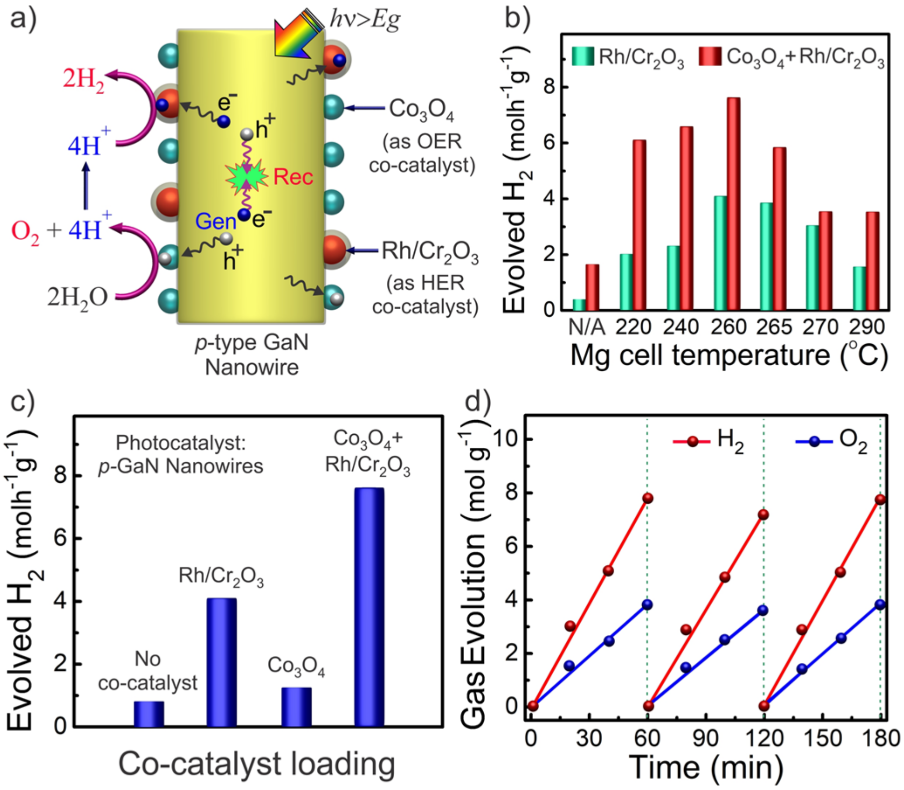

Figure 6-4: a) Schematic illustration of the carrier dynamics in overall water splitting on a dual-cocatalyst loaded GaN nanowire, showing carrier generation (Gen), recombination in the bulk (Rec), carrier diffusion towards the nanowire surfaces and trapping into appropriate co-catalysts. Co_3O_4 promotes the water oxidation for the oxygen evolution reaction, whereas Rh/Cr_2O_3 facilitates the hydrogen evolution reaction. b) H_2 evolution rate in overall pure (pH ~7.0) water splitting for different Mg-doped GaN nanowire-arrays with only Rh/Cr_2O_3 and with dual-cocatalyst. A ~2.8 cm^2 physical surface area sample (active GaN catalyst weight ~0.387 mg) was used for the experiment. With Rh/Cr_2O_3, efficient water splitting can be achieved with T_{Mg} ~ 260 °C, whereas with dual-cocatalyst, efficient H_2 generation rates can be achieved for a wider range of Mg dopant incorporation (T_{Mg} ~ 220-265 °C). c) Comparison of H_2 evolution rate from overall water splitting on GaN (Mg-260 °C) nanowires loaded with different co-catalysts, depicting the standalone and synergistic/tandem effect of HER and OER co-catalyst. The dual-cocatalyst (Co_3O_4 and Rh/Cr_2O_3) decorated GaN:Mg nanowire arrays exhibit more than ten-fold enhancement in H_2 evolution rate compared to bare GaN:Mg nanowires. d) Time course of H_2 and O_2 evolution for 3 cycles, demonstrating the repeatability of overall water splitting reaction and consistency in gas evolution rates.

The dual-cocatalyst (Co_3O_4 and Rh/Cr_2O_3) decorated GaN:Mg nanowire-arrays exhibit a two-fold enhancement in evolved H_2 rate compared to the Rh/Cr_2O_3 decorated

GaN:Mg nanowires, a seven-fold enhancement compared to the Co_3O_4 decorated GaN:Mg nanowires, and more than a ten-fold enhancement compared to bare GaN:Mg nanowires, respectively. These substantial enhancements in photocatalytic activity reveal not only the crucial roles of both reductive and oxidative co-catalysts, but more importantly, their synergistic/tandem effect in dramatically increasing the solar water splitting efficiency. Such an effect has also been observed on GaN:ZnO [223, 224] and $BiVO_4$ [225]. In this study, the absorbed-photon-conversion efficiency of dual-cocatalyst decorated GaN:Mg (T_{Mg} = 260 °C) nanowires was derived to be ~ 98%, suggesting that virtually all the photogenerated charge carriers were actively participating in the water splitting reactions rather than recombination (APPENDIX-D). Cyclic tests on *p*-GaN (T_{Mg} = 260 °C) nanowires with dual-cocatalyst were carried out and 3 repeated cycles are illustrated in Fig. 6-4d as a function of time, showing excellent stability of overall water splitting reaction with stoichiometric 2:1 hydrogen and oxygen evolution.

It is also of interest to note that, with the incorporation of Co_3O_4 co-catalyst, the H_2 generation rate becomes less sensitive to the variations of the surface charge properties. Indeed, efficient H_2 generation rates can be achieved for a wider range of Mg dopant incorporation (T_{Mg} ~ 220-265 °C) for dual-cocatalyst loaded photocatalyst system, as illustrated in Fig. 6-4b. The underlying mechanism has been carefully studied. As shown in Fig. 6-1a, the presence of downward band bending in GaN:Mg nanowires creates a hole depletion layer, which has been identified as the major rate-limiting factor for photocatalytic overall water splitting. The downward band bending in the near-surface region of GaN:Mg nanowire is reduced when in contact with Co_3O_4 (Fig. AP-A6b), which, collectively with the accelerated water oxidation process, enhances the extraction of photogenerated holes [226], hence significantly improving the efficiency of H_2 generation even for GaN:Mg nanowires with relatively larger downward band bending.

6.4 Double-band GaN/InGaN Photosynthetic Device on Si Substrate

We have subsequently investigated visible-light active, dual-cocatalyst decorated GaN/InGaN double-band nanowire photocatalysts for overall water splitting reaction. The principles of engineering GaN/InGaN double-band nanowire heterostructures are discussed earlier in section 4.4 and schematically illustrated in Fig. 4-6. However, the usage of dual-cocatalyst system can effectively compensate for the necessary over-potentials to achieve high efficiency overall water splitting, thus allowing us to realize visible-band with extended absorption wavelength. Therefore, the properties of GaN/InGaN nanowires used in this study are discussed briefly herein.

6.4.1 Synthesis and Structural Properties

The double-band nanowires are grown on top of the Mg-doped GaN nanowire template (on commercial Si wafer substrates). The InGaN band consists of five $In_{0.25}Ga_{0.75}N$:Mg segments separated by a thin GaN layer, and finally capped by a GaN:Mg layer on top [227]. The typical birds'-eye view SEM image, as shown in Fig. 6-5a, reveals that the as-grown nanowires are vertically standing on Si substrate with uniform spacing and morphology. The hyper-abrupt interface between GaN and InGaN layers, revealed from HRTEM image is also shown in the inset, demonstrating the crystalline quality of both the layers. The Mg doping concentrations were separately tuned in the GaN and InGaN segments for optimum downward band-bending. The room-temperature photoluminescence (PL) spectrum, shown in Fig. 6-5b, revealed two distinct emission peaks at ~365 and ~ 505 nm, which correspond to the bandgaps of GaN (3.4 eV) and $In_{0.25}Ga_{0.75}N$ (2.46 eV), respectively.

The indium composition within the InGaN band had been tuned to ensure necessary overpotentials for both water oxidation and proton reduction reaction, while extending the absorption threshold to harness more visible photons from solar spectrum. In other words, the bandgap of $In_xGa_{1-x}N$ was tuned to be narrow enough (E_g ~2.46 eV, x~25% as derived from PL analysis) to drive both the redox half-reactions forward. The growth temperature for GaN was ~ 790 °C, and for InGaN the growth temperature was in the range of 650-710 °C. During the synthesis of multi-stacked GaN/InGaN nanowire photocatalyst, the InGaN segments in visible-band were doped at $T_{Mg} = 200$ °C (Mg BEP of $\sim1.5\times10^{-11}$ Torr), and the top GaN segment *i.e.* the UV-band was doped at $T_{Mg} = 265$ °C (Mg BEP of $\sim5.5\times10^{-10}$

Torr). The use of N-rich conditions during nanowire growth promotes the formation of N-terminated lateral surfaces [168, 228].

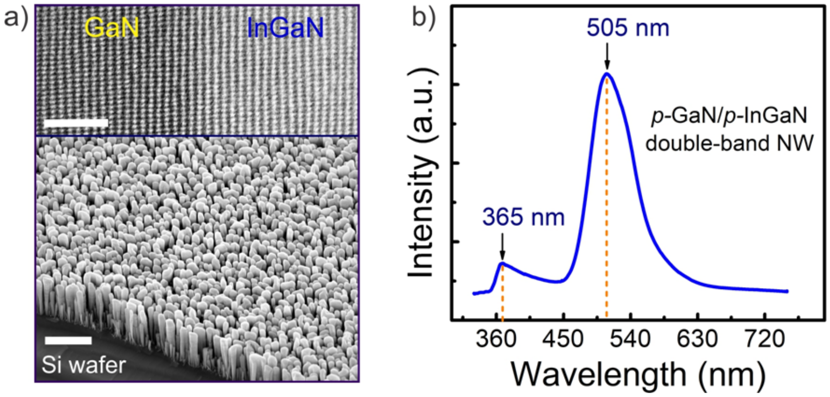

Figure 6-5: a) A 45°-tilted scanning electron microscopy image of GaN/InGaN nanowire-arrays vertically aligned on a Si wafer substrate. Scale bar, 500 nm. The inset (top) shows a high-resolution scanning transmission electron microscopy (HRSTEM-ZC) image of hyper-abrupt crystalline GaN/InGaN interface. Scale bar, 2 nm. b) Room temperature photoluminescence (PL) spectrum from as-grown double-band *p*-type GaN/InGaN nanowire heterostructure.

6.4.2 Dual-cocatalyst Loading on Double-band GaN/InGaN Nanowires

The unique double-band GaN/InGaN nanostructure enables an efficient utilization of the photogenerated carriers and prevents energy loss due to their thermal relaxation, without sacrificing the absorption efficiency in both UV and visible-light regions simultaneously. Schematically illustrated in Fig. 6-6a, is the dual-cocatalyst (Co_3O_4 and Rh/Cr_2O_3) decorated *p*-GaN/$In_{0.25}Ga_{0.75}N$ nanowire for overall neutral pH water splitting. As shown in Fig. 6-6b, the system exhibit H_2 and O_2 evolution rates of 7.14 and 3.54 mol $h^{-1}g^{-1}$ (1.14 and 0.57 mmol $h^{-1}cm^{-2}$) under concentrated sunlight illumination (~27 Suns), respectively, which is nearly twice higher than identical GaN/$In_{0.25}Ga_{0.75}N$ nanowires but with only a single photocatalyst (Rh/Cr_2O_3). The H_2 and O_2 gas evolution during overall pure (neutral pH) water splitting reaction can be clearly seen in the form of bubble. Under strict visible light irradiation (> 400 nm), the H_2 and O_2 evolution rates were measured to be 1.75 and 0.9 mol $h^{-1}g^{-1}$ (290 and 144 μmol $h^{-1}cm^{-2}$), respectively (see Fig. AP-A7).

The STH efficiency, derived from the H_2 production rate on dual-cocatalyst decorated *p*-GaN/InGaN double-band nanowires was estimated to be ~2.7%, which was measured under full arc illumination with AM1.5G filter (~27 Suns). The apparent quantum efficiency (AQE), determined from H_2 production under full arc illumination with 400 long-pass filters, was estimated to be 12.5% in the wavelength range 400–505 nm. This AQE is slightly lower than that reported by Domen's group at 419 nm [58] wavelength, however, with more extended utilization of visible photons in our study. The efficiency could be further improved by optimizing the surface coverage of Co_3O_4 nanoparticles on *p*-InGaN nanowire segments and by improving the quality and surface charge properties of InGaN:Mg nanowire-arrays.

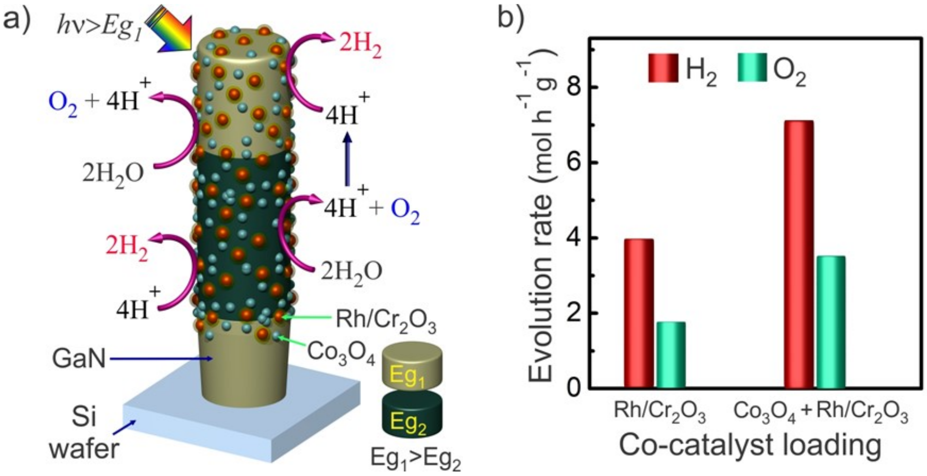

Figure 6-6: a) Schematic illustration of unassisted overall pure water splitting on a dual-cocatalyst loaded double-band nanowire heterostructure (herein, $E_{g1} \sim 3.4$ eV and $E_{g2} \sim 2.46$ eV). Water oxidation (O_2 evolution) is promoted on Co_3O_4, whereas Rh/Cr_2O_3 promotes the proton reduction reaction (H_2 evolution). b) The rate of stoichiometric H_2 and O_2 evolution in overall pure (pH~7.0) water splitting on *p*-GaN/InGaN nanowire, decorated with only Rh/Cr_2O_3 and dual-cocatalyst (Co_3O_4+Rh/Cr_2O_3) under concentrated full arc illumination with AM1.5G filter.

To understand the synergistic effect of dual-cocatalyst loading, the STH efficiency was calculated for both the photocatalyst nanostructures in the wavelength range 200-1100 nm under concentrated irradiation (~27 suns) using AM1.5G filter. The STH was estimated to be ~2.7% and 1.5% for the *p*-GaN/InGaN double-band nanowire photocatalyst with dual-cocatalyst (Co_3O_4 and Rh/Cr_2O_3) and HER co-catalyst (Rh/Cr_2O_3 only), respectively. The experiments herein were conducted under concentrated irradiation, with incident photon flux as high as $4.16x10^{21}$ photons $h^{-1}cm^{-2}$ within the absorption range of 200-505 nm under full arc illumination. It is important to mention that, under concentrated excitation the temperature is also expected to be higher which can partially contribute to the non-linear increase of the photocatalytic reactivity. However, due to natural heat radiation to the ambience, the water temperature in this study can increase only up to 318-325 K with potential reduction of the Gibb's energy to as low as 231 kJ mol^{-1}.As per the discussion in APPENDIX-C, the Gibbs energy of water splitting reaction can vary within ~231-237 kJ mol^{-1} depending on the pressure and temperature during the reaction, and the STH can be estimated in the range of ~2.6-2.7%, respectively, which lies almost within experimental error. In the wavelength range of 200-505 nm (incident intensity of ~578 mW cm^{-2}), the ECE was found as ~12.9% for the dual-cocatalyst loaded double-band nanowire photocatalyst, compared to ~7.5% for HER co-catalyst loading only. On the other hand, in the wavelength range of 400-505 nm, the calculated values for ECE were ~5.5% and 4.5%, respectively.

In the wavelength range of 200-505 nm with AM1.5G filter, the number of incident photons per second was calculated as a function of wavelength and corresponding AQE can be calculated from equation above. Considering the entire absorption spectrum (200-505 nm) for the double-band structure, which includes both UV and part of the visible photons, the AQE was derived to be ~33% for the GaN/InGaN double-band nanowire photocatalyst with dual-cocatalyst (Co_3O_4 and Rh/Cr_2O_3), compared to ~18% for the GaN/InGaN nanowires with HER co-catalyst (Rh/Cr_2O_3) only. In the visible wavelength range (400-505 nm), the AQE for GaN/InGaN photocatalyst was estimated to be ~12.5% and ~9.9% with dual-cocatalyst and with HER-cocatalyst, respectively.

6.4.3 Enhanced Efficiency and Extended Stability in OWS

It is crucial to achieve long-term stability for semiconductor photocatalysts/ photoelectrodes in overall water splitting reaction for practical applications. With significantly enhanced photocatalytic efficiency, repeated cycles of overall pure water splitting were carried out on dual-cocatalyst loaded $In_{0.25}Ga_{0.75}N$/GaN nanowire photocatalysts for over 580 hrs (24 days). Figure 6-7a shows the H_2 and O_2 evolutions from the first and last 10 cycles. No evidence of performance degradation was observed in the

H_2 evolution activities. Figure 6-7b further illustrates the rates of H_2 and O_2 evolution which remain consistent, exhibiting nearly stoichiometric (2:1) gas production during the 584 hours of balanced overall neutral pH pure water splitting reaction without bias or sacrificial agents. The photocatalytic activity of *p*-type GaN/InGaN nanowires dependes critically on Mg-dopant incorporation, as shown in Fig. 4-2d and Fig. 6-4b. For optimally doped (Mg) double-band GaN/InGaN heterostructures, slight variations in photocatalytic performances (as high as ~10%) can be observed due to fluctuations in growth conditions, sample preparation (*e.g.* co-catalyst loading) and performance evaluation. The long-term stability test herein has been conducted on such a (single) device, and the minor differences in evolution rates among repeated-cycles (Fig. 6-7b) could be observed mostly due to slight inconsistencies in manual sampling of the evolved gases and/or misalignment between the light source and the sample during water splitting reaction. To the best of our knowledge, this is the first demonstration of long-term stable operation for semiconductor photoelectrodes without protection/passivation layers for unassisted overall photocatalytic pure water splitting with STH >1%. A comprehensive comparison and discussion on the record-efficiencies and -stabilities achieved on the state-of-the-art photocatalysts are presented in section 2.2.

Herein, we briefly discuss the advancement made in our current work considering the state-of-the-art performances. Previously, Domen *et al.* reported the long-term stable operation of GaN:ZnO photocatalyst with RuO_2 as water oxidation co-catalyst, which, however, only exhibited an AQE of 0.16% at 400-500 nm [224] and an STH <0.1%. It is evident that, although the STH efficiency of ~2.7% reported in this work is lower than that of CoO nanoparticles (5%) which are barely stable in harsh photocatalytic environment [61], the performance-stability of our nanowire photocatalyst system is significantly better. Stability for 200 days had been reported on CDots-C_3N_4, but with lower STH efficiency (2%) [56] than that reported here. However, the two-step approach of water splitting adopted therein requires efficient generation as well as subsequent decomposition of H_2O_2, which puts further constraints on the bandgap of suitable photocatalyst (>1.78 eV, compared to ~1.23 eV for neutral pH overall water splitting excluding the over-potentials). The dual-cocatalyst loaded double-band nanowire photocatalyst system in this work, therefore, outperforms most of the reported typical photocatalysts in the aspects of both STH efficiency and stability for overall photocatalytic or photochemical water splitting.

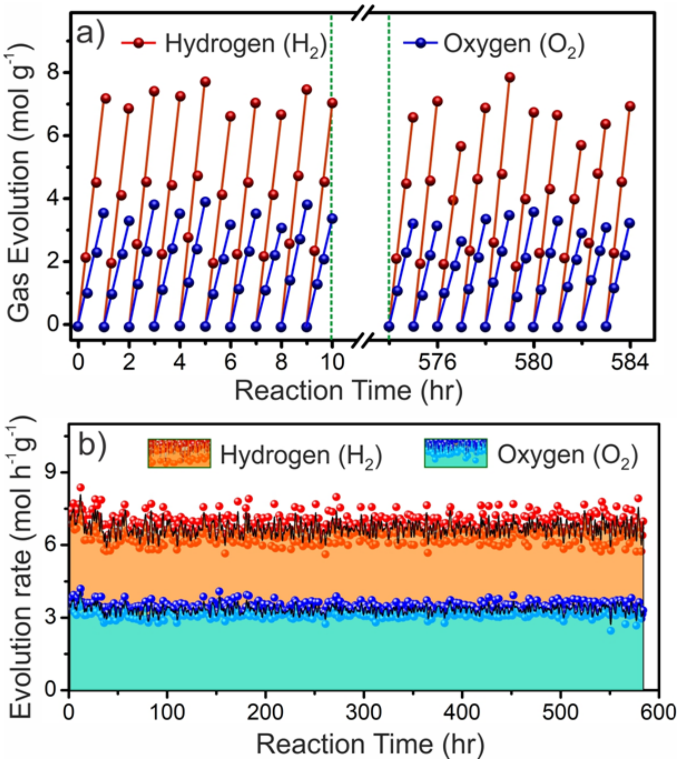

Figure 6-7: a) Repeated time evolution of H_2 and O_2 production from first and last 10-cycles among 584-cycles of unassisted overall (neutral pH) water splitting. b) Average rate of H_2 and O_2 production (7.14 and 3.54 mol h^{-1}g^{-1}, respectively) from each cycle during long-term repeated course of water splitting under concentrated sunlight illumination (~27 Suns), demonstrating excellent performance and stability of the device (area of ~3.0 cm^2 and active GaN/InGaN catalyst mass of ~0.48 mg).

As for unassisted PEC water splitting, the STH efficiency is limited to <1% while being stable for duration as low as 12 hrs without the incorporation of any photovoltaic (solar cell). When the photovoltaic cells were integrated with the photoelectrodes, the STH efficiency is boosted up to ~14% [114]. Particularly, by using photovoltaic-assisted electrolysers, 30% of STH efficiency was obtained. An enhanced STH efficiency of ~16% is reported for PEC water splitting using GaInP/GaInAs tandem absorber with significantly limited photocurrent stability [110]. Recently, stability study through electrolyte engineering has shown that, the use of a vanadium-saturated solution can suppress the photo-corrosion of vanadium-containing catalysts *e.g.* $BiVO_4$. Although the photocurrent stability up to ~450 hours [124] was achieved, the application to enhance the stability on an efficient PEC device is yet to be demonstrated. However, most of the reported unassisted PEC water splitting systems still suffer from the instability (limited to < 100 hrs)

6.5 Origin of Enhanced Efficiency and Long-term Stability

The atomic-scale origin of the *p*-type GaN/InGaN nanowires in achieving long-term stability and high efficiency from overall solar water splitting in pure water and without any sacrificial reagent has been investigated. Recent studies, both theoretical and experimental, have revealed that the Ga(In)N nanowires grown by MBE can spontaneously form atomically thin N-terminated layers, on both their top surfaces and lateral sidewalls [228]. Such a unique surface configuration was achieved by employing a Ga seeding layer during the initial nanowire nucleation and by utilizing N-rich conditions during the subsequent epitaxial processes [229] . The N-termination of all exposed surfaces protects the nanowire photocatalyst against oxidation and photo-corrosion. Significantly, the measurements herein were performed under concentrated sunlight (~27 suns), which is of utmost interest for economically viable industrial production of hydrogen using limited land area and employing minimum amount of photocatalyst. Harvesting of solar energy (a planar resource) and carrier extraction at high illumination intensity is more efficient in such vertically-aligned wafer-level nanostructures, compared to particulate photocatalyst which, in addition to exhibiting weaker light absorption, often suffers from larger grain boundary resistance because of aggregation. On the contrary, most of the photocatalysts become unstable and less-efficient under concentrated irradiation due to enhanced corrosion (self-oxidation) and second-order recombination, which therefore requires significant scalability to cover larger area under one-sun light intensity.

The substantial enhancements in photocatalytic activity and device-longevity reveal not only the crucial roles of band-flattening due to optimum Mg-dopant incorporation and high-intensity excitation, but more importantly, the synergistic/tandem effect along with the loading of both reductive and oxidative co-catalysts. The charge transfer from 1D nanowires to co-catalyst nanoparticles are no longer diffusion limited due to their smaller diameters. The perturbation in surface band-bending and the associated localized electric-fields induced due to the incorporation of HER and OER co-catalysts on optimally doped p-type nanowire surfaces steer the favorable extraction of electrons and holes into respective distinct co-catalyst nanoparticles (Fig. 6-4a), which eventually enhances carrier separation while retarding the probability of overall recombination. As predicted by the first principle calculation and experimental data based on the rate-law analysis, the most effective approach to improve the photocatalytic reactivity is to increase the concentration of photogenerated holes on the catalytic surfaces for efficiently driving multi-hole processes. Loading of Co_3O_4 nanoparticles facilitate accumulation of photogenerated holes to simultaneously drive complex four-hole water oxidation process, the sluggish and major rate-limiting step for overall water splitting. Moreover, water molecules can effectively adsorb and dissociate on Co_3O_4 surfaces to form strongly bound hydroxyl radicals which can be ascribed as trapped holes on the surface. Significantly, this can suppress the electron–hole recombination onto the surface and increase the lifetime of surface-reaching holes up to microseconds, thereby dramatically enhancing the water oxidation efficiency.

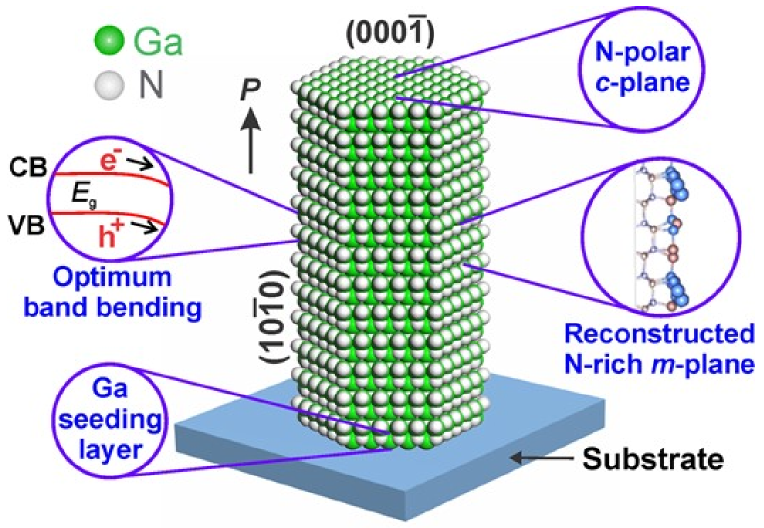

Figure 6-8: Model for single crystal wurtzite GaN nanowire with a polar, N-terminated (000$\bar{1}$) top surface and N-terminated (10$\bar{1}$0) and C_{6v}-symmetric side faces, obtained by removal of the surface Ga atoms which causes N–Ga bonds to be broken and to the re-orientation of the N bond orbitals [228]. P represents the direction of spontaneous polarization of the wurtzite crystal. The major contributing factors for the enhanced efficiency and stability are also highlighted. Adopted from *Adv. Mater.* **28**, 8388-8397 (2016).

Consequently, this improves the stability of the photocatalyst and the longevity of the artificial photosynthetic system, as - in the absence of Co_3O_4 co-catalyst nanoparticles, the inefficient accumulation of holes on the nanowire surfaces and the long-awaiting time for water adsorption, dissociation and subsequent oxidation can accelerate the decomposition of the material (via self-oxidation by photogenerated holes) under concentrated sunlight. The proximity of the nanowire photocatalysts, including the integrated nature of micro-/nano-electrodes (co-catalysts) greatly eliminates the problem of ionic diffusion for balanced water splitting reaction. Therefore, unlike PEC, these structurally-stable nanostructures can efficiently and consistently generate hydrogen from photocatalytic neutral pH water splitting, without any external bias and conductive electrolyte.

To summarize, the polarization field induced by the negative charge of N atoms on the surfaces, together with the optimally reduced surface band bending through Mg-dopant incorporation and faster water oxidation reaction enabled by Co_3O_4 loaded on nanowire surfaces, can overwhelmingly enhance the injection of photogenerated holes into the aqueous solution. The major contributing factors for a bare GaN nanowire are schematically summarized in Fig. 6-8. The H_2 production rate from overall pure water splitting is further enhanced through the synergistic and tandem effect of Co_3O_4 and Rh/Cr_2O_3 co-catalysts. The effective use of N-rich surface and GaN in enhancing the stability of semiconductor photoelectrodes has also recently been reported for *p*-$GaInP_2$ in NH_4NO_3 electrolyte [230] and for Ta_3N_5 in KPi solution [231], respectively.

The ability to easily and reproducibly fabricate wafer-scale industry-friendly engineered artificial photosynthesis devices of high performance and long-term stability can consequently lead to commercially viable large-scale clean hydrogen generation from unassisted solar-driven pure water splitting. For example, with ~2.7% efficiency and using concentrated irradiance of 27 suns, the system can potentially generate 7.14 mol h^{-1} (~160 L h^{-1} at STP) of H_2 gas per gram of photocatalyst, or most likely 11.42 mol h^{-1} (equivalent to 256 L h^{-1} at STP) of H_2 gas when a 1 m^2 module is employed. The research to further scale up the reported hydrogen generation system is currently in progress (see Chapter 9). Considering the average roof in the United States has access to usable sunlight for nearly

5.5 hours [232] per day, this artificial photosynthetic system herein can thus generate clean hydrogen under concentrated illumination for up to over 100 days so far and most likely much more as the efficiency did not drop when the stability test was concluded after 584 h. Significantly, the measurements were performed under concentrated sunlight (~27 suns), which is of utmost interest for economically viable industrial production of hydrogen using limited land area and employing minimum amount of photocatalyst [28, 116, 149]. This artificial photosynthetic system is also capable of direct hydrogen generation from harsh aqueous environment such as seawater. Moreover, its efficiency could be further optimized by synthesizing InGaN with higher indium incorporation (up to 50%). The band gap of as-obtained InGaN solid solution can be tuned to ~1.5 eV while straddling the redox potentials of water splitting under visible and near-infrared light irradiation (up to $\lambda = 1\ \mu m$)) [82].

6.6 Conclusion

We hereby demonstrated that, by combining the synergistic effect of OER and HER co-catalysts and by optimizing the surface electronic properties of the semiconductor, double-band GaN/InGaN nanowire-arrays grown on Si wafers can exhibit long-term stable operation (24 days) in unassisted pure water splitting with an STH efficiency of ~2.7% under concentrated sunlight. This work demonstrates the ability to fabricate industry-friendly artificial photosynthesis devices (GaN-based photocatalyst on Si wafers) of high performance and long-term stability for direct overall unassisted solar pure water splitting by utilizing atomically thin N-terminated surfaces, rather than the additional relatively thick surface protection/passivation layers [36, 233]. The future work, therefore, includes building a large-sale prototype of Ga(In)N nanowire based artificial photosynthesis system and demonstrate efficient and stable solar to hydrogen conversion via photocatalytic overall neutral pH water splitting.

Chapter-7

Optically Active Dilute-Antimonide III-Nitride Nanostructures for Solar Energy Harvesting

7.1 Introduction

With the exceptional structural and optical properties, III-nitride nanostructures (InGaN) have served so far as an amazing platform for realizing efficient and stable artificial photosynthesis system. This is because, Ga(In)N possesses ideal attributes for solar fuel generation through natural water splitting and CO_2 reduction, as illustrated in Fig. 1-2 and 1-5, and demonstrated in Chapter 4, 5 and 6. However, it has remained one of the Holy Grails of solar-fuel community for decades to achieve efficient and stable overall water splitting beyond blue solar spectrum (deep-visible). In addition to recent solar fuel application, the research and development of GaN-based materials, including InGaN quantum wells (QWs), has already led to high brightness blue light-emitting diodes (LEDs) [234-237]. It has remained challenging as well to achieve efficient light emitters operating in the deep visible spectral range till today, which are essentially required for phosphor-free and color tunable LED lighting. This challenge is directly related to the requirement of excessively high indium incorporation for narrow bandgap InGaN, fundamentally large lattice mismatch (~11%) between InN and GaN [238-240] and large strain-induced polarization field [241, 242]. These detrimental effects serve as serious bottlenecks towards realizing large scale practical applications of InGaN as an advanced photo catalyst for solar fuel. It is therefore extremely important to search for other elements which can serve the same purpose as indium, while preserving the advantages III-Nitride platform offers.

Alternatively, by introducing highly electronegative antimony in the host lattice, the bandgap of III-nitrides can be potentially tuned from the UV, through the deep visible, to the near- and mid-infrared wavelengths [243, 244]. The unprecedented and broader range tuning of III-nitride-antimonides' bandgap is schematically shown in Fig. 7-1, which opens new possibilities for photonic and optoelectronic devices operating in the visible and infrared wavelengths. To date, however, the epitaxial growth of dilute antimonide nitride semiconductors has remained largely unexplored, and little is known about their fundamental electronic and optical properties [245, 246]. Previously reported dilute antimonide nitride epilayers are either polycrystalline or amorphous [247-250]. There have been no theoretical studies on the electronic structure of $GaSb_xN_{1-x}$ for x in the range of 0-1% [251, 252]. Moreover, there exists a large discrepancy between the calculated bandgaps by first principles and experimentally observed ones [246, 248, 253]. Therefore, the successful development of superior quality dilute antimonide nitride heterostructures and nanostructures will provide a new quantum material platform with very promising application to high-efficiency, phosphor-free, and color tunable LEDs and lasers, and to solar energy conversion, including solar cells, solar fuels, and various electrochemical devices and systems.

7.2 Tuning the Bandgap of Dilute Antimonide GaSbN Nanostructures

We have investigated, both theoretically and experimentally, the fundamental characteristics of GaSbN in the dilute Sb limit (<1%). With the use of a new density functional theory (DFT) method based on Vienna ab-initio simulation package (VASP) [254-256], we have performed calculations on the electronic band gap and band structure of GaSbN, simultaneously capturing the $E_g(x)$ nonlinearity (for $0\% < x < 1\%$) using Heyd-Scuseria-Ernzerhof (HSE06) hybrid-functional without any empirical parameter [255]. Our calculations revealed that with ~1% Sb incorporation, an energy bandgap of ~2 eV can be reached, which is equivalent to the incorporation of more than 30% of indium in GaN. Experimentally, GaSbN nanowire heterostructures were grown by plasma-assisted molecular beam epitaxy (MBE) on Si substrate, which exhibited strong photoluminescence emission at room temperature. Moreover, the emission can be tuned from 3.4 eV to ~2 eV through controlled Sb incorporation. We have further demonstrated dilute-Sb nitride functional LEDs operating in the deep visible (green) wavelength. This work has shown the extraordinary potential of dilute Sb III-nitrides to emerge as a new quantum material platform for the development of high efficiency optoelectronic, photonic and solar energy devices.

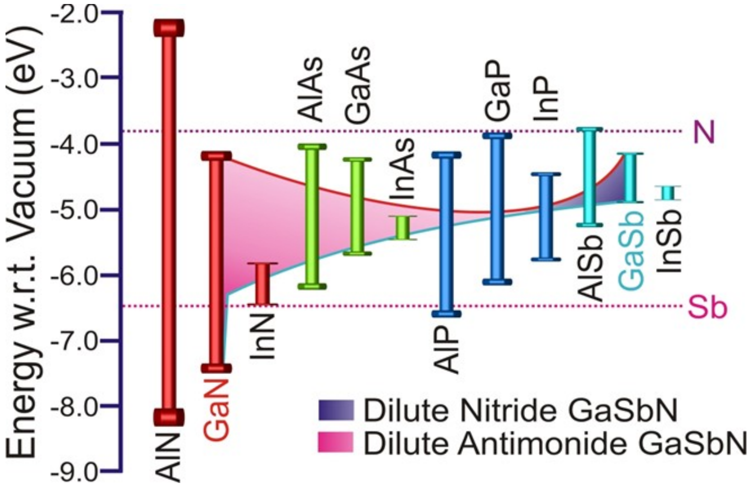

Figure 7-1: Sb and N impurity level with respect to the conduction and valence band of III-V semiconductors [257], depicting the bandgap energy calculated using BAC model [247] over whole composition range of GaSbN. The bandgap energy data for GaSbN were taken from *Appl. Phys. Lett.* **102**, 102104 (2013).

7.2.1 First Principles Calculation: Properties of Dilute-Sb GaSbN

We have first performed calculations on the electronic band gap and band structure of wurtzite GaSbN using a computationally efficient method by the Vienna ab-initio simulation package [254-256]. Bandgaps of 3.28 eV and 0.55 eV were calculated for GaN and GaSb, respectively, by employing HSE06 exchange-correlation (XC) functional with the mixing parameter $\alpha = 0.25$ and adopting a 7x7x5 k-point mesh including spin-orbit interaction. Special quasi random structure (SQS) calculation [258] was used rather than conventional coherent potential approximation (CPA), to accurately obtain Sb atom arrangement which takes into account the local strain effect in the lattice. Lattice relaxation was performed using PBESol XC functional implemented in VASP. Supercell sizes of 72, 144, 288, and 576 atoms were used to incorporate one Sb atom, which corresponds to Sb incorporations of 2.7, 1.35, 0.7 and 0.35% respectively. Figure 7-2a depicts a ball and stick model of $GaSb_xN_{1-x}$ supercell with x = 2.7% of Sb incorporation. The structure is optimized using DFT simulations, in which it can be clearly observed that - the replacement of a small and light nitrogen (N) atom by a larger and heavier antimony (Sb) atom can create strong perturbation among the nearest Ga atoms and the next-nearest N atoms in a unit cell. Energy bandgap calculation of GaSb$_x$N$_{1-x}$ versus x (shown in Fig. 7-2b, as solid blue dots) clearly captures the nonlinear curving part by our method, while simultaneously providing accurate results as the commercial software Viena Ab-initio Simulation Package (VASP) for larger value of x. The band gap variation is consistent with experiments to be described next, shown as red dots in Fig. 7-2b. The basis and the details about the first-principle calculations presented herein are described in publications elsewhere [254-256, 259].

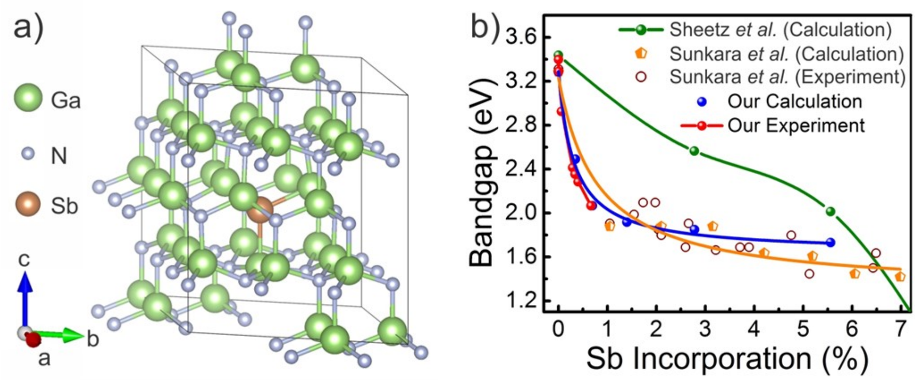

Figure 7-2: a) A ball and stick model of GaSb$_x$N$_{1-x}$ supercell with x = 2.7% of Sb incorporation, optimized using DFT simulations. The perturbation of Ga atoms near the Sb atom can clearly be observed in a unit cell. b) Energy Band gap of GaSbN vs. Sb concentration. There have been no studies, either theoretical or experimental, for GaSbN with Sb composition <1%. Our calculations herein (blue dots) demonstrate controllable tuning of the energy bandgap from 3.4 eV to 2eV in the dilute limit (<1%). Our experiments (red dots) also show excellent agreement with the theoretical calculation.

The fundamental requirement for any active photocatalyst to perform overall water splitting is that, the bandgap of the catalyst needs to properly straddle the redox potential of water molecules (nearly 1.23 eV, Fig. 1-2). With appropriate electrochemical overpotentials at both the valence and conduction band edges, the optimally required bandgap is ~2.0 eV, which can be achieved by InGaN with as high as ~40% of In-incorporation (post-growth). However, the conduction band of InGaN lowers faster than the upward shift of the valence band as a function of In composition (Fig. 1-5 and Fig. 7-3a). This puts further constraints on the usage of InGaN with high In-content (narrow-bandgap) for CO_2 reduction to hydrocarbon fuels and reduces the over-potential for proton reduction reaction in overall water splitting. Significantly, in direct contrast to the band edges of $In_xGa_{1-x}N$, the valence-band edge was found to raise rapidly with x of Sb in $GaSb_xN_{1-x}$ while the conduction-band edge lowers slowly, as shown Fig. 7-3a. Therefore, at Sb-incorporation in the dilute limit (<1%), GaSbN with reduced lattice mismatch and good crystal quality can be used to realize neutral water splitting, whereas higher Sb-content (>1%) may be suitable for acidic water splitting.

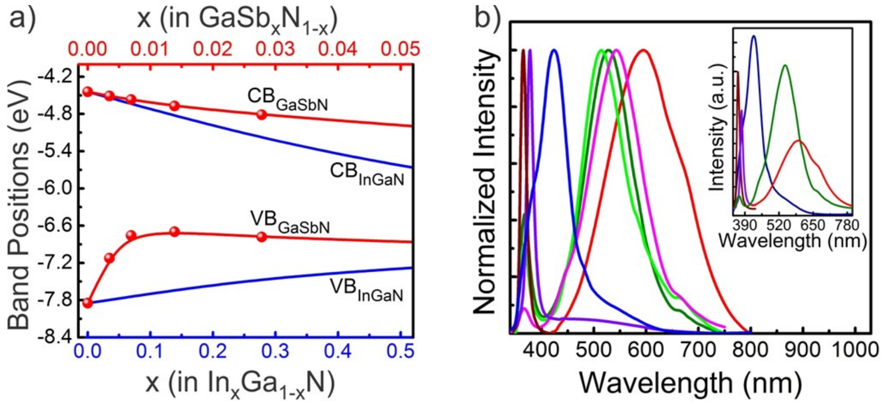

Figure 7-3: a) Conduction and valence band edge positions vs. Sb concentration. For comparison, the band edge positions of InGaN for In compositions up to 50% are also shown [82]. The bandgap energy data for InGaN were adapted from Appl. Phys. Lett. **96** (2), 021908 (2010). b) Normalized photoluminescence (PL) spectra measured at 300K for GaSbN with different Sb concentrations. The inset shows the relative constant emission intensity of GaSbN nanowire arrays.

7.2.2 Epitaxy of Dilute Antimonide GaSbN Heterostructures

Experimentally, we have investigated the growth of GaSbN nanowire heterostructures using a Veeco Gen-II MBE system equipped with a radio frequency plasma-assisted nitrogen source. The growth was performed on n-type Si (111) substrate without any external catalyst; instead Ga-seeding layer (~1 monolayer) was used for the nucleation of nanowires [168, 260, 261]. GaN-based heterostructures are generally grown at relatively high temperatures (>700 °C) [262-266]. However, controlled Sb incorporation at such elevated temperatures is challenging, due to the large Sb surface desorption and segregation. In this study, we have investigated the effect of growth rate, Ga/N flux ratio, and N/Sb flux ratio on both the incorporation of Sb as well as the material quality. By careful optimization of the growth parameters we have shown that with the use of plasma-assisted MBE, Sb can be controllably incorporated in GaN at intermediate growth temperatures. The growth parameters for GaSbN nanowires include substrate temperatures in the range of 650 to 705 °C, Ga beam equivalent pressure (BEP) of ~4×10^{-8} Torr, and Sb BEP in the range of ~5×10^{-10} Torr to ~1×10^{-7} Torr. The nitrogen plasma power is ~350 W and nitrogen flow rate is in the range of 0.3-0.5 sccm. Ge and Mg was used for n-type and p-type doping in the LED structures, respectively.

The scanning electron microscopy (SEM) image of GaSbN nanowires grown on Si substrate shows that the nanostructures are vertically aligned on the substrate and oriented along the *c*-axis. Photoluminescence measurement was performed with a 325 nm He-Cd laser as the excitation source. Shown in Fig. 7-3b are the photoluminescence spectra of GaSbN obtained with different Sb concentrations into GaN. The Sb concentrations were varied in the range of 0% to 0.66%, which was derived based on the secondary ion mass spectroscopy (SIMS) measurements performed on GaSbN film structures grown under similar conditions. A consistent redshift with increasing Sb composition is measured. To the best of our knowledge, this is the first demonstration of room-temperature photoluminescence from any dilute antimonide nitride materials [246]. This is also the first experimental demonstration of bandgap tuning (from 3.4 eV to 2.0 eV) within the extremely dilute antimonide regime (Sb concentration <1%). The estimated bandgap for different Sb incorporation is in excellent agreement with the theoretical calculation, illustrated in Fig. 7-2b. By further varying the epitaxy conditions, emission in the deep visible spectral range can also be achieved.

7.3 Structural and Optical Properties of GaSbN

For further characterization of the material properties four samples with different Sb compositions, from both the nanowire and film growths, were subsequently studied. The samples with high Sb incorporation are labeled with ‘H’ ($E_{g\,(\text{NW-H})} \sim 2.03$ eV, $E_{g\,(\text{film-H})} \sim 2.27$ eV), whereas low Sb samples are labeled with ‘L’ ($E_{g\,(\text{NW-L})} \sim 2.34$ eV, $E_{g\,(\text{film-L})} \sim 2.90$ eV). The Sb BEP for the high and low Sb samples are 3×10^{-8} and 5×10^{-9} Torr, respectively. As predicted in the first principle calculation, anomalous expansion in unit cell size was observed for the alloy bandgap reduction which can be correlated with the measured structural and optical response of GaSbN. For example, to assess the structural quality of the alloy, XRD measurements were performed on both the nanowire and film samples using a Bruker D8 Advanced Diffractometer with Cu Kα (radiation λ= 1.5418 Å). These data reveal the typical (002) and (004) peaks observed in GaN wurtzite structure (not shown), confirming the wurtzite crystalline nature of the GaSbN grown along the c-axis. Depicted in Fig. 7-4a, for higher Sb incorporation, the narrower (002) peak for GaSbN nanowires (FWHM ~ 857 arcsec) shows better crystalline quality than that of GaSbN film with a broader (002) peak (FWHM ~ 1253 arcsec). This can be attributed to the ability for accommodating strain-relaxed growth in one-dimensional (1D) GaSbN nanowires. The lattice constants of the samples with high and low Sb compositions, extracted from their XRD pattern are 5.1945 (H) and 5.1897 Å (L) for the films, and 5.1903 (H) and 5.1866 Å (L) for the nanowires, respectively. The lattice mismatch (*f*) of the GaSbN film ($E_{g\text{ (film-H)}}$ ~ 2.27 eV) in comparison to GaN agrees well with that of our theoretical estimation for 0.4% Sb incorporation (*f* ~ 0.178%). However, the lattice mismatch was reduced significantly in GaSbN nanowire structure ($E_{g\text{ (NW-H)}}$ ~ 2.03 eV, *f* ~ 0.085%) even for a smaller bandgap value, due to efficient lateral stress relaxation.

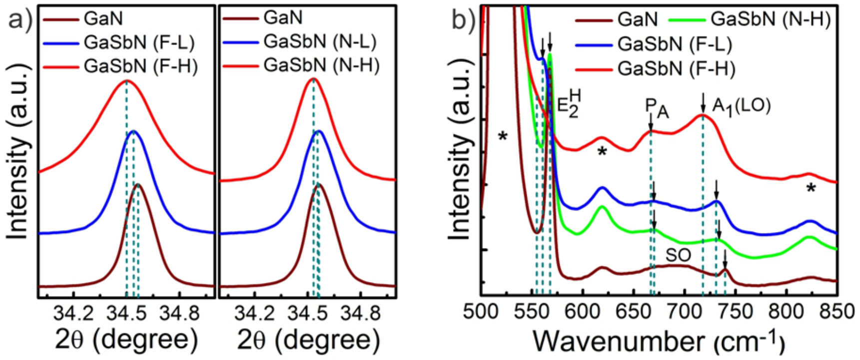

Figure 7-4: a) The prominent reflections of 002 in the XRD pattern for GaSbN films (left) and nanowires (right) compared to that for GaN. 'L' and 'H' refers to GaSbN samples with low and high Sb incorporation, as described in the text, respectively. b) Typical micro-Raman spectra of GaSbN films and nanowire vs Sb composition. Raman modes of GaN are also presented as reference. Contributions from Si substrate are marked with '*'.

The observation can further be correlated with the room-temperature micro-Raman spectroscopy analysis of the samples. The micro-Raman measurements were carried out with a 514 nm argon ion laser through a 50× objective. The focused laser spot size was ∼1 μm and the estimated power on the sample was ∼7 mW. In this study, all Raman spectra were taken in the backscattering geometry with the incident laser parallel to the hexagonal *c*-axis ([0001] direction) of the nanowires. Figure. 7-4b reveals the decoupling phenomenon of A_1(LO) phonon mode from the longitudinal optical phonon-plasmon coupled (LOPC) mode, present at 740 cm^{-1} in non-doped GaN [153]. The A_1(LO) phonon mode shifts consistently to lower frequency at increased Sb content with noticeable peak broadening. The additional peak (P_A), appeared at 670 cm^{-1} for low Sb incorporation sample and shifts to lower frequency (667 cm^{-1}) with higher intensity as the Sb content increases in the host lattice, which can be ascribed to Sb-induced local vibrational mode (LVM). This is consistent with the previous report [246] where the additional peak and corresponding shift was observed near 650 cm^{-1} for higher Sb incorporation (~1-4%). E_2^H mode in GaSbN film is also largely affected due to Sb incorporation, and the peak shifts significantly to lower frequency with increased FWHM for higher Sb composition. This peak broadening and shift is due to biaxial strain in the *c*-plane, induced by the disorder in atomic arrangement, which is also instructive of reduced crystalline quality [153]. However, the Raman scattering modes in GaSbN nanowire structures are affected only slightly due to the efficient lateral surface strain relaxation and provides better crystalline quality (narrower E_2^H peak) even at comparatively higher Sb incorporation, which can also be correlated with the lattice constants measured from XRD analysis in Fig. 7-4a. We also observed that post-growth annealing enhanced the optical properties of GaSbN nanowires.

7.4 Quantum Interaction of Sb: Impact on Optical activity of GaSbN

The level of quantum confinement that can be achieved in GaSbN/GaN QDs in the dilute regime (<1% Sb) is comparable to InGaN/GaN QDs with ~30% In composition, however, with reduced mismatch between GaSbN and GaN. Despite numerous success in bandgap tuning of GaSbN for wide Sb-compositional range, no tunable PL and EL emission was achieved [246] till today. Cathodo-luminescence (CL) and the room temperature PL emission at ~2.2 eV was reported so far for a single composition [253, 267], which coincides with the defect related 'yellow band' in GaN. Therefore, this study demonstrates the first realization of crystalline GaSbN/GaN dot-in-wire heterostructures with tunable PL emission at room temperature. Our preliminary first principle study shows that Sb incorporation into GaN creates a strong quantum-interaction between the Sb-impurity and the host GaN atoms, as depicted in Fig. 7-5a as the 3D charge density plot. Considering no structural relaxation, the N-*p*, Ga-*p* and Ga-*d* orbitals of the host valence states are strongly perturbed along with Sb-*p* orbital. Owing to larger radius and electro-negativity, Sb incorporation leads to - strong interaction and overlap between Sb-orbital and that of the nearest Ga-neighbors and next nearest N-neighbors to form extended valence states (Fig. 7-5b), and therefore, room-temperature optical activity of the nanostructures [268]. Post-growth annealing of the GaSbN nanostructures in Ar environment and above the growth temperature leads to further improvement in optical and structural properties.

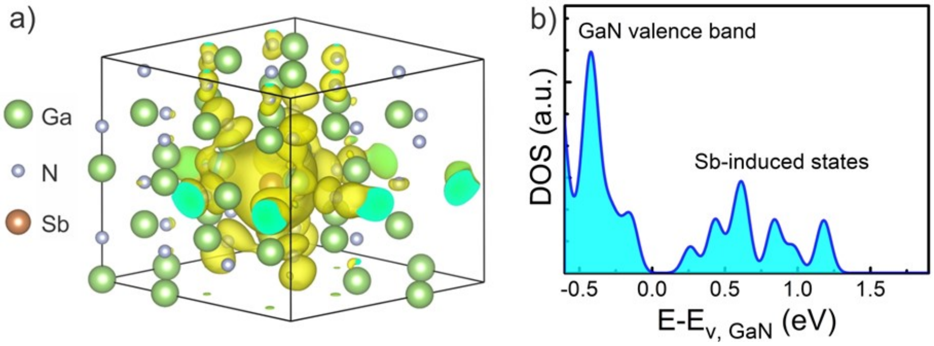

Figure 7-5: a) The charge density of states (DOS) induced due to a single Sb incorporation into GaN at x = 2.7%. b) Projected DOS of GaSb$_x$N$_{1-x}$ at the valence band side of the Fermi level, showing total DOS normalized to a single Sb atom incorporation at x = 1.4%. The band edge of GaN, E$_{v,GaN}$, is used as a reference.

The microscopic origin of the strong band-bowing in GaSbN was investigated from the ab initio point of view by calculating the density of states (DOS) of the material [259]. And the character of the impurity states can be identified from the interactions between individual atoms and their contributions to the total projected density of states. Sb atoms only contribute to the valence band (VB) of GaSb$_x$N$_{1-x}$ while having very little influence on the conduction band (CB) of the host GaN. The *p*-orbital of N and *p, d*-orbital of Ga are found to dominate at the VB edge of GaN. However, the major contributions to the extended valance band of GaSbN come from the *p*-orbital of Sb and N, as well as the *p, d*-orbital of Ga, which further reveals the strong interaction between the impurity and host atoms. It is however, surprising that the *p*-orbital of N contributes most in the extended valence states despite being the next-nearest neighbor of Sb impurity, compared to the nearest Ga neighbor. This is further supported by the real space projected charge density of the impurity states in Fig. 7-5a, which is attributed to the larger radius and strong quantum interaction of Sb atom. The effective DOS of the extended valence states are comparable to that of the GaN VB, as shown in Fig. 7-5b.

7.5 Effect of Nitrogen-modulation on Sb-incorporation in GaSbN

Both spontaneous and nitrogen-modulated GaSbN QDs were attempted to achieve enhanced Sb composition while paying close attention to structural and optical properties of the nanostructure. In nitrogen-modulated QDs, the nitrogen shutter was turned off for different duty-cycles to increase Sb content and the growth was carried on using the available nitrogen species inside the chamber. The *in situ* annealing facilitates intermixing of N-rich and N-deficient thin GaSbN layers [243], eventually leading to higher Sb incorporation, which can be evaluated by the red shift observed in PL peak energy and enhanced PL intensity (Fig. 7-6a). The XRD patterns of GaSbN/GaN QDs reveal slightly broadened and shifted (002) and (004) peaks compared to crystalline GaN nanostructures. The lattice mismatch along the *c*-axis for N-modulated QDs (derived from the patterns) are comparable to that of spontaneously grown QDs, which can be correlated to strain relaxation along the radial direction during epitaxy and annealing process.

Raman modes of GaSbN QDs in *p-i-n* GaN nanowires can be deconvolved into the weaker response from thin GaSbN layer, and the stronger response from Mg-doped p-GaN. The spectra contains typically dominated Mg related local vibrational modes (Mg-LVMs) [269] at 656 cm^{-1}, and the nominal GaN modes [153, 270] such as A_1(LO), E_2^H and E_2^L at 735, 567 and 144 cm^{-1} respectively. However, as shown in Fig. 7-6b, due to the strong confinement along *c*-axis, A_1(LO) mode intensity from GaSbN QDs was enhanced noticeably and shifted to lower frequency for higher Sb content (715 and 710 cm^{-1} for spontaneous and N-modulated QDs, respectively). Sb-LVM mode (P_A) was dominated by Mg-LVM (656 cm^{-1}) either due to its low intensity response from very thin GaSbN layer and/or shift towards low frequency due to higher Sb incorporation [246, 268]. In accordance with our Raman measurement on GaSbN nanowires, E_2^H and E_2^L mode shows similar shift (565.5 cm^{-1} and 148 cm^{-1}, respectively) for N-modulated GaSbN QDs, however, with higher intensity [271, 272].

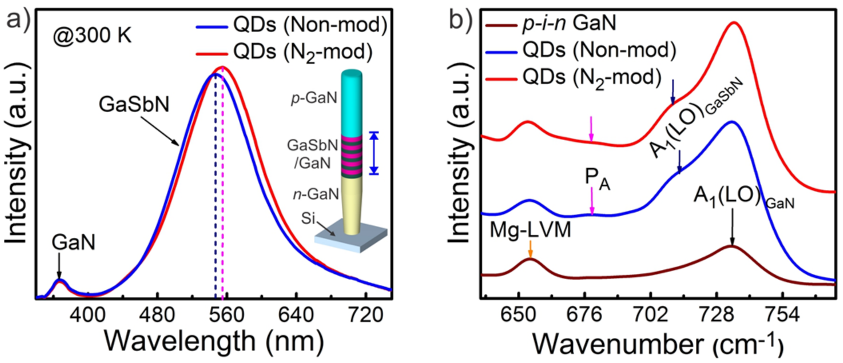

Figure 7-6: a) Room temperature PL spectra measured from GaSbN QDs, where nitrogen modulation during the epitaxy increases Sb content in the dots, leading to red-shift in PL emission. The inset shows the GaSbN/GaN quantum dots (QDs) in GaN nanowire heterostructure. b) Micro-Raman spectra of GaSbN QDs in active region of *p-i-n* GaN, showing strong intensity and shift of A_1(LO) mode due to strong confinement along c-axis.

7.6 Archetype of GaSbN Optoelectronic Device: Light Emitting Diode

We have further investigated the MBE growth of GaSbN/GaN dot-in-nanowire LED heterostructures. Strong quantum confinement can be achieved in GaSbN/GaN quantum wells/dots with Sb concentration <1% in the active region, based on the theoretical and experimental results described above. Moreover, the degree of quantum confinement and the emission wavelengths can be varied through controlled Sb incorporation. Shown in Fig. 7-7 is the schematic of GaSbN nanowire LED structure grown and processed on Si substrate. Five GaSbN (3nm)/GaN (3nm) quantum dots were incorporated along the growth direction in the active region in a manner similar to previously reported InGaN/GaN dot-in-nanowire LED structures [154, 273]. The quantum dot active region was grown at relatively low substrate temperature of ~650 °C. Other growth conditions are like those described for the GaSbN nanowire structures. n^{++}-GaN/Al/p^{++}-GaN tunnel junction (TJ) were incorporated into the LED structure (inset, Fig. 3a). The detailed study on the tunnel junction growth for optimized LED performance as well as the device fabrication process can be found elsewhere [274]. The scanning electron microscope (SEM) image reveals the growth of vertically aligned GaSbN dot-in-nanowire arrays with relatively high uniformity and areal density (bottom-right inset, Fig. 7-7).

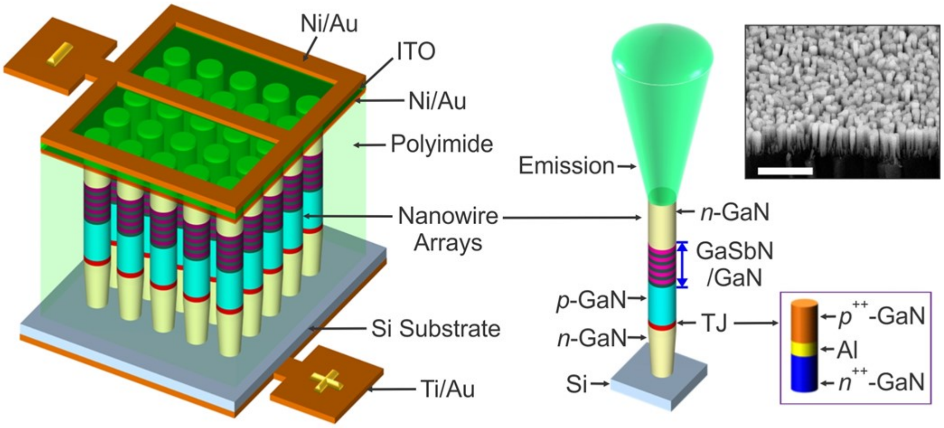

Figure 7-7: a) Schematic representation of GaSbN/GaN dot-in-wire tunnel junction (TJ) light emitting diode (LED) structure. Schematic view of different layers incorporated in the nanowire arrays of GaSbN LED is also presented. The inset on the top-right shows 45° tilted SEM image of as-grown GaSbN dot-in-nanowire arrays. Scale bar 1 μm. The schematic of the TJ is also illustrated in the inset (bottom-right) [274].

Current-voltage characteristics of the nanowire LEDs were measured at room-temperature under continuous wave biasing conditions. The devices (areal dimension of 500 μm × 500 μm) show clear rectifying characteristics. The electroluminescence (EL) intensity increases linearly with injection current up to 140 mA and gradually saturates with further increasing current, which can be attributed to electron overflow and heating effect. EL spectrum of GaSbN-TJ LED, measured from 10 mA to 200 mA of injection current, shows highly stable emission characteristics with negligible shift in the peak position, suggesting efficient and uniform carrier injection in the quantum dot active region. However, the nanowire LEDs exhibit relatively low output power (in the range of μW to sub-mW), which has been primarily limited by the light absorption of the underlying Si substrate and the large nonradiative surface recombination of nanowires. Recently, with the use of core-shell structures, it was demonstrated that the output of nanowire LEDs can be enhanced by nearly two orders of magnitude [275-278]. The details of the device characteristics, relative EQE and EL intensity as a function of injection current are not within the scope of this dissertation and can be found in our recent publication [268].

7.7 Preliminary Investigations on GaSbN as a Photocatalyst

III-Nitride nanostructure, especially InGaN offers the tremendous flexibility of bandgap tuning vs In-composition. However, as discussed before, the growth-related challenges with high In-content are yet to overcome. From recent first-principles calculations, it was evidenced that the substitutional doping of Ga(In)N by Sb can emerge to be a suitable platform for efficient photocatalyst. No dissociation of the structures was found on the thermal-stability check using *ab initio* molecular dynamics (MD) simulations, indicating that the proposed alloys are thermally stable [245]. Our primary investigations on dilute-Sb (~0.4%) GaSbN nanowire heterostructures (on Si wafer) reveal that the non-doped GaSbN demonstrates photoanodic behavior, as shown in Fig. 7-8a. This can further be correlated to the XPS measurements that the as-grown GaSbN nanostructures are intrinsically n-type (not shown here).

However, the p-type GaSbN epilayers (with different Mg-concentration) grown on n^+-p Si solar cell (SC) demonstrates strong photocathodic behavior in 1.0 M HBr solution (Fig. 7-8b), when loaded with Pt-cocatalyst nanoparticles. The n^+-p Si solar cell wafer was prepared by thermal diffusion process. The sample A_1 and A_2 grown with Mg cell temperature (T_{Mg}) around 250-270 °C shows lower onset and higher photocurrent density. These monolithically integrated photocathodes, when loaded with Pt co-catalyst nanoparticles, exhibit an applied bias photon-to-current efficiency (ABPE) of 11.5% and 9.5% respectively, at a potential of 0.31 V versus normal hydrogen electrode (Fig. 7-8c). The demonstrated efficiency is higher than the maximum efficiency of recently reported GaN/InGaN nanowires with integrated tunnel junction (~8.7% at 0.33 V) [279]. With optimum Mg-doping and co-catalyst loading and integrating GaSbN/InGaSbN nanowires on top of the device, the efficiency can be enhanced further. The integrated GaSbN/Si photocathode can exhibit a relatively prominent level of stability at a bias close to the equivalent HER potential, and the current remains nearly constant and no significant degradation was measured for the duration of 20 h (not shown here).

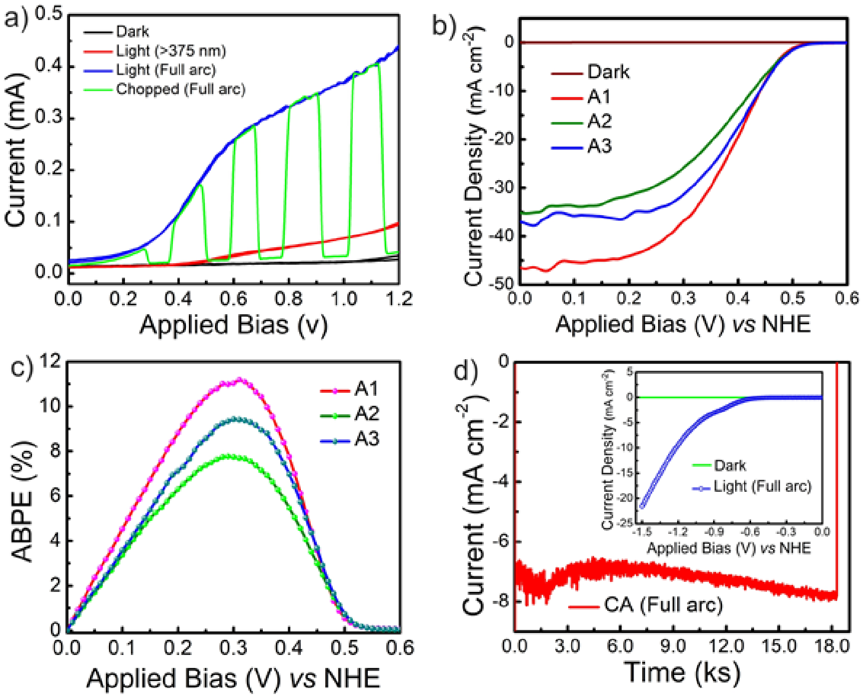

Figure 7-8: a) LSV curve obtained from non-doped GaSbN nanostructure grown on GaN template (on Si substrate). b) LSV curve obtained from p-GaSbN epilayers grown with different Mg-doping concentrations on n^+-p Si solar SC. The sample was immersed in 1.0 M HBr under 1 sun excitation. c) Applied bias photon-to-current efficiency (ABPE) calculated from the corresponding J-V curves of GaSbN epilayers on Si SC. d) The chronoamperometry (CA) measurement from photoelectrochemical (PEC) CO_2 reduction to hydrocarbon fuels at -1.2V, using the sample A_1. The CA and the LSV scans are shown in the inset.

The best dilute-Sb GaSbN photocathode sample was further explored for the photoelectrochemical reduction of CO_2 into hydrocarbon fuels using 0.5 M $KHCO_3$ electrolyte. As revealed by the first-principle calculation described in Section 7.2, the conduction band edge of dilute antimonide nitrides lower only slightly even for the narrow-bandgap material; and hence low-energy photon-excited electrons can still possess sufficient over-potentials necessary for proton and CO_2 reduction reaction [280], as schematically shown in Fig. 1-2. The Faradaic efficiencies for CH_4 and CO generation in the Cu-cocatalyst loaded GaSbN/n^+-p Si cathode were measured after ~19 ks chronoamperometric measurements at a potential from −1.2 V vs Ag/AgCl (shown in Fig.

7-8d). At −1.2 V, the Faradaic efficiency of CH_4 production is about ~5.9 %, which is more than 3 times higher than that of CO generation (1.9 %). The measured Faradaic efficiency of CH_4 production is also higher than recently reported values on Cu-cocatlayst loaded GaN nanowires on Si SC (~4% and ~0.7% for CH_4 and CO, respectively, at -1.2 V) under similar experimental condition [281]. Surprisingly, the Faradaic efficiency of the $2e^-$ reduced CO shows is lower than that of the $8e^-$ reduced CH_4 at -1.2 V bias and can increase further at more negative applied bias, which can partially be attributed to the larger over-potential available for CO_2 reduction to CH_4. It is also important to mention that CO is consumed, and H_2 is also produced during the entire process. The enhanced performance can be attributed to the visible light absorption by GaSbN, while possessing large negative potential for the conduction band-edge due to the negligible fluctuation of the conduction band-edge at the dilute-Sb limit. The performance can be enhanced further by integrating GaSbN/InGaSbN nanowire heterostructures with larger surface-to-volume ratio. However, the primary investigations herein show enormous potentials for the dilute-antimonide III-nitride heterostructures to emerge as a platform for efficient and stable photocatalyst.

7.8 Conclusion

In summary, we have successfully realized optically active dilute antimonide III-nitride nanostructures and demonstrated a viable approach of rationally tailoring the bandgap of dilute antimonide GaSbN for visible light emission at room temperature. The structural and optical properties of the material were analyzed and complemented by the first principle calculation and theoretical studies. Subsequently, we have implemented GaSbN dot-in-nanowire visible LED device as an archetype. Simultaneous and controlled incorporation of In and Sb in GaN will provide further flexibility in tuning both the conduction and valence band edge of GaN and tune the bandgap towards near-infrared regime. This work here provides new insights into the epitaxy and properties of dilute-antimonide III-nitride heterostructures and nanostructures and will have a profound impact on the development of high-efficiency, phosphor-free LEDs and a broad impact on solar energy conversion, including solar cells, solar fuels, and various electrochemical devices and systems.

Chapter-8

Synergetic Effect of In and Sb Incorporation into GaN Nanostructures in Dilute-Sb Regime

8.1 Introduction

Dilute antimonide III-nitride semiconductors, e.g., Ga(In)SbN, exhibit remarkable properties. As discussed in Chapter 7, the incorporation of a very small amount (~1%) of antimony (Sb) in GaN can reduce its energy bandgap from 3.4 eV to ~2 eV [268], which is equivalent to the incorporation of more than 30% indium in GaN, thereby providing distinct opportunities for bandgap, strain, and polarization engineering to achieve efficient light emitters and photovoltaic devices. Moreover, InGaSbN is the only known semiconductor whose conduction and valence band edges can potentially straddle water redox potentials under deep visible and near-infrared light irradiation, which is essentially required for the efficient generation of solar fuels through water splitting and CO_2 reduction.

The reduction of energy bandgap of GaN with Sb incorporation is primarily due to the upward shift of the valence band edge, which is in direct contrast to the downward shift the conduction band edge by alloying with In [82, 282]. A precise tuning of the energy bandgap, as well as the energy band edge positions can, therefore, be achieved by independently varying In and Sb compositions, which provides unique opportunities to construct quantum-confined heterostructures with type-I, type-II, or even type-III band alignments. A semiconductor with tunable energy bandgap and band edge positions is also ideally suited for photochemistry and electrochemistry studies. So far, our studies have shown that III-nitride semiconductors exhibit distinct photocatalytic properties: their nonpolar surfaces can spontaneously adsorb and deform water and CO_2 molecules [199, 280], and their surfaces can be made nitrogen-rich to protect against photo-oxidation and corrosion in harsh photocatalytic conditions [220]. By tuning the surface Fermi-level of GaN nanowires, we have demonstrated that the quantum efficiency for proton reduction can be enhanced by nearly two orders of magnitude [99, 169].

Dilute-antimonide InGaSbN can play very promising roles in realizing the narrow bandgap III-nitride photocatalysts for visible-light driven artificial photosynthesis. Previous studies suggested that Sb incorporation could help overcome the issues related to phase segregation [283] in quinary alloys (GaInNAsSb), enhance In incorporation [284], and significantly improve optical quality [285, 286]. To date, however, there have been no theoretical nor experimental reports on the epitaxy and properties of InGaSbN and related heterostructures and nanostructures. It is therefore, unclear whether Sb can possibly play the role as a surfactant [287], a constituent [285, 288] or both [283] and enhance the structural, electronic, and optical properties of InGaSbN alloys. In this chapter, we report our preliminary investigations on the role of Sb in tuning the optical bandgap of InGaN with reduced lattice mismatch.

8.2 Selective Tuning of the Bandgap and the Band-edges in Ga(In, Sb)N

It is expected that, with the incorporation of a small amount of Sb (up to 1-2%) in InGaN, *i.e.* through simultaneous incorporation of In and Sb (dilute) into GaN, the energy bandgap can be drastically reduced to the deep visible and near-infrared spectral range while maintaining a relatively small lattice mismatch to the underlying GaN template/substrate. From the first principles calculation, as shown in Fig. 8-1a, the energy bandgap of GaSbN shows large bowing at the dilute-Sb regime (<1%) due to drastic upward shift of the valence band edge, whereas the conduction band-edge is largely unaffected. On the other hand, the band-edges of InGaN gradually shifts to lower bandgap energy positions. The valence band of InGaN possesses enough over-potential to drive water oxidation reaction forward for the entire range of In composition (100%, InN). However, the electrons in the conduction band cannot reduce protons due to insufficient over-potential, at In compositions as high as ~40% (Fig. 1-5), which also introduce the issues like phase separation and the degradation in crystalline quality etc. The quaternary

InGaSbN can take the advantages of controllable band-edge tuning to realize narrow-bandgap semiconductor photocatalyst (Fig. 8-1b) while providing necessary over-potentials for both the half reactions in unassisted overall neutral pH water splitting.

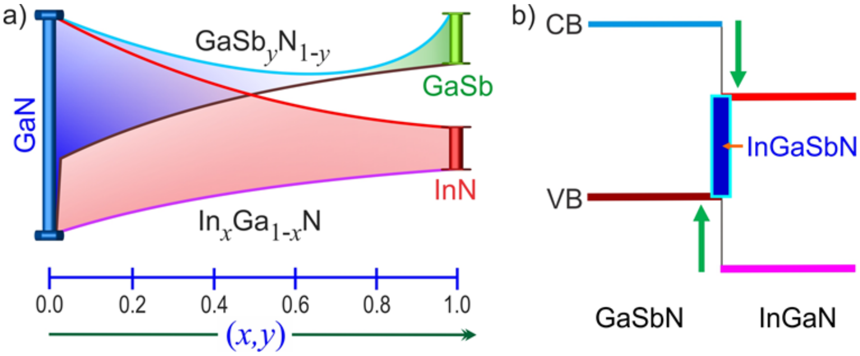

Figure 8-1: a) The bandgap energy of GaSbN calculated using BAC model [247], and that of InGaN over the whole composition range of Sb and In incorporation, respectively. The bandgap energy data for GaSbN were taken from *Appl. Phys. Lett.* **102**, 102104 (2013). The bandgap energy data for InGaN were adapted from *Appl. Phys. Lett*. **96** (2), 021908 (2010). b) Schematic illustration of tuning the GaN band-edge positions by simultaneous incorporation of In and Sb into narrow bandgap InGaSbN.

To date, however, it has remained unknown if *crystalline* dilute antimonide InGaSbN semiconductor nanostructures can be epitaxially grown and synthesized. Plasma-assisted MBE offers several advantages for the growth/synthesis of these complex structures, due to the relatively low growth temperature, precise control of antimony and nitrogen flux independent of the growth temperature, negligible background impurity incorporation, and formation of abrupt hetero-interfaces. In this task, we investigate the epitaxial growth of dilute antimonide nitride heterostructures, such as GaInSbN QWs and QDs on GaN template, and InGaSbN epilayers on silicon substrate by plasma-assisted MBE. Various growth parameters, including growth temperature, Sb flux, In/Ga flux ratio, and Ga/N flux ratio were tuned and optimized to achieve optically active InGaSbN.

8.3 Optical Activity of Ga(In, Sb)N

Optically active InGaSbN segments were incorporated into the active region of p-i-n GaN nanowires. The growth mechanism and parameters are similar as described in section

7.2.2 and the structure of the nanowire is like the depiction of GaSbN/GaN (3nm/3nm) dot-in-wire nanostructure in the inset of Fig. 7-6a. Additionally, the incorporation of large InGaSbN segments (30-40 nm) into GaN were also explored. Both the nanostructures show significant shift in optical emission wavelength compared to the InGaN/GaN nanowire heterostructure, grown without Sb under similar conditions. This can be correlated to the bandgap reduction due to the alloying effect of Sb in the dilute limit.

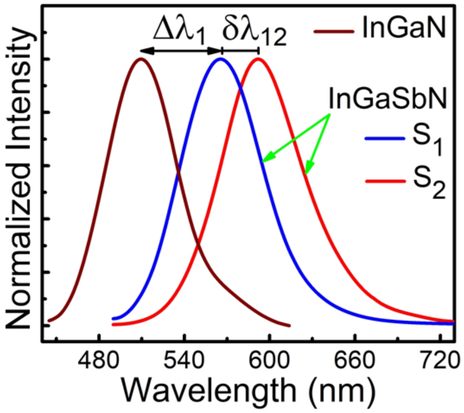

Figure 8-2: Room-temperature photoluminescence spectra of InGaN and InGaSbN, showing the tuning of optical bandgap by varying In and Sb compositions. Δλ denotes the change in emission wavelength due to the change in Sb composition, whereas δλ denotes that for the change in In composition.

We have demonstrated earlier that the optical emission from GaN nanostructures can be tuned from 364 nm to 545 nm [268] with as low as ~0.5% of Sb incorporation and significantly reduced lattice mismatch with the GaN nanowire template. Conventionally, this would otherwise require large amount of In incorporation into the nanostructures. For example, as shown in Fig. 8-2, the optical emission at 510 nm wavelength (bandgap, E_g ~2.43 eV) can be achieved with x ~20.3% into $In_xGa_{1-x}N$. However, assuming the In incorporation does not fluctuate significantly in the presence of dilute-Sb flux under similar growth conditions, the emission wavelength can be extended to ~565 nm (E_g ~2.195 eV), as shown in Fig. 8-2 (sample S_1), with x ~20.3% and y ~0.3% into quaternary $(In_xGa_{1-x})(Sb_yN1_{-y})$. To achieve optical emission at such wavelength would necessitate ~26.4% of In into standalone InGaN. Therefore, a shift of emission wavelength, Δλ ~55 nm can be achieved with the sole contribution of only ~0.3% Sb incorporation into InGaN, compared to that of additional ~6.1% indium. By superimposing these two compositions, *i.e.* with x ~26.5% and y ~0.3%, the bandgap of $(In_xGa_{1-x})(Sb_yN1_{-y})$ can be reduced further to ~2.09 eV (λ ~592 nm) which, again, would require ~31.5% of In into InGaN. Hence, considering the discussion above, it can be said that the additional ~6.2% indium contributes to the wavelength shift of δλ ~27 nm in sample S_2, however, with the inherent assumption that the increased In-flux does not alter the Sb incorporation under similar growth conditions.

8.4 Projected Density of States and Band-alignments of Ga(In, Sb)N

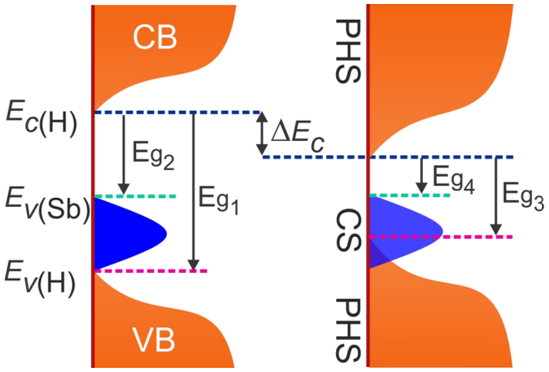

Figure 8-3: Schematic depiction of the projected density of states (DOS) in GaSbN (left) and InGaSbN (right), assuming similar Sb incorporation. Herein, PHS stands for the perturbed host states, and CS denotes the cluster states. The change in conduction band minima (ΔE_C) is, therefore, mostly due to In incorporation.

There had been no studies, neither theoretical nor experimental, on the electronic band structure of quaternary InGaSbN alloys. In section 7.4, we have discussed from the first-principle calculations on ternary GaSbN that the incorporation of Sb creates extended valence states within the bandgap of host material GaN. Consequently, the bandgap of the ternary alloy can be reduced from E_{g1} to E_{g2} due the presence of Sb-induced valence states ($E_{v(Sb)}$), schematically shown in Fig. 8-3, assuming the conduction band of the host ($E_{c(H)}$) is not affected significantly due to Sb interactions with GaN atoms in the dilute-Sb regime (<1%). Therefore, the behavior of quaternary InGaSbN alloy can be estimated as the superposition of the dominant factors in InGaN and GaSbN. For example, In-incorporation into GaN alters both the CB and VB (largely affects the CB) due to the strong perturbation of the host states (PHS), reducing the bandgap of ternary InGaN to E_{g3}. In addition, very small amount of Sb-incorporation into InGaN will further shift the valence-band due to Sb induced extended cluster states (CS), resulting in the narrow-bandgap (E_{g4}) for the quaternary InGaSbN. Hence, assuming the same Sb concentration, bandgap difference between GaSbN (E_{g2}) and InGaSbN (E_{g4}) will be primarily determined by the difference in the conduction-band edges (ΔE_c), as depicted in Fig. 8-3.

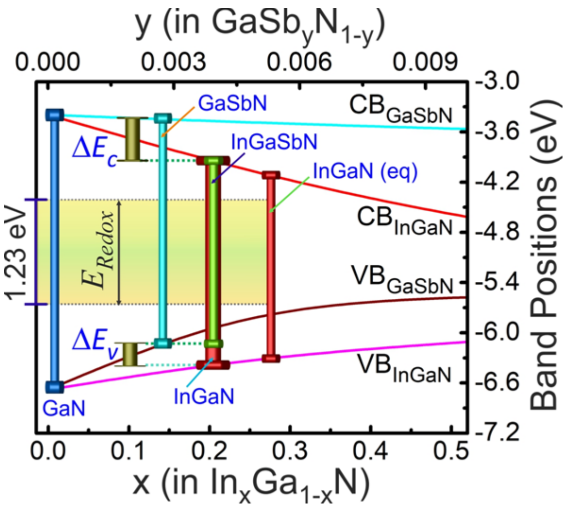

Figure 8-4: Schematic depiction of the bandgap tuning by In and Sb incorporation, and estimation of the composition and band-edge positions of the quaternary InGaSbN by superimposing the quantitative data of ternary InGaN and GaSbN. E_{Redox} denotes the redox potential of water.

Graphically, the tentative compositions of In and Sb into InGaSbN can be estimated from the PL emission wavelengths of InGaN and InGaSbN grown under similar conditions, together with the band-edge positions of InGaN and GaSbN. Considering the compositions of the optically active InGaN and InGaSbN (x ~20.3% and y ~0.3% for sample S_1), as discussed in section 8.3 (and in Fig. 8-3), the band-alignment of the ternary and quaternary semiconductors are presented graphically in Fig. 8-4 along with the redox potentials of water. The quantity ΔE_c can be correlated to that depicted in Fig. 8-3, whereas ΔE_v quantitatively represents the bandgap difference E_{g3}-E_{g4}. From the illustration, it is evident that the band-edges and the over-potentials for water splitting can be more controllably tuned using InGaSbN nanostructures for any bandgap, compared to that of their InGaN equivalents. Therefore, combining the unique properties of both Sb and In doping, the energy bandgap of dilute antimonide nitrides, *e.g.,* $(In_xGa_{1-x})(Sb_yN_{1-y})$, can be tuned to straddle the water redox potentials over a large portion of the solar spectrum, including ultraviolet, deep visible, and even possibly near-infrared with a relatively small amount of Sb (up to ~0.5%) and In (up to ~25%) incorporation. However, the investigation on the electronic and structural properties of InGaSbN quaternary alloys from an *ab initio* point of view, and study of both the band gap and band alignment vs. In and Sb concentrations is necessary to further confirm the superimposition hypothesis. These studies will be essential to determine the optimized In and Sb incorporation for both LED and water splitting applications.

8.5 Structural Properties and Crystalline Quality of Ga(In, Sb)N

Plasma-assisted MBE facilitates the synthesis of highly crystalline dilute-Sb III-nitride heterostructures with hyper-abrupt hetero-interfaces. Shown in Fig. 8-5a is the scanning transmission electron microscopy secondary-electron (STEM-SE) image of a GaN nanowire, containing a ~30-40 nm thick InGaSbN segment incorporated into it. Energy dispersive X-ray scanning (EDXS) further confirms the In composition of the segment. However, due to the dilute concentration of Sb, the elemental mapping or spectral line/point scan does not show any noticeable modulation for Sb-signal. Although Sb-signal can be detected from GaSbN segment by collecting the spectral data from a large-area scan, no detectable Sb-peak in EDX scanning was observed from InGaSbN segment due to it's small emission (K-line), and its convolution with the strong In emission (L-line). High-resolution STEM-HAADF image (Fig. 8-5b) reveals the sharp contrast between the GaN and InGaSbN layers, which can be correlated to the presence of heavier and larger In and Sb atoms into the InGaSbN segment. The diffraction pattern, as shown in the inset of Fig. 8-5b, further confirms the crystalline quality of the dilute-Sb Ga(In, Sb)N segment.

However, the signature of Sb into InGaSbN can be observed from the micro-Raman spectroscopy measurements conducted on the MBE grown epilayers on silicon substrate under similar growth conditions. Evolution of prominent micro-Raman modes from the GaSbN epilayer vs Sb-composition had been discussed in Chapter 7. Figure 8-5c presents the comparative analysis of the prominent Raman modes, observed from GaSbN and

InGaSbN epilayers, grown on silicon substrate. The spectra reveal the A_1(LO) phonon mode of GaSbN at 724 cm^{-1}, showing significant shift from the decoupled A_1(LO) mode of GaN (at 736 cm^{-1}, not shown here) and the LOPC mode of GaN at 740 cm^{-1}, even at the dilute Sb concentration. For example, to induce similar frequency shift in A_1(LO) mode of GaN, only ~0.6% Sb incorporation is required in GaSbN, compared to ~18% In in InGaN alloy [289, 290]. Due to the cumulative effect of In and dilute-Sb incorporation, an enormous shift in A_1(LO) mode (at 693 cm^{-1}) is observed from the Raman spectra measured on InGaSbN. To achieve such large red-shift from InGaN requires ~31% of In incorporation. On the contrary, the XRD measurements on InGaSbN suggests ~15% of In incorporation, assuming negligible mismatch is induced due to Sb incorporation in the dilute regime (~0.3%). The observation can further be correlated with the presence of Sb-induced additional mode (P_A), and its noticeable red-shift from 663 cm^{-1} to 638 cm^{-1}. Raman modes from silicon substrate at 520 and 620 cm^{-1} are marked with '*' in the spectra.

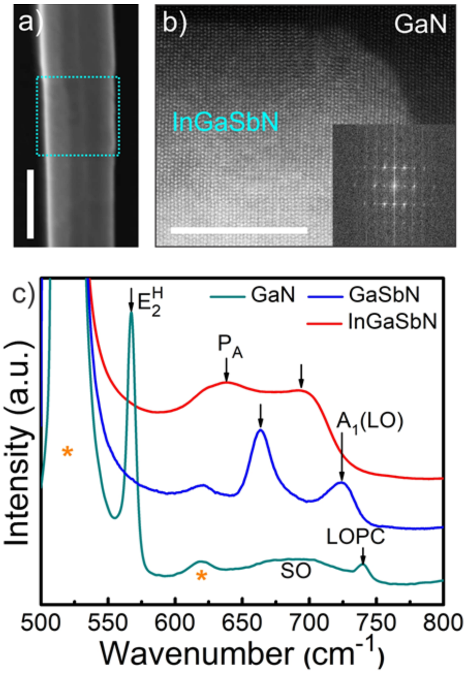

Figure 8-5: a) STEM-SE image of an InGaSbN segment into GaN nanowire. Scale bar, 30 nm. b) High-resolution STEM-HAADF image, showing the sharp contrast between the GaN and InGaSbN. Scale bar, 10 nm. The image along with the diffraction pattern (inset) confirms the crystalline quality of the nanostructure. c) Room-temperature micro-Raman spectra obtained from the GaN, GaSbN and InGaSbN on Si substrate, clearly depicting the evolution of the prominent modes. The contributions from the Si substrate are marked with ‘*’.

8.6 Conclusion

Our preliminary investigations herein successfully demonstrate the controllable tuning of GaN bandgap and band-edges through simultaneous incorporation of In and Sb. Band alignment information of InGaSbN together with those of GaSbN and InSbN can be used to design III-nitride heterojunctions with type I, II or III alignments, which is important for a broad range of applications, including LEDs, solar cells, and solar fuel devices. In addition, the availability of powerful calculation techniques can provide the distinct opportunity to derive the energy levels for GaSbN/GaN and InGaSbN quantum heterostructures, and allow us to perform thorough investigation of structural, electronic and optical properties while considering the strain effect. Doping Sb is also expected to modify the charge distribution of the non-centrosymmetric III-nitride structure and therefore change the magnitude of the spontaneous polarization field which has enormous impact on optical and electronic properties of nitride materials and devices. Therefore, further detailed studies, both theoretical and experimental, are necessary to realize the immense potential of dilute-Sb III-nitride heterostructures.

Chapter-9

Conclusion and Proposals for Future Direction

9.1 Summary of the Work

Metal-/non-metal nitride materials have attracted a great attention from the research community as a viable new generation of photocatalyst due to their unique material properties that are extremely suitable for water splitting, namely, the band gap tunability, stability against photo-corrosion, sufficient thermodynamic and kinetic potentials for water redox reaction under deep-visible excitation etc. Despite these, very limited number of studies are devoted to photochemical water splitting using metal-/non-metal nitride material. Wafer-level decomposition of neutral water into H_2 and O_2 using III-Nitride nanowires has been successfully demonstrated herein and confirmed to be a highly stable photocatalytic process. Uncontrolled surface charge properties of the nanostructures were identified as one of the greatest limiting factors in achieving efficient and stable overall water splitting on the nanowire photocatalyst. The successful demonstration of engineering the surface charge properties of the nanowires potentially alleviates one of the major obstacles for developing highly efficient artificial photosynthetic system.

In this work, we have explored the Fermi level tuning on the nonpolar surfaces of GaN and InGaN nanowire arrays through controlled *p*-type Mg dopant incorporation. The thermodynamic and kinetic potentials of the InGaN/GaN nanowire heterostructures were tested and found to be suitable for water redox reaction. Subsequently, we have developed a multi-stacked dual-band GaN:Mg/InGaN:Mg nanowire photocatalyst to utilize both UV and visible solar photons efficiently, and to reduce energy losses due to thermal relaxation of the photogenerated carriers. By tuning the near surface band bending of both GaN and InGaN nanowires in a double-band heterostructure, a substantial improvement in APCE (~69%) has been derived for neutral (pH~7.0) water splitting. This eventually led to the achievement of an AQE ~12.3% under visible light excitation and corresponding STH efficiency of ~1.5% for the multilayered nanowire heterostructure in overall water splitting under full arc illumination (concentrated, ~26 Suns) using AM1.5G filter.

Subsequently, we have addressed the fundamental issue of charge carrier trapping and recombination in the bulk of the nanowire and their detrimental effects on significantly limiting the efficiency. Accordingly, we proposed and demonstrated a new class of multi-band InGaN nanosheet photochemical diode structure, which can spontaneously induce charge carrier separation and steer charge carriers toward the distinct redox sites for water oxidation and proton reduction, respectively. In addition, the spatial separation of catalytic sites in such a nanoscale photochemical diode can effectively reduce carrier recombination and back reaction, leading to an impressive solar-to-hydrogen conversion efficiency of ~3.3% in pH neutral overall water splitting.

Finally, we have elucidated the burning issue of suppressed interfacial charge transfer and limited photochemical stability of semiconductor photocatalysts, especially under concentrated irradiation. We have successfully demonstrated that by carefully engineering the nanowires with atomically thin N-rich surfaces, together with the reduced surface band-bending through Mg-dopant incorporation, the dual-cocatalyst decorated multi-band Ga(In)N nanowires can overwhelmingly enhance the injection of photogenerated holes into the aqueous solution and can exhibit efficient (STH ~2.7%), long-term stable operation (>580 hours) in unassisted pure water splitting. The demonstrated ability to easily and reproducibly fabricate such wafer-scale industry-friendly engineered artificial photosynthesis devices of high performance and long-term stability can consequently lead to commercially viable large-scale clean hydrogen generation from unassisted solar-driven pure water splitting.

The progress in computational studies can significantly support the research community in understanding and predicting the prospect of advanced materials by analyzing the properties such as the electronic density of states and band structure, etc. This opens the broad avenue for the rational design of efficient photocatalysts for water splitting. As such, we have further explored, both theoretically and experimentally, a new generation of semiconductor (III-nitride), namely dilute-antimonide (Sb) Ga(In)N for extended visible light absorption. Here we have realized, for the first time, optically active dilute-Sb GaSbN nanostructures, which can emit (absorb) visible light due to very small amount of Sb incorporation into GaN in the dilute limit (<1%). We have further demonstrated that the band-edges (and hence the bandgap) of GaN can be controllably tuned through simultaneous incorporation of In and Sb (in the dilute limit), which holds enormous promise for visible-light driven water splitting.

9.2 Work In-progress and Future Directions

The design, growth, fabrication and performance evaluation techniques implemented using III-nitride nanostructures so far hold a very good promise in developing a suitable artificial photosynthetic system. However, there are still a lot of rooms for improving the performance of the nanostructured photocatalysts, via careful exploration of the interfacial properties of III-nitride nanostructures, and promotion of different earth abundant high-performance water oxidation and reduction co-catalysts nanoparticles for efficient and stable neutral water splitting under full arc solar spectrum. We are currently working on some of the promising strategies that can lead us to a viable approach for extending the efficiency and stability of the photocatalyst. Future directions towards achieving an industry-ready, efficient and stable artificial photosynthetic system therefore includes - the engineering and design of innovative junction architectures, optimization of the existing active materials for enhanced charge carrier separation and transfer, realization of narrow-bandgap material for extended visible light absorption while simultaneously reducing the gas evolution overpotentials and maintaining chemical and physical stability.

9.2.1 Moving Towards the Goal of 10% STH Landmark

The development of an efficient photocatalyst that can utilize nearly the entire solar spectrum is a key challenge. It has remained one of the Holy Grails of solar-fuel community for decades to achieve efficient and stable overall water splitting beyond blue solar spectrum. Table 9-1 highlights some of the limiting chemical conversion efficiencies for different water splitting approaches depending on the configuration of absorbing materials to produce one molecule of hydrogen, namely S2 (single-band, two photons absorbed to generate two active electron-hole pairs), D2 (dual-band, two-photons) and D4 (dual-band, four-photons) etc. [21]. λ_1 and λ_2 in the table represents equal-photon absorption wavelengths for D2 and D4 approach, calculated based on the photons available in AM1.5G solar spectrum. In the range of optical absorption wavelength edge explored so far in this study, i.e. ~505 nm, the theoretical limit for chemical conversion efficiency (using S2 or D2 approach) in overall water splitting is ~8-9% (~7-8%) using 0.8 eV (1.0 eV) of energy losses. Therefore, the absorption edge needs to be extended significantly towards the longer wavelengths which will enhance the theoretical maximum for the achievable efficiency of harnessing solar energy.

9.2.1.a Single-absorber Photocatalysts for One-step OWS

Significant research efforts have been made to enhance the In incorporation in InGaN, which can function as an ideal material system to achieve high efficiency water splitting by utilizing the entire solar spectrum. However, the growth of high crystalline quality InGaN with higher In content has been extremely challenging due to the large lattice mismatch (11%) between InN and GaN which results in solid phase miscibility gap, and low In-incorporation in InGaN due to the high vapor pressure of In over Ga. Additionally, the strong In surface segregation creates In-rich clusters with high density of defects that enhance the non-radiative recombination of the photogenerated carriers, limiting the device performance significantly. Moreover, when InGaN is grown beyond a critical thickness (which drops exponentially at higher In composition) misfit dislocations are formed. Therefore, the realization of high quality and high In-content (narrow-bandgap) InGaN with sufficient thickness for efficient solar absorption is quite challenging. In this context we are currently working on different strategies to address the above-mentioned challenges, as discussed in the following sections.

Intermediate band and up-conversion designs, introduced by the materials that possess an electronic band within the conventional semiconductor bandgap, had been successfully utilized in enhancing the efficiency of single-bandgap solar cells and other photovoltaic devices. An intermediate band material can incorporate a partially filled impurity energy band within the bandgap of host semiconductor, thus making it capable of absorbing below-bandgap photons. Compounds with wide band gaps, such as GaP, ZnS, ZnTe, and GaN provide a higher possibility of intermediate band formation. Theoretical, as well as experimental investigations on Mn-doped GaN have confirmed that deep Mn impurity bands can be formed within the energy level (impurity band of $Mn^{2+/3+}$) in the middle of the GaN bandgap. Therefore, the optimally doped InGaN:Mn nanostructures can lead towards developing more efficient multiple-band photocatalysts with extended absorption spectrum within single-absorber platform. In this study, we have already demonstrated a large bandgap-narrowing by incorporating very small amount of Sb (dilute regime, <1%) into Ga(In)N, which is also a very promising approach to realize narrow-bandgap III-nitride materials for efficient one-step overall water splitting using single-absorber.

The material quality and absorption efficiency, however, is of great concern for the narrow-bandgap Ga(In)N materials, due to high In content, or dissimilar Sb/Mn incorporation. It was revealed by recent studies that the color emission of III-nitride nanowire LEDs can be readily tuned by changing In compositions within the active region through variations of the nanowire diameters in a single epitaxial growth step. The nanowire diameters and spatial separations are tuned by controllably selecting the active growth sites, using a thin Ti mask (~10 nm thick) with well-defined opening apertures [291]. Our studies have found that selective area growth (SAG) of InGaN quantum dots within nanowires shows excellent material quality and supports higher In incorporation compared to self-organized spontaneous growth. This is supported by significantly enhanced photoluminescence intensity (~100 times) and red shifted peak position. This approach can be adopted for developing high In-content InGaN nanostructures with excellent crystalline quality, and tunable absorption range for solar water splitting application [292]. Using a split-spectrum irradiation system, the proposed photocatalyst structure can also be used for the better utilization of higher wavelength photons (> 505 nm) alongside with the nanostructured photocatalyst developed in this thesis to enhance the efficiency further. Besides, the spectral absorption is expected to be extended by incorporating the intermediate-band materials (Mn) and by selective area growth of dilute-antimonide III-nitride nanowires, where the crystalline quality will not be compromised too much due to foreign material introduction.

Table 9-1: Ideal realizable limiting efficiencies for different OWS schemes.

Scheme	λ_1 (nm) [E_{g1} (eV)]	λ_2 (nm) [E_{g2} (eV)]	U_{loss} (eV)	η_p (%)
S2	-	555 [2.23]	1	12.33
	-	610 [2.03]	0.8	17.1
D2	509 [2.44]	612 [2.03]	1	17.22
	550 [2.25]	685 [1.81]	0.8	23.84
D4	660 [1.88]	925 [1.34]	1	21.25
	723 [1.72]	1120 [1.11]	0.8	27.12

9.2.1.b Multiple-absorber Integration for Tandem/Z-scheme OWS

It is important to note that, one of the significant constraints in this study is the limited apparent quantum efficiency (AQE) within the absorption threshold. The theoretical maximum efficiencies presented in Table 9-1 and discussed in section 1.7 are based on the assumption that all the incident photons within the threshold wavelength are absorbed to generate active electrons and holes, and all the photoexcited carriers can effectively participate in the redox reaction (AQE ~100%). Despite the significantly enhanced charge carrier separation (reduced recombination) and transport efficiency, the maximum AQE corresponding to STH ~3.3% (ECE ~17.5%) achieved in this dissertation is limited to ~45% (Fig. 5-8), which is primarily due to the low fill-factor (50-60%) of the nanostructured photocatalysts on the substrate. With a threshold absorption wavelength of ~485 nm (Eg ~2.56 eV) for the photochemical diode, maximum of ~103.4 μmol $h^{-1}cm^{-2}$ H_2 can be produced with a theoretical limit on STH around ~6.81% (on ECE ~41.84%) under normalized irradiation (1 sun). Therefore, assuming negligible reflection and scattering of the incident photons, major reduction in the derived STH can be attributed to the loss of incident photons that transmit through the physical-gap of the nanostructured photocatalyst, or which are absorbed by the Si wafer that does not contribute in the redox reaction. On the contrary, increasing the fill-factor of the nanostructures (beyond optimum) suppresses the photochemical reactivity due to limited mass-transport. To achieve STH efficiency of ~10% under such condition (AQE ~49%), a photocatalyst with narrower bandgap of ~1.9 eV (absorption threshold wavelength ~650 nm) is ideally required which can produce ~153.4 μmol $h^{-1}cm^{-2}$ of hydrogen under normalized irradiation. However, considering the loss factors of 1.0 eV and 0.8 eV for a practical system, the threshold absorption wavelength (bandgap) for S2 approach is limited to 555 nm (2.23 eV) and 610 nm (2.03 eV), respectively (Table 9-1), for unassisted overall water splitting.

The efficiency bottleneck for the S2 approach of water splitting can potentially be addressed by adopting the D2 or D4 approach where dual- or multi-band semiconductors are integrated into a single device through junction engineering. D2 approach allows the maximum realizable efficiency of ~24% with bandgap of the materials as high as 1.8 eV and 2.3 eV, respectively. The scheme can be readily implemented on the Ga(In, Sb)N platform explored in this dissertation without substantially sacrificing the material quality, and without high In- and Sb-contents. As discussed in Chapter 7 and 8, the energy band edge positions of Ga(In, Sb)N can be independently tuned by varying In and Sb compositions to construct quantum-confined heterostructures with type-I, type-II, or even type-III band alignments. By engineering lateral p-n heterojunctions with GaSbN, InGaN and InGaSbN, the band-edges can straddle the redox potentials, and a water splitting device of ~10% STH can be realized using D2 approach without majority carrier recombination.

Besides, numerous low-bandgap foreign materials can be integrated with Ga(In, Sb)N to from p-n junctions, which can preferentially act as selective oxygen or hydrogen evolution catalyst. For example, carbon materials especially graphite oxide and graphitic carbon nitride with tunable p- or n- conductivity and controllable properties can be incorporated on the sidewalls of the Ga(In, Sb)N nanostructures which can act as an efficient and stable catalyst when loaded with suitable co-catalysts. Synergetic chemical coupling effects between Co_3O_4 and reduced graphene oxide (RGO) or RuO_2 on g-C_3N_4 sheets had been widely explored, revealing new methodologies for developing advanced inorganic–organic photocatalysts for solar energy conversion. Besides, other two-dimensional materials, *e.g.* nanostructured molybdenum disulfide (MoS_2), also possess the potential to efficiently catalyze water oxidation and reduction reaction because of their substantial amount of catalytic edge sites with high surface energy. Therefore, MoS_2 nanocrystalline layers can be an attractive and cost-effective option for integration and possess immense potential for the realization of high surface area *p-n* heterojunction (say, *p*-MoS_2 nanocrystalline layers on the sidewall of *n*-Ga(In, Sb)N nanowire heterostructures) for overall water splitting using D2 approach. Absorption threshold of already developed III-nitrides can further be extended by successfully loading MoS_2 nanocrystalline layers or nanoparticles on the sidewalls of the MBE grown nanostructures.

Finally, an advanced strategy that can be applied potentially to realize overall water splitting with narrow-bandgap dual light absorbers is the monolithic integration of nanostructured larger-bandgap semiconductor with a p^+-n junction of the smaller-bandgap semiconductor. The two bands can be employed in the Z-scheme of water splitting via suitable mediators, or form p-n photochemical diode by connecting via ohmic contact or tunnel junction (TJ) for majority carrier recombination. Type-III band alignment between narrow bandgap InGaN and Ga(In, Sb)N can be very useful in this regard. However, realization of lateral ohmic contact/TJ at the nanoscale for unassisted overall water splitting is still very challenging and demands careful investigations. Nonetheless, the development of an axial photochemical diode by connecting the two semiconductor segments of the double-band nanowire/nanosheet with a transparent tunnel junction or transparent ohmic contact can also significantly enhance the STH efficiency and is of future concern [199, 200]. To realize the STH limit of 27% using D4 approach (Table 9-1), p^+-n Si junction with its energy bandgap of 1.12 eV had been paired with $In_xGa_{1-x}P$, $Al_xGa_{1-x}As$ and $CH_3NH_3Pb[I_{1-x}Br_x]_3$ as the top light absorber, which can exhibit an ideal energy bandgap of 1.75 eV by varying the alloy compositions. Alternatively, defect-free InGaN nanowire structures with energy bandgap of ~1.75 eV (indium composition, ~52%) had been monolithically integrated with Si solar cell to realize high efficiency photocathode or photoanode in PEC water splitting. The reduction of AQE due to low nanowire fill-factor can be partially compensated by incorporating Si solar cell substrate as one of the narrow-bandgap light absorber in conjunction with the current Ga(In, Sb)N nanostructures. However, incorporation of suitable catalyst-layer on the back-side of Si solar cell (substrate) would be required [94] for overall water splitting.

9.2.1.c Improving Other Limiting Factors in Photocatalytic OWS

Water oxidation is one of the key limiting processes in overall solar water splitting redox reaction due to the sluggishness of four-holes driven reaction mechanism. Atomistic modeling shows that water can be adsorbed dissociatively on GaN surface with negligible dissociation barrier, and photogenerated holes in GaN have sufficient energy to drive the overall water oxidation reaction through a sequence of intermediate steps at pure GaN/water interface [46, 293, 294]. Although the theoretical investigations can provide mechanistic insights including possible reaction intermediates, the details of the water oxidation mechanism on III-nitrides have not been experimentally elucidated. Therefore, it is necessary to explore the interfacial water-decomposition reactions on as grown and catalyst-functionalized III-nitride nanowire surfaces to develop a better understanding of charge carrier transport mechanism. Surface states play a key role in determining the water oxidation efficiency for many of the photocatalytic materials. Recombination at the surface states and the forward water oxidation reaction are the competitive pathways for determining the overall efficiency [295-297]. Therefore, the nature and precise role of the surface states and other potential rate limiting factors in water oxidation must be fully understood to develop strategies to overcome the efficiency barrier for the redox reaction. This can be performed using the combination of techniques, such as photoluminescence, photoconductivity, contact potential difference (CPD) measurement by Kelvin probe technique and the surface photovoltage spectroscopy (SPS) in conjunction with x-ray photoelectron spectroscopy (XPS) and ultraviolet photoelectron spectroscopy (UPS). Unique to the nonpolar surfaces of III-nitrides is that the occupied surface states are bunched near the band-edge or positioned outside of the bandgap [162, 163], which leads to extremely small surface recombination velocity (~ 10^3 cm s^{-1} for GaN). Furthermore, as per the discussion in section 1.4.3 and 2.4, it is imperative to investigate the modification of photocatalyst surface, either by addition of water oxidation co-catalyst (such as IrO_x, Co-Pi, $Co(OH)_2/Co_3O_4$, $Ni(OH)_2$, NiO_x, $NiFeO_x$ *etc.*) or by passivation of the surface states (such as Alumina) or by using the combination of both approaches to mitigate the surface recombination and to improve water oxidation efficiency [298-302]. Through these studies, we aim to elucidate the mechanism and efficiency limit for oxidation reaction on III-nitride nanowires and the integrated devices with a broad range of alloy compositions (bandgaps), thereby providing a functional photocatalytic system for a wide range of photochemical and electrochemical reactions.

9.2.2 Enhancing the Stability for Practical Implementation

As discussed in section 1.4.3, the photochemical instability and the photo-corrosion problem of a semiconductor photocatalyst can be considered from both the thermodynamic and the kinetic point of view. With that in mind, thermodynamic stability against the material's self-decomposition process guarantees the overall resistance against photo-corrosion regardless of the kinetic processes. However, despite the inherent instability of a material from thermodynamic point of view, certain measures can be taken to make them stable kinetically, while thoroughly considering the specific phenomena at the semiconductor-electrolyte interface, required overpotentials and intermediate steps of the photochemical reaction.

For example, for the physical protection of the unstable surface, a dense layer of a stable material can be used as a coating to avoid its direct contact with the electrolyte, without blocking the light transmission through the layer significantly. Such a thin oxide layer can also be formed in situ during the photochemical reaction due to the initial oxidation of the material itself, which after a certain thickness, can prevent the photocatalyst from further oxidation, thus making them stable kinetically, while potentially serving as a hole blocking layer for some photocathodes. To name a few, MoS_2, TiO_2, NiOx and Al_2O_3 have been widely used as a surface protection layer in the PEC water splitting cells. For example, a thin layer of MoS_2 onto the n^+-p planar Si photocathode can exhibit over 100 hours of stability in the electrolyte. And with the protection of the MoS_2

layer, the 1T-MoS_2/p-Si photocathode demonstrated stability over 70 days showing no noticeable degradation in performance. The other approaches widely explored to promote long-term stability includes - engineering the surface charge properties and band-structure to controllably tune desired carrier transport, and loading of suitable co-catalysts on the surface for carrier accumulation and reduced recombination, etc.

Photochemical stability is a very critical issue in solar hydrogen production. III–V materials with relative narrow bandgaps suffer from the photo-corrosion under harsh PEC conditions. In contrast to traditional III–V compounds, wherein the chemical bonds are mostly covalent, the chemical bonds in III-nitrides such as Ga(In)N are strongly ionic. Because of the strong ionicity of nitrides, the surface states are located mostly near the band edges, which prevent them from being non-radiative recombination centers. Consequently, the Fermi level is not pinned in the energy gap of III-nitrides, thereby suppressing the participation of these states in the self-oxidation and photo-corrosion processes, resulting in photostability. However, the presence of any surface defects, which often depends on the growth method, may lead to Fermi-level pinning in the bandgap and photodegrade the material. By employing an in-situ Ga seeding layer and by growing the nanowires under nitrogen rich-conditions in this dissertation, we have already achieved nitrogen-termination of Ga(In)N nanowire surfaces, which was supported by detailed X-ray absorption spectroscopy measurements, high resolution STEM studies and ab initio materials modeling. The nitrogen-termination passivates the GaN nanowires against attack by air/aqueous electrolytes and leads to extraordinary stability in harsh water splitting reaction (section 6.5). Shown in Fig. 6-7, more than 580 hours stable and efficient overall water splitting reaction, evidenced by the constant hydrogen and oxygen evolution rate over time, was achieved without using any extra protection/passivation layers (which often limits the interfacial charge transfer and hence the STH efficiency significantly). However, for large-scale practical realization of an artificial photosynthetic system, it is important to move towards the goal for 10,000 hours of device-longevity in overall water splitting. To further enhance the performance demonstrated in this thesis, the approaches need to be investigated in detail on the Ga(In, Sb)N platform.

Water oxidation is well-known to be critically challenging in terms of the kinetics and energetics, thus restricting the pace of devising an efficient and cost-effective artificial photosystem. Nonetheless, there is substantial room, as well as challenges from the perspectives of the dynamics and energetics of photo-holes, the bottleneck in determining water oxidation efficiency, which requires materials of optimized composition, favourable structure, and morphology. General strategies to externally address such issues involve loading co-catalysts or constructing heterojunctions, etc. Considering MoS_2 can contribute as a highly-functioning HER co-catalyst, as well as a low-bandgap light absorber in conjunction with the Ga(In, Sb)N nanowires in D2 or D4 approach (section 9.2.1.b), detailed investigation on the integration method will be of immediate interest. Integration of Co_3O_4 with surface-engineered (N-rich) Ga(In, Sb)N nanostructures have already demonstrated extended stability and efficiency. In this context, Manganese oxides, which play unique role in natural photosystem in the form of the $CaMn_4O_4$ cluster, have drawn significant attention to the research community lately as an OER co-catalyst, and will be investigated. In search of the most suitable co-catalyst system, impact of other promising HER co-catalyst (such as WO_3, WSe_2, SnO_2) and OER co-catalyst (such as PbS, MnO_2, IrO_2) will also be explored [137, 138]. Future studies also include the utilization of alternate proton reduction cocatalyst such as metallic Ni_2P [303] to fabricate cost-effective photocatalytic water splitting system and to pave the way for practical application.

Sufficient overpotentials (thermodynamic drive) for O_2 evolution reaction need to be ensured through valence-band engineering, say by incorporating suitable elements for producing valence band hybridization effect to enhance the photo-holes' mobility and to reduce their trapping. Keeping in mind that the band structure in the bulk is different from that on the surface and on different facets of the photocatalyst, more in-depth investigations into electronic configurations on different surfaces combined with the crystal facet engineering is very crucial. Mechanisms of the more intricate surface reactions should be studied intensively by varying the surface species and consequently investigating overpotential changes. In future, we will further perform a detailed analysis of the surface electronic structure of Ga(In, Sb)N nanowires through multi-disciplinary approaches, including first-principles DFT calculations. This, together with detailed structural and photo-electrochemical characterization and surface modification techniques described, will provide engineered optimum surface properties for high efficiency, highly stable photocatalytic system.

9.2.3 III-Nitride Nanostructures for Photocatalytic CO_2 Reduction

Hydrogen gas, well-known as a clean, renewable and carbon-free energy carrier possesses the highest energy density by mass (143 MJ Kg), but it suffers from low volumetric energy densities. On the other hand, hydrocarbon fuels offer the optimum volumetric energy density, and therefore can alleviate issues associated with hydrogen storage. Besides, existing gasoline infrastructure is compatible with hydrocarbon fuels and can be employed with limited modifications, thus avoiding expensive liquid H_2 infrastructure development. Therefore, there is an immense potential in solar water splitting both for carbon-free energy and environment, as it can be utilized not only to mitigate the energy crisis but also to reduce CO_2 from the environment. Liquid fuel (i.e., CH_3OH) can be produced by catalytic hydrogenation of CO_2 from environment and H_2 been separately obtained from solar water splitting, as follows:

$$CO_2 + 3H_2 \rightarrow CH_3OH + H_2O$$

On the other hand, solar water (vapor) oxidation can be integrated with CO_2 reduction on the same photocatalyst surface to produce liquid alcohol or other hydrocarbon fuels (CO, CH_4 or CH_3OH), by utilizing the electrons and protons released from water oxidation reaction, as given below:

$$CO_2 + 2e^- + 2H^+ \rightarrow HCOOH \qquad -0.61\text{ V (vs NHE at pH=7.0)}$$

$$CO_2 + 2e^- + 2H^+ \rightarrow CO + H_2O \qquad -0.53\text{ V (vs NHE at pH=7.0)}$$

$$CO_2 + 4e^- + 4H^+ \rightarrow HCHO + H_2O \qquad -0.48\text{ V (vs NHE at pH=7.0)}$$

$$CO_2 + 6e^- + 6H^+ \rightarrow CH_3OH + H_2O \qquad -0.38\text{ V (vs NHE at pH=7.0)}$$

$$CO_2 + 8e^- + 8H^+ \rightarrow CH_4 + 2H_2O \qquad -0.24\text{ V (vs NHE at pH=7.0)}$$

The reduction potentials for CO_2 to hydrocarbons are also illustrated in Fig. 1-2 with respect to the GaN band-edges and water redox potentials. Experimental investigations in our lab has confirmed that p-type III-nitride material is more favorable for CH_4 evolution from CO_2 reduction. We have investigated *n*-GaN/*p*-InGaN nanowire structure to initially explore the performance in photocatalytic CO_2 reduction. Figure 9-1a shows the room temperature photoluminescence (PL) from the nanowire structure (the inset shows SEM image). Quantitative CH_4 evolution from photocatalytic CO_2 reduction experiment is illustrated in Fig. 9-1b, which shows that ~0.63 mmol of CH_4 can be produced per gram of photocatalyst material after ~6 hours of photochemical reaction. Negligible amount of CH_3OH evolution was observed during the reaction. However, the reaction kinetics can be engineered by tuning the surface charge properties for selective reduction of CO_2 into other hydrocarbon fuels and is currently under investigation. We believe that the double-band InGaN:Mg/GaN:Mg photochemical diode nanosheet/nanotube photocatalyst, developed for photocatalytic water splitting in Chapter 5, and the dilute-antimonide Ga(In, Sb)N nanostructure in Chapter 7 and 8, can be efficiently utilized for photochemical and photoelectrochemical reduction of carbon dioxide into useable hydrocarbon fuels with further enhancement in efficiency. However, this will require careful optimization of material compositions, cocatalyst loading, and engineering of carrier transfer at the interface of substrate (Si) and III-nitrides.

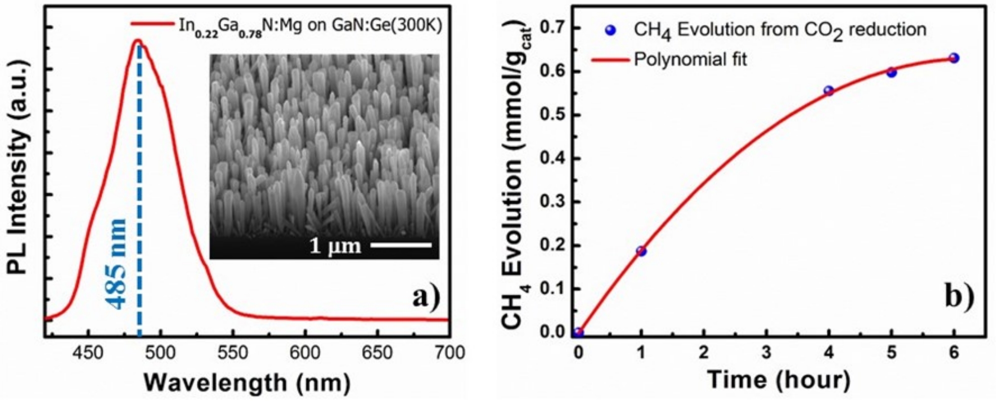

Figure 9-1: a) Room temperature PL spectrum of the GaN:Ge/InGaN:Mg nanowire photocatalyst with a broad emission peak at ~485nm (Eg ~2.56). The inset shows a 45° tilted SEM image of the nanowires, vertically aligned on Si substrate. b) CH_4 evolution from CO_2 reduction reaction under the full arc illumination using AM1.5 filter.

9.2.4 Realization of Large-scale Artificial Photosynthetic System

Direct splitting of pure or sea water with significantly enhanced device-longevity (with no tandem device or photovoltaics) at *concentrated sunlight* holds enormous promise for hydrogen generation at *pH neutral condition* without any external bias, sacrificial reagent or conductive electrolytes. Numerous semiconductor catalysts have been investigated during the last several decades but still suffer from low efficiency, poor long-term stability and are not consisting of industry-friendly compounds and processing techniques. High-efficiency devices for photovoltaic-assisted photoelectrochemical water splitting and electrolysis are reported in conductive electrolytes with selective pH adjustments. In this dissertation, we have gradually developed an artificial photosynthetic device (*small scale*) using standard materials widely used in the industry, i.e. gallium nitride (GaN) alloys on silicon wafers, which produces hydrogen efficiently by directly splitting pure water with long-term stable operation without applied bias or sacrificial agents.

Large-scale practical implementation of such artificial photosynthetic system is fundamentally limited due to the challenges such as – availability, synthesis-scalability of the photocatalyst and adaptation to existing technologies, cost-effectiveness, efficiency and long-term stability of the device which provides further economic viability. As discussed in section 2.4, Si wafers are cheaper and largely produced (over 10,000 million square inches per year, driving nearly US$3-trillion consumer electronics market). Similarly, GaN has been widely used industrially in solid-state lighting, blue/green laser diodes, and high-power electronic devices, thus making it the second most invested semiconductor material only next to Si (a combined market value exceeding $100-billion). The dual-cocatalyst decorated double-band GaN/InGaN nanowire-arrays on Si wafers (Chapter 6) exhibit a solar-to-hydrogen (STH) conversion efficiency of ~2.7% for overall pure water splitting without bias or sacrificial reagent under concentrated sunlight on a 3 cm^2 sample. With ~2.7% efficiency and using concentrated irradiance of 27 suns, the system can produce 11.42 mol h^{-1} (equivalent to 256 L h^{-1} at STP) of H_2 gas when a 1 m^2 module is employed. This is the energy equivalent of 0.767 kWh (23 g h^{-1} of H_2). No performance degradation was observed in 584 hours of unassisted water splitting reaction in pure water, which can potentially generate clean hydrogen under concentrated illumination for up to over 100 days so far or more (with 5.5 hours of usable sunlight per day). In addition, the GaN/InGaN photochemical diode (PCD) system (Chapter 5) can be used to implement 1.09 kWh system (32.66 g h^{-1} of H_2) using 1 m^2 module under concentrated ~32 suns irradiation. However, the long-term stability of the PCD system with dual-cocatalyst is yet to be confirmed.

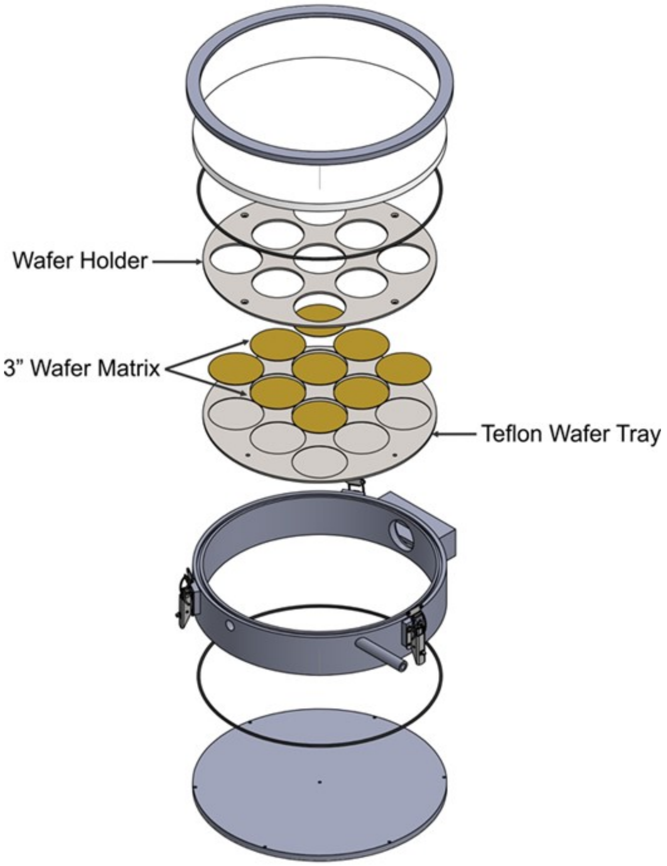

Figure 9-2: Schematic presentation of a photocatalytic water splitting cell for large-scale realization of overall pure water splitting. III-nitride photocatalysts can be grown on commercially available and recyclable 3-inch Si-wafers, and an array of such photocatalyst devices can be integrated within a cell.

In the future work, we propose to address the fundamental challenges through innovations in epitaxy, nanotechnology, surface chemistry and device engineering, which leverages the distinctive advantages of industry-ready Ga(In, Sb)N nanowire photocatalysts and the well-established, low cost, large-area Si-wafer platform. By developing nearly dislocation-free In-rich InGaN nanowire materials on Si substrate and combining with highly efficient HER and OER electrocatalyst, together with suitable surface protection layers, can lead towards the STH efficiency of over 10% and stability over 10,000 hours. Building on the pioneering work performed in this dissertation, and incorporating the potential modifications suggested herein, the proposed solar technology can be implemented into small to medium scale applications ranging from 100 W for domestic use to 100 kW for commercial use, thereby enabling a broad range of opportunities. With the targeted ~10% STH efficiency and 10,000 hours of stable operation, a 1 m^2 module of the dual-cocatalyst loaded GaN/InGaN photocatalyst system can generate energy equivalent to 2.84 kWh (85.3 g h^{-1} of H_2) under concentrated excitation (~27 suns). The primary challenge in this regard is the large-scale synthesis of the nanowire photocatalysts. As shown in Fig. 9-2, MBE grown highly crystalline and uniform GaN/InGaN nanowire arrays on (3-inch) Si wafers can be assembled to form the large-area wafer matrix (like in a solar panel) in a photocatalytic water splitting cell, without any wired connection. Integrating such array of wafers in a large-area module allows selective replacement of an individual wafer if needed, while preserving the continuity of operation. Finally, further optimization of the light intensity, temperature and pressure of the water splitting cell will be necessary, as the activation energy of the reaction can change, depending on the type of co-catalysts and the reaction environment. Therefore, a database will need to be prepared based on an initial prototype. Additional challenges include maintaining the efficiency-level of laboratory prototype at the large-scale system, efficient separation of hydrogen from the produced gas mixture and is currently under investigation.

Success of this project will bring tremendous economic and societal benefits. The use of unassisted photocatalytic water splitting approach without any external bias and sacrificial reagent, will significantly enhance the efficiency and reduce the manufacturing cost and complexity of the system. The realization of highly efficient photocatalytic solar-to-hydrogen system with long-term stability will enable the cost-effective production of clean hydrogen from abundant water source. The water splitting process has a positive impact to the environment in addition to reducing CO_2 emissions, which is not possible for the conventional fossil fuel-derived hydrogen process. Moreover, the proposed solar technology uses the enormous and renewable solar energy as the energy source, which is a promising solution for the global warming crisis. In addition, successful demonstration of highly efficient and stable hydrogen generation system (via water splitting) will eventually lead towards the integrated artificial photosynthetic system to produce hydrocarbon fuels by selective reduction of CO_2, as shown schematically in Fig. 9-3.

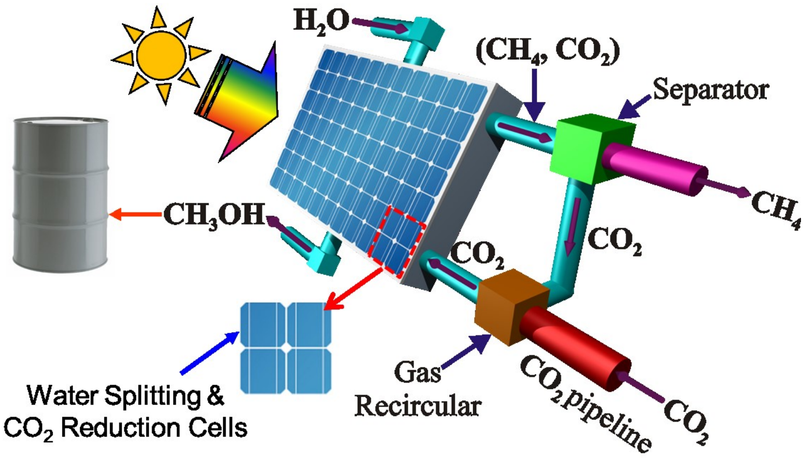

Figure 9-3: Schematic illustration of a potential artificial photosynthetic system, which can integrate the efficient photocatalytic water splitting and CO_2 reduction devices (cells) to produce hydrocarbon fuels.

9.3 Conclusion

Metal/non-metal-nitrides have emerged as a new generation of photocatalysts over the last decade, due to their unique optoelectronic and photocatalytic properties. However, to enter the real-time implementation of devices that harnesses solar energy for practical usage, a suitable photocatalyst need to possess the capability for significantly enhanced light absorption from the wide range of the solar spectrum, rapid carrier collection or extraction, lower cost and toxicity, and most of all, extended photocatalytic stability. The thermodynamics and kinetics of interfacial carrier transfer and reaction in water splitting also need to be studied and improved to achieve better performance. Owing to the tunable bandgaps, and excellent optoelectronic and catalytic properties, it is expected that metal/non-metal-nitrides will stimulate further research to overcome the efficiency and reliability bottlenecks for commercially viable artificial photosynthetic devices in future.

APPENDIX-A

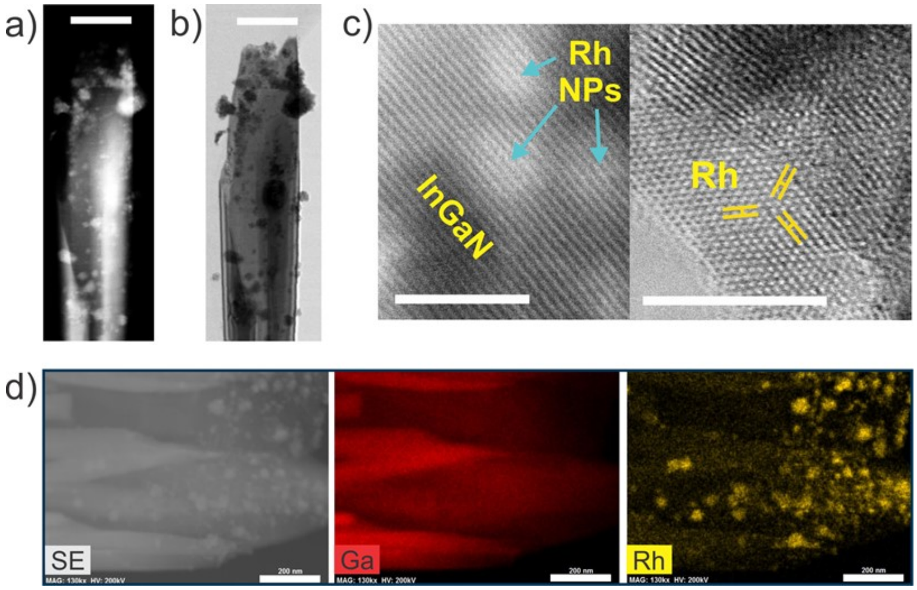

Figure AP-A1: Selective loading of co-catalysts on the cathode surface of a photochemical diode. STEM-ZC/BF images of Rh-nanoparticles' deposition on the reduction sites (*cathode* surface) of InGaN photochemical diode nanostructure is shown in a) and b), respectively. c) HRSTEM-BF lattice image of a Rh deposited InGaN photochemical diode surface, which clearly depicts the existence of Rh nanoparticles, and the crystalline quality of Rh cluster. Scale bar, 5 nm. d) STEM-SE and EDXS imaging of single InGaN photochemical diode nanosheets (cathode surface), decorated with Rh-nanoparticles. Comparing SE image and EDXS elemental mapping of Rh shows negligible signal from particle deposition on the anode surface (back, outer surface), clearly highlighting the relative difference in particle deposition density. Scale bar, 200 nm.

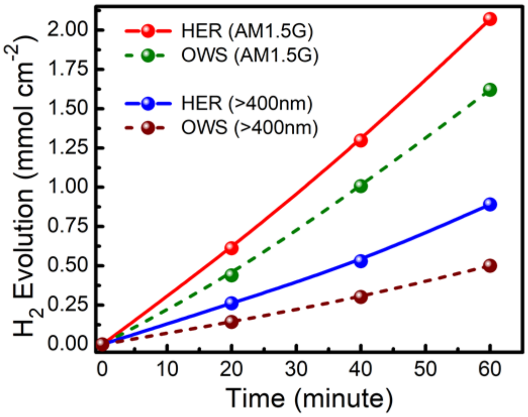

Figure AP-A2: Photocatalytic hydrogen evolution from a double-band photochemical diode. Comparative hydrogen production as a function of time from the photochemical diode nanosheet arrays in hydrogen evolution reaction using aqueous methanol solution (denoted as HER) and in neutral pH overall water splitting (denoted as OWS), under concentrated excitation of ~32 suns using AM1.5G and 400 long pass filters.

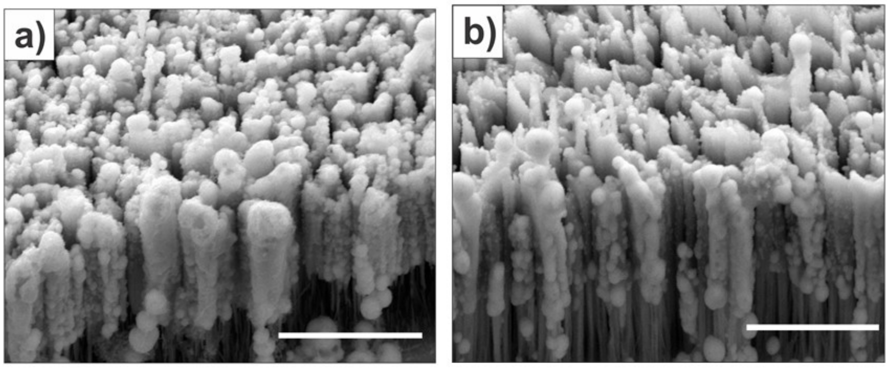

Figure AP-A3: Structural stability of double-band GaN/InGaN photochemical diodes. SEM image of the *p*-GaN/*p*-$In_{0.22}Ga_{0.78}N$ photochemical diode photocatalyst after ~4 hours of a) overall neutral pH (~7.0) water splitting (OWS) reaction b) and hydrogen evolution reaction (HER) in aqueous methanol solution, demonstrating the stability of the nanostructures. Rh/Cr_2O_3 core-shell nanostructures and Rh nanoparticles were deposited as a cocatalyst on the photochemical diode arrays in a) and b) for OWS and HER, respectively. The stability of the co-catalysts was also checked using TEM analysis and does not show noticeable degradation. Scale bar, 1 μm.

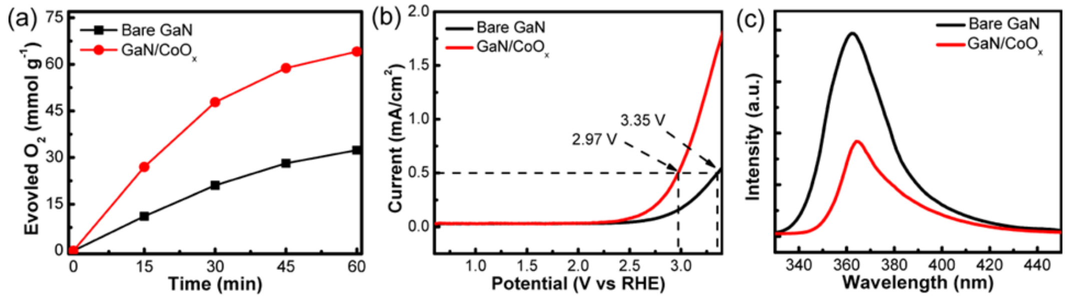

Figure AP-A4: Co_3O_4 as an OER co-catalysts on GaN nanowires. a) Oxygen (O_2) evolution from bare GaN nanowires and the Co_3O_4 decorated GaN nanowires in the presence of $AgNO_3$ as sacrificial agent. b) Linear sweep voltammetry (LSV) scans (J-E curve) for GaN nanowires on Si (111) substrate, with and without the OER co-catalyst (Co_3O_4) in potassium phosphate buffer solution (pH~7) under dark condition. c) Room temperature photoluminescence spectra measured on optimally doped *p*-type GaN nanowires and *p*-GaN/Co_3O_4 System.

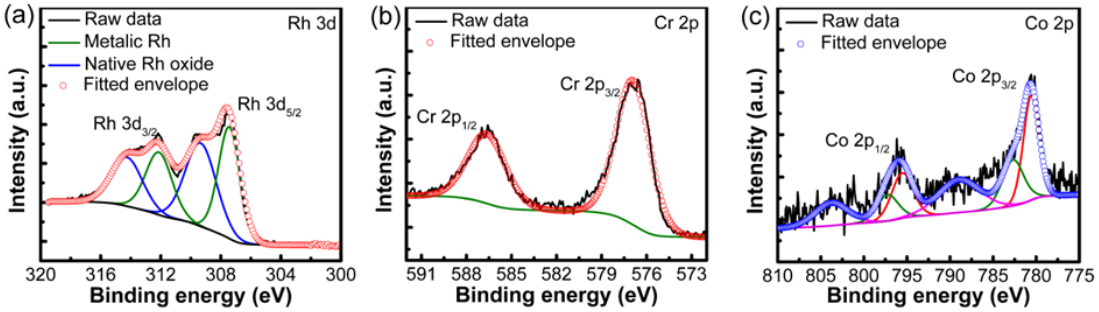

Figure AP-A5: Signature of HER and OER co-catalysts on GaN nanowire. XPS spectrum of the a) Rh 3d, b) Cr 2p, and c) Co 2p obtained from the dual-cocatalyst decorated GaN nanowires for overall water splitting. Two spin-doublets were resolved from Rh 3d peak. The Rh $3d_{5/2}$ peaks observed at 307.5 eV (green line) and 309.5 eV (blue line) are attributed to metallic Rh^0 and native Rh oxide[218], respectively. One spin-doublet was revealed from Cr 2p peak. The Cr $2p_{3/2}$ peak appeared at 576.9 eV is ascribed to the presence of Cr_2O_3 [218], indicating that the valence state of Cr is trivalent. Co $2p_{3/2}$, Co $2p_{1/2}$, and satellite peaks of Co were resolved for Co 2p peaks. In accordance with the previous discussion, Co $2p_{3/2}$ and Co $2p_{1/2}$ appeared at 780.7 and 795.8 eV is ascribe to the presence of Co_3O_4 [219]. It is worthwhile mentioning that, Rh/Cr_2O_3 (core-shell) nanostructures and Co_3O_4 nanoparticles are used as the co-catalysts for hydrogen evolution reaction (HER) and oxygen evolution reaction (OER), respectively.

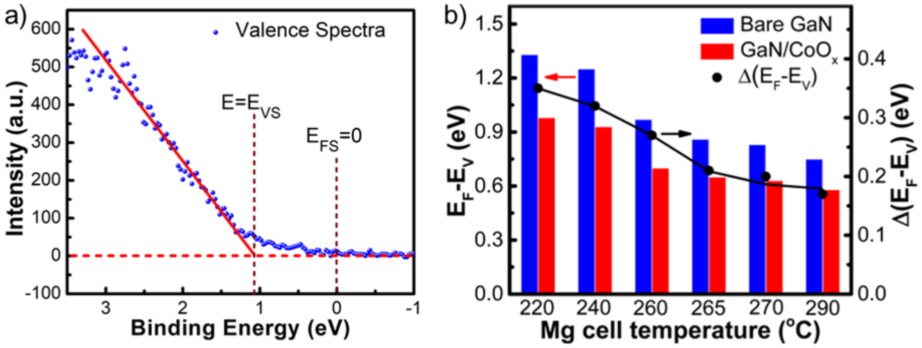

Figure AP-A6: Surface charge properties of Co_3O_4 loaded GaN nanowires. a) Measuring the position of surface valence band (VB) maximum (E_{VS}), from the intersection between the linear extrapolation of valence band leading edge and the extended baseline. The surface Fermi level is assumed to be at zero (E_{FS}, binding energy = 0 eV) [221]. b) Valence band maximum relative to the Fermi-level (E_F-E_V) for p-type GaN nanowires with different Mg-dopant incorporation, derived from the valence spectra measurement using angle-resolved X-ray photoelectron spectroscopy (ARXPS). The measurements were conducted on the non-polar surfaces of GaN nanowires, with and without the Co_3O_4, and Δ(E_F-E_V) refers to the variation (reduction) of E_F-E_V due to Co_3O_4 deposition.

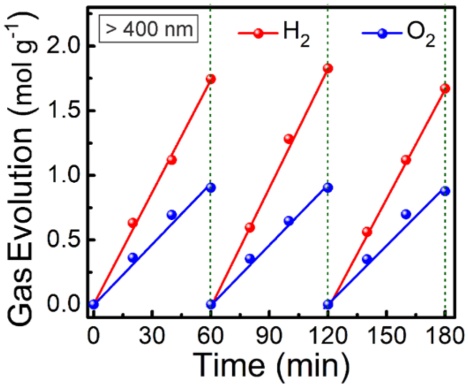

Figure AP-A7: Visible-light activity of dual-cocatalyst loaded double-band Nanowires. Repeated cycles for H_2 and O_2 evolution from the double-band *p*-type GaN/InGaN nanowire heterostructures, under visible light irradiation using a 300 W Xenon lamp (and 400 nm long pass filter) with an intensity equivalent to ~27 suns. The average H_2 and O_2 evolution rates in overall pure (pH ~7.0) water splitting were measured to be 1.75 mol $h^{-1}g^{-1}$ and 0.9 mol $h^{-1}g^{-1}$, respectively. A sample of ~3 cm^2 in surface area (active GaN/InGaN catalyst weight ~0.48 mg) was used for the experiment.

APPENDIX-B

PL intensity and suppressed carrier recombination in GaN photochemical diode

To reveal the origin of reduction in PL intensity for photochemical diodes, we further investigated the characteristics of photochemical diode nanostructures compared to axially symmetric nanowires. The photoluminescence (PL) signal strength has often been directly correlated with the charge carrier trapping, their migration and transfer efficiency, and corresponding photocatalytic activity of the device. In numerous studies, the PL intensity of photocatalytic material was found to decrease as a function of noble metal loading. This has been ascribed to the electron-scavenging effect of metal nanoparticles that acts as electron acceptor owing to their larger work function [134-136]. Apart from noble metals, PL intensity also gets reduced in general due to the efficient electron and hole capture by hydrogen evolution reaction (HER) co-catalyst (such as WO_3, WSe_2, SnO_2) and oxygen evolution reaction (OER) co-catalyst (such as PbS, MnO_2, Co_3O_4), respectively [137, 138]. In our previous studies on III-nitride nanowires, Rh/Cr_2O_3 core-shell structure had been successfully used as efficient HER co-catalyst [99, 169] and CoOx had been explored to act as an efficient OER co-catalyst in numerous other reports [304]. The PL intensity from co-catalyst nanoparticle decorated GaN nanowires was found to be reduced by 50-60% (Fig. AP-B1a) due to electron and hole trapping by Rh/Cr_2O_3 and Co_3O_4 respectively. Simultaneous deposition of both HER and OER co-catalysts also reduces the PL intensity further [138, 139]. However, as depicted in Fig. AP-B1a, six-fold reduction in the PL intensity has been observed for bare GaN photochemical diode compared to that of bare GaN nanowires, grown under similar condition.

Structural, optical and catalytic properties of GaN photochemical diodes

The prominent reflections of 002 in the X-ray diffraction (XRD) pattern shows negligible broadening or shift for GaN:Mg photochemical diodes compared to that of the nanowires. As shown in Fig. AP-B1b, the narrow peak widths of the 002 (and 004, not shown here) reflection further confirms the single crystalline structure of the as-grown Mg-doped GaN photochemical diodes; and the lattice constant extracted from the XRD pattern is *c* = 0.5186 nm, which is comparable to the wurtzite crystal structure of non-doped and Mg-doped GaN nanowires with the c-axis (0001) aligned along the growth direction [220].

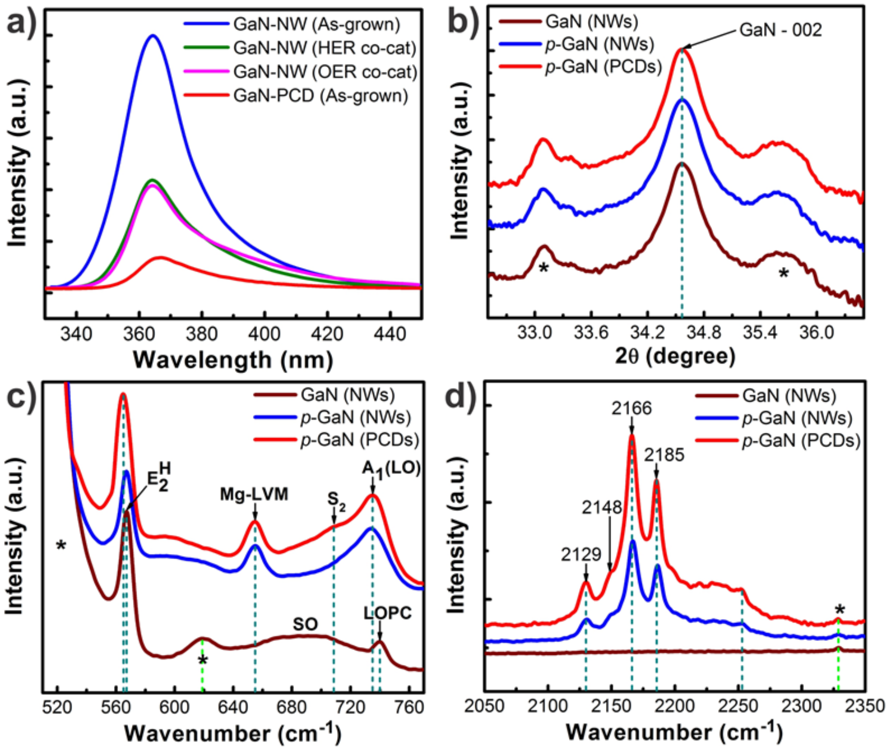

Figure AP-B1: (a) Room temperature µ-PL spectrum from as-grown and co-catalyst decorated (Rh//Cr_2O_3 for HER and Co_3O_4 for OER) GaN nanowire arrays. The µ-PL spectrum from as-grown GaN photochemical diodes clearly shows ~6-fold reduction in PL intensity compared to that of GaN nanowires. (b) The prominent reflections of 002 in the XRD pattern for GaN nanowires and photochemical diodes. Log(Intensity) of the spectrum is plotted in a linear scale. Typical micro-Raman spectra of non-doped GaN nanowires and Mg-doped GaN nanowires, along with Mg-doped GaN photochemical diodes (c) from 510 cm^{-1} to 770 cm^{-1} and (d) from 2050 cm^{-1} to 2350 cm^{-1}. Mg-cell temperature was optimized to 265 °C for both GaN nanowires and photochemical diodes to provide enhanced photocatalytic activity. The spectra in XRD and micro-Raman are vertically shifted for visual clarity. Signal contributions from the background/substrate are marked with '*' in the respective figures.

Typical room-temperature Raman spectroscopy of GaN photochemical diodes also unveils spectral response like that of optimally Mg-doped GaN nanowire arrays. As depicted in Fig. AP-B1c, both p-GaN nanowires and photochemical diodes reveal the pronounced Mg-induced local vibrational modes (LVMs) at 655 cm^{-1}, and decoupling phenomenon of A_1(LO) phonon mode (735 cm^{-1}) from the longitudinal optical phonon-plasmon coupled (LOPC) mode, present at 740 cm^{-1} in non-doped GaN nanowires [153]. The appearance of S_2 mode (709 cm^{-1}) in photochemical diode can be ascribed to the decoupling and enhancement of surface optical (SO) phonon mode due to high surface to volume ratio and higher fill factor, compared to GaN nanowire arrays [305] (not shown here). Besides, 1~2 cm^{-1} shift in E_2^H peak position is also observed in *p*-GaN, which can be ascribed to the increased tensile strain due to Mg-doping in nanowires, followed by Mg-doping gradient in photochemical diodes. Room-temperature Raman spectroscopy of *p*-GaN in the high energy range also reveals four distinct modes at 2129, 2148, 2166 and 2185 cm^{-1}, as shown in Fig. AP-B1d, which can be attributed to the LVMs associated with Mg-H complexes or H-decorated nitrogen vacancies [153, 269].

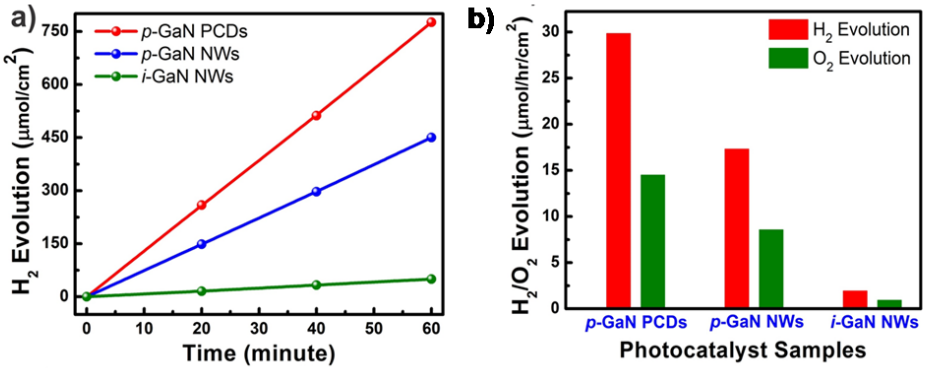

Figure AP-B2: (a) Time evolution of the amount of hydrogen from neutral pH overall water splitting (OWS) reactions on non-doped GaN nanowires, Mg-doped GaN nanowires and photochemical diodes under concentrated full arc excitation of ~26 suns, using a 300W Xenon lamp. Rh/Cr_2O_3 core-shell nanoparticles were photo-deposited as hydrogen evolution reaction (HER) co-catalyst on all the photocatalyst samples prior to the water splitting reaction. (b) Stoichiometric H_2 and O_2 evolution rate from overall neutral (pH~7.0) water splitting reactions on different photocatalyst samples under normalized excitation condition (100 mW/cm^2), depicting 75% enhancement in photocatalytic activity of GaN photochemical diodes compared to that of Mg-doped GaN nanowires.

With the same Mg cell-temperature and growth condition, one of the sidewalls of GaN photochemical diode becomes highly p-type due to Mg-doping gradient, compared to the uniform dopant distribution on the surface of axially symmetric GaN nanowires. This can potentially contribute to the larger shift in E_2^H peak position (Fig. AP-B1c) and enhanced intensity of high energy modes (Fig. AP-B1d). Nearly 75% enhancement in photocatalytic activity of *p*-GaN photochemical diodes compared to that of the axially symmetric *p*-GaN nanowires under similar excitation (Fig. AP-B2) further confirms the crystalline quality and efficient migration of charge carriers towards the surface of the photochemical diode nanostructures. GaN nanostructures were used for the comparative study instead of InGaN to avoid the ambiguity, such as peak broadening and shifts in XRD and Raman spectroscopy associated with Indium-fluctuation in different samples and regions.

APPENDIX-C

Estimation of AQE, ECE and STH of the double-band p-GaN/p-InGaN PCD

The refractive index mismatch between GaN and InGaN (for In composition ~20-25%) is negligible, and hence the light propagation and absorption inside a layered structure can generally be calculated by using a multi-layer reflectivity model. The reflection from GaN/InGaN interfaces can be ignored for both UV (average reflection~0.05%) and visible light (average reflection~0.005%). Our dual-band nanostructure mimics the D_2 approach of photocatalytic water splitting, as GaN absorption spectrum largely excludes visible light whereas InGaN can absorb both UV and visible spectrum [169].

To derive the AQE for the photocatalytic overall water splitting, the number of incident photons in the wavelength range of 200-485 nm (PL peak ~485 nm) was estimated from the lamp. The AQE was then derived using the following process. The incident power on the sample can be calculated using equation (7) in section 1.6, where $A_{\mathrm{substrate}}$ is the sample area (~ 3.0 cm^2) and β_{ff} is the nanowire fill factor (unity). $\rho_{\mathrm{incident}}(\lambda)$ is the incident power intensity on the sample, which was derived by measurements using a broadband detector (Thermopile Sensor, Newport-818P-100-55) and considering the power spectrum of the lamp and optical filter, while mimicking the experimental configuration.

Calculation of AQE using AM1.5G filter in the UV-visible range (200-485 nm)

In what follows, we first describe the calculation of the AQE with the use of AM1.5G optical filter. The total incident power on the sample is estimated to be 611 mW cm^{-2} in the wavelength range of 200-485 nm with AM1.5G filter. The number of incident photons per second is calculated from equation (6) as a function of wavelength. The total number of incident photons per second within 200-485 nm wavelength range, and corresponding AQE can be calculated from equation (6) and (7). Considering the entire absorption spectrum (200-485 nm) for the double-band structure, which includes both UV and part of the visible photons, the AQE was derived to be ~45.85% for the photochemical diode nanostructures, compared to ~20% for the axially symmetric double-band nanowires on Si substrate.

Calculation of the AQE in the visible wavelength range (400-485 nm)

The total incident power intensity (on the sample surface) in the visible wavelength range (393-485 nm) were calculated to be 376 mW cm^{-2}, which corresponds to an AQE of ~20% and ~12% for the photochemical diode and the nanowire structure, respectively.

Calculation of ECE and STH using AM1.5G filter

The ECE was calculated from equation[21] (9) and found to be ~17.5% for the photochemical diode, compared to ~7.5% for the nanowire counterpart in the wavelength range of (200-485 nm). On the other hand, in the wavelength range of 400-485 nm, the calculated values for ECE were ~8.75% and 5.3%, respectively. Solar to hydrogen conversion efficiency (STH) was calculated for both the photocatalyst nanostructures in the wavelength range 200-1100 nm using AM1.5G filter. The STH was estimated to be ~3.3% and 1.5% for the photochemical diodes and nanowire structures, respectively. The effect of pressure and temperature on STH-estimation was neglected herein to avoid ambiguity. For example, considering the initial low-pressure of the reaction chamber (~10 kPa) and final high-temperature of water (~318-325 K), the Gibbs energy of water splitting reaction can be as low as ~231 kJ mol^{-1}. However, the water temperature is low at the beginning (~293 K), and the chamber pressure increases gradually as the reaction proceeds forward under concentrated irradiation. Therefore, the Gibbs energy of water splitting reaction can vary within ~231-237 kJ mol^{-1}, and the STH can be estimated in the range of ~3.21-3.3%, respectively, which lies almost within experimental error.

Efficiency of the photochemical diode in aqueous methanol solution

The photocatalytic activity of Mg-doped $In_{0.22}Ga_{0.78}N/GaN$ nanostructures in HER inside aqueous CH_3OH solution (5:1 water/alcohol ratio) provided H_2 evolution rate of ~2.07 mmol $h^{-1}cm^{-2}$ under full arc illumination using AM1.5G filter. Corresponding apparent quantum efficiency (AQE) was estimated to be ~58.6% for an incident intensity of ~610.8 mW cm^{-2} in the wavelength range of 200-485 nm. Supplementary Fig. S9 shows the comparative hydrogen evolution per unit area (substrate) for different excitation and experimental conditions. Under visible light irradiation using a 400 nm long pass filter, for an incident intensity of ~376.2 mW cm^{-2} in the wavelength range of 393-485 nm, the H_2 evolution rate was measured ~0.89 mmol h^{-1}cm^{-2} with an estimated AQE of ~35.5% for HER.

APPENDIX-D

Calculation of Absorbed photon to current conversion efficiency (APCE) on GaN

To derive the APCE for the photocatalytic overall water splitting, the number of incident photons in the wavelength range of 200-365 nm were estimated from the lamp spectrum, which represents the overlapped wavelength between the absorption spectrum of GaN nanowires and the power spectrum of the lamp. The absorbed photons were estimated based on the GaN nanowire height of 600 nm, the absorption coefficient of GaN in the wavelength of 200-365 nm, and nanowire fill factor (on the silicon substrate). The fill factor was estimated from the top view SEM image of the GaN nanowire arrays for all the samples. The light reflection from the water-GaN interface was estimated using the refractive indices of water and GaN. The APCE was derived from the following process:

First, the reflection co-efficient of GaN, $r_{\mathrm{GaN}}(\lambda)$, is derived from the reflectance of GaN, $R_{\mathrm{GaN}}(\lambda)$.

$$r_{\mathrm{GaN}}(\lambda) = \left(\frac{1+\sqrt{R_{\mathrm{GaN}}(\lambda)}}{1-\sqrt{R_{\mathrm{GaN}}(\lambda)}}\right) \tag{1}$$

The reflectance at water-GaN interface is then derived as follows:

$$R_{\mathrm{W}/\mathrm{G}}(\lambda) = \left(\frac{r_{\mathrm{GaN}}(\lambda)-r_{\mathrm{W}}}{r_{\mathrm{GaN}}(\lambda)+r_{\mathrm{W}}}\right)^2 \tag{2}$$

where r_{W} is the reflection co-efficient of water (1.33). The transmittance at water-GaN interface can then be calculated as follows:

$$T_{\mathrm{W}/\mathrm{G}}(\lambda) = 1 - R_{\mathrm{W}/\mathrm{G}}(\lambda) \tag{3}$$

The wavelength dependent absorption (%) by GaN nanowire can be written as:

$$\gamma_{\mathrm{abs}}(\lambda) = 1 - \mathrm{e}^{-\alpha(\lambda)z} \tag{4}$$

where z is the length of the nanowire and $\alpha(\lambda)$ is the absorption co-efficient of GaN.

The absorbed power (mW) by the GaN nanowires can be derived as,

$$P_{\mathrm{abs}}(\lambda) = P_{\mathrm{incident}}(\lambda) \times T_{\mathrm{w}/_{\mathrm{G}}}(\lambda) \times \gamma_{\mathrm{abs}}(\lambda) \times A_{\mathrm{sample}} \times \beta_{\mathrm{ff}} \tag{5}$$

where A_{sample} is the sample area (2.8 cm^2) and β_{ff} is the nanowire fill factor calculated from the top view SEM images of all the samples. $P_{\mathrm{incident}}(\lambda)$ was derived from the lamp spectrum considering the light reflection at the air-water interface.

The number of absorbed photons per second is calculated from,

$$N_{\mathrm{ph}}(\lambda) = \frac{P_{\mathrm{abs}}(\lambda)}{E_{\mathrm{ph}}(\lambda)} \tag{6}$$

where $E_{\mathrm{ph}}(\lambda) = \frac{hc}{\lambda}$. The total number of absorbed photons per second in 200-365 nm wavelengths can then be calculated as follows:

$$N_{\mathrm{ph}}(200-365) = \int_{200}^{365} \frac{P_{\mathrm{abs}}(\lambda) \times \lambda}{hc} d\lambda \tag{7}$$

The estimated $N_{\mathrm{ph}}(200-365) = 1 \times 10^{18}$ per second. The APCE is then derived from the following equation:

$$\mathrm{ACPE} = 2 \times \frac{\text{Number of evolved } \mathrm{H_2} \text{ molecules per hour}}{\text{Number of absorbed photons per hour}} \times 100\ \% \tag{8}$$

$$\mathrm{APCE} = 2 \times \frac{I_{\mathrm{H_2}} \times 10^{-6} \times N_{\mathrm{a}}}{N_{\mathrm{ph}}(200-365) \times 3600} \times 100\ \% \tag{9}$$

where N_{a} is the Avogadro's number, and $I_{\mathrm{H_2}}$ is the evolved H_2 (μmol per hour) from overall water splitting reaction. The APCE derived using this approach may be over-estimated by ~10%, as the light reflection from the substrate and from the scattering between the nanowires can cause extended photon absorption that is not considered herein.

List of Publications

Patent Applications

1. **Faqrul A. Chowdhury** and Zetian Mi, “Optically Active Dilute-Antimonide III-Nitride Nanostructure Optoelectronic Devices”. US 62/529,915. Filed on July 7, 2017.
2. Zetian Mi, M. G. Kibria, **Faqrul A. Chowdhury**, “Methods and Systems Relating to Photochemical Water Splitting”. US 15/329,619. Filed on July 31, 2015.

Book Chapters

1. Shizhao Fan, Songrui Zhao, **Faqrul A. Chowdhury**, Renjie Wang, and Zetian Mi, “*Molecular Beam Epitaxial Growth of III-Nitride Nanowire Heterostructures and Emerging Device Applications*”. Handbook of GaN Semiconductor Materials and Devices, edited by Wengang (Wayne) Bi, Haochung (Henry) Kuo, Peicheng Ku, Bo Shen. ISBN-9781498747134, *CRC Press* (2017).

Peer Reviewed Journal Articles

1. **Faqrul A. Chowdhury**, Michel Trudeau, Hong Guo and Zetian Mi, “A Photochemical Diode Artificial Photosynthesis System for Unassisted High Efficiency Overall Pure Water Splitting”, ***Nature Communications***, 9:1707 (2018). **(Featured, Editors’ Highlight,** *Nat. Commun.*; **Collection: Green Chemistry**/Water Splitting, *Nature***)**

2. **Faqrul A. Chowdhury**[*]**,** Xiangjiu Guan[*], Yongjie Wang, Nick Pant, Srinivas Vanka, Michel L. Trudeau, Liejin Guo, Lionel Vayssieres and Zetian Mi, “Stable, Efficient and Industry-friendly nanowire device for sustainable solar hydrogen generation”, ***under Review,*** (August 2018). **[‘*’ *co-first authors***]

3. **F. A. Chowdhury**, S. M. Sadaf, Q. Shi, Y.-C. Chen, H. Guo and Z. Mi, “Optically Active Dilute-Antimonide III-Nitride Nanostructures for Optoelectronic Devices”, ***Applied Physics Letters***, 111, 061101 (2017). **(Featured, Cover Article,** August 2017**)**

4. **Faqrul A. Chowdhury**, Z. Mi, M. G. Kibria and M. L. Trudeau, “Group III-nitride Nanowire Structures for Photocatalytic Hydrogen Evolution under Visible Light Irradiation”, ***APL Materials***, 3, 104408 (2015). **(Editors’ Pick, 2015)**

5. M. G. Kibria, **F. A. Chowdhury**, S. Zhao, B. AlOtaibi, M. L. Trudeau, H. Guo and Z. Mi, “Visible Light Driven Efficient Overall Water Splitting Using p-type Group III-Nitride Nanowire Arrays”, ***Nature Communications***, 6, 6797 (2015).

6. Xiangjiu Guan, **Faqrul Alam Chowdhury**, Nick Pant, Liejin Guo, Lionel Vayssieres and Zetian Mi, “Efficient Unassisted Overall Photocatalytic Seawater Splitting on GaN-based Nanowire-Arrays”, ***Journal of Physical Chemistry C***, Article ASAP, DOI: 10.1021/acs.jpcc.8b00875 (2018).

7. M. G. Kibria, **F. A. Chowdhury**, M. L. Trudeau, H. Guo and Z. Mi, “Dye-sensitized InGaN nanowire arrays for efficient hydrogen production under visible light irradiation”, ***Nanotechnology***, 26, 285401 (2015).

8. Md Kibria, **F. Chowdhury**, S. Zhao, M. Trudeau, H. Guo and Z. Mi, “Defect-engineered GaN:Mg Nanowire Arrays for Overall Water Splitting under Violet Light”, ***Applied Physics Letters***, 106, 113105 (2015).

9. Qing Shi, Ying-Chih Chen, **Faqrul A. Chowdhury**, Zetian Mi, Vincent Michaud-Rioux and Hong Guo, “Band engineering of GaSbN alloy for solar fuel application” ***Physical Review Materials***, 1, 034602 (2017).

10. Y. Wang, B. AlOtaibi, **F. A. Chowdhury**, S. Fan, M. G. Kibria, L. Li, C.-J. Li and Z. Mi, “Photoelectrochemical Reduction of Carbon Dioxide using Ge doped GaN Nanowire Photoanodes”, ***APL Materials***, 3, 116106 (2015).

11. M. G. Kibria, S. Zhao, **F. A. Chowdhury**, Q. Wang, H. P. T. Nguyen, M. L. Trudeau, H. Guo and Z. Mi, “Tuning the Surface Fermi Level on *p*-type GaN Nanowires for Efficient Overall Water Splitting*”,* ***Nature Communications***, 5, 3825 (2014).

12. Md Golam Kibria, Ruimin Qiao, Wanli Yang, Idris Boukahil, Xianghua Kong, **Faqrul Alam Chowdhury**, Michel L Trudeau, Wei Ji, Hong Guo, FJ Himpsel, Lionel Vayssieres and Zetian Mi , "Atomic-Scale Origin of Long-Term Stability and High Performance of p-GaN Nanowire Arrays for Photocatalytic Overall Pure Water Splitting", ***Advanced*** **Materials**, 28 (38), 8388-8397 (2016).

Conference/Meetings/Proceedings/ Technical Articles

1. **Faqrul A. Chowdhury**, Hong Guo and Zetian Mi, "Surmounting the Carrier-transport and Stability-bottleneck of III-Nitride Nanowire Solar Water-splitting Device for Efficient and Sustainable Hydrogen Generation", *MRS Fall Meeting*, Boston, Massachusetts, USA, November 25-30, 2018.

2. **Faqrul A. Chowdhury** and Zetian Mi, "Visible Light Driven Sustainable Solar Hydrogen Generation using Efficient, Stable and Industry-Friendly III-Nitride Nanowire Device", *International Workshop on Nitride Semiconductors (IWN)*, Kanazawa, Japan, November 11-16, 2018.

3. **Faqrul A. Chowdhury**, Qing Shi, Hong Guo and Zetian Mi, "Optically Active Dilute-Antimonide Ga(In,Sb)N Nanostructures for Deep-visible Optoelectronics and Solar Fuel Applications", *34th North American Molecular Beam Epitaxy (NAMBE) Conference*, Banff, Alberta, Canada, September 30 - October 05, 2018.

4. **Faqrul A. Chowdhury**, Hong Tran, Hong Guo and Zetian Mi, "On the Efficiency and Long-term Stability of MBE-grown III-Nitride Nanostructures for Unassisted Overall Water Splitting", *34th North American Molecular Beam Epitaxy (NAMBE) Conference*, Banff, Alberta, Canada, September 30 - October 05, 2018.

5. **Faqrul A. Chowdhury**, Qing Shi, Sharif Sadaf, Hong Guo and Zetian Mi, "Bandgap Tuning of Optically Active Dilute-Antimonide GaSbN Nanowire Heterostructures for Visible Optoelectronics", *33rd North American Molecular Beam Epitaxy Conference*, Galveston, Texas, USA, October 16-18, 2017.

6. **Faqrul A. Chowdhury**, Ishiang Shih, Hong Guo and Zetian Mi, "Synergistic Effect of In and Sb Incorporation in Dilute-Antimonide InGaSbN Nanostructures for Deep-visible Light Emission", *33rd North American Molecular Beam Epitaxy Conference*, Galveston, Texas, USA, October 16-18, 2017.

7. **Faqrul A. Chowdhury**, Sharif Sadaf, Qing Shi, Ishiang Shih, Hong Guo and Zetian Mi, "Optically Active Dilute-Antimonide GaSbN Nanowire Heterostructures for Visible Optoelectronic Devices", *E-MRS ICNS 12 Meeting*, Strasbourg, France, July 24-28, 2017.

8. **Faqrul A. Chowdhury**, Renjie Wang, Ishiang Shih, Hong Guo and Zetian Mi, "Synergistic Effect of In and Sb in Dilute-Antimonide InGaSbN Nanowire Heterostructures for Deep-visible Light Emitting Devices", *E-MRS ICNS 12 Meeting*, Strasbourg, France, July 24-28, 2017.

9. **Faqrul A. Chowdhury**, Qing Shi, Sharif Sadaf, Hong Guo and Zetian Mi, "Bandgap Tuning of Optically Active Dilute-Antimonide GaSbN Nanowire Heterostructures for Visible Light Emitting Devices", *59th Electronic Materials Conference*, South Bend, Indiana, USA, June 28-30, 2017.

10. **Faqrul A. Chowdhury**, Xiangjiu Guan, Aagnik Pant, Xianghua Kong, Md Golam Kibria, Hong Guo, Franz Himpsel, Lionel Vayssieres, and Zetian Mi, "High Efficiency and Highly Stable Photocatalytic Overall Water Splitting on III-Nitride Nanowire Arrays", *2017 MRS Spring Meeting*, Phoenix, Arizona, USA, April 17-21, 2017.

11. **Faqrul A. Chowdhury** and Zetian Mi, "Tuning the bandgap and surface charge properties of III-Nitride nanowires for high efficiency solar-to-hydrogen conversion", *32nd North American Molecular Beam Epitaxy Conference*, Saratoga Springs, New York, USA, September 18-21, 2016.

12. **Faqrul A. Chowdhury** and Zetian Mi, "Nanowire Photochemical Diodes for Efficient Solar-to-Hydrogen Conversion", *58th Electronic Materials Conference*, Newark, Delaware, USA, June 24-26, 2016.

13. **Faqrul A. Chowdhury**, M. G. kibria, and Zetian Mi, “Deep Visible Overall Water Splitting Using InGaN Nanowires - Driving Towards the Threshold”, *57th Electronic Materials Conference*, Columbus, Ohio, USA, June 24-26, 2015.

14. Xiangjiu Guan, **Faqrul. A. Chowdhury**, Lionel Vayssieres, Liejin Guo and Zetian Mi, “Photocatalytic Seawater Splitting on Metal-Nitride Nanowires”. 9th *Global Forum on Advanced Materials and Technologies* (GFMAT), Toronto, Ontario, Canada, June 26–July 01, 2016.

15. Md Golam Kibria, **Faqrul Alam Chowdhury**, and Zetian Mi, “Achieving artificial photosynthesis with nanowires”, Technical Article, SPIE Newsroom, February 2015.

16. M. G. Kibria**, F. A. Chowdhury**, H. P. T. Nguyen, S. Zhao, and Z. Mi, “Overall Water Splitting under Broadband Light Using InGaN/GaN Nanowire Heterostructures”. *IEEE Summer Topical Meeting Series*, Montreal, Quebec, Canada, July 14-16, 2014.

17. M. G. Kibria**, F. A. Chowdhury**, H. P. T. Nguyen, S. Zhao, and Z. Mi, “Overall Water Splitting under Broadband Light Using InGaN/GaN Nanowire Heterostructures”. *Proceedings of IEEE Summer Topical Meeting Series*, *Pages 19-20,* July 14, 2014.

18. M. G. Kibria, **F. A. Chowdhury**, Z. Mi, “Tuning the Surface Charge Properties of p-GaN Nanowire Arrays for High Efficiency Water Splitting”, *2014 MRS Spring Meeting*, San Francisco, April 21-25, 2014.

19. M. G. Kibria, **F. A. Chowdhury**, S. Zhao, Z. Mi, “Band-Engineered InGaN Nanowires Arrays for High Efficiency Water Splitting Under Visible Light Irradiation”, *30th NAMBE Conference*, Banff, Alberta, Oct 5-11, 2013.

20. M. G. Kibria, **F. A. Chowdhury**, S. Zhao, Q. Wang, Z. Mi, “Doping Effect on Photocatalytic Activity of GaN Nanowires Arrays for Overall Water Splitting”, *McGill Engineering Research Showcase (MERS)*, Oct 18, 2013.

21. M. G. Kibria, **F. A. Chowdhury**, S. Zhao, Z. Mi, "Doping Effect on Photocatalytic Activity of GaN Nanowires Arrays for Pure Water Splitting", *MRS Fall Meeting*, Boston, USA, Nov 25-30, 2012.

REFERENCES

[1] D. Abbott, "Keeping the Energy Debate Clean: How Do We Supply the World's Energy Needs?," *Proceedings of the IEEE,* vol. 98, pp. 42-66, 2010.

[2] A. Fujishima, X. Zhang, and D. A. Tryk, "Heterogeneous photocatalysis: From water photolysis to applications in environmental cleanup," *International Journal of Hydrogen Energy,* vol. 32, pp. 2664-2672, 2007.

[3] J. O. M. Bockris, "Energy, Global Warming and the Future," *Nova Publishing Online: New York, NY, USA,,* 2011.

[4] T. R. Cook, D. K. Dogutan, S. Y. Reece, Y. Surendranath, T. S. Teets, and D. G. Nocera, "Solar Energy Supply and Storage for the Legacy and Nonlegacy Worlds," *Chemical Reviews,* vol. 110, pp. 6474-6502, 2010.

[5] C.-H. Liao, C.-W. Huang, and J. C. S. Wu, "Hydrogen Production from Semiconductor-based Photocatalysis via Water Splitting," *Catalysts,* vol. 2, pp. 490-516, 2012.

[6] J. A. Turner, M. C. Williams, and K. Rajeshwar, "Hydrogen economy based on renewable energy sources.," *The Electrochemical Society Interface,* vol. 13, p. 24, Fall 2004.

[7] K. Rajeshwar, R. McConnell, and S. Licht, "Solar Hydrogen Generation: Toward a Renewable Energy Future," *Springer,* 2008.

[8] J. R. Bolton, "Solar photoproduction of hydrogen: A review," *Solar Energy,* vol. 57, pp. 37-50, 1996.

[9] J. O. M. Bockris, "Hydrogen," *Materials,* vol. 4, pp. 2073-2091, 2011.

[10] J. Su and L. Vayssieres, "A Place in the Sun for Artificial Photosynthesis?," *ACS Energy Letters,* vol. 1, pp. 121-135, 2016.

[11] F. E. Osterloh and B. A. Parkinson, "Recent developments in solar water-splitting photocatalysis," *MRS Bulletin,* vol. 36, pp. 17-22, 2011.

[12] N. S. Lewis and D. G. Nocera, "Powering the planet: Chemical challenges in solar energy utilization," *Proceedings of the National Academy of Sciences,* vol. 103, pp. 15729-15735, October 24, 2006.

[13] N. S. Lewis, "Research opportunities to advance solar energy utilization," *Science,* vol. 351, 2016.

[14] Y. Tachibana, L. Vayssieres, and J. R. Durrant, "Artificial photosynthesis for solar water-splitting," *Nat Photon,* vol. 6, pp. 511-518, 2012.

[15] R. E. Blankenship, D. M. Tiede, J. Barber, G. W. Brudvig, G. Fleming, M. Ghirardi*, et al.*, "Comparing Photosynthetic and Photovoltaic Efficiencies and Recognizing the Potential for Improvement," *Science,* vol. 332, p. 805, 2011.

[16] J. A. Turner, "Sustainable Hydrogen Production," *Science,* vol. 305, p. 972, 2004.

[17] P.-T. Chen, C.-L. Sun, and M. Hayashi, "First-Principles Calculations of Hydrogen Generation Due to Water Splitting on Polar GaN Surfaces," *The Journal of Physical Chemistry C,* vol. 114, pp. 18228-18232, 2010.

[18] K. Maeda, K. Teramura, D. Lu, T. Takata, N. Saito, Y. Inoue*, et al.*, "Photocatalyst releasing hydrogen from water," *Nature,* vol. 440, p. 295, 2006.

[19] Z. Zou, J. Ye, K. Sayama, and H. Arakawa, "Direct splitting of water under visible light irradiation with an oxide semiconductor photocatalyst," *Nature,* vol. 414, pp. 625-627, 2001.

[20] A. Fujishima and K. Honda, "Electrochemical Photolysis of Water at a Semiconductor Electrode," *Nature,* vol. 238, pp. 37-38, 07/07/print 1972.

[21] J. R. Bolton, S. J. Strickler, and J. S. Connolly, "Limiting and realizable efficiencies of solar photolysis of water," *Nature,* vol. 316, pp. 495-500, 1985.

[22] T. Markvart, "Light harvesting for quantum solar energy conversion," *Progress in Quantum Electronics,* vol. 24, pp. 107-186, 2000.

[23] J. R. Bolton and D. O. Hall, "Photochemical Conversion and Storage of Solar Energy," *Annual Review of Energy,* vol. 4, pp. 353-401, 1979.

[24] A. J. Bard, "Design of semiconductor photoelectrochemical systems for solar energy conversion," *The Journal of Physical Chemistry,* vol. 86, pp. 172-177, 1982.

[25] I. McConnell, G. Li, and G. W. Brudvig, "Energy Conversion in Natural and Artificial Photosynthesis," *Chemistry & Biology,* vol. 17, pp. 434-447, 2010.

[26] D. Gust, T. A. Moore, and A. L. Moore, "Solar Fuels via Artificial Photosynthesis," *Accounts of Chemical Research,* vol. 42, pp. 1890-1898, 2009.

[27] X. Chen, S. Shen, L. Guo, and S. S. Mao, "Semiconductor-based Photocatalytic Hydrogen Generation," *Chemical Reviews,* vol. 110, pp. 6503-6570, 2010.

[28] Y. Tachibana, L. Vayssieres, and J. R. Durrant, "Artificial photosynthesis for solar water-splitting," *Nature Photonics,* vol. 6, pp. 511-518, 2012.

[29] A. Kudo and Y. Miseki, "Heterogeneous photocatalyst materials for water splitting," *Chemical Society Reviews,* vol. 38, pp. 253-278, 2009.

[30] T. Hisatomi, J. Kubota, and K. Domen, "Recent advances in semiconductors for photocatalytic and photoelectrochemical water splitting," *Chemical Society Reviews,* vol. 43, pp. 7520-7535, 2014.

[31] S. S. Mao and S. H. Shen, "HYDROGEN PRODUCTION Catalysing artificial photosynthesis," *Nature Photonics,* vol. 7, pp. 944-946, 2013.

[32] M. Gratzel, "Photoelectrochemical cells," *Nature,* vol. 414, pp. 338-344, 2001.

[33] C. R. Jiang, S. J. A. Moniz, A. Q. Wang, T. Zhang, and J. W. Tang, "Photoelectrochemical devices for solar water splitting - materials and challenges," *Chemical Society Reviews,* vol. 46, pp. 4645-4660, 2017.

[34] F. E. Osterloh, "Inorganic nanostructures for photoelectrochemical and photocatalytic water splitting," *Chemical Society Reviews,* vol. 42, pp. 2294-2320, 2013.

[35] X. B. Chen, C. Li, M. Gratzel, R. Kostecki, and S. S. Mao, "Nanomaterials for renewable energy production and storage," *Chemical Society Reviews,* vol. 41, pp. 7909-7937, 2012.

[36] S. Hu, M. R. Shaner, J. A. Beardslee, M. Lichterman, B. S. Brunschwig, and N. S. Lewis, "Amorphous TiO_2 coatings stabilize Si, GaAs, and GaP photoanodes for efficient water oxidation," *Science,* vol. 344, pp. 1005-1009, 2014.

[37] Y. J. Lin, S. Zhou, S. W. Sheehan, and D. W. Wang, "Nanonet-Based Hematite Heteronanostructures for Efficient Solar Water Splitting," *Journal of the American Chemical Society,* vol. 133, pp. 2398-2401, 2011.

[38] T. W. Kim and K. S. Choi, "Nanoporous $BiVO_4$ Photoanodes with Dual-Layer Oxygen Evolution Catalysts for Solar Water Splitting," *Science,* vol. 343, pp. 990-994, 2014.

[39] M. C. Liu, Y. B. Chen, J. Z. Su, J. W. Shi, X. X. Wang, and L. J. Guo, "Photocatalytic hydrogen production using twinned nanocrystals and an unanchored NiSx co-catalyst," *Nature Energy,* vol. 1, p. 8, 2016.

[40] X. B. Chen, L. Liu, P. Y. Yu, and S. S. Mao, "Increasing Solar Absorption for Photocatalysis with Black Hydrogenated Titanium Dioxide Nanocrystals," *Science,* vol. 331, pp. 746-750, 2011.

[41] Z. G. Zou, J. H. Ye, K. Sayama, and H. Arakawa, "Direct splitting of water under visible light irradiation with an oxide semiconductor photocatalyst," *Nature,* vol. 414, pp. 625-627, 2001.

[42] K. H. Bevan, M. S. Hossain, A. Iqbal, and Z. Wang, "Exploring Bridges between Quantum Transport and Electrochemistry. I," *The Journal of Physical Chemistry C,* vol. 120, pp. 179-187, 2016.

[43] M. S. Hossain and K. H. Bevan, "Exploring Bridges between Quantum Transport and Electrochemistry. II. A Theoretical Study of Redox-Active Monolayers," *The Journal of Physical Chemistry C,* vol. 120, pp. 188-194, 2016.

[44] W. Schmickler, *Interfacial Electrochemistry,* vol. 1st ed.; Oxford University Press: New York, 1996.

[45] R. Memming, *Semiconductor Electrochemistry,* vol. 1st ed.; WILEY-VCH Verlag, 2007.

[46] X. Shen, Y. A. Small, J. Wang, P. B. Allen, M. V. Fernandez-Serra, M. S. Hybertsen*, et al.*, "Photocatalytic Water Oxidation at the GaN (10$\bar{1}$0)−Water Interface," *The Journal of Physical Chemistry C,* vol. 114, pp. 13695-13704, 2010.

[47] A. V. Akimov, J. T. Muckerman, and O. V. Prezhdo, "Nonadiabatic Dynamics of Positive Charge during Photocatalytic Water Splitting on GaN(10-10) Surface: Charge Localization Governs Splitting Efficiency," *Journal of the American Chemical Society,* vol. 135, pp. 8682-8691, 2013.

[48] J. Wang, L. S. Pedroza, A. Poissier, and M. V. Fernández-Serra, "Water Dissociation at the GaN(10$\bar{1}$0) Surface: Structure, Dynamics and Surface Acidity," *The Journal of Physical Chemistry C,* vol. 116, pp. 14382-14389, 2012.

[49] Á. Valdés, Z. W. Qu, G. J. Kroes, J. Rossmeisl, and J. K. Nørskov, "Oxidation and Photo-Oxidation of Water on TiO2 Surface," *The Journal of Physical Chemistry C,* vol. 112, pp. 9872-9879, 2008.

[50] Á. Valdés and G. J. Kroes, "Cluster Study of the Photo-Oxidation of Water on Rutile Titanium Dioxide (TiO_2)," *The Journal of Physical Chemistry C,* vol. 114, pp. 1701-1708, 2010.

[51] J. Tang, J. R. Durrant, and D. R. Klug, "Mechanism of photocatalytic water splitting in TiO_2. Reaction of water with photoholes, importance of charge carrier dynamics, and evidence for four-hole chemistry," *Journal of the American Chemical Society,* vol. 130, pp. 13885-13891, 2008.

[52] S. Crawford, E. Thimsen, and P. Biswas, "Impact of Different Electrolytes on Photocatalytic Water Splitting," *Journal of The Electrochemical Society,* vol. 156, pp. H346-H351, 2009.

[53] T. Shinagawa and K. Takanabe, "Towards Versatile and Sustainable Hydrogen Production through Electrocatalytic Water Splitting: Electrolyte Engineering," *ChemSusChem,* vol. 10, pp. 1318-1336, 2017.

[54] S. M. Ji, H. Jun, J. S. Jang, H. C. Son, P. H. Borse, and J. S. Lee, "Photocatalytic hydrogen production from natural seawater," *Journal of Photochemistry and Photobiology A: Chemistry,* vol. 189, pp. 141-144, 2007.

[55] K. Maeda, H. Masuda, and K. Domen, "Effect of electrolyte addition on activity of $(Ga_{1-x}Zn_x)(N_{1-x}O_x)$ photocatalyst for overall water splitting under visible light," *Catalysis Today,* vol. 147, pp. 173-178, 2009.

[56] J. Liu, Y. Liu, N. Liu, Y. Han, X. Zhang, H. Huang*, et al.*, "Metal-free efficient photocatalyst for stable visible water splitting via a two-electron pathway," *Science,* vol. 347, p. 970, 2015.

[57] K. Maeda, K. Teramura, D. L. Lu, T. Takata, N. Saito, Y. Inoue*, et al.*, "Photocatalyst releasing hydrogen from water - Enhancing catalytic performance holds promise for hydrogen production by water splitting in sunlight," *Nature,* vol. 440, pp. 295-295, 2006.

[58] Q. Wang, T. Hisatomi, Q. Jia, H. Tokudome, M. Zhong, C. Wang*, et al.*, "Scalable water splitting on particulate photocatalyst sheets with a solar-to-hydrogen energy conversion efficiency exceeding 1%," *Nature Materials,* vol. 15, p. 611, 2016.

[59] H. Liu, J. Yuan, Z. Jiang, W. F. Shangguan, H. Einaga, and Y. Teraoka, "Novel photocatalyst of V-based solid solutions for overall water splitting," *Journal of Materials Chemistry,* vol. 21, pp. 16535-16543, 2011.

[60] F. Tessier, P. Maillard, Y. Lee, C. Bleugat, and K. Domen, "Zinc Germanium Oxynitride: Influence of the Preparation Method on the Photocatalytic Properties for Overall Water Splitting," *Journal of Physical Chemistry C,* vol. 113, pp. 8526-8531, 2009.

[61] L. Liao, Q. Zhang, Z. Su, Z. Zhao, Y. Wang, Y. Li*, et al.*, "Efficient solar water-splitting using a nanocrystalline CoO photocatalyst," *Nat Nano,* vol. 9, pp. 69-73, 2014.

[62] H. Kato, K. Asakura, and A. Kudo, "Highly Efficient Water Splitting into H_2 and O_2 over Lanthanum-Doped $NaTaO_3$ Photocatalysts with High Crystallinity and Surface Nanostructure," *Journal of the American Chemical Society,* vol. 125, pp. 3082-3089, 2003.

[63] Y. Li, L. Zhu, Y. Yang, H. Song, Z. Lou, Y. Guo*, et al.*, "A Full Compositional Range for a $(Ga_{1-x}Zn_x)(N_{1-x}O_x)$ Nanostructure: High Efficiency for Overall Water Splitting and Optical Properties," *Small,* vol. 11, pp. 871-876, 2015.

[64] K. Maeda, K. Teramura, and K. Domen, "Effect of post-calcination on photocatalytic activity of $(Ga_{1-x}Zn_x)(N_{1-x}O_x)$ solid solution for overall water splitting under visible light," *Journal of Catalysis,* vol. 254, pp. 198-204, 2008.

[65] Y. Ham, T. Hisatomi, Y. Goto, Y. Moriya, Y. Sakata, A. Yamakata*, et al.*, "Flux-mediated doping of $SrTiO_3$ photocatalysts for efficient overall water splitting," *Journal of Materials Chemistry A,* vol. 4, pp. 3027-3033, 2016.

[66] H. Kato, Y. Sasaki, N. Shirakura, and A. Kudo, "Synthesis of highly active rhodium-doped $SrTiO_3$ powders in Z-scheme systems for visible-light-driven photocatalytic overall water splitting," *Journal of Materials Chemistry A,* vol. 1, pp. 12327-12333, 2013.

[67] G. Zhang, Z.-A. Lan, L. Lin, S. Lin, and X. Wang, "Overall water splitting by Pt/g-C_3N_4 photocatalysts without using sacrificial agents," *Chemical Science,* vol. 7, pp. 3062-3066, 2016.

[68] J. Su, Y. Wei, and L. Vayssieres, "Stability and Performance of Sulfide-, Nitride-, and Phosphide-Based Electrodes for Photocatalytic Solar Water Splitting," *The Journal of Physical Chemistry Letters,* vol. 8, pp. 5228-5238, 2017.

[69] S. Chen and L.-W. Wang, "Thermodynamic Oxidation and Reduction Potentials of Photocatalytic Semiconductors in Aqueous Solution," *Chemistry of Materials,* vol. 24, pp. 3659-3666, 2012.

[70] T. Hisatomi, K. Takanabe, and K. Domen, "Photocatalytic Water-Splitting Reaction from Catalytic and Kinetic Perspectives," *Catalysis Letters,* vol. 145, pp. 95-108, 2015.

[71] F. E. Osterloh, "Inorganic Materials as Catalysts for Photochemical Splitting of Water," *Chemistry of Materials,* vol. 20, pp. 35-54, 2008.

[72] T. Kida, Y. Minami, G. Guan, M. Nagano, M. Akiyama, and A. Yoshida, "Photocatalytic activity of gallium nitride for producing hydrogen from water under light irradiation," *Journal of Materials Science,* vol. 41, pp. 3527-3534, 2006.

[73] R. M. Navarro Yerga, M. C. Álvarez Galván, F. del Valle, J. A. Villoria de la Mano, and J. L. G. Fierro, "Water Splitting on Semiconductor Catalysts under Visible-Light Irradiation," *ChemSusChem,* vol. 2, pp. 471-485, 2009.

[74] K. Maeda, "Photocatalytic water splitting using semiconductor particles: History and recent developments," *Journal of Photochemistry and Photobiology C: Photochemistry Reviews,* vol. 12, pp. 237-268, 2011.

[75] H. Gerischer, "On the stability of semiconductor electrodes against photodecomposition," *Journal of Electroanalytical Chemistry and Interfacial Electrochemistry,* vol. 82, pp. 133-143, 1977.

[76] K. Maeda, K. Teramura, N. Saito, Y. Inoue, and K. Domen, "Photocatalytic Overall Water Splitting on Gallium Nitride Powder," *Bulletin of the Chemical Society of Japan,* vol. 80, pp. 1004-1010, 2007.

[77] M. G. Walter, E. L. Warren, J. R. McKone, S. W. Boettcher, Q. Mi, E. A. Santori*, et al.*, "Solar Water Splitting Cells," *Chemical Reviews,* vol. 110, pp. 6446-6473, 2010.

[78] K. Maeda and K. Domen, "Photocatalytic Water Splitting: Recent Progress and Future Challenges," *The Journal of Physical Chemistry Letters,* vol. 1, pp. 2655-2661, 2010.

[79] C. G. Van de Walle and D. Segev, "Microscopic origins of surface states on nitride surfacesa)," *Journal of Applied Physics,* vol. 101, p. 081704, 2007.

[80] M. Bertelli, P. Löptien, M. Wenderoth, A. Rizzi, R. G. Ulbrich, M. C. Righi*, et al.*, "Atomic and electronic structure of the nonpolar GaN ($1\bar{1}00$) surface," *Physical Review B,* vol. 80, p. 115324, 2009.

[81] A. G. Bhuiyan, A. Hashimoto, and A. Yamamoto, "Indium nitride (InN): A review on growth, characterization, and properties," *Journal of Applied Physics,* vol. 94, pp. 2779-2808, 2003.

[82] P. G. Moses and C. G. Van de Walle, "Band bowing and band alignment in InGaN alloys," *Applied Physics Letters,* vol. 96, p. 021908, 2010.

[83] Z. Z. Bandić, P. M. Bridger, E. C. Piquette, and T. C. McGill, "Minority carrier diffusion length and lifetime in GaN," *Applied Physics Letters,* vol. 72, pp. 3166-3168, 1998.

[84] S. C. Jain, M. Willander, J. Narayan, and R. V. Overstraeten, "III–nitrides: Growth, characterization, and properties," *Journal of Applied Physics,* vol. 87, pp. 965-1006, 2000.

[85] B. Monemar and G. Pozina, "Group III-nitride based hetero and quantum structures," *Progress in Quantum Electronics,* vol. 24, pp. 239-290, 2000.

[86] F. K. Yam and Z. Hassan, "InGaN: An overview of the growth kinetics, physical properties and emission mechanisms," *Superlattices and Microstructures,* vol. 43, pp. 1-23, 2008.

[87] H. S. Jung, Y. J. Hong, Y. Li, J. Cho, Y.-J. Kim, and G.-C. Yi, "Photocatalysis Using GaN Nanowires," *ACS Nano,* vol. 2, pp. 637-642, 2008.

[88] T. Stoica, R. Meijers, R. Calarco, T. Richter, and H. Lüth, "MBE growth optimization of InN nanowires," *Journal of Crystal Growth,* vol. 290, pp. 241-247, 2006.

[89] S. A. Dayeh, E. T. Yu, and D. Wang, "III−V Nanowire Growth Mechanism: V/III Ratio and Temperature Effects," *Nano Letters,* vol. 7, pp. 2486-2490, 2007.

[90] A. J. Nozik and R. Memming, "Physical Chemistry of Semiconductor−Liquid Interfaces," *The Journal of Physical Chemistry,* vol. 100, pp. 13061-13078, 1996.

[91] J. Kiwi, "Electron injection studies on semiconductor surfaces active in water splitting processes," *Chemical Physics Letters,* vol. 83, pp. 594-599, 1981.

[92] S. Zhao, S. Fathololoumi, K. H. Bevan, D. P. Liu, M. G. Kibria, Q. Li*, et al.*, "Tuning the Surface Charge Properties of Epitaxial InN Nanowires," *Nano Letters,* vol. 12, pp. 2877-2882, 2012.

[93] J. H. Kim, Y. Jo, J. H. Kim, J. W. Jang, H. J. Kang, Y. H. Lee*, et al.*, "Wireless Solar Water Splitting Device with Robust Cobalt-Catalyzed, Dual-Doped BiVO4 Photoanode and Perovskite Solar Cell in Tandem: A Dual Absorber Artificial Leaf," *ACS Nano,* vol. 9, pp. 11820-11829, 2015.

[94] S. Y. Reece, J. A. Hamel, K. Sung, T. D. Jarvi, A. J. Esswein, J. J. H. Pijpers*, et al.*, "Wireless Solar Water Splitting Using Silicon-Based Semiconductors and Earth-Abundant Catalysts," *Science,* vol. 334, p. 645, 2011.

[95] M. G. Kibria, F. A. Chowdhury, S. Zhao, B. AlOtaibi, M. L. Trudeau, H. Guo, *et al.*, "Visible light-driven efficient overall water splitting using p-type metal-nitride nanowire arrays," *Nature Communications,* vol. 6, p. 6797, 2015.

[96] Q. Wang, T. Hisatomi, Y. Suzuki, Z. Pan, J. Seo, M. Katayama, *et al.*, "Particulate Photocatalyst Sheets Based on Carbon Conductor Layer for Efficient Z-Scheme Pure-Water Splitting at Ambient Pressure," *Journal of the American Chemical Society,* vol. 139, pp. 1675-1683, 2017.

[97] C. Liu, J. Tang, H. M. Chen, B. Liu, and P. Yang, "A Fully Integrated Nanosystem of Semiconductor Nanowires for Direct Solar Water Splitting," *Nano Letters,* vol. 13, pp. 2989-2992, 2013.

[98] Z. Zou, J. Ye, K. Sayama, and H. Arakawa, "Direct splitting of water under visible light irradiation with an oxide semiconductor photocatalyst," *Nature,* vol. 414, p. 625, 2001.

[99] M. G. Kibria, S. Zhao, F. A. Chowdhury, Q. Wang, H. P. T. Nguyen, M. L. Trudeau, *et al.*, "Tuning the surface Fermi level on p-type gallium nitride nanowires for efficient overall water splitting," *Nature Communications,* vol. 5, p. 3825, 2014.

[100] H. Liu, J. Yuan, Z. Jiang, W. Shangguan, H. Einaga, and Y. Teraoka, "Novel photocatalyst of V-based solid solutions for overall water splitting," *Journal of Materials Chemistry,* vol. 21, pp. 16535-16543, 2011.

[101] Y. Lee, H. Terashima, Y. Shimodaira, K. Teramura, M. Hara, H. Kobayashi, *et al.*, "Zinc Germanium Oxynitride as a Photocatalyst for Overall Water Splitting under Visible Light," *The Journal of Physical Chemistry C,* vol. 111, pp. 1042-1048, 2007.

[102] J.-W. Jang, C. Du, Y. Ye, Y. Lin, X. Yao, J. Thorne, *et al.*, "Enabling unassisted solar water splitting by iron oxide and silicon," *Nature Communications,* vol. 6, p. 7447, 2015.

[103] H. Kaneko, T. Minegishi, M. Nakabayashi, N. Shibata, Y. Kuang, T. Yamada, *et al.*, "A Novel Photocathode Material for Sunlight-Driven Overall Water Splitting: Solid Solution of ZnSe and Cu(In,Ga)Se_2," *Advanced Functional Materials,* vol. 26, pp. 4570-4577, 2016.

[104] J. H. Kim, H. Kaneko, T. Minegishi, J. Kubota, K. Domen, and J. S. Lee, "Overall Photoelectrochemical Water Splitting using Tandem Cell under Simulated Sunlight," *ChemSusChem,* vol. 9, pp. 61-66, 2016.

[105] Y.-H. Lai, D. W. Palm, and E. Reisner, "Multifunctional Coatings from Scalable Single Source Precursor Chemistry in Tandem Photoelectrochemical Water Splitting," *Advanced Energy Materials,* vol. 5, pp. n/a-n/a, 2015.

[106] P. Xu, J. Feng, T. Fang, X. Zhao, Z. Li, and Z. Zou, "Photoelectrochemical cell for unassisted overall solar water splitting using a $BiVO_4$ photoanode and Si nanoarray photocathode," *RSC Advances,* vol. 6, pp. 9905-9910, 2016.

[107] P. Bornoz, F. F. Abdi, S. D. Tilley, B. Dam, R. van de Krol, M. Graetzel, *et al.*, "A Bismuth Vanadate–Cuprous Oxide Tandem Cell for Overall Solar Water Splitting," *The Journal of Physical Chemistry C,* vol. 118, pp. 16959-16966, 2014.

[108] T. W. Kim and K.-S. Choi, "Nanoporous $BiVO_4$: Photoanodes with Dual-Layer Oxygen Evolution Catalysts for Solar Water Splitting," *Science,* vol. 343, p. 990, 2014.

[109] S. Rai, A. Ikram, S. Sahai, S. Dass, R. Shrivastav, and V. R. Satsangi, "Morphological, optical and photoelectrochemical properties of Fe_2O_3-GNP composite thin films," *RSC Advances,* vol. 4, pp. 17671-17679, 2014.

[110] J. L. Young, M. A. Steiner, H. Döscher, R. M. France, J. A. Turner, and Todd G. Deutsch, "Direct solar-to-hydrogen conversion via inverted metamorphic multi-junction semiconductor architectures," *Nature Energy,* vol. 2, p. 17028, 2017.

[111] B. AlOtaibi, S. Fan, S. Vanka, M. G. Kibria, and Z. Mi, "A Metal-Nitride Nanowire Dual-Photoelectrode Device for Unassisted Solar-to-Hydrogen Conversion under Parallel Illumination," *Nano Letters,* vol. 15, pp. 6821-6828, 2015.

[112] S. Ye, C. Ding, R. Chen, F. Fan, P. Fu, H. Yin*, et al.*, "Mimicking the Key Functions of Photosystem II in Artificial Photosynthesis for Photoelectrocatalytic Water Splitting," *Journal of the American Chemical Society,* 2018.

[113] W.-H. Cheng, M. H. Richter, M. M. May, J. Ohlmann, D. Lackner, F. Dimroth*, et al.*, "Monolithic photoelectrochemical device for 19% direct water splitting," *arXiv:1706.01493,* 2017.

[114] M. M. May, H.-J. Lewerenz, D. Lackner, F. Dimroth, and T. Hannappel, "Efficient direct solar-to-hydrogen conversion by in situ interface transformation of a tandem structure," *Nature Communications,* vol. 6, p. 8286, 2015.

[115] D. Kang, J. L. Young, H. Lim, W. E. Klein, H. Chen, Y. Xi*, et al.*, "Printed assemblies of GaAs photoelectrodes with decoupled optical and reactive interfaces for unassisted solar water splitting," *Nature Energy,* vol. 2, p. 17043, 2017.

[116] O. Khaselev and J. A. Turner, "A Monolithic Photovoltaic-Photoelectrochemical Device for Hydrogen Production via Water Splitting," *Science,* vol. 280, p. 425, 1998.

[117] S. Okamoto, M. Deguchi, and S. Yotsuhashi, "Modulated III–V Triple-Junction Solar Cell Wireless Device for Efficient Water Splitting," *The Journal of Physical Chemistry C,* vol. 121, pp. 1393-1398, 2017.

[118] J. Jia, L. C. Seitz, J. D. Benck, Y. Huo, Y. Chen, J. W. D. Ng*, et al.*, "Solar water splitting by photovoltaic-electrolysis with a solar-to-hydrogen efficiency over 30%," *Nature Communications,* vol. 7, p. 13237, 2016.

[119] S. Licht, B. Wang, S. Mukerji, T. Soga, M. Umeno, and H. Tributsch, "Efficient Solar Water Splitting, Exemplified by RuO_2-Catalyzed AlGaAs/Si Photoelectrolysis," *The Journal of Physical Chemistry B,* vol. 104, pp. 8920-8924, 2000.

[120] G. Peharz, F. Dimroth, and U. Wittstadt, "Solar hydrogen production by water splitting with a conversion efficiency of 18%," *International Journal of Hydrogen Energy,* vol. 32, pp. 3248-3252, 2007.

[121] O. Khaselev, A. Bansal, and J. A. Turner, "High-efficiency integrated multijunction photovoltaic/electrolysis systems for hydrogen production," *International Journal of Hydrogen Energy,* vol. 26, pp. 127-132, 2001.

[122] E. Verlage, S. Hu, R. Liu, R. J. R. Jones, K. Sun, C. Xiang*, et al.*, "A monolithically integrated, intrinsically safe, 10% efficient, solar-driven water-splitting system based on active, stable earth-abundant electrocatalysts in conjunction with tandem III-V light absorbers protected by amorphous TiO2 films," *Energy & Environmental Science,* vol. 8, pp. 3166-3172, 2015.

[123] N. A. Kelly and T. L. Gibson, "Design and characterization of a robust photoelectrochemical device to generate hydrogen using solar water splitting," *International Journal of Hydrogen Energy,* vol. 31, pp. 1658-1673, 2006.

[124] D. K. Lee and K.-S. Choi, "Enhancing long-term photostability of $BiVO_4$ photoanodes for solar water splitting by tuning electrolyte composition," *Nature Energy,* vol. 3, pp. 53-60, 2018.

[125] M. G. Kibria, H. P. T. Nguyen, K. Cui, S. Zhao, D. Liu, H. Guo*, et al.*, "One-Step Overall Water Splitting under Visible Light Using Multiband InGaN/GaN Nanowire Heterostructures," *ACS Nano,* vol. 7, pp. 7886-7893, 2013.

[126] D. Wang, A. Pierre, M. G. Kibria, K. Cui, X. Han, K. H. Bevan*, et al.*, "Wafer-level photocatalytic water splitting on GaN nanowire arrays grown by molecular beam epitaxy," *Nano letters,* vol. 11, pp. 2353-2357, 2011.

[127] A. Kubacka, M. Fernández-García, and G. Colón, "Advanced Nanoarchitectures for Solar Photocatalytic Applications," *Chemical Reviews,* vol. 112, pp. 1555-1614, 2012.

[128] H. Tong, S. Ouyang, Y. Bi, N. Umezawa, M. Oshikiri, and J. Ye, "Nano-photocatalytic Materials: Possibilities and Challenges," *Advanced Materials,* vol. 24, pp. 229-251, 2012.

[129] R. Godin, A. Kafizas, and J. R. Durrant, "Electron transfer dynamics in fuel producing photosystems," *Current Opinion in Electrochemistry,* vol. 2, pp. 136-143, 2017.

[130] A. J. Nozik, "p-n photoelectrolysis cells," *Applied Physics Letters,* vol. 29, pp. 150-153, 1976.

[131] F. Meng, J. Li, S. K. Cushing, M. Zhi, and N. Wu, "Solar Hydrogen Generation by Nanoscale p–n Junction of p-type Molybdenum Disulfide/n-type Nitrogen-Doped Reduced Graphene Oxide," *Journal of the American Chemical Society,* vol. 135, pp. 10286-10289, 2013.

[132] K. Zhang, W. Kim, M. Ma, X. Shi, and J. H. Park, "Tuning the charge transfer route by p-n junction catalysts embedded with CdS nanorods for simultaneous efficient hydrogen and oxygen evolution," *Journal of Materials Chemistry A,* vol. 3, pp. 4803-4810, 2015.

[133] O. Ahmed Zelekew and D.-H. Kuo, "A two-oxide nanodiode system made of double-layered p-type Ag_2O@n-type TiO_2 for rapid reduction of 4-nitrophenol," *Physical Chemistry Chemical Physics,* vol. 18, pp. 4405-4414, 2016.

[134] J. Liqiang, Q. Yichun, W. Baiqi, L. Shudan, J. Baojiang, Y. Libin, *et al.*, "Review of photoluminescence performance of nano-sized semiconductor materials and its relationships with photocatalytic activity," *Solar Energy Materials and Solar Cells,* vol. 90, pp. 1773-1787, 2006.

[135] S. F. Chen, J. P. Li, K. Qian, W. P. Xu, Y. Lu, W. X. Huang, *et al.*, "Large scale photochemical synthesis of M@TiO_2 nanocomposites (M = Ag, Pd, Au, Pt) and their optical properties, CO oxidation performance, and antibacterial effect," *Nano Research,* vol. 3, pp. 244-255, 2010.

[136] A. Bumajdad and M. Madkour, "Understanding the superior photocatalytic activity of noble metals modified titania under UV and visible light irradiation," *Physical Chemistry Chemical Physics,* vol. 16, pp. 7146-7158, 2014.

[137] Z. Lin, J. Li, Z. Zheng, L. Li, L. Yu, C. Wang, *et al.*, "A Floating Sheet for Efficient Photocatalytic Water Splitting," *Advanced Energy Materials,* vol. 6, pp. n/a-n/a, 2016.

[138] J. Yang, D. Wang, H. Han, and C. Li, "Roles of Cocatalysts in Photocatalysis and Photoelectrocatalysis," *Accounts of Chemical Research,* vol. 46, pp. 1900-1909, 2013.

[139] A. Li, T. Wang, X. Chang, W. Cai, P. Zhang, J. Zhang, *et al.*, "Spatial separation of oxidation and reduction co-catalysts for efficient charge separation: Pt@TiO_2@MnO_x hollow spheres for photocatalytic reactions," *Chemical Science,* vol. 7, pp. 890-895, 2016.

[140] S. J. A. Moniz, S. A. Shevlin, D. J. Martin, Z.-X. Guo, and J. Tang, "Visible-light driven heterojunction photocatalysts for water splitting - a critical review," *Energy & Environmental Science,* vol. 8, pp. 731-759, 2015.

[141] R. Li, X. Tao, R. Chen, F. Fan, and C. Li, "Synergetic Effect of Dual Co-catalysts on the Activity of p-Type Cu_2O Crystals with Anisotropic Facets," *Chemistry – A European Journal,* vol. 21, pp. 14337-14341, 2015.

[142] D. Wang, T. Hisatomi, T. Takata, C. Pan, M. Katayama, J. Kubota, *et al.*, "Core/Shell Photocatalyst with Spatially Separated Co-Catalysts for Efficient Reduction and Oxidation of Water," *Angewandte Chemie International Edition,* vol. 52, pp. 11252-11256, 2013.

[143] Q. Zhang, R. Li, Z. Li, A. Li, S. Wang, Z. Liang, *et al.*, "The dependence of photocatalytic activity on the selective and nonselective deposition of noble metal cocatalysts on the facets of rutile TiO_2," *Journal of Catalysis,* vol. 337, pp. 36-44, 2016.

[144] S. Min, F. Wang, and G. Lu, "Graphene-induced spatial charge separation for selective water splitting over TiO_2 photocatalyst," *Catalysis Communications,* vol. 80, pp. 28-32, 2016.

[145] R. Li, F. Zhang, D. Wang, J. Yang, M. Li, J. Zhu, *et al.*, "Spatial separation of photogenerated electrons and holes among {010} and {110} crystal facets of $BiVO_4$," *Nat Commun,* vol. 4, p. 1432, 2013.
[146] L. Mu, Y. Zhao, A. Li, S. Wang, Z. Wang, J. Yang, *et al.*, "Enhancing charge separation on high symmetry $SrTiO_3$ exposed with anisotropic facets for photocatalytic water splitting," *Energy & Environmental Science,* vol. 9, pp. 2463-2469, 2016.
[147] Q. Zhang, Z. Li, S. Wang, R. Li, X. Zhang, Z. Liang, *et al.*, "Effect of Redox Cocatalysts Location on Photocatalytic Overall Water Splitting over Cubic $NaTaO_3$ Semiconductor Crystals Exposed with Equivalent Facets," *ACS Catalysis,* vol. 6, pp. 2182-2191, 2016.
[148] R. Li, H. Han, F. Zhang, D. Wang, and C. Li, "Highly efficient photocatalysts constructed by rational assembly of dual-cocatalysts separately on different facets of $BiVO_4$," *Energy & Environmental Science,* vol. 7, pp. 1369-1376, 2014.
[149] N. S. Lewis, "Developing a scalable artificial photosynthesis technology through nanomaterials by design," *Nature Nanotechnology,* vol. 11, p. 1010, 2016.
[150] "File: Wurtzite polyhedra.png—Wikipedia, the free encyclopedia."
[151] J. Arbiol, S. Estradé, J. D. Prades, A. Cirera, F. Furtmayr, C. Stark, *et al.*, "Triple-twin domains in Mg doped GaN wurtzite nanowires: structural and electronic properties of this zinc-blende-like stacking," *Nanotechnology,* vol. 20, p. 145704, 2009.
[152] H. Hiroshi, "Properties of GaN and related compounds studied by means of Raman scattering," *Journal of Physics: Condensed Matter,* vol. 14, p. R967, 2002.
[153] Q. Wang, X. Liu, M. G. Kibria, S. Zhao, H. P. T. Nguyen, K. H. Li, *et al.*, "p-Type dopant incorporation and surface charge properties of catalyst-free GaN nanowires revealed by micro-Raman scattering and X-ray photoelectron spectroscopy," *Nanoscale,* vol. 6, pp. 9970-9976, 2014.
[154] H. P. T. Nguyen, S. Zhang, K. Cui, X. Han, S. Fathololoumi, M. Couillard, *et al.*, "p-Type Modulation Doped InGaN/GaN Dot-in-a-Wire White-Light-Emitting Diodes Monolithically Grown on Si(111)," *Nano Letters,* vol. 11, pp. 1919-1924, 2011.
[155] D. Holec, P. M. F. J. Costa, M. J. Kappers, and C. J. Humphreys, "Critical thickness calculations for InGaN/GaN," *Journal of Crystal Growth,* vol. 303, pp. 314-317, 2007.
[156] C.-Y. Wang, H. Groenzin, and M. J. Shultz, "Direct Observation of Competitive Adsorption between Methanol and Water on TiO_2: An in Situ Sum-Frequency Generation Study," *Journal of the American Chemical Society,* vol. 126, pp. 8094-8095, 2004.
[157] J. Schneider and D. W. Bahnemann, "Undesired Role of Sacrificial Reagents in Photocatalysis," *The Journal of Physical Chemistry Letters,* vol. 4, pp. 3479-3483, 2013.
[158] T. Kawai and T. Sakata, "Photocatalytic hydrogen production from liquid methanol and water," *Journal of the Chemical Society, Chemical Communications,* pp. 694-695, 1980.
[159] D. Zhuang and J. H. Edgar, "Wet etching of GaN, AlN, and SiC: a review," *Materials Science and Engineering: R: Reports,* vol. 48, pp. 1-46, 2005.
[160] W. Luo, B. Liu, Z. Li, Z. Xie, D. Chen, Z. Zou, *et al.*, "Stable response to visible light of InGaN photoelectrodes," *Applied Physics Letters,* vol. 92, p. 262110, 2008.
[161] Y. J. Hwang, C. H. Wu, C. Hahn, H. E. Jeong, and P. Yang, "Si/InGaN Core/Shell Hierarchical Nanowire Arrays and their Photoelectrochemical Properties," *Nano Letters,* vol. 12, pp. 1678-1682, 2012.
[162] T. D. Moustakas, "The role of extended defects on the performance of optoelectronic devices in nitride semiconductors," *physica status solidi (a),* vol. 210, pp. 169-174, 2013.
[163] J. S. Foresi and T. D. Moustakas, "Metal contacts to gallium nitride," *Applied Physics Letters,* vol. 62, pp. 2859-2861, 1993.

[164] L. Ivanova, S. Borisova, H. Eisele, M. Dähne, A. Laubsch, and P. Ebert, "Surface states and origin of the Fermi level pinning on nonpolar GaN($1\bar{1}00$) surfaces," *Applied Physics Letters,* vol. 93, p. 192110, 2008.

[165] K. Aryal, B. N. Pantha, J. Li, J. Y. Lin, and H. X. Jiang, "Hydrogen generation by solar water splitting using p-InGaN photoelectrochemical cells," *Applied Physics Letters,* vol. 96, p. 052110, 2010.

[166] B. AlOtaibi, H. P. T. Nguyen, S. Zhao, M. G. Kibria, S. Fan, and Z. Mi, "Highly Stable Photoelectrochemical Water Splitting and Hydrogen Generation Using a Double-Band InGaN/GaN Core/Shell Nanowire Photoanode," *Nano Letters,* vol. 13, pp. 4356-4361, 2013.

[167] R. Dahal, B. N. Pantha, J. Li, J. Y. Lin, and H. X. Jiang, "Realizing InGaN monolithic solar-photoelectrochemical cells for artificial photosynthesis," *Applied Physics Letters,* vol. 104, p. 143901, 2014.

[168] F. A. Chowdhury, Z. Mi, M. G. Kibria, and M. L. Trudeau, "Group III-nitride nanowire structures for photocatalytic hydrogen evolution under visible light irradiation," *APL Materials,* vol. 3, p. 104408, 2015.

[169] M. G. Kibria, F. A. Chowdhury, S. Zhao, B. AlOtaibi, M. L. Trudeau, H. Guo*, et al.*, "Visible light-driven efficient overall water splitting using p-type metal-nitride nanowire arrays," *Nat Commun,* vol. 6, 2015.

[170] M. Li, K. Gao, X. Wan, Q. Zhang, B. Kan, R. Xia*, et al.*, "Solution-processed organic tandem solar cells with power conversion efficiencies >12%," *Nat Photon,* vol. 11, pp. 85-90, 2017.

[171] K. Zhang, M. Ma, P. Li, D. H. Wang, and J. H. Park, "Water Splitting Progress in Tandem Devices: Moving Photolysis beyond Electrolysis," *Advanced Energy Materials,* vol. 6, pp. n/a-n/a, 2016.

[172] M. S. Prévot and K. Sivula, "Photoelectrochemical Tandem Cells for Solar Water Splitting," *The Journal of Physical Chemistry C,* vol. 117, pp. 17879-17893, 2013.

[173] J. Brillet, J.-H. Yum, M. Cornuz, T. Hisatomi, R. Solarska, J. Augustynski*, et al.*, "Highly efficient water splitting by a dual-absorber tandem cell," *Nat Photon,* vol. 6, pp. 824-828, 2012.

[174] S. Bai and Y. Xiong, "Some recent developments in surface and interface design for photocatalytic and electrocatalytic hybrid structures," *Chemical Communications,* vol. 51, pp. 10261-10271, 2015.

[175] R. Marschall, "Semiconductor Composites: Strategies for Enhancing Charge Carrier Separation to Improve Photocatalytic Activity," *Advanced Functional Materials,* vol. 24, pp. 2421-2440, 2014.

[176] M. Batzill, "Fundamental aspects of surface engineering of transition metal oxide photocatalysts," *Energy & Environmental Science,* vol. 4, pp. 3275-3286, 2011.

[177] A. Boonchun, N. Umezawa, T. Ohno, S. Ouyang, and J. Ye, "Role of photoexcited electrons in hydrogen evolution from platinum co-catalysts loaded on anatase TiO$_2$: a first-principles study," *Journal of Materials Chemistry A,* vol. 1, pp. 6664-6669, 2013.

[178] S. Mubeen, J. Lee, N. Singh, S. Kramer, G. D. Stucky, and M. Moskovits, "An autonomous photosynthetic device in which all charge carriers derive from surface plasmons," *Nat Nano,* vol. 8, pp. 247-251, 2013.

[179] Q. Wang, T. Hisatomi, Q. Jia, H. Tokudome, M. Zhong, C. Wang*, et al.*, "Scalable water splitting on particulate photocatalyst sheets with a solar-to-hydrogen energy conversion efficiency exceeding 1%," *Nat Mater,* vol. 15, pp. 611-615, 2016.

[180] C. R. Cox, J. Z. Lee, D. G. Nocera, and T. Buonassisi, "Ten-percent solar-to-fuel conversion with nonprecious materials," *Proceedings of the National Academy of Sciences,* vol. 111, pp. 14057-14061, 2014.

[181] M. H. Lee, K. Takei, J. Zhang, R. Kapadia, M. Zheng, Y.-Z. Chen*, et al.*, "p-Type InP Nanopillar Photocathodes for Efficient Solar-Driven Hydrogen Production," *Angewandte Chemie International Edition,* vol. 51, pp. 10760-10764, 2012.

[182] J. L. Young, M. A. Steiner, H. Döscher, R. M. France, J. A. Turner, and Todd G. Deutsch, "Direct solar-to-hydrogen conversion via inverted metamorphic multi-junction semiconductor architectures," *Nature Energy,* vol. 2, p. 201728, 2017.

[183] A. J. Nozik, "Photochemical diodes," *Applied Physics Letters,* vol. 30, pp. 567-569, 1977.

[184] T.-F. Yeh, C.-Y. Teng, S.-J. Chen, and H. Teng, "Nitrogen-Doped Graphene Oxide Quantum Dots as Photocatalysts for Overall Water-Splitting under Visible Light Illumination," *Advanced Materials,* vol. 26, pp. 3297-3303, 2014.

[185] H. Doscher, J. F. Geisz, T. G. Deutsch, and J. A. Turner, "Sunlight absorption in water - efficiency and design implications for photoelectrochemical devices," *Energy & Environmental Science,* vol. 7, pp. 2951-2956, 2014.

[186] M. Zhao, H. Xu, H. Chen, S. Ouyang, N. Umezawa, D. Wang*, et al.*, "Photocatalytic reactivity of {121} and {211} facets of brookite TiO_2 crystals," *Journal of Materials Chemistry A,* vol. 3, pp. 2331-2337, 2015.

[187] J. L. Giocondi and G. S. Rohrer, "Spatial Separation of Photochemical Oxidation and Reduction Reactions on the Surface of Ferroelectric $BaTiO_3$," *The Journal of Physical Chemistry B,* vol. 105, pp. 8275-8277, 2001.

[188] R. Li, Y. Weng, X. Zhou, X. Wang, Y. Mi, R. Chong*, et al.*, "Achieving overall water splitting using titanium dioxide-based photocatalysts of different phases," *Energy & Environmental Science,* vol. 8, pp. 2377-2382, 2015.

[189] S. Barbet, R. Aubry, M. A. di Forte-Poisson, J. C. Jacquet, D. Deresmes, T. Mélin*, et al.*, "Surface potential of n- and p-type GaN measured by Kelvin force microscopy," *Applied Physics Letters,* vol. 93, p. 212107, 2008.

[190] H. Sezen, E. Ozbay, O. Aktas, and S. Suzer, "Transient surface photovoltage in n- and p-GaN as probed by x-ray photoelectron spectroscopy," *Applied Physics Letters,* vol. 98, p. 111901, 2011.

[191] Z. Zhang and J. T. Yates, "Band Bending in Semiconductors: Chemical and Physical Consequences at Surfaces and Interfaces," *Chemical Reviews,* vol. 112, pp. 5520-5551, 2012.

[192] Y. Yang, M. Forster, Y. Ling, G. Wang, T. Zhai, Y. Tong*, et al.*, "Acid Treatment Enables Suppression of Electron–Hole Recombination in Hematite for Photoelectrochemical Water Splitting," *Angewandte Chemie,* vol. 128, pp. 3464-3468, 2016.

[193] M. R. Morris, S. R. Pendlebury, J. Hong, S. Dunn, and J. R. Durrant, "Effect of Internal Electric Fields on Charge Carrier Dynamics in a Ferroelectric Material for Solar Energy Conversion," *Advanced Materials,* vol. 28, pp. 7123-7128, 2016.

[194] H. Q. Doan, K. L. Pollock, and T. Cuk, "Transient optical diffraction of GaN/aqueous interfaces: Interfacial carrier mobility dependence on surface reactivity," *Chemical Physics Letters,* vol. 649, pp. 1-7, 2016.

[195] M. M. Waegele, X. Chen, D. M. Herlihy, and T. Cuk, "How Surface Potential Determines the Kinetics of the First Hole Transfer of Photocatalytic Water Oxidation," *Journal of the American Chemical Society,* vol. 136, pp. 10632-10639, 2014.

[196] D. Barreca, G. Carraro, A. Gasparotto, C. Maccato, M. E. A. Warwick, K. Kaunisto*, et al.*, "Fe_2O_3–TiO_2 Nano-heterostructure Photoanodes for Highly Efficient Solar Water Oxidation," *Advanced Materials Interfaces,* vol. 2, pp. n/a-n/a, 2015.

[197] S. Zhao, B. H. Le, D. P. Liu, X. D. Liu, M. G. Kibria, T. Szkopek, *et al.*, "p-Type InN Nanowires," *Nano Letters,* vol. 13, pp. 5509-5513, 2013.

[198] L. Liao, Q. Zhang, Z. Su, Z. Zhao, Y. Wang, Y. Li, *et al.*, "Efficient solar water-splitting using a nanocrystalline CoO photocatalyst," *Nature nanotechnology,* vol. 9, pp. 69-73, 2014.

[199] B. AlOtaibi, S. Fan, D. Wang, J. Ye, and Z. Mi, "Wafer-Level Artificial Photosynthesis for CO2 Reduction into CH4 and CO Using GaN Nanowires," *ACS Catalysis,* vol. 5, pp. 5342-5348, 2015.

[200] S. Fan, I. Shih, and Z. Mi, "A Monolithically Integrated InGaN Nanowire/Si Tandem Photoanode Approaching the Ideal Bandgap Configuration of 1.75/1.13 eV," *Advanced Energy Materials,* vol. 7, pp. n/a-n/a, 2017.

[201] J. Gu, Y. Yan, J. L. Young, K. X. Steirer, N. R. Neale, and J. A. Turner, "Water reduction by a p-GaInP2 photoelectrode stabilized by an amorphous TiO_2 coating and a molecular cobalt catalyst," *Nature Materials,* vol. 15, pp. 456, 2016.

[202] H. J. Ahn, K. Y. Yoon, M. J. Kwak, and J. H. Jang, "A Titanium-Doped SiOx Passivation Layer for Greatly Enhanced Performance of a Hematite-Based Photoelectrochemical System," *Angewandte Chemie-International Edition,* vol. 55, pp. 9922-9926, 2016.

[203] J. Sato, N. Saito, Y. Yamada, K. Maeda, T. Takata, J. N. Kondo, *et al.*, "RuO_2-loaded β-Ge_3N_4 as a non-oxide photocatalyst for overall water splitting," *Journal of the American Chemical Society,* vol. 127, pp. 4150-4151, 2005.

[204] F. A. Frame, T. K. Townsend, R. L. Chamousis, E. M. Sabio, T. Dittrich, N. D. Browning, *et al.*, "Photocatalytic water oxidation with nonsensitized IrO_2 nanocrystals under visible and UV light," *Journal of the American Chemical Society,* vol. 133, pp. 7264-7267, 2011.

[205] H. Kato, K. Asakura, and A. Kudo, "Highly efficient water splitting into H_2 and O_2 over lanthanum-doped $NaTaO_3$ photocatalysts with high crystallinity and surface nanostructure," *Journal of the American Chemical Society,* vol. 125, pp. 3082-3089, 2003.

[206] T. K. Townsend, N. D. Browning, and F. E. Osterloh, "Nanoscale Strontium Titanate Photocatalysts for Overall Water Splitting," *Acs Nano,* vol. 6, pp. 7420-7426, 2012.

[207] J. Yang, H. Yan, X. Zong, F. Wen, M. Liu, and C. Li, "Roles of cocatalysts in semiconductor-based photocatalytic hydrogen production," *Philosophical Transactions of the Royal Society of London A: Mathematical, Physical and Engineering Sciences,* vol. 371, 2013.

[208] Y. Wang, T. Zhou, K. Jiang, P. Da, Z. Peng, J. Tang, *et al.*, "Reduced mesoporous Co_3O_4 nanowires as efficient water oxidation electrocatalysts and supercapacitor electrodes," *Advanced Energy Materials,* vol. 4, 2014.

[209] H. Tüysüz, Y. J. Hwang, S. B. Khan, A. M. Asiri, and P. Yang, "Mesoporous Co_3O_4 as an electrocatalyst for water oxidation," *Nano Research,* vol. 6, pp. 47-54, 2013.

[210] M. Liao, J. Feng, W. Luo, Z. Wang, J. Zhang, Z. Li, *et al.*, "Co_3O_4 Nanoparticles as Robust Water Oxidation Catalysts Towards Remarkably Enhanced Photostability of a Ta_3N_5 Photoanode," *Advanced Functional Materials,* vol. 22, pp. 3066-3074, 2012.

[211] Y. Hou, F. Zuo, A. P. Dagg, J. Liu, and P. Feng, "Branched WO_3 nanosheet array with layered C_3N_4 heterojunctions and CoO_x nanoparticles as a flexible photoanode for efficient photoelectrochemical water oxidation," *Advanced Materials,* vol. 26, pp. 5043-5049, 2014.

[212] F. Zhang, A. Yamakata, K. Maeda, Y. Moriya, T. Takata, J. Kubota, *et al.*, "Cobalt-Modified Porous Single-Crystalline $LaTiO_2N$ for Highly Efficient Water Oxidation under Visible Light," *Journal of the American Chemical Society,* vol. 134, pp. 8348-8351, 2012.

[213] L. Hu, Q. Peng, and Y. Li, "Selective Synthesis of Co_3O_4 Nanocrystal with Different Shape and Crystal Plane Effect on Catalytic Property for Methane Combustion," *Journal of the American Chemical Society,* vol. 130, pp. 16136-16137, 2008.

[214] P. Zhang, T. Wang, X. Chang, L. Zhang, and J. Gong, "Synergistic cocatalytic effect of carbon nanodots and Co_3O_4 nanoclusters for the photoelectrochemical water oxidation on hematite," *Angewandte Chemie International Edition,* vol. 55, pp. 5851-5855, 2016.

[215] S. C. Riha, B. M. Klahr, E. C. Tyo, S. n. Seifert, S. Vajda, M. J. Pellin*, et al.*, "Atomic layer deposition of a submonolayer catalyst for the enhanced photoelectrochemical performance of water oxidation with hematite," *ACS nano,* vol. 7, pp. 2396-2405, 2013.

[216] M. Kibria, F. Chowdhury, S. Zhao, B. AlOtaibi, M. Trudeau, H. Guo*, et al.*, "Visible light-driven efficient overall water splitting using p-type metal-nitride nanowire arrays," *Nature communications,* vol. 6, p. 6797, 2015.

[217] K. Maeda, K. Teramura, D. Lu, N. Saito, Y. Inoue, and K. Domen, "Roles of Rh/Cr_2O_3 (Core/Shell) Nanoparticles Photodeposited on Visible-light-responsive $(Ga_{1-x}Zn_x)(N_{1-x}O_x)$ Solid Solutions in Photocatalytic Overall Water Splitting," *The Journal of Physical Chemistry C,* vol. 111, pp. 7554-7560, 2007.

[218] K. Maeda, K. Teramura, D. Lu, N. Saito, Y. Inoue, and K. Domen, "Roles of Rh/Cr_2O_3 (core/shell) nanoparticles photodeposited on visible-light-responsive $(Ga_{1-x}Zn_x)(N_{1-x}O_x)$ solid solutions in photocatalytic overall water splitting," *Journal of Physical Chemistry C,* vol. 111, pp. 7554-7560, 2007.

[219] Y. Liang, Y. Li, H. Wang, J. Zhou, J. Wang, T. Regier*, et al.*, "Co_3O_4 nanocrystals on graphene as a synergistic catalyst for oxygen reduction reaction," *Nature materials,* vol. 10, pp. 780-786, 2011.

[220] M. G. Kibria, R. Qiao, W. Yang, I. Boukahil, X. Kong, F. A. Chowdhury*, et al.*, "Atomic-Scale Origin of Long-Term Stability and High Performance of p-GaN Nanowire Arrays for Photocatalytic Overall Pure Water Splitting," *Advanced Materials,* vol. 28, pp. 8388-8397, 2016.

[221] M. Kibria, S. Zhao, F. Chowdhury, Q. Wang, H. Nguyen, M. Trudeau*, et al.*, "Tuning the surface Fermi level on p-type gallium nitride nanowires for efficient overall water splitting," *Nature communications,* vol. 5, p. 5825, 2014.

[222] M. Kibria, S. Zhao, F. Chowdhury, Q. Wang, H. Nguyen, M. Trudeau*, et al.*, "Tuning the surface Fermi level on p-type gallium nitride nanowires for efficient overall water splitting," *Nature communications,* vol. 5, 2014.

[223] K. Maeda, A. Xiong, T. Yoshinaga, T. Ikeda, N. Sakamoto, T. Hisatomi*, et al.*, "Photocatalytic overall water splitting promoted by two different cocatalysts for hydrogen and oxygen evolution under visible light," *Angewandte Chemie,* vol. 122, pp. 4190-4193, 2010.

[224] T. Ohno, L. Bai, T. Hisatomi, K. Maeda, and K. Domen, "Photocatalytic water splitting using modified GaN:ZnO solid solution under visible light: long-time operation and regeneration of activity," *Journal of the American Chemical Society,* vol. 134, pp. 8254-8259, 2012.

[225] R. G. Li, H. X. Han, F. X. Zhang, D. G. Wang, and C. Li, "Highly efficient photocatalysts constructed by rational assembly of dual-cocatalysts separately on different facets of $BiVO_4$," *Energy & Environmental Science,* vol. 7, pp. 1369-1376, 2014.

[226] A. Yamakata, M. Kawaguchi, N. Nishimura, T. Minegishi, J. Kubota, and K. Domen, "Behavior and Energy States of Photogenerated Charge Carriers on Pt-or CoO_x-Loaded $LaTiO_2N$ Photocatalysts: Time-Resolved Visible to Mid-Infrared Absorption Study," *The Journal of Physical Chemistry C,* vol. 118, pp. 23897-23906, 2014.

[227] M. Kibria, F. Chowdhury, S. Zhao, B. AlOtaibi, M. Trudeau, H. Guo*, et al.*, "Visible light-driven efficient overall water splitting using p-type metal-nitride nanowire arrays," *Nature communications,* vol. 6, 2015.

[228] M. G. Kibria, R. Qiao, W. Yang, I. Boukahil, X. Kong, F. A. Chowdhury, *et al.*, "Atomic-Scale Origin of Long-Term Stability and High Performance of p-GaN Nanowire Arrays for Photocatalytic Overall Pure Water Splitting," *Advanced Materials,* 2016.

[229] Y. L. Chang, F. Li, A. Fatehi, and Z. T. Mi, "Molecular beam epitaxial growth and characterization of non-tapered InN nanowires on Si(111)," *Nanotechnology,* vol. 20, p. 6, 2009.

[230] H. L. Wang, T. Deutsch, A. Welch, and J. A. Turner, "The stability of illuminated p-$GaInP_2$ semiconductor photoelectrode," *International Journal of Hydrogen Energy,* vol. 37, pp. 14009-14014, 2012.

[231] M. Zhong, T. Hisatomi, Y. Sasaki, S. Suzuki, K. Teshima, M. Nakabayashi, *et al.*, "Highly Active GaN-Stabilized Ta_3N_5 Thin-Film Photoanode for Solar Water Oxidation," *Angewandte Chemie-International Edition,* vol. 56, pp. 4739-4743, 2017.

[232] J. A. Turner, "A Realizable Renewable Energy Future," *Science,* vol. 285, p. 687, 1999.

[233] C. Pan, T. Takata, M. Nakabayashi, T. Matsumoto, N. Shibata, Y. Ikuhara, *et al.*, "A Complex Perovskite-Type Oxynitride: The First Photocatalyst for Water Splitting Operable at up to 600 nm," *Angewandte Chemie International Edition,* vol. 54, pp. 2955-2959, 2015.

[234] S. Nakamura, M. Senoh, and T. Mukai, "High-power InGaN/GaN double-heterostructure violet light emitting diodes," *Applied Physics Letters,* vol. 62, pp. 2390-2392, 1993.

[235] S. Nakamura, T. Mukai, and M. Senoh, "High-brightness InGaN/AlGaN double-heterostructure blue-green-light-emitting diodes," *Journal of Applied Physics,* vol. 76, pp. 8189-8191, 1994.

[236] S. Nakamura, "III-V nitride-based light-emitting diodes," *Diamond and Related Materials,* vol. 5, pp. 496-500, 1996.

[237] S. Nakamura, "InGaN-based blue/green LEDs and laser diodes," *Advanced Materials,* vol. 8, pp. 689-692, 1996.

[238] S. Strite and H. Morkoç, "GaN, AlN, and InN: A review," *Journal of Vacuum Science & Technology B,* vol. 10, pp. 1237-1266, 1992.

[239] K. Kim, W. R. L. Lambrecht, and B. Segall, "Elastic constants and related properties of tetrahedrally bonded BN, AlN, GaN, and InN," *Physical Review B,* vol. 53, pp. 16310-16326, 1996.

[240] A. F. Wright, "Elastic properties of zinc-blende and wurtzite AlN, GaN, and InN," *Journal of Applied Physics,* vol. 82, pp. 2833-2839, 1997.

[241] F. Bernardini and V. Fiorentini, "Spontaneous versus Piezoelectric Polarization in III–V Nitrides: Conceptual Aspects and Practical Consequences," *physica status solidi (b),* vol. 216, pp. 391-398, 1999.

[242] A. E. Romanov, T. J. Baker, S. Nakamura, and J. S. Speck, "Strain-induced polarization in wurtzite III-nitride semipolar layers," Journal of Applied Physics, vol. 100, p. 023522, 2006.

[243] N. Segercrantz, K. M. Yu, M. Ting, W. L. Sarney, S. P. Svensson, S. V. Novikov, *et al.*, "Electronic band structure of highly mismatched $GaN_{1-x}Sb_x$ alloys in a broad composition range," *Applied Physics Letters,* vol. 107, p. 142104, 2015.

[244] A. X. Levander, K. M. Yu, S. V. Novikov, A. Tseng, C. T. Foxon, O. D. Dubon, *et al.*, "$GaN_{1-x}Bi_x$: Extremely mismatched semiconductor alloys," *Applied Physics Letters,* vol. 97, p. 141919, 2010.

[245] R. M. Sheetz, E. Richter, A. N. Andriotis, S. Lisenkov, C. Pendyala, M. K. Sunkara, *et al.*, "Visible-light absorption and large band-gap bowing of $GaN_{1-x}Sb_x$ from first principles," *Physical Review B,* vol. 84, p. 075304, 2011.

[246] S. Sunkara, V. K. Vendra, J. B. Jasinski, T. Deutsch, A. N. Andriotis, K. Rajan, *et al.*, "New Visible Light Absorbing Materials for Solar Fuels, Ga(Sb_x)N_{1-x}," *Advanced Materials,* vol. 26, pp. 2878-2882, 2014.

[247] K. M. Yu, W. L. Sarney, S. V. Novikov, D. Detert, R. Zhao, J. D. Denlinger, *et al.*, "Highly mismatched N-rich $GaN_{1-x}Sb_x$ films grown by low temperature molecular beam epitaxy," *Applied Physics Letters,* vol. 102, p. 102104, 2013.

[248] S. V. Novikov, K. M. Yu, A. Levander, D. Detert, W. L. Sarney, Z. Liliental-Weber, *et al.*, "Molecular beam epitaxy of highly mismatched N-rich $GaN_{1-x}Sb_x$ and $InN_{1-x}As_x$ alloys," *Journal of Vacuum Science & Technology B,* vol. 31, p. 03C102, 2013.

[249] W. L. Sarney, S. P. Svensson, S. V. Novikov, K. M. Yu, W. Walukiewicz, and C. T. Foxon, "$GaN_{1-x}Sb_x$ highly mismatched alloys grown by low temperature molecular beam epitaxy under Ga-rich conditions," *Journal of Crystal Growth,* vol. 383, pp. 95-99, 2013.

[250] W. L. Sarney, S. P. Svensson, S. V. Novikov, K. M. Yu, W. Walukiewicz, M. Ting, *et al.*, "Exploration of the growth parameter space for MBE-grown $GaN_{1-x}Sb_x$ highly mismatched alloys," *Journal of Crystal Growth,* vol. 425, pp. 255-257, 2015.

[251] E. Artacho, D. Sánchez-Portal, P. Ordejón, A. García, and J. M. Soler, "Linear-Scaling ab-initio Calculations for Large and Complex Systems," *physica status solidi (b),* vol. 215, pp. 809-817, 1999.

[252] C.-K. Skylaris, P. D. Haynes, A. A. Mostofi, and M. C. Payne, "Introducing ONETEP: Linear-scaling density functional simulations on parallel computers," *The Journal of Chemical Physics,* vol. 122, p. 084119, 2005.

[253] M. Shaw, K. M. Yu, M. Ting, R. E. L. Powell, W. L. Sarney, S. P. Svensson, *et al.*, "Composition and optical properties of dilute-Sb $GaN_{1-x}Sb_x$ highly mismatched alloys grown by MBE," *Journal of Physics D: Applied Physics,* vol. 47, p. 465102, 2014.

[254] V. Michaud-Rioux, L. Zhang, and H. Guo, "RESCU: A real space electronic structure method," *Journal of Computational Physics,* vol. 307, pp. 593-613, 2016.

[255] Y.-C. Chen, J.-Z. Chen, V. Michaud-Rioux, L. Zhang, and H. Guo, *McGill University preprint.,* 2016.

[256] D. R. Hamann, "Optimized norm-conserving Vanderbilt pseudopotentials," *Physical Review B,* vol. 88, p. 085117, 2013.

[257] K. Alberi, J. Wu, W. Walukiewicz, K. M. Yu, O. D. Dubon, S. P. Watkins, *et al.*, "Valence-band anticrossing in mismatched III-V semiconductor alloys," *Physical Review B,* vol. 75, p. 045203, 2007.

[258] A. Zunger, S. H. Wei, L. G. Ferreira, and J. E. Bernard, "Special quasirandom structures," *Physical Review Letters,* vol. 65, pp. 353-356, 1990.

[259] Q. Shi, Y.-C. Chen, F. A. Chowdhury, Z. Mi, V. Michaud-Rioux, and H. Guo, "Band engineering of GaSbN alloy for solar fuel applications," *Physical Review Materials,* vol. 1, p. 034602, 2017.

[260] C. Yi-Lu, L. Feng, F. Arya, and M. Zetian, "Molecular beam epitaxial growth and characterization of non-tapered InN nanowires on Si(111)," *Nanotechnology,* vol. 20, p. 345203, 2009.

[261] Y. L. Chang, F. Li, and Z. Mi, "Optimization of the structural and optical quality of InN nanowires on Si(111) by molecular beam epitaxy," *Journal of Vacuum Science & Technology B, Nanotechnology and Microelectronics: Materials, Processing, Measurement, and Phenomena,* vol. 28, pp. C3B7-C3B11, 2010.

[262] A. Hierro, A. R. Arehart, B. Heying, M. Hansen, U. K. Mishra, S. P. DenBaars, *et al.*, "Impact of Ga/N flux ratio on trap states in n-GaN grown by plasma-assisted molecular-beam epitaxy," *Applied Physics Letters,* vol. 80, pp. 805-807, 2002.

[263] D. J. As, T. Frey, D. Schikora, K. Lischka, V. Cimalla, J. Pezoldt, *et al.*, "Cubic GaN epilayers grown by molecular beam epitaxy on thin β-SiC/Si (001) substrates," *Applied Physics Letters,* vol. 76, pp. 1686-1688, 2000.

[264] D. Sansaptak, Nidhi, W. Feng, S. S. James, and K. M. Umesh, "Growth and Characterization of N-Polar GaN Films on Si(111) by Plasma Assisted Molecular Beam Epitaxy," *Japanese Journal of Applied Physics,* vol. 51, p. 115503, 2012.

[265] B. M. McSkimming, C. Chaix, and J. S. Speck, "High active nitrogen flux growth of GaN by plasma assisted molecular beam epitaxy," *Journal of Vacuum Science & Technology A,* vol. 33, p. 05E128, 2015.

[266] W. Wang, H. Wang, W. Yang, Y. Zhu, and G. Li, "A new approach to epitaxially grow high-quality GaN films on Si substrates: the combination of MBE and PLD," *Scientific Reports,* vol. 6, p. 24448, 2016.

[267] K. M. Yu, S. V. Novikov, M. Ting, W. L. Sarney, S. P. Svensson, M. Shaw, *et al.*, "Growth and characterization of highly mismatched GaN1−xSbx alloys," *Journal of Applied Physics,* vol. 116, p. 123704, 2014.

[268] F. A. Chowdhury, S. M. Sadaf, Q. Shi, Y.-C. Chen, H. Guo, and Z. Mi, "Optically active dilute-antimonide III-nitride nanostructures for optoelectronic devices," *Applied Physics Letters,* vol. 111, p. 061101, 2017.

[269] A. Kaschner, H. Siegle, G. Kaczmarczyk, M. Straßburg, A. Hoffmann, C. Thomsen, *et al.*, "Local vibrational modes in Mg-doped GaN grown by molecular beam epitaxy," *Applied Physics Letters,* vol. 74, pp. 3281-3283, 1999.

[270] R. Cuscó, L. Artús, D. Pastor, F. B. Naranjo, and E. Calleja, "Local vibrational modes of H complexes in Mg-doped GaN grown by molecular beam epitaxy," *Applied Physics Letters,* vol. 84, pp. 897-899, 2004.

[271] J. H. D. d. Silva, S. W. d. Silva, and J. C. Galzerani, "Crystallization process of amorphous GaSb films studied by Raman spectroscopy," *Journal of Applied Physics,* vol. 77, pp. 4044-4048, 1995.

[272] C. E. M. Campos and P. S. Pizani, "Morphological studies of annealed GaAs and GaSb surfaces by micro-Raman spectroscopy and EDX microanalysis," *Applied Surface Science,* vol. 200, pp. 111-116, 2002.

[273] Y.-L. Chang, J. L. Wang, F. Li, and Z. Mi, "High efficiency green, yellow, and amber emission from InGaN/GaN dot-in-a-wire heterostructures on Si(111)," *Applied Physics Letters,* vol. 96, p. 013106, 2010.

[274] S. M. Sadaf, Y. H. Ra, T. Szkopek, and Z. Mi, "Monolithically Integrated Metal/Semiconductor Tunnel Junction Nanowire Light-Emitting Diodes," *Nano Letters,* vol. 16, pp. 1076-1080, 2016.

[275] H. P. T. Nguyen, S. Zhang, A. T. Connie, M. G. Kibria, Q. Wang, I. Shih, *et al.*, "Breaking the Carrier Injection Bottleneck of Phosphor-Free Nanowire White Light-Emitting Diodes," *Nano Letters,* vol. 13, pp. 5437-5442, 2013.

[276] S. Zhang, A. T. Connie, D. A. Laleyan, H. P. T. Nguyen, Q. Wang, J. Song, *et al.*, "On the Carrier Injection Efficiency and Thermal Property of InGaN/GaN Axial Nanowire Light Emitting Diodes," *IEEE Journal of Quantum Electronics,* vol. 50, pp. 483-490, 2014.

[277] H. P. T. Nguyen, M. Djavid, S. Y. Woo, X. Liu, A. T. Connie, S. Sadaf, *et al.*, "Engineering the Carrier Dynamics of InGaN Nanowire White Light-Emitting Diodes by Distributed p-AlGaN Electron Blocking Layers," *Scientific Reports,* vol. 5, p. 7744, 2015.

[278] S. M. Sadaf, S. Zhao, Y. Wu, Y. H. Ra, X. Liu, S. Vanka, *et al.*, "An AlGaN Core–Shell Tunnel Junction Nanowire Light-Emitting Diode Operating in the Ultraviolet-C Band," *Nano Letters,* vol. 17, pp. 1212-1218, 2017.

[279] S. Fan, B. AlOtaibi, S. Y. Woo, Y. Wang, G. A. Botton, and Z. Mi, "High Efficiency Solar-to-Hydrogen Conversion on a Monolithically Integrated InGaN/GaN/Si Adaptive Tunnel Junction Photocathode," *Nano Letters,* vol. 15, pp. 2721-2726, 2015.

[280] B. AlOtaibi, X. Kong, S. Vanka, S. Y. Woo, A. Pofelski, F. Oudjedi*, et al.*, "Photochemical Carbon Dioxide Reduction on Mg-Doped Ga(In)N Nanowire Arrays under Visible Light Irradiation," *ACS Energy Letters,* vol. 1, pp. 246-252, 2016.

[281] Y. Wang, S. Fan, B. AlOtaibi, Y. Wang, L. Li, and Z. Mi, "A Monolithically Integrated Gallium Nitride Nanowire/Silicon Solar Cell Photocathode for Selective Carbon Dioxide Reduction to Methane," *Chemistry – A European Journal,* vol. 22, pp. 8809-8813, 2016.

[282] M. César, Y. Ke, W. Ji, H. Guo, and Z. Mi, "Band gap of $In_xGa_{1-x}N$: A first principles analysis," *Applied Physics Letters,* vol. 98, p. 202107, 2011.

[283] J. S. Harris Jr, "The opportunities, successes and challenges for GaInNAsSb," *Journal of Crystal Growth,* vol. 278, pp. 3-17, 2005.

[284] W. Ha, V. Gambin, S. Bank, M. Wistey, H. Yuen, K. Seongsin*, et al.*, "Long-wavelength GaInNAs(Sb) lasers on GaAs," *Quantum Electronics, IEEE Journal of,* vol. 38, pp. 1260-1267, 2002.

[285] K. Volz, V. Gambin, W. Ha, M. A. Wistey, H. Yuen, S. Bank*, et al.*, "The role of Sb in the MBE growth of (GaIn)(NAsSb)," *Journal of Crystal Growth,* vol. 251, pp. 360-366, 2003.

[286] L. H. Li, V. Sallet, G. Patriarche, L. Largeau, S. Bouchoule, L. Travers*, et al.*, "Investigations on GaInNAsSb quinary alloy for 1.5 μm laser emission on GaAs," *Applied Physics Letters,* vol. 83, pp. 1298-1300, 2003.

[287] X. Yang, M. J. Jurkovic, J. B. Heroux, and W. I. Wang, "Molecular beam epitaxial growth of InGaAsN:Sb/GaAs quantum wells for long-wavelength semiconductor lasers," *Applied Physics Letters,* vol. 75, pp. 178-180, 1999.

[288] S. R. Bank, M. A. Wistey, L. L. Goddard, H. B. Yuen, V. Lordi, and J. S. Harris, "Low-threshold continuous-wave 1.5-μm GaInNAsSb lasers grown on GaAs," *Quantum Electronics, IEEE Journal of,* vol. 40, pp. 656-664, 2004.

[289] M. R. Correia, S. Pereira, E. Pereira, J. Frandon, and E. Alves, "Raman study of the A_1(LO) phonon in relaxed and pseudomorphic InGaN epilayers," *Applied Physics Letters,* vol. 83, pp. 4761-4763, 2003.

[290] D. Alexson, L. Bergman, R. J. Nemanich, M. Dutta, M. A. Stroscio, C. A. Parker*, et al.*, "Ultraviolet Raman study of A_1(LO) and E_2 phonons in $In_xGa_{1-x}N$ alloys," *Journal of Applied Physics,* vol. 89, pp. 798-800, 2000.

[291] Y.-H. Ra, R. Wang, S. Y. Woo, M. Djavid, S. M. Sadaf, J. Lee*, et al.*, "Full-Color Single Nanowire Pixels for Projection Displays," *Nano Letters,* vol. 16, pp. 4608-4615, 2016.

[292] H. Sekiguchi, K. Kishino, and A. Kikuchi, "Emission color control from blue to red with nanocolumn diameter of InGaN/GaN nanocolumn arrays grown on same substrate," *Applied Physics Letters,* vol. 96, p. 231104, 2010.

[293] X. Shen, P. B. Allen, M. S. Hybertsen, and J. T. Muckerman, "Water Adsorption on the GaN ($10\bar{1}0$) Nonpolar Surface," *The Journal of Physical Chemistry C,* vol. 113, pp. 3365-3368, 2009.

[294] M. Z. Ertem, N. Kharche, V. S. Batista, M. S. Hybertsen, J. C. Tully, and J. T. Muckerman, "Photoinduced Water Oxidation at the Aqueous GaN ($10\bar{1}0$) Interface: Deprotonation Kinetics of the First Proton-Coupled Electron-Transfer Step," *ACS Catalysis,* vol. 5, pp. 2317-2323, 2015.

[295] K. M. H. Young and T. W. Hamann, "Enhanced photocatalytic water oxidation efficiency with $Ni(OH)_2$ catalysts deposited on α-Fe_2O_3 via ALD," *Chemical Communications,* vol. 50, pp. 8727-8730, 2014.

[296] B. Klahr, S. Gimenez, F. Fabregat-Santiago, T. Hamann, and J. Bisquert, "Water Oxidation at Hematite Photoelectrodes: The Role of Surface States," *Journal of the American Chemical Society,* vol. 134, pp. 4294-4302, 2012.

[297] B. Klahr and T. Hamann, "Water Oxidation on Hematite Photoelectrodes: Insight into the Nature of Surface States through In Situ Spectroelectrochemistry," *The Journal of Physical Chemistry C,* vol. 118, pp. 10393-10399, 2014.

[298] K. M. H. Young, B. M. Klahr, O. Zandi, and T. W. Hamann, "Photocatalytic water oxidation with hematite electrodes," *Catalysis Science & Technology,* vol. 3, pp. 1660-1671, 2013.

[299] M. W. Kanan and D. G. Nocera, "In Situ Formation of an Oxygen-Evolving Catalyst in Neutral Water Containing Phosphate and Co^{2+}," *Science,* vol. 321, p. 1072, 2008.

[300] D. K. Zhong, M. Cornuz, K. Sivula, M. Gratzel, and D. R. Gamelin, "Photo-assisted electrodeposition of cobalt-phosphate (Co-Pi) catalyst on hematite photoanodes for solar water oxidation," *Energy & Environmental Science,* vol. 4, pp. 1759-1764, 2011.

[301] F. Le Formal, N. Tetreault, M. Cornuz, T. Moehl, M. Gratzel, and K. Sivula, "Passivating surface states on water splitting hematite photoanodes with alumina overlayers," *Chemical Science,* vol. 2, pp. 737-743, 2011.

[302] S. D. Tilley, M. Cornuz, K. Sivula, and M. Grätzel, "Light-Induced Water Splitting with Hematite: Improved Nanostructure and Iridium Oxide Catalysis," *Angewandte Chemie International Edition,* vol. 49, pp. 6405-6408, 2010.

[303] Z. Sun, H. Zheng, J. Li, and P. Du, "Extraordinarily efficient photocatalytic hydrogen evolution in water using semiconductor nanorods integrated with crystalline Ni_2P cocatalysts," *Energy & Environmental Science*, vol. 8, 2015.

[304] M. Zhong, T. Hisatomi, Y. Kuang, J. Zhao, M. Liu, A. Iwase*, et al.*, "Surface Modification of CoOx Loaded $BiVO_4$ Photoanodes with Ultrathin p-Type NiO Layers for Improved Solar Water Oxidation," *Journal of the American Chemical Society,* vol. 137, pp. 5053-5060, 2015.

[305] J. Wang, F. Demangeot, R. Péchou, A. Ponchet, A. Cros, and B. Daudin, "Anticrossing of axial and planar surface-related phonon modes in Raman spectra of self-assembled GaN nanowires," *Physical Review B,* vol. 85, p. 155432, 2012.